

THE INFLUENCE OF SEA ICE AND HYDROGRAPHY ON THE TIMING,  
DISTRIBUTION, AND INTENSITY OF PHYTOPLANKTON BLOOMS IN THE  
RAPIDLY CHANGING CHUKCHI SEA (ARCTIC OCEAN)

A DISSERTATION  
SUBMITTED TO THE DEPARTMENT OF EARTH SYSTEM SCIENCE  
AND THE COMMITTEE ON GRADUATE STUDIES  
OF STANFORD UNIVERSITY  
IN PARTIAL FULFILLMENT OF THE REQUIREMENTS  
FOR THE DEGREE OF  
DOCTOR OF PHILOSOPHY

Kate Elizabeth Lowry

November 2016

© 2016 by Kate Elizabeth Lowry. All Rights Reserved.

Re-distributed by Stanford University under license with the author.



This work is licensed under a Creative Commons Attribution-Noncommercial 3.0 United States License.

<http://creativecommons.org/licenses/by-nc/3.0/us/>

This dissertation is online at: <http://purl.stanford.edu/vz619fm8134>

I certify that I have read this dissertation and that, in my opinion, it is fully adequate in scope and quality as a dissertation for the degree of Doctor of Philosophy.

**Kevin Arrigo, Primary Adviser**

I certify that I have read this dissertation and that, in my opinion, it is fully adequate in scope and quality as a dissertation for the degree of Doctor of Philosophy.

**Karen Casciotti**

I certify that I have read this dissertation and that, in my opinion, it is fully adequate in scope and quality as a dissertation for the degree of Doctor of Philosophy.

**Rob Dunbar**

I certify that I have read this dissertation and that, in my opinion, it is fully adequate in scope and quality as a dissertation for the degree of Doctor of Philosophy.

**Leif Thomas**

Approved for the Stanford University Committee on Graduate Studies.

**Patricia J. Gumport, Vice Provost for Graduate Education**

*This signature page was generated electronically upon submission of this dissertation in electronic format. An original signed hard copy of the signature page is on file in University Archives.*

# Abstract

This dissertation examines the influence of sea ice and hydrography on phytoplankton blooms in the seasonally ice-covered Chukchi Sea in the western Arctic Ocean, where rapidly changing environmental conditions are dramatically altering marine ecosystems. Motivated in large part by the discovery of a massive under-ice phytoplankton bloom in 2011 during the NASA-funded Impacts of Climate on EcoSystems and Chemistry of the Arctic Pacific Environment (ICESCAPE) program, this research seeks to elucidate phytoplankton bloom dynamics in the Chukchi Sea. Signaling a potentially major ecosystem transition, the unexpected discovery indicated that recent reductions in sea ice thickness and age have transformed the under-ice light environment through the presence of expansive melt ponds that transmit sufficient light for photosynthesis, resulting in a shift in bloom timing to earlier in the year, prior to sea ice retreat. Through studies of the spatial and temporal distribution of under-ice blooms, physical drivers of phytoplankton bloom development, and characteristics of the under-ice environment that contribute to extraordinary phytoplankton growth beneath the ice, the objective of this work is to improve our understanding of this highly productive yet relatively understudied region. My approach in this research combines satellite remote sensing of ocean color and sea ice with observational and experimental fieldwork as part of four polar oceanographic expeditions aboard *USCGC Healy*.

In Chapter 1, I use satellite imagery to map evidence of under-ice blooms over the 15-year satellite record in the Chukchi Sea and distinguish them from marginal ice zone blooms that begin after sea ice retreat. Results of this work demonstrate that under-ice blooms have been prevalent for more than a decade prior to shipboard observations and are likely widespread across the region. To understand what factors control phytoplankton bloom distributions and magnitude, in Chapter 2, I relate phytoplankton abundance to hydrography and show that nutrient-rich winter water pathways in the Chukchi Sea are consistently associated with phytoplankton blooms both under the ice and in open water.

The culmination of this study is a new conceptual model for phytoplankton blooms in the Chukchi Sea that links the flow of highly productive winter water pathways to the presence of biological hotspots. In Chapter 3, I use novel early-season measurements of spring under-ice phytoplankton, nutrients, and hydrography to understand physical controls on the development of phytoplankton blooms in ice-covered waters. Results of this work illustrate that blooms form in stratified waters beneath fully consolidated sea ice, while enhanced convective mixing beneath sea ice with leads impedes the development of under-ice blooms through vertical mixing that reduces light availability in the upper mixed layer. Characteristics of the under-ice light environment are further explored in Chapter 4, in which I present results from shipboard incubation experiments that illustrate the effects of visible light and ultra-violet radiation on phytoplankton growth and physiology. This study indicates that the under-ice environment is ideally suited for phytoplankton bloom development due to reduced damaging visible and ultra-violet radiation in surface waters beneath the ice as compared to open water. The integrative work of these four chapters greatly advances our knowledge of the effects of climate change on biological processes in the Arctic Ocean and establishes the foundation for investigating the implications of these changes for the ecosystem as a whole.

# Acknowledgments

I would like to acknowledge the many individuals who have made my education at Stanford University not only possible but also incredibly enjoyable and worthwhile. Thank you to everyone who contributed positively to my experiences, including those not listed here.

First and foremost, I would like to thank my advisor Kevin Arrigo for his tremendous support and mentorship over the years. Since our first interaction when I was an undergraduate student in 2009, Kevin has consistently encouraged me to do my very best work and provided abundant and life-changing opportunities for my training as a polar researcher, scientist, and oceanographer. I cannot imagine a better graduate advisor.

I would also like to thank the Arrigo Lab for creating a highly effective, supportive, and fun work environment. Through field expeditions, conference travel, daily lunches, and more, it has been a pleasure to get to know and learn from each of you. Thank you to my office mates Matt Mills and Gert van Dijken, fellow students Kate Lewis, Hannah Joy-Warren, Ginny Selz, Casey Schine, and Aaron Strong, and past Arrigo Lab members Anne-Carlijn Alderkamp, Molly Palmer, Zach Brown, and Ben Saenz. I will always be grateful for all that you have taught me and for the wonderful encouragement and memories.

Thank you to my doctoral committee members, Robert Dunbar, Karen Casciotti, and Leif Thomas, for the many helpful conversations and thoughtful suggestions that have shaped the work of this dissertation. You have each inspired my development as an oceanographer through your research, teaching, and mentoring, and I am grateful to have had you on my committee. Nicole Ardoin, thank you very much for serving as the chair for my defense.

There are many colleagues and friends that I would like to thank for making my experience at Stanford University so meaningful. In particular, thank you to Cindy Wilber, Deana Fabbro-Johnston, Julie Kennedy, Rodolfo Dirzo, Bill Gomez, and Cliff Nass for your support during my undergraduate and graduate years. Thank you to the faculty and staff

of the Department of Earth System Science for being a source of academic and administrative support as well as scientific inspiration. Similarly, thank you to the students and postdoctoral researchers across departments at Stanford for many motivational and thought-provoking conversations about marine science and conservation, social and environmental justice, global climate change, and science policy that will guide my future endeavors.

I would like to give a special acknowledgment to the many friends who encouraged me throughout the process of pursuing and completing my degree. Thank you Cara Brook, Megan Grove Aroz, Jolene Kokroko, Claire Menke, Jessica Perez, TC Robbins, Whitney Spence Hodge, and Tiffany Wang Albrecht for being such amazing and supportive best friends and housemates over the last 10 years. Kate Lewis, Hannah Joy-Warren, Jennifer Wang, David Koweek, and Ben Bryant, thank you for your encouragement and help, especially during my final defense preparations. Thank you to all my Otero friends, including Chris Lowman, Justin Solomon, Nikil Viswanathan, and Mike Delgado, for being a support network since my first days on campus. Finally, thank you to my best friends from home, Kristine Graham Rasmussen and Stacey Shubert Fontenot, for your support and visits.

I would also like to thank several family members who have played critical roles in my education. Thank you to my mother, Barbara Waelde, for working extremely hard to ensure that I have always been able to access the best possible educational opportunities. Thank you to my father, Jim Lowry, for encouraging me to leave my comfort zone and try new things, such as moving away to the high school that eventually led me to Stanford. Lynn Waelde, Ashok Srivastava, and Leela Srivastava, thank you for providing amazing support and guidance that contributed enormously to my educational experience and academic career. Additionally, thank you to Joan Gossett, Wayne Gossett, as well as my other aunts, uncles, cousins, and grandparents for all your support through life.

Finally, I am extremely thankful for the love and support from Chris Peterson that has carried me through the many challenges and rewards associated with completing a PhD program. Since our first meeting on an Antarctic research expedition before I began as a doctoral student, Chris has been an incredible companion and partner. Over the last six years, Chris has been abundantly supportive both at home through delicious meals, laughter, and listening, and in the field through his work as Chief Mate aboard *RVIB Nathaniel B. Palmer* and even as a volunteer research assistant aboard *USCGC Healy*. Chris, you are one of the most hardworking and patient people that I have ever met and I feel so blessed to have and reciprocate your endless love, support, understanding, and encouragement.

This work would not be possible without financial support from a number of sources. My graduate education was funded by the National Science Foundation Graduate Research Fellowship Program, the Stanford University Vice Provost for Graduate Education Gerald J. Lieberman Fellowship, and the Stanford University Department of Earth System Science. Field expeditions to the Chukchi Sea and subsequent scientific analyses and communications were funded through research grants to Kevin R. Arrigo from the National Aeronautics and Space Administration and the National Science Foundation. Research was also supported by the Stanford University School of Earth, Energy, and Environmental Sciences through the McGee Research Grant Program. Additional acknowledgments follow each chapter.

# Contents

<b>Abstract</b>	<b>iv</b>
<b>Acknowledgments</b>	<b>vi</b>
<b>0 Introduction</b>	<b>1</b>
0.1 The Chukchi Sea . . . . .	1
0.2 Background . . . . .	2
0.2.1 Circulation and water mass properties . . . . .	2
0.2.2 Phytoplankton in seasonally ice-covered waters . . . . .	4
0.3 Motivation and Objective . . . . .	5
0.3.1 Rapid physical and biogeochemical changes . . . . .	5
0.3.2 Implications for phytoplankton blooms and the marine ecosystem . . . . .	7
0.3.3 An improved understanding of phytoplankton bloom dynamics . . . . .	8
<b>1 Satellite evidence of under-ice phytoplankton blooms (1998–2012)</b>	<b>10</b>
1.1 Introduction . . . . .	11
1.2 Methods . . . . .	13
1.2.1 Study region . . . . .	13
1.2.2 Satellite data . . . . .	14
1.2.3 Bloom type classification . . . . .	16
1.2.4 Bloom type maps . . . . .	18
1.2.5 Changes in mean Chl <i>a</i> concentration over the 14-day MIZ period . . . . .	19
1.3 Results . . . . .	20
1.3.1 Date of ice retreat . . . . .	20
1.3.2 Bloom type maps . . . . .	20

1.3.3	Sensitivity analysis . . . . .	23
1.3.4	Sensor comparison . . . . .	25
1.3.5	Comparison with in situ observations . . . . .	25
1.3.6	Changes in mean Chl <i>a</i> concentration over the 14-day MIZ period . . . . .	27
1.3.7	Interannual trends in bloom types . . . . .	29
1.3.8	Spatial patterns by bloom type . . . . .	30
1.4	Discussion . . . . .	32
1.4.1	Methodological considerations . . . . .	32
1.4.2	Prevalence of under-ice blooms . . . . .	36
1.4.3	Sea ice retreat and phytoplankton bloom type . . . . .	37
1.4.4	Implications and future work . . . . .	39
<b>2</b>	<b>The influence of winter water on phytoplankton blooms</b>	<b>41</b>
2.1	Introduction . . . . .	42
2.2	Methods . . . . .	45
2.2.1	Study region . . . . .	45
2.2.2	Field methods and laboratory analysis . . . . .	45
2.2.3	Classification of winter water (WW) . . . . .	48
2.2.4	Hydrographic analysis . . . . .	48
2.2.5	Open water duration . . . . .	49
2.3	Results . . . . .	49
2.3.1	Presence and flow of WW . . . . .	49
2.3.2	Vertical sections . . . . .	50
2.4	Discussion . . . . .	70
2.4.1	Significance of nutrient-rich WW for phytoplankton blooms . . . . .	70
2.4.2	Contribution of WW to biological hotspots . . . . .	73
2.4.3	Evidence for under-ice blooms . . . . .	74
2.4.4	Conceptual model of phytoplankton blooms in the Chukchi Sea . . . . .	76
<b>3</b>	<b>Under-ice bloom development controlled by convective mixing</b>	<b>80</b>
3.1	Introduction . . . . .	81
3.2	Materials and Methods . . . . .	85
3.2.1	Data collection . . . . .	85
3.2.2	Data analysis . . . . .	88

3.2.3	Model of irradiance, production, and critical depth beneath sea ice with leads . . . . .	92
3.3	Results . . . . .	94
3.3.1	Physical environment . . . . .	94
3.3.2	Nutrients, phytoplankton, and productivity . . . . .	97
3.3.3	Hydrographic sections . . . . .	98
3.3.4	Hydrographic and bio-physical relationships . . . . .	108
3.3.5	Theoretical model of irradiance, primary production, and critical depth beneath sea ice with leads . . . . .	112
3.4	Discussion . . . . .	113
3.4.1	Enhanced convective mixing beneath sea ice with leads . . . . .	113
3.4.2	Importance of leads in the absence of convection . . . . .	115
3.4.3	Modest under-ice blooms even beneath fully consolidated sea ice . . . . .	116
3.4.4	Implications for marine ecosystems in the changing Arctic Ocean . . . . .	117
<b>4</b>	<b>Effects of visible light and ultraviolet radiation on under-ice phytoplankton</b>	<b>119</b>
4.1	Introduction . . . . .	120
4.2	Methods . . . . .	122
4.2.1	Field sampling . . . . .	122
4.2.2	Experimental design and sampling . . . . .	123
4.2.3	Analytical methods . . . . .	125
4.2.4	Sea ice cover . . . . .	128
4.2.5	Statistical analysis . . . . .	128
4.3	Results . . . . .	129
4.3.1	Experiment starting conditions . . . . .	129
4.3.2	Phytoplankton biomass response . . . . .	129
4.3.3	Phytoplankton physiological response . . . . .	136
4.4	Discussion . . . . .	140
4.4.1	Effects of UVR and PAR on polar marine phytoplankton . . . . .	140
4.4.2	Short-term phytoplankton acclimation . . . . .	141
4.4.3	Long-term phytoplankton growth . . . . .	142
4.4.4	Implications for phytoplankton in the under-ice environment . . . . .	143

# List of Tables

1.1	Summary statistics for phytoplankton bloom area classification . . . . .	22
2.1	Biogeochemical properties for winter water and non-winter water . . . . .	54
3.1	Statistical relationships between physical and environmental properties . . . .	110
3.2	Statistical relationships between physical and biological properties . . . . .	111
3.3	Multiple linear regression analysis for predicting phytoplankton biomass . . .	112
4.1	Incubation experiment design . . . . .	124
4.2	Experiment starting conditions . . . . .	130
4.3	Phytoplankton cellular ratios, nutrient uptake, and variable fluorescence . . .	136

# List of Figures

0.1	Map and circulation schematic of the Chukchi Sea . . . . .	2
1.1	Maps of ice retreat and ocean color retrievals in the study region . . . . .	15
1.2	Conceptual model for under-ice versus marginal ice zone (MIZ) blooms . . . . .	17
1.3	Annual maps of under-ice, probable under-ice, and MIZ blooms . . . . .	21
1.4	Bloom type maps for year 2011 displaying sensitivity analysis . . . . .	24
1.5	Ocean color sensor comparison for SeaWiFS versus MODIS Aqua . . . . .	26
1.6	Validation of bloom type at <i>in situ</i> under-ice bloom locations . . . . .	27
1.7	Time series plots of mean chlorophyll <i>a</i> following ice retreat . . . . .	28
1.8	Trend in MIZ bloom observations over the 13-year time series . . . . .	29
1.9	Cumulative frequency of under-ice and MIZ blooms (1998–2012) . . . . .	31
1.10	Map of dominant bloom type in the Chukchi Sea . . . . .	32
1.11	Time series of under-ice bloom magnitude and date of ice retreat . . . . .	39
2.1	Map of the Chukchi Sea illustrating the flow pathway and transect locations . . . . .	46
2.2	Hydrographic sections of absolute geostrophic velocity . . . . .	51
2.3	Hydrographic sections for the Central Channel transect . . . . .	52
2.4	Hydrographic sections for the Chukchi North transect . . . . .	56
2.5	Hydrographic sections for the Chukchi Slope West transect . . . . .	59
2.6	Fv:Fm along the Chukchi Slope West transect . . . . .	61
2.7	Hydrographic sections for the Hanna Shoal North transect . . . . .	62
2.8	Hydrographic sections for the Chukchi Slope Center transect . . . . .	65
2.9	Hydrographic sections for the Chukchi Slope East transect . . . . .	67
2.10	Hydrographic sections for the Hanna Shoal Southeast transect . . . . .	69
2.11	Potential temperature versus nitrate for all transects . . . . .	71
2.12	Depth-integrated chlorophyll <i>a</i> in winter water and non-winter water . . . . .	73

3.1	Photographs of sea ice with melt ponds and leads and under-ice waters . . . . .	84
3.2	Station map for the Chukchi Sea during SUBICE in May–June 2014 . . . . .	86
3.3	Maps of physical properties in the Chukchi Sea . . . . .	95
3.4	Hydrographic sections for the Hanna Ridge transect . . . . .	100
3.5	Hydrographic sections for the Hanna Shoal North transect . . . . .	101
3.6	Hydrographic sections for the Central Shelf transect . . . . .	103
3.7	Hydrographic sections for the Chukchi Northwest transect . . . . .	104
3.8	Hydrographic sections for the Hanna Shoal West transect . . . . .	106
3.9	Hydrographic sections for the Central Channel transect . . . . .	107
3.10	Hydrographic sections for the Chukchi North transect . . . . .	109
3.11	Theoretical model of under-ice light, production, and critical depth . . . . .	114
4.1	Map of starting locations for incubation experiments . . . . .	123
4.2	Relative changes in phytoplankton biomass and nutrients . . . . .	131
4.3	Chlorophyll <i>a</i> concentrations in individual experiments . . . . .	132
4.4	Particulate organic carbon/nitrogen concentrations in individual experiments	133
4.5	Average growth rates over four days in individual experiments . . . . .	134
4.6	Nitrate concentrations in individual experiments . . . . .	137
4.7	Relative changes in variable fluorescence . . . . .	138
4.8	Fv:Fm in individual experiments . . . . .	139
4.9	Maximum phytoplankton photosynthetic and growth rates . . . . .	140

# Chapter 0

## Introduction

### 0.1 The Chukchi Sea

Located north of the Bering Strait between Alaska and Russian Siberia, the Chukchi Sea is the gateway of the Pacific Ocean to the Arctic (Fig. 0.1). With an average depth of 50 meters and a total area of 620,000 km<sup>2</sup> (*Jakobsson et al.*, 2004), the Chukchi Sea is a broad and relatively shallow marginal Arctic continental shelf sea that comprises 10% of the total Arctic shelf area. The nature of the Chukchi Sea as an inflow shelf (*Carmack and Wassmann*, 2006) that ventilates the upper halocline of the Arctic Ocean (*Woodgate et al.*, 2005a) necessitates a thorough understanding of the dynamic physical and biogeochemical processes that modify Pacific-origin water masses as they transit the shelf.

Our current knowledge highlights the Chukchi Sea as a region of intense summer biological activity with a rich benthic community that supports abundant populations of marine mammals and seabirds (*Dunton et al.*, 2005; *Loeng et al.*, 2005; *Grebmeier et al.*, 2006). In recent decades, the Arctic Ocean has experienced unprecedented reductions in sea ice cover and thickness (*Serreze et al.*, 2007; *Kwok and Rothrock*, 2009; *Stroeve et al.*, 2011) accompanied by an increased heat and freshwater flux through the Bering Strait (*Woodgate et al.*, 2012). The impact of these changes on the global carbon cycle and the marine ecosystem of the Chukchi Sea (*Loeng et al.*, 2005; *Bates et al.*, 2011; *Grebmeier*, 2012; *Grebmeier et al.*, 2015) are only recently beginning to be understood. Of particular biological interest is how the primary producers that form the base of the food web are affected by this extreme transformation of the physical environment. Previous work suggests that phytoplankton communities are already responding to reduced sea ice cover and thickness, with evidence

of increased primary production in open water (*Arrigo and van Dijken, 2011, 2015*) and underneath sea ice (*Arrigo et al., 2012, 2014*). To better understand the biogeochemical implications of these findings and the complex interplay between them, a further elucidation of phytoplankton bloom dynamics in the Chukchi Sea is necessary.

## 0.2 Background

### 0.2.1 Circulation and water mass properties

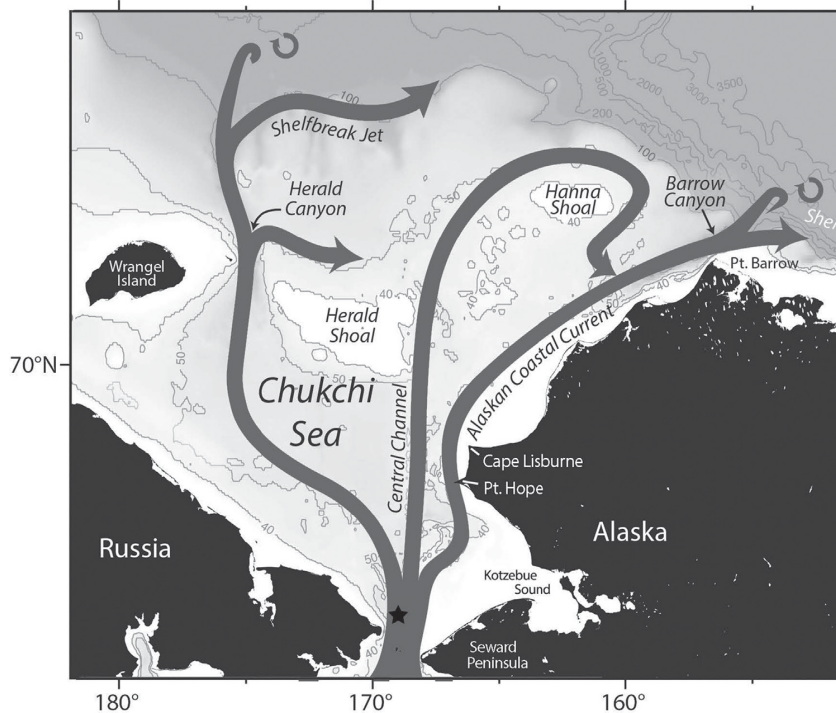


Figure 0.1: Map of the Chukchi Sea illustrating the general circulation of Pacific water across the shallow continental shelf. Figure reproduced under license from *Pickart et al. (2016)*.

Water flows northward through the Bering Strait due to the sea surface height differential that results from the salinity difference between the Pacific and Arctic Oceans (*Coachman et al., 1975*). Upon reaching the Chukchi Sea, the flow of Pacific-origin water is steered into three branches (Fig. 0.1) based on water mass properties set within the Bering Sea

(*Coachman et al.*, 1975; *Overland and Roach*, 1987; *Weingartner et al.*, 2005). Bathymetry is an important driver of circulation; each branch follows local isobaths, steering around or between the shallow features of Herald (20 m) and Hanna (30 m) Shoals (Fig. 0.1). Differences in salinity and nutrient concentrations between the pathways generate significant variations in biogeochemical properties across the shelf (*Walsh et al.*, 1989; *Cooper et al.*, 1997; *Codispoti et al.*, 2005, 2013). The western and central pathways of Anadyr Water (AW) and Bering Shelf Water (BSW) are rich in nutrients (pre-bloom  $\text{NO}_3^- > 10\text{--}15 \mu\text{mol L}^{-1}$ ), owing to under-utilization in the western Bering Sea, as compared to the the nutrient-poor eastern Alaska Coastal Water (ACW) (pre-bloom  $\text{NO}_3^- < 10 \mu\text{mol L}^{-1}$ ), which is influenced by river runoff and the biological uptake of nutrients in the eastern Bering Sea. The three water masses flow through Bering Strait in different proportions, with early estimates approximating the ratio of water masses as 6:3:1 for AW:BSW:ACW (*Coachman et al.*, 1975).

Water mass properties are heavily influenced by the seasonal cycle of sea ice in the Bering and Chukchi Seas. In the winter, sea ice formation causes brine rejection that effectively mixes the entire water column to extremely cold temperatures ( $-1.8^\circ\text{C}$ ) (*Woodgate et al.*, 2005b). Polynya formation and leads in the sea ice continue to convectively form this cold and dense Winter Water (WW) on the Chukchi shelf throughout the winter (*Pickart et al.*, 2016). Deep mixing via brine rejection also occurs upstream in the Bering Sea, resupplying the surface waters with nutrients from depth and forming the extremely cold, dense, and nutrient-rich Pacific Winter Water (PWW) that drains through the Chukchi Sea in the spring and eventually fills the Arctic Ocean halocline. As sea ice retreats in spring and summer, the water column becomes re-stratified as surface waters freshen and warm (*Woodgate and Aagaard*, 2005a). WW remaining on the Chukchi shelf in the summer is gradually replaced by relatively warm Pacific Summer Water (PSW) (*Weingartner et al.*, 2005; *Gong and Pickart*, 2015). Model results and *in situ* observations show that the salinity of most of the Chukchi Sea is controlled primarily by the seasonal cycle of the Bering Strait, while the variation in temperature is more influenced by local ice conditions and atmospheric forcing (*Woodgate et al.*, 2005b; *Spall*, 2007). Interestingly, PWW has a relatively wide salinity range (31.5–33.5) that encompasses that of PSW (32.0–33.0) and is therefore more easily distinguished from other water masses by its near freezing temperatures that are much colder than PSW ( $> 0^\circ\text{C}$ ) (*Woodgate et al.*, 2012). Circulation also plays an important role in sea ice retreat, with ice retreating earlier along the major flow paths and later over the more isolated shoals (*Paquette and Bourke*, 1981; *Martin and Drucker*, 1997).

## 0.2.2 Phytoplankton in seasonally ice-covered waters

The Chukchi Sea is an extremely productive ecosystem, with some of the highest values of depth-integrated primary production and chlorophyll *a* (Chl *a*) measured anywhere in the world (*Springer and McRoy*, 1993; *Arrigo et al.*, 2012). Although sea ice algae play a large role in the less productive Central Arctic (*Gosselin et al.*, 1997) and early in the season in the Chukchi Sea (*Gradinger*, 2009), phytoplankton are estimated to be responsible for more than 90% of the total primary production in this region (*Hill and Cota*, 2005). Intense phytoplankton blooms have been observed throughout the Chukchi shelf, with spatial variation attributed to differences in water masses, nutrient availability, and environmental forcing (*Cota et al.*, 1996; *Wang et al.*, 2005; *Lee et al.*, 2007). The southeastern Chukchi Sea and Barrow Canyon have specifically been identified as hot spots for primary production (*Sukhanova et al.*, 2009), while waters near the coast of Alaska in the ACW (*Coupel et al.*, 2012) and off the continental slope generally have lower biomass (*Lee et al.*, 2012). Although fewer *in situ* measurements are available for the southwestern Chukchi Sea, this region is thought to be extremely productive (*Wang et al.*, 2005) due to the flow of nutrient-rich AW.

Phytoplankton in the Arctic Ocean are limited by a combination of light and nutrients. Recent work suggests that light availability influences the timing, rate, and possibly the species composition of phytoplankton blooms, while the total amount of production is limited by nutrients (*Tremblay et al.*, 2008; *Tremblay and Gagnon*, 2009). Inhibition of phytoplankton by ultraviolet radiation (UVR) may also play a role in limiting phytoplankton growth in surface waters, with an apparent species-specific response (*Hessen et al.*, 2012). In the Chukchi Sea, nitrogen (N) is a major control on primary production (e.g. *Hansell et al.* (1993); *Codispoti et al.* (2009)), with surface waters generally depleted in nitrate in the summer (*Wang et al.*, 2006). Increased ammonium concentrations in bottom waters on the shelf indicate that regenerated production is also an important source of N for phytoplankton (*Wang et al.*, 2006; *Brown et al.*, 2015a), particularly in areas such as the ACW where high incorporation of carbon into proteins was measured in spite of very low  $\text{NO}_3^-$  conditions (*Lee et al.*, 2009). Silica concentrations may also play a role in determining community composition, with some evidence for silicate ( $\text{Si(OH)}_4$ ) limitation of diatoms in surface waters (*Walsh et al.*, 2011). Grazing is not considered to be a significant control on phytoplankton biomass in the Chukchi Sea, with meso- and microzooplankton consuming only 44% of the annual primary production (*Campbell et al.*, 2009; *Sherr et al.*, 2009). This small grazing pressure has been attributed to low rates of zooplankton reproduction and

advection through the Bering Strait in the spring and may contribute to reduced viability of a commercial fishery in the region (*Hunt et al.*, 2013; *Grebmeier et al.*, 2006).

Phytoplankton biomass in open waters of the Chukchi Sea is often greatest at intermediate depths where nutrient concentrations are high but light availability is not limiting, forming the characteristic subsurface chlorophyll maximum (SCM) that is prevalent in these waters (*Walsh et al.*, 1989; *Hill et al.*, 2005; *Ardyna et al.*, 2013; *Brown et al.*, 2015b; *Martini et al.*, 2016). Large cells ( $>5 \mu\text{m}$ ) such as diatoms frequently dominate the SCM in the Chukchi Sea, while nutrient-depleted surface waters commonly support smaller cells ( $<5 \mu\text{m}$ ) such as prasinophytes (*Hill et al.*, 2005; *Joo et al.*, 2012). Sea ice retreat is widely believed to control the timing of phytoplankton blooms due to reduced light availability in ice-covered waters. As sea ice melts, the water column stratifies and increased irradiance stimulates phytoplankton growth, resulting in ice-edge or marginal ice zone (MIZ) blooms that are considered to be ubiquitous throughout the Arctic (*Perrette et al.*, 2011). This paradigm has been supported in the Chukchi Sea by observations of high phytoplankton biomass near the ice edge (*Wang et al.*, 2005; *Hameedi*, 1978) and in the MIZ on the Chukchi Slope (*Coupel et al.*, 2012; *Lee et al.*, 2012). However, our observations during the NASA-funded Impacts of Climate on EcoSystems and Chemistry of the Arctic Pacific Environment (ICESCAPE) field program in 2010-2011 revealed that light conditions underneath first-year sea ice are sufficient for primary production, as evidenced by the presence of an immense phytoplankton bloom in the water column that extended for more than 100 kilometers into the consolidated ice pack (*Arrigo et al.*, 2012). Thus, the characteristic SCM observed in these waters may be linked to the seasonal evolution of under-ice phytoplankton blooms (*Brown et al.*, 2015b). These findings demonstrate that phytoplankton bloom dynamics in the Chukchi Sea are more complex than previously thought and motivate further analysis of the controls of sea ice and hydrography on primary production in this region.

## 0.3 Motivation and Objective

### 0.3.1 Rapid physical and biogeochemical changes

The Chukchi Sea is undergoing rapid transition of physical, chemical, and biological processes that are complex and highly related, such that transformations to the physical environment have large implications for biogeochemistry, primary production, and upper trophic level organisms. The most well-studied physical change to the Arctic Ocean is the extreme

reduction in sea ice. Summer minimum sea ice extent has decreased by  $\sim 10\%$  per decade since 1979, (*Comiso et al.*, 2008), with the lowest extent on record in 2012 (*Parkinson and Comiso*, 2013) and near-record low extents in more recent years (*Perovich and Richter-Menge*, 2015). The most extreme changes have occurred in the Western Arctic where the Chukchi Sea is located (*Stroeve et al.*, 2011), with ice retreating nearly two months earlier and advancing more than one month later relative to 1979 (*Stammerjohn et al.*, 2012). Changes in sea ice cover also include reductions in sea ice thickness (*Kwok and Rothrock*, 2009) and a decrease in the average age of the ice (*Maslanik et al.*, 2011). Multi-year ice in the Chukchi Sea has been largely replaced by first-year sea ice (*Comiso*, 2012) that retreats in the spring and summer and advances in the fall and winter.

One consequence of changes in sea ice that has been relatively understudied until recently is that of increased light penetration to the water column through thinner sea ice (*Perovich and Polashenski*, 2012). First-year sea ice in the Chukchi Sea has a significantly higher melt pond fraction than multi-year ice due to the relatively flat nature of thin ice that allows large melt ponds to form (*Polashenski et al.*, 2012). Results from ICESCAPE show that ice with melt ponds can transmit up to 55% of incident light due to the lack of a surface scattering layer (*Frey et al.*, 2011). This remarkable transmittance is more than three times that of bare ice with the same thickness. The presence of high melt pond fractions have been implicated in increased radiative forcing in the extreme sea ice loss years of 2007 and 2011 (*Rösel and Kaleschke*, 2012) and is suspected to play a large role in illuminating the water column for phytoplankton growth underneath first-year sea ice (*Arrigo et al.*, 2012, 2014).

A potential driver for the extreme changes in sea ice loss and thinning is an increased flux of heat from the Pacific Ocean through Bering Strait. A decade-long study (2001–2011) demonstrated that the summer inflow to the Chukchi Sea has increased in volume, heat, and freshwater content (*Woodgate et al.*, 2012). Over the 10-year study period, the transport volume through Bering Strait increased from  $\sim 0.7$  Sv in 2001 to  $\sim 1.1$  Sv in 2011. Forcing of this increased flow was attributed to a  $\sim 30\%$  increase in the sea level difference pressure head accompanied by a decrease in the southwestward winds that oppose the flow of water. The effect of this extreme increase on the water mass properties, circulation, and WW residence time in the Chukchi Sea has significant implications for the timing of sea ice retreat (*Spall*, 2007), ventilation of the Arctic Ocean halocline (*Woodgate et al.*, 2005a), and nutrient availability for phytoplankton (*Wang et al.*, 2005).

Increased sea ice melt and freshwater input may enhance summertime stratification of the water column, creating an additional barrier for nutrient exchange between bottom waters and the euphotic zone (*Tremblay et al.*, 2008). In addition to this potential biogeochemical response to physical changes, there are other factors that may affect nutrient availability and carbon cycling in the Chukchi Sea. For example, there is evidence for increased high-latitude storms (*Sorteberg and Walsh*, 2008) and intensification of easterly winds on the northern Chukchi shelf (*Pickart et al.*, 2011) that may drive increased upwelling of nutrients. There is also evidence of ocean acidification on the Chukchi Shelf, with recent observations of seasonal aragonite undersaturation (*Bates et al.*, 2009) following the remineralization of organic matter produced as phytoplankton drawdown DIC in surface waters (*Bates et al.*, 2005). This aragonite undersaturation is thought to be a new occurrence resulting from increased summertime uptake of atmospheric CO<sub>2</sub> by surface waters of the Chukchi Sea (*Gao et al.*, 2012) and indicates that bottom waters may be seasonally corrosive to benthic calcifying organisms (*Bates et al.*, 2009).

### 0.3.2 Implications for phytoplankton blooms and the marine ecosystem

Although the full extent of these physical and biogeochemical changes on the marine ecosystem is not well known, there is evidence that phytoplankton are already responding to the rapidly transforming environment. For example, saxitoxic dinoflagellates associated with paralytic shellfish poisoning were observed on the Chukchi shelf for the first time in 2002 and 2003 (*Walsh et al.*, 2011). Additionally, as more freshwater is added to the Arctic Ocean, there appears to have been a shift in phytoplankton community composition from larger to smaller cells (*Li et al.*, 2009) that have a greater surface-area-to-volume ratio for effective nutrient acquisition but support a different food web structure. In the Chukchi Sea, small cells were recently found to be most abundant, while larger cells remained the biggest contributors to total biomass and Chl *a* (*Joo et al.*, 2012). There is also evidence for an uncoupling between phytoplankton and bacteria in the Chukchi Sea (*Kirchman et al.*, 2009), with bacterial respiration exceeding primary production in off-shelf waters and during non-peak production times of year (*Hill and Cota*, 2005).

The most striking of the apparent impacts of climate change on phytoplankton in the Chukchi Sea are related to total primary production, bloom intensity, and the spatial and temporal distribution of phytoplankton blooms relative to sea ice cover. Satellite estimates indicate that primary production in open water after sea ice retreats has increased by 42%

in the Chukchi Sea from 1998–2012 (*Arrigo and van Dijken, 2015*). Our finding of a massive under-ice phytoplankton bloom with some of the highest values of depth-integrated biomass observed in any pelagic ocean ecosystem (up to 1300 mg Chl a m<sup>-2</sup>) (*Arrigo et al., 2014*) suggests that at least some of this increase in satellite-derived primary production is due to an increased uncovering of under-ice blooms as sea ice retreats earlier. The capability of ice-covered waters to support such high phytoplankton biomass indicates that the under-ice environment on the Chukchi shelf, with its high pre-bloom nutrient availability, moderate irradiance, and effective UVR attenuation, may be perfectly situated to support extremely large and productive phytoplankton blooms. Comparing satellite estimates of primary production in ice-covered waters with field measurements beneath the ice during ICESCAPE demonstrated that current estimates of total primary production in this region may be ~10-fold too low (*Arrigo et al., 2014*).

Although the historical presence and spatial distribution of phytoplankton blooms under sea ice is unknown due to sparse sampling of ice-covered waters, the remarkable transition of multi-year ice to thinner first-year ice with higher melt pond fraction and light transmission (*Maslanik et al., 2011; Polashenski et al., 2012*) indicates that under-ice blooms are a relatively recent and widespread phenomenon. If they are indeed new to the Arctic, the presence of these blooms signifies a shift in the timing of phytoplankton bloom onset and peak biomass to earlier in the season, before the sea ice retreats. This transformation is likely accompanied by a shift in bloom distribution and intensity, as the water column underneath thinning sea ice on the Chukchi shelf becomes an increasingly suitable environment for phytoplankton growth. The combination of under-ice blooms with earlier sea ice retreat and increased heat and volume flux through the Bering Strait has the potential to significantly alter phytoplankton bloom dynamics in the Chukchi Sea, with poorly understood consequences for upper trophic levels. Furthermore, phytoplankton blooms underneath sea ice can substantially increase heating of the upper water column below the ice due to increased absorption by phytoplankton of shortwave radiation (*Pegau, 2002*), possibly contributing to the positive feedback loop of sea ice melt.

### 0.3.3 An improved understanding of phytoplankton bloom dynamics

As evidence increasingly indicates that phytoplankton in the Chukchi Sea are undergoing significant changes in terms of bloom timing, intensity, and location relative to ice cover, this dissertation seeks to contribute a more comprehensive characterization of phytoplankton

bloom dynamics in this seasonally ice-covered and rapidly changing region. Through a combination of observational and experimental fieldwork and satellite remote sensing, this work investigates the influence of sea ice and hydrography on the timing, distribution, and intensity of phytoplankton blooms in the Chukchi Sea. Data are presented from the ICESCAPE cruises in June-July 2010 and 2011 and a subsequent expedition in May-June 2014 as part of the NSF-funded Study of Under-ice Blooms in the Chukchi Ecosystem (SUBICE) program.

This dissertation is comprised of four chapters, each focusing on a different aspect of phytoplankton bloom dynamics in the Chukchi Sea. Chapter 1 investigates the temporal and spatial distribution of under-ice phytoplankton blooms from years 1998 to 2013, using satellite data to test the hypothesis that under-ice blooms are widespread and have been present in years prior to their discovery in 2011. Chapter 2 elucidates the role of hydrography in controlling the spatial distribution, duration, and intensity of summer phytoplankton blooms, using field observations from ICESCAPE to understand the importance of the flow of nutrient-rich WW for phytoplankton blooms on the Chukchi shelf. In Chapter 3, the first-ever spring measurements from SUBICE of phytoplankton, nutrients, and hydrography beneath the ice are used along with a theoretical model to explore controls on the development of under-ice phytoplankton blooms, with a focus on the role of open water leads and convective mixing. Finally, results from incubation experiments performed during SUBICE are presented in Chapter 4 to address the effects of visible light and UVR on phytoplankton growth and physiology, testing the hypothesis that the under-ice light environment is ideally situated for blooms. Through these studies, this dissertation seeks to elucidate the influence of sea ice and hydrography on phytoplankton bloom dynamics in order to better comprehend the effects of climate change on this rapidly transforming marine ecosystem.

## Chapter 1

# Satellite evidence of under-ice phytoplankton blooms (1998–2012)

KATE E. LOWRY, GERT L. VAN DIJKEN, KEVIN R. ARRIGO

*Earth System Science, Stanford University, Stanford, California, USA*

*The discovery in 2011 of a massive phytoplankton bloom underneath first-year sea ice in the western Arctic has prompted an investigation of the spatial and temporal distribution of under-ice phytoplankton blooms. Here, we explore the satellite record from years 1998 to 2012 for evidence of under-ice blooms on the Chukchi Sea shelf. Phytoplankton blooms were categorized as either under-ice blooms, probable under-ice blooms, or marginal ice zone blooms, depending on bloom timing in relation to the timing of ice retreat. Annual bloom type maps reveal that under-ice phytoplankton blooms were present in every year of the satellite record. Averaged over all years, the combination of under-ice blooms and probable under-ice blooms covered a portion of the observable study area that was 2.5-fold higher than that of marginal ice zone blooms (71.5% and 28.5%, respectively). This finding strongly contradicts the traditional view that phytoplankton in seasonally ice-covered waters bloom only after ice retreat and instead indicates that blooms are initiated whenever light and nutrient availability is sufficient for photosynthesis, a condition often reached early in the season underneath first-year sea ice on nutrient-rich continental shelves. Spatial patterns in bloom*

*type were distinguished relative to the date of ice retreat, with probable under-ice blooms dominating the nutrient-rich western Chukchi Sea and at higher latitudes where ice retreats later, while marginal ice zone blooms were most common in the southern and eastern Chukchi Sea where ice retreats earlier. Our results suggest that under-ice phytoplankton blooms are widespread in the Chukchi Sea and had been prevalent there for more than a decade prior to their discovery in 2011.*

This chapter was originally published in *Deep-Sea Research Part II* and is reproduced with permission from the publisher. ©2014. This manuscript version is made available under the CC-BY-NC-ND 4.0 license: <http://creativecommons.org/licenses/by-nc-nd/4.0/>

Lowry, K.E., Van Dijken, G.L., and Arrigo, K.R. Evidence of under-ice phytoplankton blooms in the Chukchi Sea from 1998 to 2012. *Deep-Sea Res. II* 105 (2014) 105-117, doi: 10.1016/j.dsr2.2014.03.013.

## 1.1 Introduction

The seasonally ice-covered marginal shelf seas of the Arctic Ocean are highly productive ecosystems that are characterized in large part by spring phytoplankton blooms that form the base of the food web, supporting a rich array of upper trophic level organisms (*Loeng et al.*, 2005). Until recently, phytoplankton blooms in this region were thought to begin only after the sea ice retreats and the water column stratifies, providing sufficient light for photosynthesis (*Hill and Cota*, 2005; *Sakshaug and Skjoldal*, 1989). However, the discovery in 2011 of a massive phytoplankton bloom underneath first-year sea ice in the Chukchi Sea *Arrigo et al.* (2012) challenges this long-standing paradigm, revealing that substantial phytoplankton growth is possible in ice-covered seas. The exceptionally high biomass and growth rates across a spatial extent of more than 100 kilometers (*Arrigo et al.*, 2012, 2014) suggest that under-ice blooms are important yet overlooked features of Arctic marine ecosystems.

Concurrent with this finding, studies of the under-ice light environment also indicate that phytoplankton blooms may be a widespread phenomenon underneath the ice. In recent decades, multi-year ice over Arctic continental shelves has been largely replaced with thinner, flatter, first-year ice (*Comiso*, 2012; *Kwok and Rothrock*, 2009; *Maslanik et al.*, 2011; *Stroeve*

*et al.*, 2011) with a significantly higher melt pond fraction (*Polashenski et al.*, 2012). Because melt-ponded ice transmits 3–10 times more light than bare ice of the same thickness (*Frey et al.*, 2011), the presence of more first-year ice with a higher melt pond fraction corresponds to an increase in the illumination of the water column beneath the sea ice (*Perovich et al.*, 2011). In the eastern Chukchi Sea where the under-ice bloom was observed, up to 55% of the incident light was transmitted through the ice to the water column below. This high transmission paired with very high nutrient concentrations ( $\text{NO}_3^-$ : 15–20  $\mu\text{M}$ ) created an extremely favorable environment for under-ice phytoplankton primary production (*Arrigo et al.*, 2012).

Considering that more than half of the Arctic Ocean consists of continental shelf waters and that pre-bloom surface nutrient concentrations are very high over 30–50% of the Arctic continental shelf (*Zhang et al.*, 2010), *Arrigo et al.* (2014) estimate that approximately 25% of the Arctic Ocean may be favorable for phytoplankton blooms underneath the ice. The Chukchi Sea in particular stands out as a region with extremely high pre-bloom nutrient concentrations ( $\text{NO}_3^-$ : > 10  $\mu\text{M}$  in non-coastal waters), due to a combination of local remineralization and brine rejection leading to convective wintertime mixing as well as the northward advection of nutrients through the Bering Strait (*Zhang et al.*, 2010). Within the Chukchi Sea there is a nutrient gradient that increases from east to west, with the western Chukchi Sea and the East Siberian Sea filled with nutrient-rich Anadyr water that contains unutilized nutrients from the Bering Sea (*Coachman et al.*, 1975; *Hansell et al.*, 1993). Combined, the presence of high pre-bloom surface nutrients and increased light penetration of the thin ice cover in recent decades suggest that under-ice blooms have likely occurred throughout the region and in years prior to their discovery in 2011.

If phytoplankton blooms prior to ice retreat are indeed widespread, it will be necessary to adjust our traditional understanding of Arctic marine ecosystems. Food web and ecosystem studies in this region (*Arrigo and van Dijken*, 2011; *Hill and Cota*, 2005; *Sakshaug and Skjoldal*, 1989) currently rely on a widely accepted narrative in which, prior to bloom development, the sea ice retreats and the water column stratifies, allowing the bloom to form in well-illuminated waters trailing the ice edge. Blooms initiated in this way are termed ice-edge or marginal ice zone (MIZ) blooms and are proposed to be ubiquitous features throughout the Arctic (*Perrette et al.*, 2011), with many upper trophic level species timing their migrations and life cycles to feed on this large biological pulse (*Loeng et al.*, 2005). The ecological importance of MIZ blooms has been broadly recognized, with estimates that

28–33% of net primary production (NPP) in the Arctic occurs on the shelf within two weeks of ice retreat (*Pabi et al.*, 2008). However, a comparison of satellite-based estimates of annual NPP with field observations in the region of the 2011 *in situ* under-ice bloom, which cannot be seen by ocean color satellite sensors, indicate that satellite-based estimates in some areas may be 10-fold too low (*Arrigo et al.*, 2014). Considering that the presence of phytoplankton blooms prior to ice retreat represents a shift in the timing of peak NPP and that timing is critical for upper trophic level organisms (*Kahru et al.*, 2010; *Loeng et al.*, 2005), our understanding of this ecosystem crucially depends on our ability to characterize the magnitude, history, and importance of under-ice blooms.

In this study, we investigate the temporal and spatial distributions of under-ice blooms in the Chukchi Sea to provide context for the massive bloom observed in 2011 and to gain a more comprehensive understanding of phytoplankton bloom dynamics in this rapidly changing ecosystem. The remote location of this region combined with the difficulty of sampling in ice-covered waters necessitates the use of new approaches to assess the importance of phytoplankton growth beneath the ice. Using satellite data, we identify phytoplankton blooms within two weeks of sea ice retreat and distinguish blooms that were initiated prior to ice retreat (i.e. under-ice blooms) from those that began after ice retreat (i.e. MIZ blooms) based on the amount of phytoplankton biomass present at the time of sea ice retreat. We assume that high chlorophyll *a* (Chl *a*) concentrations at the time of ice retreat indicate a phytoplankton bloom that had developed under the ice, while low initial Chl *a* concentrations that increase following ice retreat are indicative of a MIZ bloom. Furthermore, considering that non-coastal waters of the Chukchi Sea shelf are characterized by high surface nutrient availability, we assume that areas without a bloom in the two weeks following ice retreat likely supported a bloom that depleted surface nutrients prior to ice retreat (i.e. a probable under-ice bloom), preventing the onset of a subsequent MIZ bloom in open water. Combined, this approach enables an evaluation of the prevalence of under-ice phytoplankton blooms throughout the Chukchi Sea over a 15-year period from 1998 to 2012.

## 1.2 Methods

### 1.2.1 Study region

The study region for this analysis consists of non-coastal (> 50 km from land) continental shelf waters (< 200 m) within the Chukchi Sea and a portion of the East Siberian Sea

(Fig. 1.1A). The total area included in the analysis was approximately 425,000 km<sup>2</sup>. For comparison, the total area of the Chukchi Sea, including off-shelf waters, is 620,000 km<sup>2</sup> (*Jakobsson, 2002*). Coastal waters were excluded from the analysis due to the high concentrations of colored dissolved organic matter (CDOM) in this region, which can bias satellite retrievals of Chl *a* (*Matsuoka et al., 2011*).

### 1.2.2 Satellite data

**Sea ice cover.** Daily sea ice concentrations were obtained for the study region for years 1998–2012 from the Special Sensor Microwave/Imager (SSM/I) at 25 km resolution. Maps of the date of sea ice retreat were created for each year, with the date of retreat defined for a given pixel as the first day in a year that the ice concentration dropped below 50%. This 50% threshold best approximated the ice edge that is visible in MODIS (Moderate Resolution Imaging Spectroradiometer) Aqua quasi-true color images and is consistent with methods used to detect the ice edge by *Arrigo et al. (2012)* and *Arrigo and van Dijken (2011)*. The mean date of ice retreat over the time series was calculated for each pixel in the study region (Fig. 1.1A).

The study was repeated using an open water threshold of 10% ice concentration to assess the potential bias resulting from ocean color retrievals in mixed ice-ocean pixels and in waters adjacent to the sea ice edge as described by *Bélangier et al. (2007)*. This threshold corresponds to a reduced prevalence of mixed-ice ocean pixels and a decreased proximity to the ice edge as compared with the 50% threshold for ice retreat used in this study, thus providing a good basis for evaluating the possible impact of sub-pixel contamination and the adjacency effect on the results of the analysis.

**Chlorophyll *a*.** Ocean color images from SeaWiFS (Sea-viewing Wide Field-of-view Sensor) at 4.6 km resolution and MODIS Aqua at 1.1 km resolution were obtained for the study region over the 15-year time series, with SeaWiFS images used for years 1998–2002 (Reprocessing 2010.0) and MODIS images used for years 2003–2012 (Reprocessing 2012.0 for years 2003–2010 and Reprocessing 2013.0 for years 2011–2012). Daily composite ocean color maps were created from individual Level 2 scenes that were projected onto an equal area grid of the Chukchi Sea with a pixel resolution of 1.49 km<sup>2</sup>. Satellite observations of Chl *a* at each pixel were recorded during the 14-day MIZ period following ice retreat (*Arrigo et al., 2008*; *Pabi et al., 2008*) and were used as a proxy for phytoplankton biomass. The

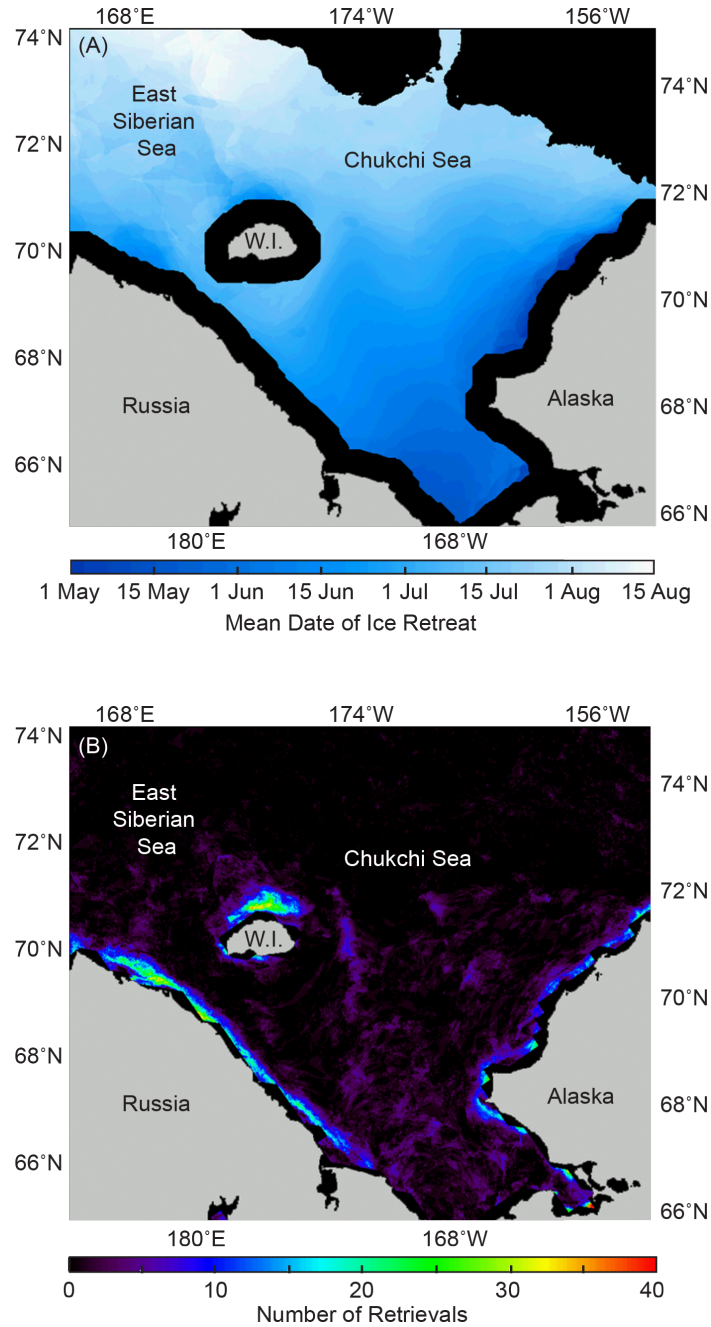


Figure 1.1: Maps of the study region displaying (A) the mean date of ice retreat and (B) the cumulative number of Chl *a* retrievals over the 15-year time series that occurred within one week prior to the date of sea ice retreat. W.I. = Wrangel Island.

potential bias of using data from multiple ocean color sensors was evaluated by comparing results using both SeaWiFS and MODIS for the five overlapping years (2003–2007).

For some pixels, Chl *a* concentrations were retrieved prior to the calculated date of ice retreat (Fig. 1.1B), indicating that open water was present earlier than the sea ice data suggested. This mismatch results from the large difference in pixel size between sea ice and ocean color data and was most frequent in areas along the coast where land-fast ice was present and sea ice was less consolidated. Approximately 70% of the pixels with early retrievals were removed from the analysis by the exclusion of all pixels within 50 km of land. The remaining pixels with early retrievals were included in the study after verifying that the bloom type maps (described below) were within 3% of each other when created with and without the inclusion of these pixels.

### 1.2.3 Bloom type classification

**Phytoplankton bloom detection.** Phytoplankton blooms were defined based on the Chl *a* concentration over the two-week period following sea ice retreat, such that pixels with values exceeding a threshold of  $2.5 \text{ mg m}^{-3}$  were classified as either under-ice or MIZ blooms, as described below. Some pixels were classified as probable under-ice blooms, based on the classification schema also described below. Due to extensive cloud cover in this region that limits the satellite retrieval of Chl *a* at each pixel location to only  $4.26 \pm 1.04$  days of the two-week MIZ period, phytoplankton blooms were only classified and included in this study for observable pixels, with a pixel defined as observable over the MIZ period if it contained at least one satellite retrieval of Chl *a* per week, with at least one retrieval within two days of ice retreat. Similarly, we defined the observable area for a given year as the collective area represented by the observable pixels in that year (assuming a resolution of  $1.49 \text{ km}^2$  per pixel).

**Under-ice and MIZ blooms.** Phytoplankton blooms identified within two weeks of ice retreat were classified as either under-ice blooms or MIZ blooms based on the timing of bloom initiation (defined when the Chl *a* concentration first exceeded the bloom threshold) relative to ice retreat. If the first Chl *a* retrieval (within two days of ice retreat) exceeded the bloom threshold, the bloom was assumed to have developed underneath the ice and was classified as an under-ice bloom. Conversely, if the Chl *a* concentration exceeded the bloom threshold only after the first retrieval, the bloom was assumed to have developed in open water and

was classified as a MIZ bloom. This bloom classification is based on our conceptual model (Fig. 1.2) that depicts under-ice blooms as characterized by high initial Chl *a* concentrations that decrease over time after ice retreat as surface nutrients are depleted and MIZ blooms as characterized by low initial Chl *a* concentrations that increase over time after ice retreat as the water column stratifies.

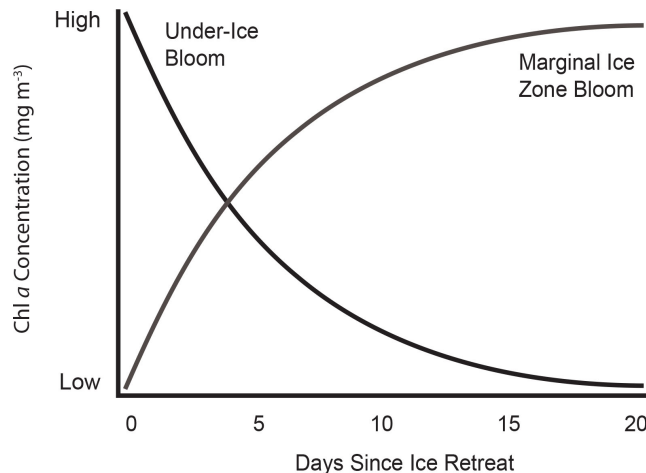


Figure 1.2: Conceptual model illustrating the theory used to distinguish under-ice blooms from MIZ blooms; under-ice blooms have high Chl *a* concentrations at the time of ice retreat while MIZ blooms have initially low concentrations that increase over a two to three week period.

Due to the cloud cover limitations described above, the first retrieval was considered suitable for diagnosing under-ice phytoplankton blooms if it was obtained within two days of ice retreat. Assuming a typical pre-bloom Chl *a* concentration of  $0.02 \text{ mg m}^{-3}$  and an extremely high phytoplankton growth rate of  $0.69 \text{ d}^{-1}$  (corresponding to one doubling per day), it would take more than a week for a bloom to reach the bloom threshold of  $2.5 \text{ mg m}^{-3}$ . Thus, it is extremely unlikely that a MIZ bloom could develop fast enough to exceed the bloom threshold within two days of ice retreat and be mistakenly classified as an under-ice bloom. Furthermore, as is shown in Section 1.3.6, the initial mean Chl *a* concentration for under-ice blooms identified in this study often exceeds  $8 \text{ mg m}^{-3}$ , which is more than 3-fold higher than the threshold we use to define a bloom.

Based on these factors, we considered the bloom threshold of  $2.5 \text{ mg m}^{-3}$  appropriate for identifying and distinguishing under-ice blooms from MIZ blooms. Nevertheless, to assess the sensitivity of bloom classification to the Chl *a* concentration used to define a bloom, we

also repeated the analysis using different Chl *a* thresholds ( $1.5 \text{ mg m}^{-3}$ ,  $3.5 \text{ mg m}^{-3}$ , and  $5.0 \text{ mg m}^{-3}$ ). Additionally, because MIZ blooms could take longer than two weeks to reach the bloom threshold, depending on mixing and stratification conditions, we also repeated the analysis using a three-week MIZ period. As is detailed in Section 1.3.3, qualitatively similar results were obtained using different Chl *a* thresholds and a longer period for MIZ bloom detection.

**Probable under-ice blooms.** Observable pixels that did not exceed the bloom threshold within the two-week MIZ period were classified as probable under-ice blooms. This decision relies extensively on previous studies revealing that pre-bloom surface nutrient levels are very high in this region, with  $\text{NO}_3^-$  concentrations ranging from  $> 10 \text{ }\mu\text{M}$  in the Bering Shelf Water of the eastern and central Chukchi Sea to  $> 15 \text{ }\mu\text{M}$  in the Anadyr Water of the western Chukchi Sea (*Coachman et al.*, 1975; *Hansell et al.*, 1993; *Lee et al.*, 2007; *Walsh et al.*, 1989). With such high nutrient availability (except for the Alaskan Coastal Waters which were excluded from the analysis when we masked pixels within 50 km of the coast), the entire study region should be pre-conditioned to support a near-surface phytoplankton bloom either underneath the ice or within the MIZ period. Thus, if a bloom did not develop within the MIZ period, it is very likely that those waters had already supported a bloom prior to ice retreat (i.e., an under-ice bloom) that depleted the nutrients in the upper water column, preventing a bloom after ice retreat (assuming there was no subsequent mixing of nutrients into surface waters).

The validity of the probable under-ice bloom classification was confirmed by comparing our bloom type results for years 2010 and 2011 with *in situ* observations at the location of the under-ice bloom reported by *Arrigo et al.* (2012, 2014). As is described in more detail in Section 1.3.5, the vast majority (81.7%) of the area that was observable by satellite in the vicinity of the verified *in situ* under-ice bloom was classified by this study as a probable under-ice bloom due to the low surface Chl *a* concentrations that characterized the area following ice retreat.

#### 1.2.4 Bloom type maps

Maps of bloom type were created for each year based on the bloom classification criteria described above. Summary statistics were computed for each year based on the percent of observable area that was attributed to each bloom type, with weighted means and standard

deviations over the time series calculated by assigning a weight to each year based on the number of observable pixels in each year relative to the total number of observable pixels over the time series. The under-ice and probable under-ice bloom percentages were summed to produce a combined under-ice and probable under-ice bloom category, which is equivalent to the percentage of observable area not classified as MIZ blooms. The bloom type percentages for each year were plotted as a function of time to assess trends in under-ice blooms and MIZ blooms over the 15-year time series.

In order to explore spatial patterns, cumulative maps for each bloom type were created based on the number of years between 1998 and 2012 that an individual pixel was classified as each bloom type. A dominant bloom type map was created from the cumulative bloom type maps, with each pixel assigned to the bloom type that was observed most frequently over the time series. Approximately 15% of the study area was excluded from the dominant bloom type map because multiple bloom types were observed with equal frequency and a dominant bloom type could not be assigned.

### **1.2.5 Changes in mean Chl *a* concentration over the 14-day MIZ period**

For each year of the time series, we calculated the daily mean Chl *a* concentration for each bloom type over the MIZ period to assess how bloom types differ in biomass following ice retreat. For example, on the day of ice retreat for each pixel (i.e. day 0), the mean Chl *a* concentration was computed separately for all under-ice, probable under-ice, and MIZ bloom pixels with retrievals on day 0. This process was repeated for each of the 14 days in the MIZ period, with results plotted for each year as the number of days since ice retreat versus the mean Chl *a* concentration for each bloom type on that day. Due to cloud cover, the sample size and pixel locations for each bloom type varied daily, with the mean Chl *a* concentration for a given day based on a subsample of the observable pixels. However, the large daily subsample size (mean = 1344, 6713, and 3688 pixels for under-ice, probable under-ice, and MIZ blooms, respectively) allowed discernable trends in mean Chl *a* concentration to be distinguished when comparing bloom types over the MIZ period.

## 1.3 Results

### 1.3.1 Date of ice retreat

The timing of sea ice retreat varied greatly throughout the study region during the 15-year time series. The map of the mean date of sea ice retreat from 1998 to 2012 (Fig. 1.1A) reveals that ice retreated generally from the southeast to the northwest. Sea ice retreated latest in the year 1998, with a mean date of ice retreat over the whole study region of 26 July. Sea ice retreated earliest in 2007, with a mean date of ice retreat over the whole study region more than a month earlier, on 21 June.

Across all years, sea ice retreated earliest along the Alaskan coast, where a polynya sometimes forms, and in the southern Chukchi Sea, where ice retreat begins in May. Sea ice cover was most persistent in the northern Chukchi Sea, with open water often not exposed until September, near the end of the phytoplankton growth season observable by satellite. Extensive persistent ice cover was present in the northwestern portion of the study region in years 1998, 2000, and 2001, while a smaller amount of multiyear ice remained in years 1999 and 2002. No persistent or multiyear ice was observed in the study region after 2003.

### 1.3.2 Bloom type maps

**Spatial coverage.** The fraction of the ocean surface visible to ocean color satellites (colored regions in Fig. 1.3) varied interannually due to differences in cloud cover and the distribution of sea ice (Table 1.1). Over the time series, the mean annual spatial coverage of the bloom type maps was  $45,216 \pm 25,569$  km<sup>2</sup>. This area represented approximately 10.6% of the total study region. The years with the smallest spatial coverage were 1998 and 2000, at only  $\sim 15,000$  km<sup>2</sup>. Conversely, the years with the greatest spatial coverage were 2005, at approximately 92,000 km<sup>2</sup>, and 2007 and 2011 at  $\sim 81,000$  and  $\sim 84,000$  km<sup>2</sup>, respectively. In general, spatial coverage was much better in the southern Chukchi Sea (66–70°N) than at higher latitudes (70–74°N), which were more frequently subject to cloud cover and persistent ice cover that either retreated late in the growing season, or in some cases, not at all.

**Bloom types.** Between 1998 and 2012, the annual maps of bloom type reveal that the Chukchi Sea has supported phytoplankton blooms both underneath the sea ice and in the MIZ following ice retreat (Fig. 1.3). Generally, blooms of the same type were clustered together throughout the study region, as indicated by large patches of uniform colors in

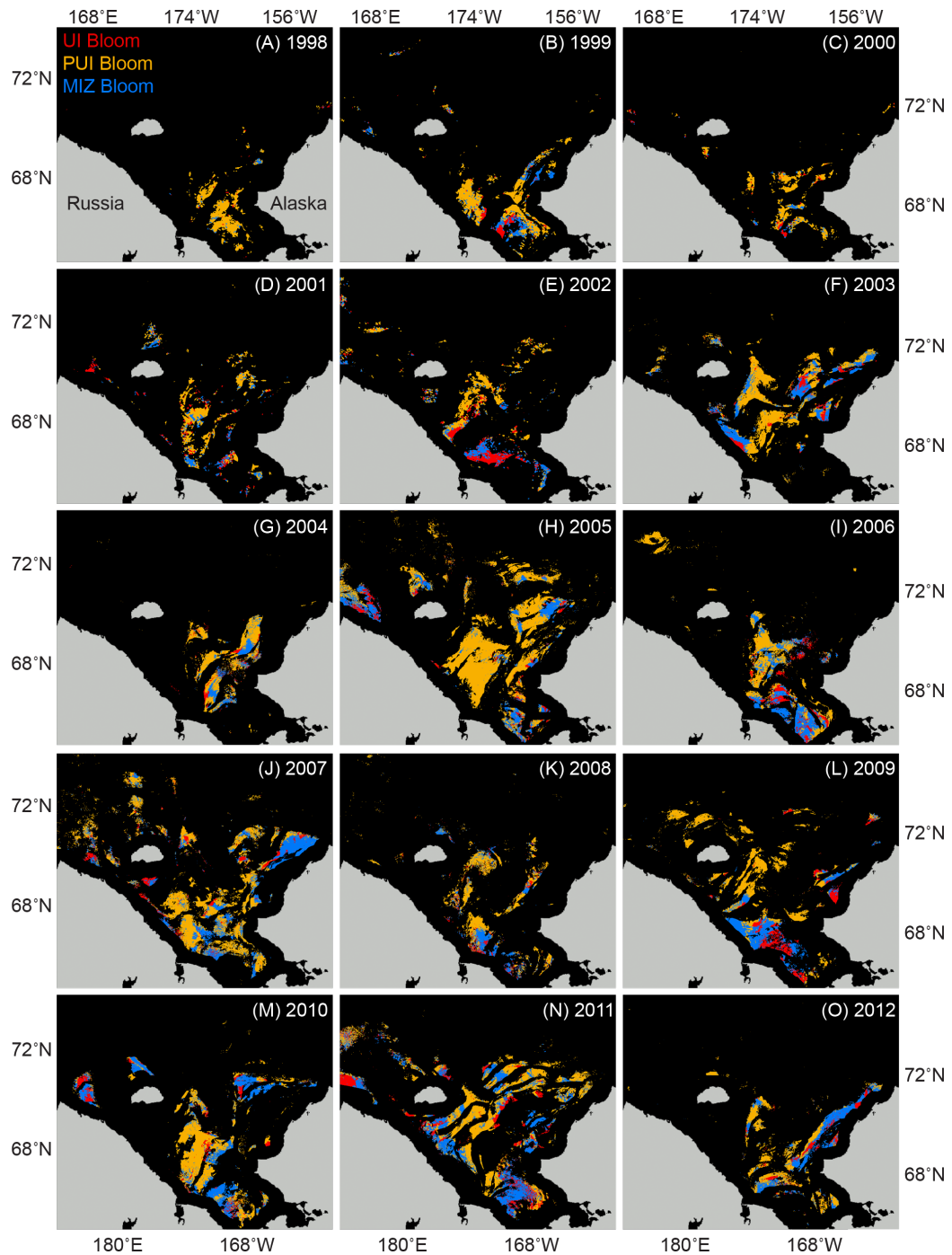


Figure 1.3: Bloom type maps for years 1998–2012. The locations of under-ice (UI) blooms are illustrated in red, probable under-ice (PUI) blooms in orange, and marginal ice zone (MIZ) blooms in blue. Black corresponds to areas without observable pixels.

Year	Observable Area (km <sup>2</sup> )	UI Bloom (% Area)	PUI Bloom (% Area)	MIZ Bloom (% Area)	UI + PUI Bloom (% Area)
1998	15068	3.23	91.0	5.78	94.2
1999	31110	10.3	65.9	23.8	76.2
2000	14910	10.8	77.5	11.7	88.3
2001	25960	15.7	61.0	23.3	76.7
2002	33361	26.2	48.4	25.5	74.5
2003	52831	9.54	60.7	29.8	70.2
2004	26756	8.97	66.7	24.3	75.7
2005	91848	6.38	73.8	19.9	80.1
2006	46408	14.0	50.2	35.8	64.2
2007	80669	8.47	60.6	30.9	69.1
2008	30910	10.5	62.3	27.2	72.8
2009	50521	17.0	53.6	29.4	70.6
2010	58977	9.93	54.6	35.5	64.5
2011	84495	14.8	50.5	34.7	65.3
2012	34400	10.9	51.2	37.9	62.1
Mean	45215	11.6	59.9	28.5	71.5
SD	24569	4.95	10.0	7.32	7.32

Table 1.1: Summary statistics for the percentage of observable area attributed to each bloom type based on annual bloom type maps from 1998 to 2012, with weighted means and unbiased standard deviations (SD) given for the bloom percentages. The total number of observable pixels (i.e. individual bloom type classifications) over the time series was 455,184. UI = Under-Ice; PUI = Probable Under-Ice; MIZ = Marginal Ice Zone.

the bloom type maps. The most common bloom type in the Chukchi Sea was the probable under-ice bloom (orange), followed by MIZ blooms (blue), and then under-ice blooms (red). All three types of blooms were present in each year of the time series.

**Percent of observable area by bloom type.** Since the spatial coverage of the annual bloom type maps is highly variable each year due to cloud and sea ice cover, we chose to quantify the spatial extent of each type of bloom as a percent of the observable study area

(Table 1.1). For example, in 2011, there were 8409 under-ice bloom pixels corresponding to an area of 12,529 km<sup>2</sup>. Since the total observable area in 2011 was 84,495 km<sup>2</sup>, under-ice blooms represented 14.8% of the observable study area. The remaining area was divided between MIZ blooms (34.7%) and probable under-ice blooms (50.5%). Despite the variability in annual spatial coverage, there was no significant relationship between bloom type and the number of observable pixels. Thus, bloom type classifications are not biased by data availability.

From 1998 to 2012, under-ice blooms covered a mean of  $11.6 \pm 4.95\%$  of the observable study area (Table 1.1), with a minimum of 3.23% in 1998 and a maximum of 26.2% in 2002. Probable under-ice blooms represented  $59.9 \pm 10.0\%$  of the observable study area on average, with a minimum of 48.4% in 2002 and a maximum of 91.0% in 1998. Combined, under-ice and probable under-ice blooms covered a mean of  $71.5 \pm 7.32\%$  of the observable study region (Table 1.1), with a maximum value of 94.2% in 1998 and a minimum value of 62.1% in 2006. In contrast, MIZ blooms represented only  $28.5 \pm 7.32\%$  of the observable study region (Table 1.1), with a minimum of 5.78% in 1998 and a maximum of 37.9% in 2012. Trends in bloom type over the time series are discussed in Section 1.3.7.

### 1.3.3 Sensitivity analysis

Maps of bloom type changed little when a different Chl *a* threshold was used. For example, spatial patterns were virtually unchanged in bloom type maps created using a Chl *a* threshold as high as  $> 5.0 \text{ mg m}^{-3}$  (Fig. 1.4A) instead of the  $2.5 \text{ mg m}^{-3}$  used in this study (Fig. 1.4B). Although the percentage of observable area attributed to each bloom type varied slightly in response to the bloom threshold employed, the combination of under-ice and probable under-ice blooms characterized the majority of the study area over a reasonable range of Chl *a* thresholds, while MIZ blooms remained representative of only a minority of the study area. For example, the weighted mean percent of observable area attributed to MIZ blooms for all years was 34.8% with a threshold of  $1.5 \text{ mg m}^{-3}$  and 23.2% with a threshold of  $3.5 \text{ mg m}^{-3}$ , as compared to the 28.5% found in this study. Similarly, the weighted mean percent of observable area attributed to under-ice blooms was 22.4% with a threshold of  $1.5 \text{ mg m}^{-3}$  and 7.63% with a threshold of  $3.5 \text{ mg m}^{-3}$ , as compared to the 11.6% found in this study.

When we repeated the original analysis using a three-week MIZ period (Fig. 1.4C), the

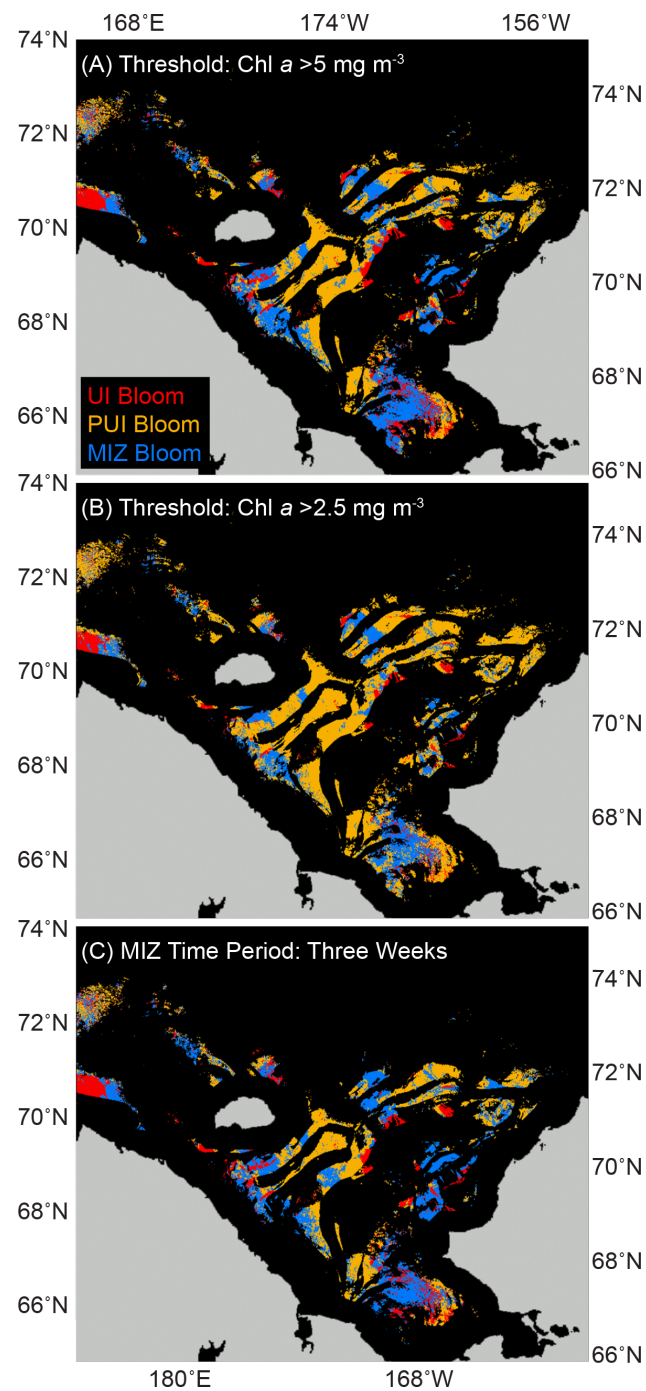


Figure 1.4: Bloom type maps for year 2011 as an example revealing qualitatively similar spatial patterns when using (A) a bloom threshold of Chl *a* > 5 mg m<sup>-3</sup>, (B) a bloom threshold of Chl *a* > 2.5 mg m<sup>-3</sup> as employed by this study, and (C) a three-week period for detection of MIZ blooms with a threshold of Chl *a* > 2.5 mg m<sup>-3</sup>.

spatial patterns in the bloom type maps were again similar to those obtained with the two-week MIZ period used in this study (Fig. 1.4B). The weighted mean percent attributed to MIZ blooms was 36.3% with the three-week period, as compared with 28.5% obtained using the two-week period. The percent attributed to under-ice blooms remained approximately the same, while the percent attributed to probable under-ice blooms dropped from 59.9% to 51.8%. Thus, although the longer MIZ period increased the prevalence of MIZ blooms, the combination of under-ice and probable under-ice blooms still represented the majority of the study area using either a two or three-week MIZ period (71.5% and 63.7%, respectively). Considering that employing the longer MIZ period reduced the observable area by 21.6% due to the requirement of at least one retrieval per pixel in each week of the MIZ period, this study relies on the shorter MIZ period that increases the observable area while providing similar results.

#### 1.3.4 Sensor comparison

Bloom type classification results were consistent based on ocean color data obtained from SeaWiFS and those obtained from MODIS during the five years of sensor overlap from 2003 to 2007 (Fig. 1.5). Although SeaWiFS imagery yielded a slightly higher number of under-ice bloom pixels, results from the two sensors generally compared very well and were almost identical for the probable under-ice bloom category that is the most common bloom type in the study region.

#### 1.3.5 Comparison with in situ observations

The location of the massive under-ice phytoplankton bloom that was observed *in situ* in the Chukchi Sea (Arrigo *et al.*, 2012) is shown on the bloom type map for 2011 (Fig. 1.6A). As described by Arrigo *et al.* (2014), the *in situ* under-ice bloom was characterized by extremely high depth-integrated Chl *a* concentrations (e.g.  $> 1000 \text{ mg m}^{-2}$ ) underneath the ice that decreased in adjacent open water areas (e.g.  $< 200 \text{ mg m}^{-3}$ ). The decrease in biomass was accompanied by a vertical migration of both the bloom and the nitracline. Under the ice, peak Chl *a* concentrations were located at the surface (near the ice/seawater interface) where nitrate concentrations were not yet depleted, while in open water peak Chl *a* concentrations were located in the subsurface (e.g. 25 m) where nitrate concentrations were increasingly depleted with distance from the ice edge. Surface Chl *a* concentrations were very low (e.g.  $0.38 \text{ mg m}^{-3}$ ) in open water adjacent to the ice edge, mirroring the low nitrate

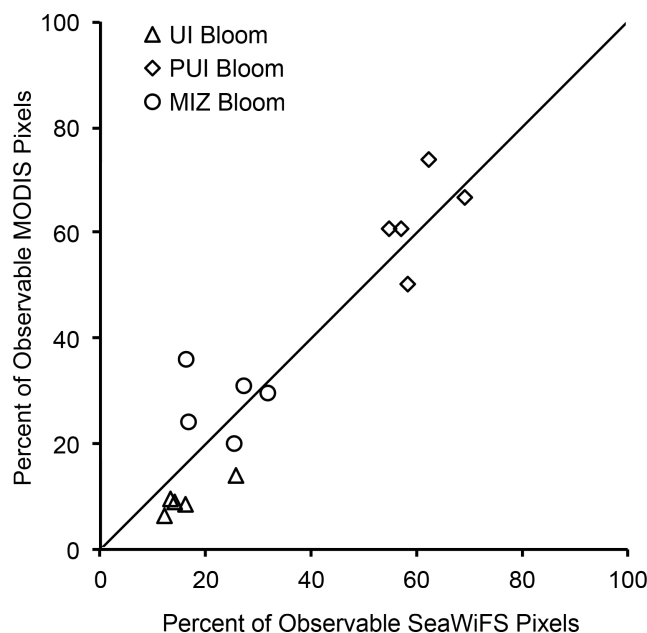


Figure 1.5: Sensor comparison of the percentage of observable pixels attributed to each bloom type, based on results obtained from both SeaWiFS and MODIS Aqua for years 2003–2007, with the 1:1 line plotted for reference.

concentrations (e.g. 0.01  $\mu\text{M}$ ) also found in surface waters outside of the ice. Together, these characteristics indicate that the bloom was ongoing under the ice but had aged and sunk out of the upper water column by the time the ice retreated from the nearby open waters (Arrigo *et al.*, 2014).

In the vicinity of the massive under-ice bloom (indicated by the rectangle on Fig. 1.6A), our analysis reveals that the bloom type distribution in 2011 was 81.7% probable under-ice bloom, 12.7% MIZ bloom, and 5.57% under-ice bloom. The fact that the dominant bloom type in this region was probable under-ice bloom rather than under-ice bloom is unsurprising given that the *in situ* surface Chl *a* concentrations observed in open water were too low to be classified as a bloom using our detection methods. Our results indicate that the majority of the Chl *a* associated with the massive under-ice phytoplankton bloom was no longer present at the time of ice retreat. This comparison of *in situ* data with our bloom type map results provides validation for the probable under-ice bloom classification used in this study to describe areas that had previously harbored under-ice blooms prior to ice retreat.

Similar to the field observations in 2011, there was strong biogeochemical evidence of a prior under-ice bloom observed in the same region in 2010 (Arrigo *et al.*, 2014). The bloom

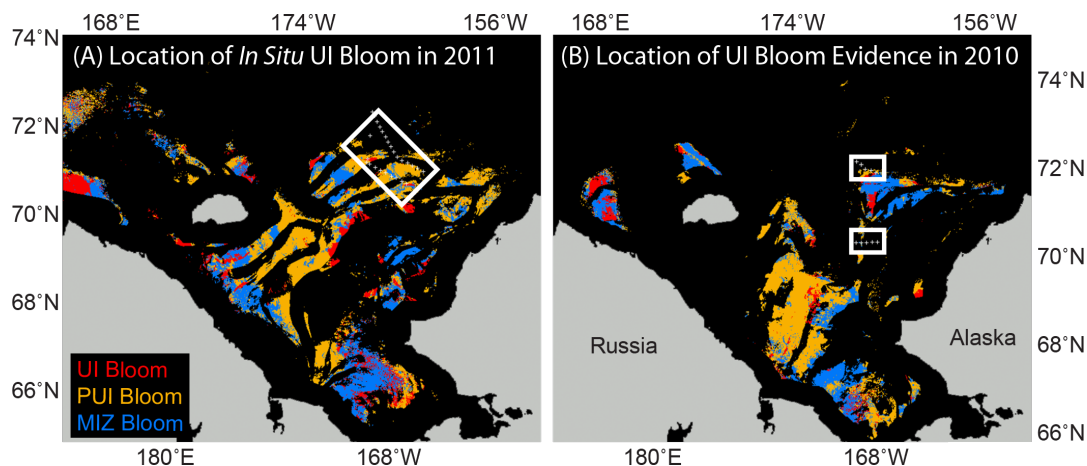


Figure 1.6: Bloom type maps in (A) 2011 with the location of the under-ice bloom observed *in situ* and (B) 2010 with the locations of biogeochemical evidence of a previous under-ice bloom. White boxes indicate general locations and stations are marked with plus signs.

type map for 2010 (Fig. 1.6B) also reveals a combination of probable under-ice blooms and under-ice blooms at the northernmost location with *in situ* observations containing evidence of a previous under-ice bloom (indicated by the upper rectangle on Fig. 1.6B). Due to cloud cover, there were very few observable pixels near the southernmost location with biogeochemical evidence of a previous under-ice bloom (indicated by the lower rectangle on Fig. 1.6B), although of the observable pixels, the majority were classified as probable under-ice blooms.

### 1.3.6 Changes in mean Chl *a* concentration over the 14-day MIZ period

Consistent with our conceptual model, the Chl *a* concentration for under-ice blooms at the time of ice retreat was highest at the start of the MIZ period, with an initial mean Chl *a* concentration in many years that exceeded  $8 \text{ mg m}^{-3}$  (Fig. 1.7). This remarkably high Chl *a* concentration for all under-ice blooms was much greater than the bloom threshold of  $2.5 \text{ mg m}^{-3}$  used to define these blooms, indicating that phytoplankton blooms underneath the ice frequently reach very high biomass. Averaged across the 15-year time series, the mean Chl *a* concentration of under-ice blooms significantly decreased over the MIZ period, from  $6.86 \text{ mg m}^{-3}$  on day 0 to  $2.45 \text{ mg m}^{-3}$  on day 14, corresponding to a 64.3% decrease ( $p < 0.001$ ).

Similar to under-ice blooms, the mean Chl *a* concentration of probable under-ice blooms

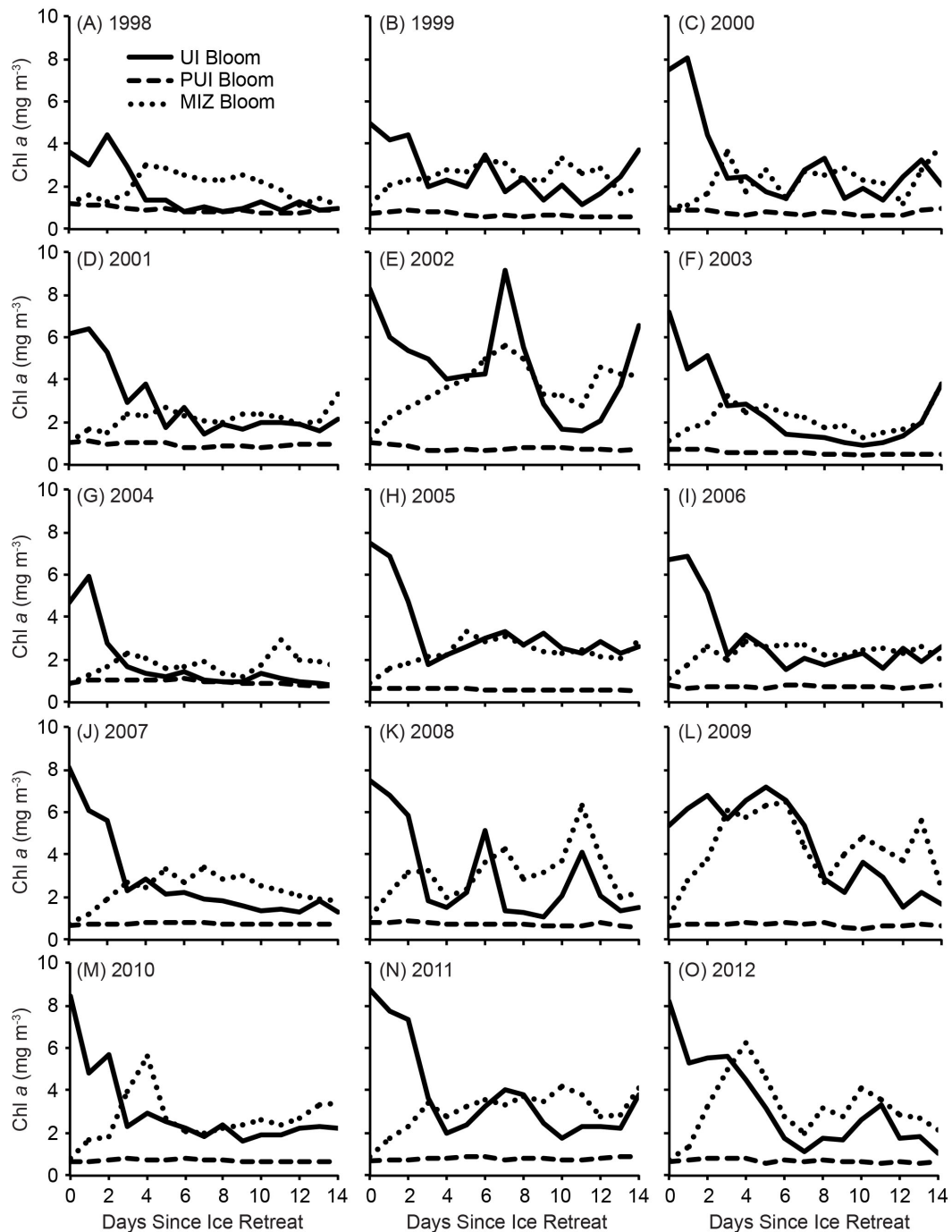


Figure 1.7: Time series plots of mean Chl *a* ( $\text{mg m}^{-3}$ ) for each bloom type over the two-week MIZ period following ice retreat. Solid line = under-ice blooms, dashed line = probable under-ice blooms, and dotted line = MIZ blooms.

over all years also decreased significantly (by 10.5%,  $p < 0.0001$ ) over the MIZ period from 0.82 to 0.73 mg m<sup>-3</sup>. Conversely, the mean Chl *a* concentration for MIZ blooms exhibited no significant trend over the MIZ period, with the timing of peak mean Chl *a* concentration highly variable beyond the first two days of open water (Fig. 1.7).

### 1.3.7 Interannual trends in bloom types

The percent of MIZ blooms significantly increased from a mean of 13.8% in 1998–2000 to 36.0% in 2010–2012 (Fig. 1.8), corresponding to a 161% increase over the 15-year time series. There was no significant trend in under-ice blooms from 1998 to 2012. Conversely, there was a decreasing trend in probable under-ice blooms, since this bloom type is defined as the residual of MIZ and under-ice blooms. However, the important caveat for the trend in probable under-ice blooms is that our classification methods require that each pixel of the study region be assigned only one bloom type for a given year, when in reality an area could support multiple types of bloom (i.e. an under-ice bloom that terminated prior to ice retreat followed by a MIZ bloom). Unfortunately, our methods provide no way to determine whether the increase in MIZ blooms is in replacement of, or in addition to, other blooms types. Thus, the decrease in probable under-ice blooms in this study may be a statistical artifact driven by the observed increase in MIZ blooms.

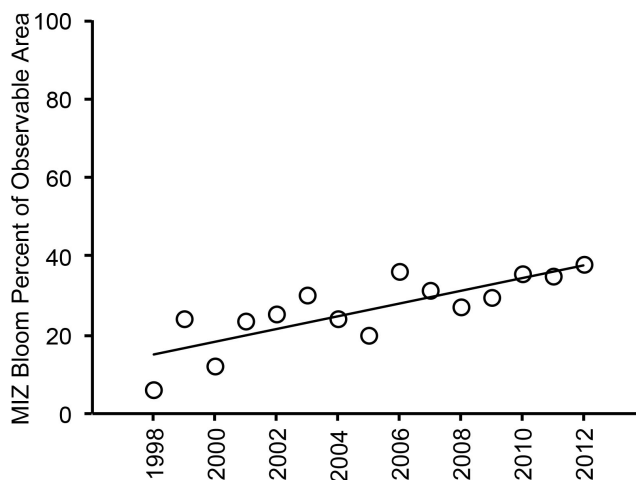


Figure 1.8: Trend from years 1998 to 2012 in the percent of observable area attributed to MIZ blooms ( $R^2 = 0.65$ ,  $p < 0.001$ ).

### 1.3.8 Spatial patterns by bloom type

**Cumulative bloom type.** The number of years each pixel contained either an under-ice bloom, a probable under-ice bloom, or a MIZ bloom was summed and used to create maps of the cumulative frequency of each bloom type (Fig. 1.9). As the maps reveal, individual pixels rarely had more than eight years with the same bloom type. More commonly, pixels contained less than five of the fifteen total years with the same bloom type, due in large part to the cloud cover and sea ice that restricts the average number of years with any type of bloom to  $2.79 \pm 1.93$  years per pixel.

Even with this relatively low number of blooms per pixel, the cumulative bloom type maps reveal distinct spatial patterns in the location and frequency of each of the bloom types. Under-ice blooms (Fig. 1.9A) are located most frequently in the southern Chukchi Sea, followed by the eastern Chukchi Sea and to the west of Wrangel Island. Conversely, probable under-ice blooms (Fig. 1.9B) are widespread throughout the region and are concentrated most heavily in the western Chukchi Sea. Finally, MIZ blooms (Fig. 1.9C) are located in similar areas as under-ice blooms but over a larger extent in these locations, including the southern and especially southwestern part of the Chukchi Sea, the eastern Chukchi, and in small patches north and to the west of Wrangel Island.

**Dominant bloom type.** Data from the cumulative bloom type maps were combined to create a map of the dominant bloom type for each pixel in the study region with valid data (Fig. 1.10). Across the Chukchi Sea shelf and surrounding areas, the probable under-ice bloom category dominates. Consistent with the cumulative bloom type results, probable under-ice blooms are especially common in the large expanse of the western Chukchi Sea and at higher latitudes where sea ice retreat occurs later in the season. On the other hand, MIZ blooms are dominant in areas where sea ice consistently retreats earlier, such as the southern Chukchi Sea, off of the Alaskan Coast, and to some degree off of the Siberian Coast and in the central Chukchi Sea. Likewise, under-ice blooms are dominant in relatively small patches off of the Alaskan and Siberian coasts and in the central Chukchi Sea.

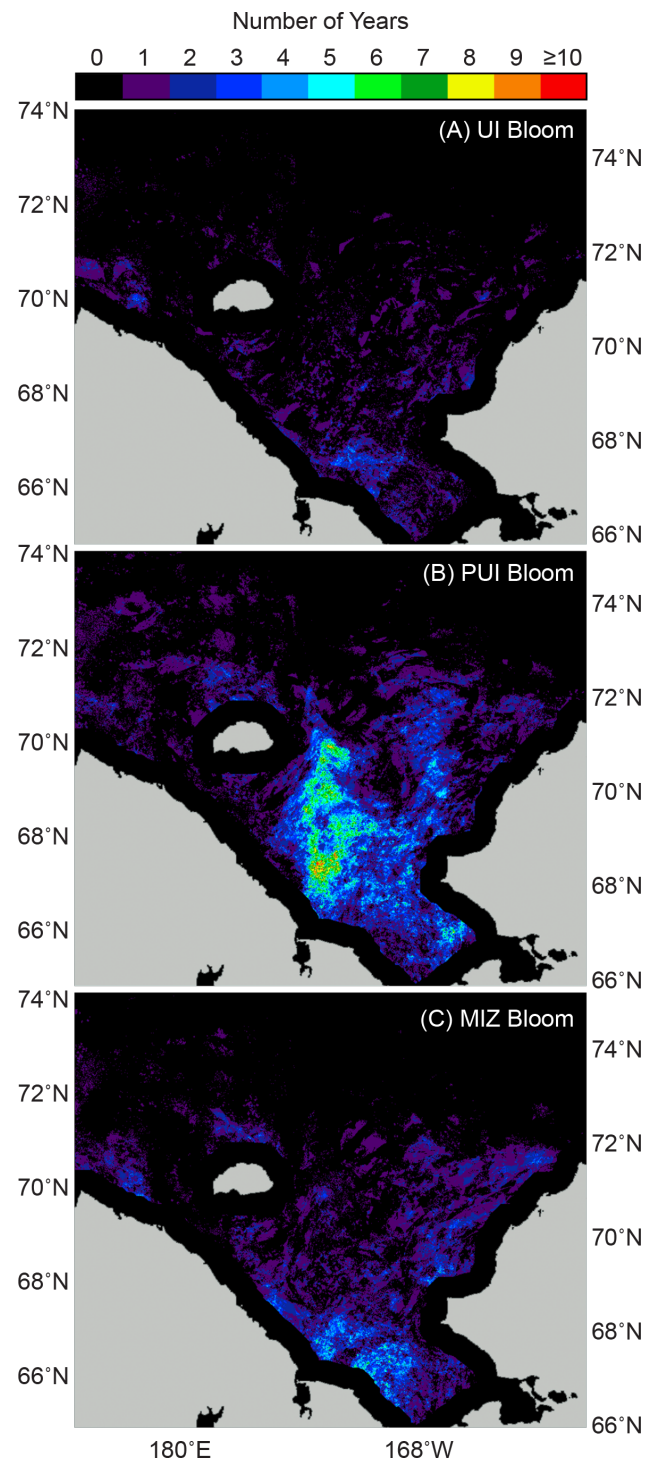


Figure 1.9: Maps of the cumulative frequency of each bloom type, based on the total number of years in the 15-year time series that each bloom type was observed for a given pixel.

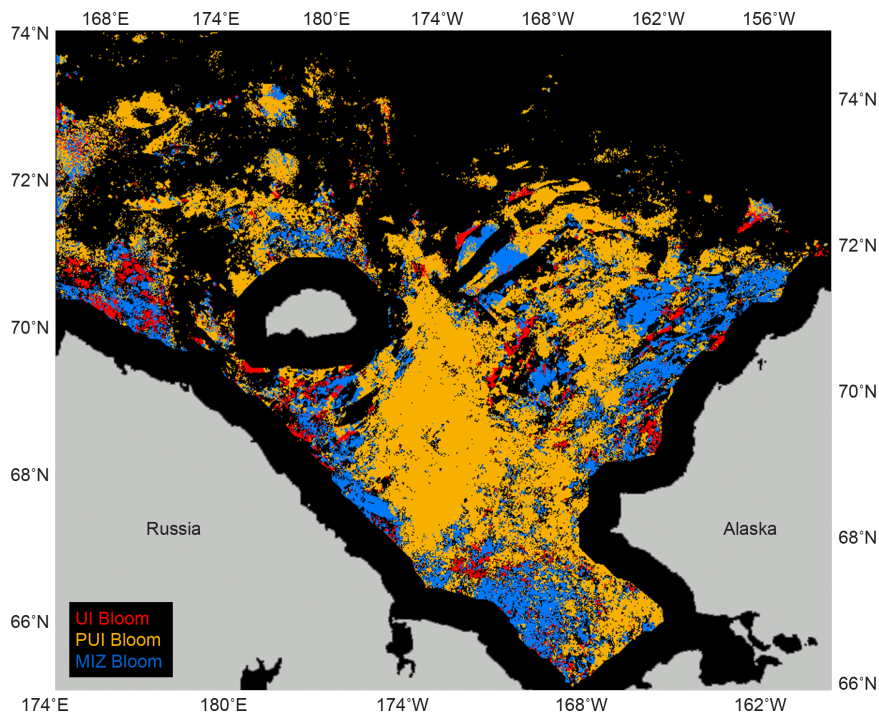


Figure 1.10: Dominant bloom type map, calculated from the cumulative bloom type maps (Fig. 1.9). Each pixel is assigned to the bloom type that occurred most frequently over the time series. Black = no data or multiple dominant bloom types.

## 1.4 Discussion

### 1.4.1 Methodological considerations

This study is the first to use satellite imagery to estimate the prevalence of under-ice phytoplankton blooms in the Arctic. The methods employed here were developed to be as conservative as possible in terms of distinguishing under-ice blooms from MIZ blooms and identifying probable under-ice bloom areas. Here, we address several factors that benefit from additional consideration in the context of this study.

**Probable under-ice bloom classification.** The most important potential weakness of our approach is in classifying a pixel without a bloom during the 14-day MIZ period as a probable under-ice bloom. This classification was based on three main assumptions. First, we assume that pre-bloom surface nutrient concentrations are high in early spring throughout the Chukchi Sea, such that a phytoplankton bloom would be expected in waters with

sufficient light availability. Although wintertime nutrient measurements are sparse in this region, the assumption of high nutrients is supported by a combination of model results and field observations. For example, simulated monthly nitrate values in the Arctic Ocean (Zhang *et al.*, 2010) suggest that non-coastal waters on the Chukchi Sea shelf are preconditioned for phytoplankton growth with pre-bloom surface  $\text{NO}_3^-$  concentrations in excess of  $15 \mu\text{M}$ . Similarly, *in situ* data from the Shelf-Basin Interaction (SBI) project in May 2002 reveal that surface waters on the Chukchi shelf are nutrient-replete in the spring, with  $\text{NO}_3^-$  values up to  $20 \mu\text{M}$  in the upper 15 meters of the water column (Codispoti *et al.*, 2005). Finally, observations north and south of the Bering Strait demonstrate that nutrient-rich Anadyr ( $\text{NO}_3^-$ :  $> 15 \mu\text{M}$ ) and Bering Shelf Water ( $\text{NO}_3^-$ :  $> 10 \mu\text{M}$ ) flow into the Chukchi Sea (Coachman *et al.*, 1975; Hansell *et al.*, 1993; Lee *et al.*, 2007; Walsh *et al.*, 1989), providing an ample supply of nutrients for spring phytoplankton growth that is supplemented by local regeneration of nutrients on the shelf (Codispoti *et al.*, 2005, 2009; Cooper *et al.*, 1997; Henriksen *et al.*, 1993; Walsh *et al.*, 1989; Brown *et al.*, 2015a).

Second, we assume that an under-ice phytoplankton bloom would likely deplete surface nutrients prior to ice retreat, preventing the onset of a future phytoplankton bloom within the MIZ period. This assumption is consistent with high nutrient drawdown associated with the under-ice bloom observed in 2011 (Arrigo *et al.*, 2012, 2014) and phytoplankton uptake measured throughout the eastern Chukchi Sea in 2010 and 2011 (Mills *et al.*, 2015). Similarly, early estimates of nutrient deficits in the southern Chukchi Sea in July 1985–1988 (Hansell *et al.*, 1993) suggest that up to 90% of the initial  $\text{NO}_3^-$  stock is removed from the water column by phytoplankton. Additionally, model simulations of the under-ice bloom by Palmer *et al.* (2014) illustrate that under-ice phytoplankton blooms can draw down  $\text{NO}_3^-$  in the upper 20 m of the water column from  $16 \mu\text{M}$  to  $< 2 \mu\text{M}$  between the time that melt ponds form (initiating the under-ice bloom) and the ice retreats ( $\sim 20$  days).

Finally, we assume that our defined MIZ period is sufficiently long for a phytoplankton bloom to form in nutrient-rich ice-free surface waters (without being advected away prior to bloom detection, as is discussed below). Thus, if a bloom is not observed within two weeks of ice retreat, it is likely that surface nutrients were previously depleted by an under-ice bloom. Although extending the MIZ bloom detection period to 21 days increased the percent of MIZ blooms from  $28.5 \pm 7.32\%$  to  $36.3 \pm 7.73\%$ , the value remained low relative to that of the combination of under-ice and probable under-ice blooms ( $63.7 \pm 7.73\%$ ).

Most importantly, the suitability of the probable under-ice bloom category is confirmed

by the comparison with *in situ* observations. More than 80% of the observable region in the vicinity of the under-ice bloom discovered in 2011 by *Arrigo et al.* (2012) was characterized by low surface Chl *a* concentrations in the two weeks following ice retreat, leading our analysis to classify the area as a probable under-ice bloom. The fact that this probable under-ice bloom was in fact a massive and well-documented under-ice bloom provides support for our approach used to define probable under-ice blooms as areas where a bloom is not observed in open water following ice retreat. Additionally, the 13% decrease in mean Chl *a* concentration for probable under-ice blooms over the two-week MIZ period (from 0.83 to 0.72 mg m<sup>-3</sup>) further supports the claim that these open water retrievals represent the end stages of a previous under-ice bloom.

**Advection.** Another possible weakness of our approach is that we assume that Chl *a* concentrations at each pixel represent the same water over the 14-day MIZ period rather than accounting for the flow of water and phytoplankton through the study region. However, this omission of advection is unlikely to play a significant role in influencing the results of our analysis. First, the mean northward flow of water across the Chukchi shelf is  $\sim 4$  km d<sup>-1</sup> (*Weingartner et al.*, 2005), which corresponds to a mean advection distance of  $\sim 56$  km over the 14-day MIZ period. Considering that the auto-correlation length scale for a daily satellite image is around 50–100 km (*Doney et al.*, 2003), the water that is advected into a pixel during the MIZ period is likely of a similar Chl *a* concentration as the water that is being replaced. Additionally, large-scale advection of phytoplankton from open water to under the ice is unlikely due to the northwestward direction of ice retreat that is distinct from that of the typical flow of water in the Chukchi Sea, which divides into three branches that flow to the north, the northeast, and the east, but not the northwest (*Weingartner et al.*, 2005). Furthermore, as *Arrigo et al.* (2014) illustrate, the mean velocity of ice retreat is nearly as fast (11 km d<sup>-1</sup>) as the fastest moving currents in the region (13 km d<sup>-1</sup>) measured by Acoustic Doppler Current Profiler (and therefore considerably faster than the mean northward flow velocity of 4 km d<sup>-1</sup> as described above).

Regardless, although we cannot account for the flow of water through the region, we can evaluate the potential impact of advection on our bloom classification results by considering different scenarios of phytoplankton transport into ice-covered and open waters. For example, in the unlikely event that a bloom was advected into an under-ice area that had not previously supported phytoplankton growth, the classification of that area would result in a

slight overestimation of under-ice blooms and a slight underestimation of either MIZ blooms or probable under-ice blooms, depending on whether the area would have otherwise been classified as a MIZ bloom. Conversely, if a bloom was advected into open waters that would have otherwise been classified as a probable under-ice bloom, the result would be a slight overestimation of MIZ blooms and a slight underestimation of probable under-ice blooms, with no effect on under-ice blooms. Although the list of plausible advection scenarios and outcomes extends beyond those listed here, to the best of our knowledge there is no scenario that is likely to present a significant or systematic bias in our bloom type classification results. The under-ice and probable under-ice blooms identified by this study are therefore not merely artifacts of advection. This point is further illustrated by the coherent spatial nature of phytoplankton bloom categories in the bloom type maps, particularly for the probable under-ice blooms that dominate the region.

**Pixel contamination by sea ice.** Two additional factors that could affect the classification of under-ice blooms are related to ocean color retrievals near the ice edge and in waters containing small amounts of sea ice, known as the adjacency effect and sub-pixel contamination, respectively (*Bélangier et al.*, 2007). The adjacency effect is due to the light reflection by ice in an adjacent pixel that interferes with the blue-to-green reflectance ratio of the target pixel and can result in a large ( $> 35\%$ ) underestimation of Chl *a* at high concentrations ( $> 0.5 \text{ mg m}^{-3}$ ) within 10–20 km of the ice edge. Conversely, sub-pixel contamination results in a systematic overestimation of Chl *a* concentrations in mixed ice-ocean pixels (*Bélangier et al.*, 2007). We note that the adjacency effect can also result in a small ( $< 35\%$ ) overestimation of Chl *a* at low concentrations (e.g.  $0.05 \text{ mg m}^{-3}$ ), but considering our high bloom threshold ( $2.5 \text{ mg m}^{-3}$ ), it is unlikely to impact the results of our study. Thus, the adjacency effect could lead to an underestimation of under-ice blooms, while the sub-pixel contamination could lead to an overestimation of under-ice blooms.

If under-ice blooms in our analysis were largely a consequence of sub-pixel contamination, there would have been a marked decrease in under-ice bloom area when we repeated our analysis with a more conservative ice retreat threshold (10% ice concentration). This is because a lower threshold would have resulted in fewer mixed-ice ocean pixels and a greater distance between observable pixels and the adjacent ice edge. Instead, the percent of under-ice blooms increased from 11.6% to 14.3% when the ice threshold was lowered to 10%. Similarly, the percent of probable under-ice blooms increased from 59.9% to 67.1%, leading

to a substantial increase in the percent of combined under-ice and probable under-ice blooms (from 71.5% to 81.4%) and a concurrent decrease in the percent of MIZ blooms (from 28.5% to 18.6%). A comparison of these values suggests that the under-ice blooms are not subject to overestimation due to sub-pixel contamination resulting from the 50% threshold. In fact, it is more likely that the adjacency effect leads to a small underestimation of under-ice blooms that results in a slight overestimation of probable under-ice and MIZ blooms in this study.

### 1.4.2 Prevalence of under-ice blooms

Our results suggest that under-ice blooms are widespread and prevalent in the Chukchi Sea, with satellite observations of high phytoplankton biomass at the time of ice retreat occurring in every year of the 15-year time series beginning in 1998. Combined, under-ice and probable under-ice blooms covered a total of  $\sim 72\%$  of the study region, with probable under-ice blooms representing blooms that terminated prior to ice retreat and under-ice blooms representing blooms that were ongoing at the time of ice retreat. Probable under-ice blooms ( $\sim 60\%$ ) were five-fold more common than under-ice blooms ( $\sim 12\%$ ) over the time series, likely related to the timing of ice retreat (discussed in Section 1.4.3).

Probable under-ice blooms were most common in the western Chukchi Sea (Fig. 1.10), which is also the portion of the study region that likely contains the highest pre-bloom surface nutrient concentrations due to the input and circulation of nutrient-rich Anadyr Water on the western Chukchi shelf (*Coachman et al.*, 1975; *Weingartner et al.*, 1998, 2005). This finding is consistent with satellite observations from 1998 to 2002 of the western Chukchi Sea that showed low Chl *a* concentrations ( $< 1 \text{ mg m}^{-3}$ ) beginning at the time of ice retreat in June and July that remained low through August (*Wang et al.*, 2005), further supporting our assumption that under-ice blooms in this region deplete surface nutrients and sink out of the upper water column prior to ice retreat, preventing the onset of a subsequent open water bloom. Thus, our probable under-ice bloom results indicate that more than half of the total observable area of the Chukchi Sea likely harbored blooms that fully developed and terminated before ice retreat from 1998 to 2012.

Our findings challenge the long-standing notion that blooms in seasonally ice-covered regions begin only after ice retreat and suggest instead that phytoplankton frequently bloom underneath first-year ice on nutrient-rich continental shelf systems. Over the study period, MIZ blooms were observed in just over a quarter of the study region ( $28.5 \pm 7.32\%$ ). This

result is in contrast with reports by *Perrette et al.* (2011) that MIZ blooms were nearly ubiquitous throughout the Arctic Ocean from 1998 to 2007, including in the Chukchi Sea. This discrepancy exists primarily for two main reasons. First, *Perrette et al.* (2011) did not distinguish MIZ blooms from under-ice blooms; therefore any bloom recorded within the MIZ period was classified as a MIZ bloom (referred to in their study as an ice-edge bloom). Second, the Chl *a* bloom threshold used by *Perrette et al.* (2011) was five-fold lower ( $0.5 \text{ mg m}^{-3}$ ) than the threshold used in our study ( $2.5 \text{ mg m}^{-3}$ ). For comparison, we repeated our analysis using the parameters of *Perrette et al.* (2011), which also include an extended MIZ period (20 days) and a more conservative sea ice concentration (10%) for determining the date of ice retreat. The resulting bloom classification over our 15-year time series was  $79.1 \pm 10.7\%$  under-ice bloom,  $5.06 \pm 4.82\%$  probable under-ice bloom, and  $15.9 \pm 7.39\%$  MIZ bloom (based on weighted means; annual data not shown). Therefore, contrary to the work of *Perrette et al.* (2011), MIZ blooms are not the dominant bloom type in the Chukchi Sea.

### 1.4.3 Sea ice retreat and phytoplankton bloom type

As the Arctic environment continues to evolve in response to climate change (*Loeng et al.*, 2005), phytoplankton in the Chukchi Sea and other Arctic marginal seas will be increasingly affected by changing sea ice dynamics such as earlier ice retreat, thinning ice cover, and an increased prevalence of melt ponds (*Comiso*, 2012; *Perovich and Polashenski*, 2012; *Polashenski et al.*, 2012; *Stroeve et al.*, 2011; *Wang and Overland*, 2009). Considering that first-year ice with a high melt pond fraction is already characteristic of the Chukchi Sea shelf (*Maslanik et al.*, 2011), perhaps the most relevant metric of change affecting phytoplankton blooms in this region is the date of sea ice retreat. Thus, characterizing how the timing of ice retreat in the Chukchi Sea influences phytoplankton bloom type is essential for understanding the current and future state of primary producers in Arctic shelf seas.

In our study, probable under-ice blooms were generally observed in areas with significantly later sea ice retreat than that of under-ice blooms, with the mean date of ice retreat more than eight days later for probable under-ice blooms (18 June  $\pm$  15.8 days) than for under-ice blooms (9 June  $\pm$  17.6 days;  $p < 0.0001$ ). The difference in the timing of ice retreat for these two bloom types is not unexpected given that probable under-ice blooms represent blooms that became nutrient limited and terminated prior to sea ice retreat, while under-ice blooms represent blooms that were uncovered at an earlier stage such that phytoplankton

biomass in surface waters still exceeded the Chl *a* threshold at the time of ice retreat.

Similarly, MIZ blooms were generally found in areas where ice retreated significantly earlier than the areas where under-ice or probable under-ice blooms were found, with a mean date of ice retreat for MIZ blooms (8 June  $\pm$  15.6 days;  $p < 0.0001$ ) that was half a day earlier than that of under-ice blooms and nine days earlier than that of probable under-ice blooms. Because MIZ blooms form only in waters with adequate surface nutrient concentrations, it follows that these blooms occur most frequently in areas where under-ice blooms have not had sufficient time to fully deplete the surface nutrients. In many cases, under-ice blooms may transition into MIZ blooms as the sea ice retreats, exposing the early-stage bloom to open water.

Based on these observations, we predict that earlier ice retreat will lead to an earlier uncovering of under-ice phytoplankton blooms. This prediction is supported by the mean Chl *a* concentration of the first retrieval of under-ice blooms, which significantly increased over the 15 years of this study (Fig. 1.11A) and varied in conjunction with the date of sea ice retreat (Fig. 1.11B). For example, in 1998 when the mean date of ice retreat was latest (26 July), the mean Chl *a* concentration of under-ice blooms was the lowest of all years ( $4.44 \text{ mg m}^{-3}$ ). Nine years later in 2007, sea ice retreated earliest with a mean date of sea ice retreat more than a month before (22 June). The mean Chl *a* concentration of under-ice blooms in 2007 was nearly twice that of 1998, with a value of  $8.6 \text{ mg m}^{-3}$  Chl *a*. Although the shift toward earlier ice retreat in our study was not significant due to the short time series, it was nearly so ( $p = 0.052$ ). Additionally, there is a significant trend in the date of ice retreat across the Arctic Ocean, with a mean decrease of 2–4 days per year (*Arrigo and van Dijken*, 2011). The increase in the mean Chl *a* concentration of under-ice blooms at the time of ice retreat that we observed as ice retreated earlier throughout the Arctic corresponds to an earlier uncovering of under-ice blooms that will likely continue into the future.

Earlier ice retreat may also be responsible for the increase in the area of MIZ blooms from 1998 to 2012. As described above, waters with earlier ice retreat are more likely to have higher surface nutrient availability to support MIZ blooms, while areas with later ice retreat are more likely to harbor under-ice blooms that fully deplete surface nutrients before ice retreat. Thus, earlier ice retreat likely leads to an increase in the area that is suitable for MIZ blooms, explaining the increase in MIZ blooms over the time series and the prevalence

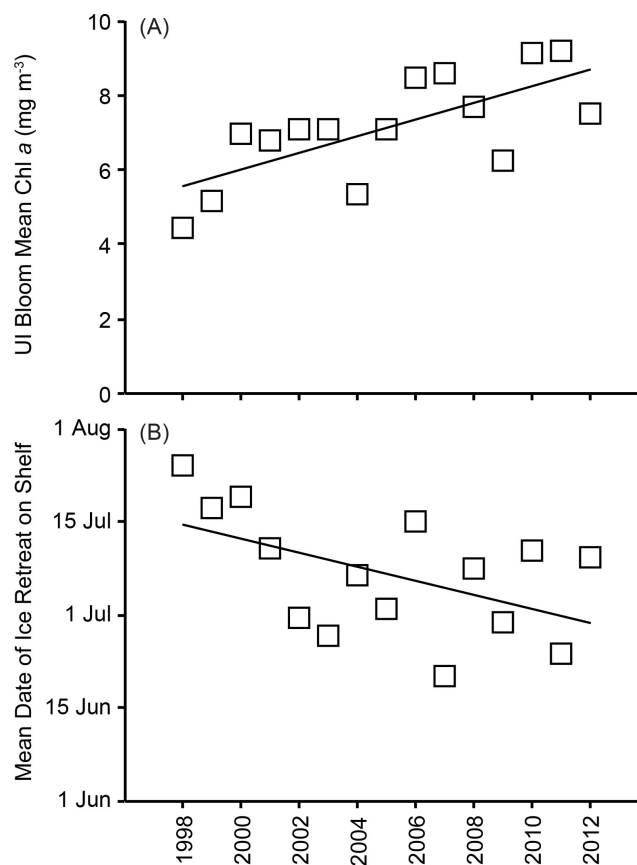


Figure 1.11: Time series from years 1998 to 2012 of (A) mean Chl *a* of under-ice blooms at first retrieval ( $R^2 = 0.50$ ,  $p < 0.01$ ) and (B) the date of sea ice retreat in the study area ( $R^2 = 0.26$ ,  $p = 0.052$ ).

of MIZ blooms in areas that retreated significantly later than under-ice and probable under-ice blooms. As ice continues to retreat earlier in the future, MIZ blooms may become more prevalent in this region.

#### 1.4.4 Implications and future work

Our findings of the existence of under-ice blooms throughout the Chukchi Sea are consistent with the increase in light penetration through first-year melt-ponded sea ice that has become characteristic of the region in recent decades (Frey *et al.*, 2011; Kwok and Rothrock, 2009; Maslanik *et al.*, 2011) and the discovery in 2011 that massive phytoplankton blooms can occur underneath fully consolidated sea ice (Arrigo *et al.*, 2012). The present study is the first to provide a characterization of the spatial and temporal extent of under-ice blooms in

this rapidly changing marine ecosystem and illustrates that phytoplankton bloom dynamics are more complex in this region than previously thought. Considering that approximately 72% of the study region likely supported under-ice blooms between 1998 and 2012, the contribution of phytoplankton primary production underneath the ice must be included in estimates of total NPP in this region. This necessary addition presents a challenge to future research, particularly as more than half of the study area harbors blooms that terminate prior to ice retreat and are almost invisible to satellite sensors.

Similarly, it will be important to better understand the ecological implications of future under-ice blooms as phytoplankton bloom dynamics in this region continue to evolve. Our results suggest that phytoplankton consistently bloom prior to ice retreat in the Chukchi Sea, with potentially large implications for upper trophic level organisms that time their migrations to arrive in the Arctic to feed on MIZ blooms (*Loeng et al.*, 2005). Physical properties such as nutrient availability, sea ice thickness, and melt pond coverage will play a large role in shaping the future of under-ice phytoplankton blooms in this region. Even if under-ice blooms continue to be uncovered earlier and transition more frequently to MIZ blooms, earlier ice retreat will inevitably lead to earlier phytoplankton blooms, consistent with observations by *Kahru et al.* (2010). Combined, these factors may enhance the already rich benthic community of the Chukchi Sea, which supports abundant populations of marine mammals and seabirds (*Dunton et al.*, 2005; *Grebmeier et al.*, 2006; *Loeng et al.*, 2005). Clearly, our understanding of phytoplankton bloom dynamics in this complex ecosystem will benefit greatly from further studies and fieldwork in this region.

## Acknowledgments

This material is based upon work supported by the National Science Foundation Graduate Research Fellowship under Grant no. DGE-0645962 to K.E. Lowry and the Ocean Biology and Biogeochemistry Program and the Cryosphere Science Program of the National Aeronautics and Space Administration under Grant no. NNX10AF42G to K.R. Arrigo. The authors would also like to acknowledge two anonymous reviewers and the members of the Arrigo Lab at Stanford University for their helpful suggestions that led to the publication of this manuscript.

## Chapter 2

# The influence of winter water on phytoplankton blooms

KATE E. LOWRY, MATTHEW M. MILLS, ZACHARY W. BROWN, KEVIN R. ARRIGO

*Earth System Science, Stanford University, Stanford, California, USA*

ROBERT S. PICKART

*Woods Hole Oceanographic Institution, Woods Hole, Massachusetts, USA*

NICHOLAS R. BATES

*Bermuda Institute of Ocean Sciences, St. Georges, Bermuda*

*The flow of nutrient-rich winter water (WW) through the Chukchi Sea plays an important and previously uncharacterized role in sustaining summer phytoplankton blooms. Using hydrographic and biogeochemical data collected as part of the ICESCAPE program (June–July 2010–11), we examined phytoplankton bloom dynamics in relation to the distribution and circulation of WW (defined as water with potential temperature  $\leq -1.6^{\circ}\text{C}$ ) across the Chukchi shelf. Characterized by high concentrations of nitrate (mean:  $12.3 \pm 5.13 \mu\text{mol L}^{-1}$ ) that typically limits primary production in this region, WW was correlated with extremely high phytoplankton biomass, with mean chlorophyll *a* concentrations that were three-fold higher in WW ( $8.64 \pm 9.75 \mu\text{g L}^{-1}$ ) than in adjacent warmer water ( $2.79 \pm 5.58 \mu\text{g L}^{-1}$ ). Maximum chlorophyll *a* concentrations ( $\sim 30 \mu\text{g L}^{-1}$ ) were typically positioned at the interface between nutrient-rich WW and shallower,*

*warmer water with more light availability. Comparing satellite-based calculations of open water duration to phytoplankton biomass, nutrient concentrations, and oxygen saturation revealed widespread evidence of under-ice blooms prior to our sampling, with biogeochemical properties indicating that blooms had already terminated in many places where WW was no longer present. Our results suggest that summer phytoplankton blooms are sustained for a longer duration along the pathways of nutrient-rich WW and that biological hotspots in this region (e.g. the mouth of Barrow Canyon) are largely driven by the flow and confluence of these extremely productive pathways of WW that flow across the Chukchi shelf.*

This chapter was originally published in *Deep-Sea Research Part II* and is reproduced with permission from the publisher. ©2015. This manuscript version is made available under the CC-BY-NC-ND 4.0 license: <http://creativecommons.org/licenses/by-nc-nd/4.0/>

Lowry, K.E., Pickart, R.S., Mills, M.M., Brown, Z.W., Van Dijken, G. L., Bates, N.B., and Arrigo, K.R. The influence of winter water on phytoplankton blooms in the Chukchi Sea. *Deep-Sea Res. II* 118 (2015) 53-72, doi: 10.1016/j.dsr2.2015.06.006.

## 2.1 Introduction

Located north of the Bering Strait between Alaska and Far East Russia, the Chukchi Sea is the gateway of the Pacific Ocean to the Arctic. With a total area of 620,000 km<sup>2</sup> and a median depth of approximately 50 m (*Jakobsson, 2002*), the Chukchi Sea contains a wide and shallow continental shelf that comprises 10% of the total Arctic Ocean shelf area (*Jakobsson et al., 2004; Carmack and Wassmann, 2006*). The importance of the Chukchi Sea as an inflow shelf sea (*Carmack and Wassmann, 2006*) that ventilates the upper halocline of the Arctic Ocean (*Woodgate and Aagaard, 2005a; Woodgate et al., 2005a*) motivates a thorough understanding of the physical and biogeochemical processes that modify Pacific-origin water masses as they transit the shelf en route to the basin.

The Chukchi Sea is a region of intense summer biological activity with a rich benthic community that supports abundant populations of marine mammals and seabirds (*Loeng et al., 2005; Dunton et al., 2005; Grebmeier et al., 2006*). In recent decades, the Arctic

Ocean has experienced unprecedented reductions in sea ice cover and thickness (*Kwok and Rothrock, 2009; Serreze et al., 2007; Stroeve et al., 2011*), accompanied by an increased heat and freshwater flux through the Bering Strait (*Woodgate et al., 2012*). The impacts of these changes on the global carbon cycle (*Bates et al., 2011*) and the marine ecosystem of the Chukchi Sea (*Grebmeier, 2012*) are only beginning to be understood. Of particular interest is how the primary producers that form the base of the food web are being affected by the pronounced changes in the physical environment. Previous work suggests that phytoplankton are already responding to reduced sea ice cover and thickness, with evidence for increased primary production in open water (*Arrigo and van Dijken, 2011*) and beneath the thinning sea ice cover (*Arrigo et al., 2012, 2014; Palmer et al., 2014, 2013; Lowry et al., 2014*). To fully comprehend the significance of these changes, it is necessary to further our understanding of bloom dynamics in this region.

Pacific-origin water flows northward through the Bering Strait due to the sea surface height differential resulting from the salinity difference between the Arctic and Pacific Oceans (*Coachman et al., 1975*). Upon entering the Chukchi Sea, the flow is steered primarily by shelf bathymetry into three branches, which to some degree are distinguished by water mass properties set within the Bering Sea (*Coachman et al., 1975; Overland and Roach, 1987; Weingartner et al., 2005*). Differences in temperature, salinity ( $S$ ), and nutrient concentrations between these pathways result in significant variations in biogeochemical properties across the shelf (*Walsh et al., 1989; Cooper et al., 1997; Codispoti et al., 2005, 2013*). In summertime, the easternmost pathway advects Alaskan Coastal Water, which is relatively warm ( $> 2^{\circ}\text{C}$ ), fresh ( $S < 32$ ), and nutrient-poor (pre-bloom  $\text{NO}_3^- < 10 \mu\text{mol L}^{-1}$ ) due to the input of river runoff and the biological utilization of nutrients in the eastern Bering Sea. The middle flow branch, which progresses through the Central Channel between Hanna and Herald Shoals, consists largely of colder and saltier Bering Shelf Water (BSW) with moderate nutrient concentrations (pre-bloom  $\text{NO}_3^- > 10 \mu\text{mol L}^{-1}$ ). The westernmost branch follows Hope Valley into Herald Canyon and transports a large amount of Anadyr Water (AW), which is the saltiest of the three Chukchi Sea water masses and has the highest nutrient concentration (pre-bloom  $\text{NO}_3^- > 15 \mu\text{mol L}^{-1}$ ), owing to the upwelling of nutrient-rich waters in the Northern Bering Sea (*Hansell et al., 1993; Lee et al., 2007*). The precise division of transport between the branches is currently unknown. Using relatively sparse mooring data, *Woodgate et al. (2005b)* estimated a roughly even split between the branches, but recent shipboard surveys suggest that, in summer, the majority of the flow is contained

in the two eastern branches (*Gong and Pickart, 2015; Itoh et al., 2015*).

The water mass properties in the Chukchi Sea are heavily influenced by the seasonal cycle of sea ice, both locally on the Chukchi shelf and to the south in the Bering Sea. In the winter, sea ice formation causes brine rejection that can mix the entire water column and cool it to the freezing point (approximately  $-1.9^{\circ}\text{C}$ ) (e.g. *Woodgate et al., 2005b*). When the convection reaches the bottom it suspends regenerated nutrients from the sediments into the water column. The resulting water mass, known as winter water (WW), is cold, dense, and high in nutrients. The water so formed in the Bering Sea flows northward through Bering Strait during the winter months and into the spring (*Woodgate et al., 2005b*). However, the occurrence of leads and polynyas on the Chukchi shelf during the winter can lead to further re-freezing and the formation of “hyper-saline” WW (*Weingartner et al., 1998; Itoh et al., 2012*).

Although there are few winter and spring measurements in the Chukchi Sea, modeling results (*Zhang et al., 2010*) and field studies (e.g. *Codispoti et al., 2005*) indicate that surface waters are nutrient-replete in the Chukchi Sea, with  $\text{NO}_3^-$  concentrations as high as 10–20  $\mu\text{mol L}^{-1}$  in non-coastal shelf waters. As sea ice retreats in the summer, the water column becomes re-stratified as surface waters freshen and warm due to a combination of ice melt, solar heating, and the influx of Pacific summer waters from the Bering Sea (*Woodgate and Aagaard, 2005b; Gong and Pickart, 2015*). The WW remaining on the Chukchi shelf is gradually modified by mixing with these waters and/or by direct solar heating (*Weingartner et al., 2005; Gong and Pickart, 2015*). As a result, the presence of WW on the shelf in summer is spatially variable, with residence times determined by the bathymetry and circulation of the Chukchi Sea (*Pickart et al., 2016*). By the end of summer, all of the WW gets flushed from the shelf, largely through Herald Canyon in the west (*Pickart et al., 2010*) and Barrow Canyon in the east (*Pickart et al., 2005; Woodgate et al., 2005b; Itoh et al., 2015*).

The high nutrient content and persistence of WW on the Chukchi shelf through the spring and summer suggests that this water mass plays an important, yet previously uncharacterized, role in influencing phytoplankton blooms. In this study, we examine the relationship between the early-summer hydrographic conditions in the Chukchi Sea and the phytoplankton blooms that occur on the shelf, with specific focus on the role of the nutrient-rich WW in initiating and sustaining phytoplankton blooms both before and after sea ice retreat. We assess the biological significance of WW in the summer as it drains across the Chukchi shelf by relating the location of WW to biogeochemical properties such as phytoplankton

biomass, oxygen ( $O_2$ ) saturation, and concentrations of nutrients and dissolved inorganic carbon (DIC). To fully elucidate the relationship between WW and phytoplankton blooms in this seasonally ice-free ecosystem, we incorporate field results from both under the sea ice and in open water, and use satellite imagery of sea ice to provide further environmental context.

## 2.2 Methods

### 2.2.1 Study region

As part of the NASA-funded Impacts of Climate on EcoSystems and Chemistry of the Arctic Pacific Environment (ICESCAPE) program, two field campaigns were carried out in the Chukchi Sea aboard USCGC Healy, from 18 June to 16 July 2010 (HLY1001) and from 28 June to 24 July 2011 (HLY1101). The present analysis focuses on the continental shelf of the northeastern Chukchi Sea, using data from seven transects that together span the shallow shelf waters of this region (Fig. 2.1). Six of the seven transects considered here were occupied in 2011, while the southernmost transect (the Central Channel line) was sampled in 2010. The Chukchi North and Hanna Shoal North transects were occupied on both cruises, providing an opportunity to compare hydrographic conditions between 2010 and 2011. Except where otherwise noted, data presented for these two transects were collected in 2011 when the sampling was more comprehensive.

### 2.2.2 Field methods and laboratory analysis

**Shipboard sampling.** Vertical profiles of temperature, salinity, dissolved  $O_2$ , fluorescence, and photosynthetically active radiation (PAR) were obtained approximately every 15 km using a Sea-Bird 911+ conductivity-temperature-depth instrument (CTD) with an SBE43  $O_2$  sensor (Sea-Bird Electronics), a fluorometer (AQIII, Chelsea Technologies Group, Ltd.), and a PAR sensor (QSP2300, Biospherical Instruments, Inc.). The CTD system was mounted on a rosette with twelve 30-liter Niskin bottles. Water samples were collected at a set of standard depths (5, 10, 25, 50, 75, 100, 150, and 200 m), and also at the depth of the fluorescence maximum and near the bottom (typically within 2–5 m of the seafloor). Most of the stations were occupied on the shelf and hence were shallower than 60 m. The

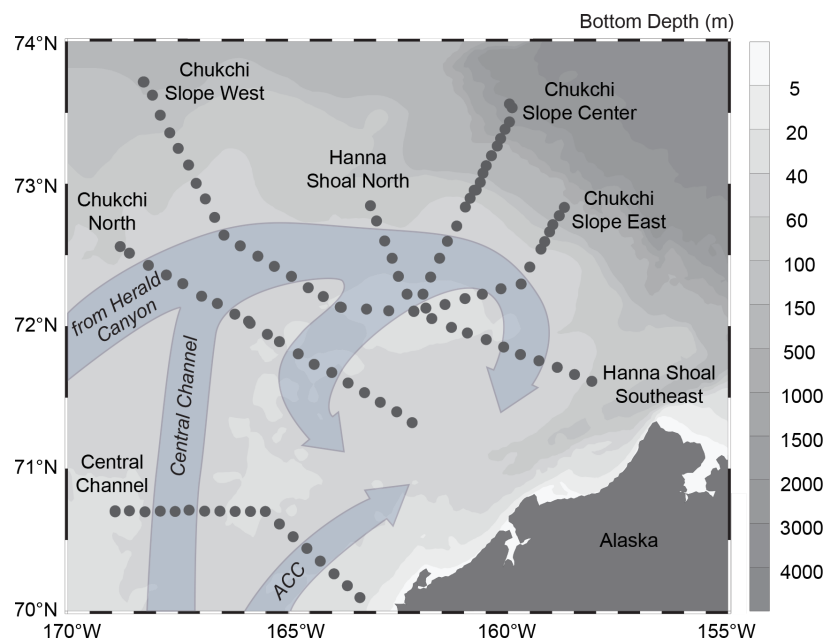


Figure 2.1: Map of the northeastern Chukchi Sea illustrating bathymetry, the seven transects sampled as part of our field campaign in 2010–2011 that we focus on in this study, and the main pathway of winter water (WW) as it flowed across the Chukchi shelf during our sampling period (as identified and described in more detail by *Pickart et al. (2016)*).

temperature and conductivity sensors were calibrated pre- and post-cruise at Sea-Bird Electronics, and the conductivity sensor was also calibrated during the cruise using the deepest water sample salinity data. Based on this information, the estimated accuracies are  $0.008^{\circ}\text{C}$  for temperature and 0.004 for salinity on the shelf, and  $0.002^{\circ}\text{C}$  and 0.002, respectively, in deeper water.

Water samples were taken for  $\text{O}_2$  concentration using standard Winkler titrations for sensor calibration and for a suite of biogeochemical properties, including nutrients, dissolved inorganic carbon (DIC), chlorophyll *a* (Chl *a*), and particulate organic carbon (POC). Methods for these analyses are briefly presented below, with additional detail provided by *Arrigo et al. (2014)*.

Currents were measured on both cruises using *Healy's* hull-mounted Ocean Surveyor 150 KHz acoustic Doppler current profiler (ADCP). The data were acquired using the UH-DAS software package from the University of Hawaii, with additional processing done using the CODAS3 software utility (<http://currents.soest.hawaii.edu>). Following this, the barotropic tidal signal was removed from each profile using the Oregon State University

model (<http://volkov.oce.orst.edu/tides>; (Padman and Erofeeva, 2004). The uncertainty of the final product is estimated to be  $\pm 2 \text{ cm s}^{-1}$ .

**Nutrients and dissolved inorganic carbon.** Discrete water column samples were analyzed for nutrients on board the ship with a Seal Analytical continuous-flow AutoAnalyzer 3 using a modification of the method of Armstrong *et al.* (1967). In this study, we focus primarily on nitrate ( $\text{NO}_3^-$ ), but also consider concentrations of silicate ( $\text{Si(OH)}_4$ ) and phosphate ( $\text{PO}_4^{3-}$ ). Seawater samples for DIC were collected at each station into pre-cleaned  $\sim 300 \text{ mL}$  borosilicate bottles, poisoned with  $\text{HgCl}_2$  to halt biological activity, and then sealed after the cast. The analysis was done post-cruise at the Bermuda Institute of Ocean Sciences (BIOS) using a highly precise ( $\sim 0.025\%$ ;  $< 0.5 \text{ mmol kg}^{-1}$ ) gas extraction/coulometric detection system (Bates *et al.*, 2005), along with Certified Reference Materials (provided by A. G. Dickson, Scripps Institution of Oceanography). The resulting accuracy was  $0.05\%$  ( $\sim 0.5 \text{ mmol kg}^{-1}$ ).

**Phytoplankton.** Samples for Chl *a* were filtered onto 25 mm Whatman GF/F filters (nominal pore size  $0.7 \mu\text{m}$ ), placed in 5 mL of 90% acetone, and then extracted in the dark at  $3^\circ\text{C}$  for 24 hrs. Chl *a* was measured fluorometrically (Holm-Hansen *et al.*, 1965) on-board using a Turner 10-AU fluorometer (Turner Designs, Inc.) calibrated with pure Chl *a* (Sigma). POC samples were collected by filtering water samples onto pre-combusted ( $450^\circ\text{C}$  for 4 hrs) 25 mm Whatman GF/F filters. Filter blanks were produced by passing  $\sim 50 \text{ mL}$  of  $0.2 \mu\text{m}$  filtered seawater through a GF/F. All filters were then immediately dried at  $60^\circ\text{C}$  and stored dry until analysis. Prior to analysis, samples and blanks were fumed with concentrated HCl, dried at  $60^\circ\text{C}$ , and packed into tin capsules (Costech Analytical Technologies, Inc.) for elemental analysis on an Elementar Vario EL Cube (Elementar Analysensysteme GmbH, Hanau, Germany) interfaced to a PDZ Europa 20–20 isotope ratio mass spectrometer (Sercon Ltd., Cheshire, UK). Standards included peach leaves and glutamic acid.

At select stations, we also determined the maximum efficiency of photosystem II (Fv:Fm) from discrete water column samples by fast repetition rate fluorometry (FRRf) (Kolber *et al.*, 1998), with excitation at 470 nm. These samples were collected, dark acclimated for  $\sim 30 \text{ min}$  at *in situ* temperatures, and measured on the FRRf within one hour of collection. Blanks for individual samples analyzed by FRRf were prepared by gentle filtration through a  $0.2 \mu\text{m}$  polycarbonate syringe filter before measurement using identical protocols. All Fv:Fm values

were corrected for blank effects (*Cullen and Davis, 2003*).

### 2.2.3 Classification of winter water (WW)

Consistent with several companion studies (*Pickart et al., 2016; Brown et al., 2015a; Mills et al., 2015*), WW is defined here as the water with potential temperature ( $\theta$ ) below  $-1.6^\circ\text{C}$ . This distinguishes the most recently ventilated, and therefore most pure, WW from the modified (via solar heating and/or mixing with summer water masses) 'remnant' WW ( $-1.6^\circ\text{C} < \theta < -1^\circ\text{C}$ ) also found on the Chukchi shelf in the summer (*Gong and Pickart, 2015*). We note that related studies (e.g. *Brown et al., 2015a; Mills et al., 2015; Strong et al., 2016*) exclude waters with relatively low  $\text{NO}_3^-$  ( $< 10 \mu\text{mol L}^{-1}$ ) from the definition of WW to avoid misidentifying cold, near-surface sea ice melt water. However, in the seven transects of this study, all near-surface ( $< 10 \text{ m}$ ) water samples colder than  $-1.6^\circ\text{C}$  were characterized by salinities greater than 31.5 and were part of a continuous water mass that extended from depth to the surface. For this reason, we include all samples meeting the temperature requirement ( $\theta \leq -1.6^\circ\text{C}$ ) in our definition of WW, regardless of nutrient content.

### 2.2.4 Hydrographic analysis

Vertical sections of water column variables were constructed using either the DIVA gridding package in Ocean Data View 4 (*Schlitzer, 2014*) or a Laplacian-spline interpolator (see *Pickart et al., 2013*). We consider sections of  $\theta$ , salinity, absolute geostrophic velocity,  $\text{NO}_3^-$ , DIC, Chl *a*, POC, and  $\text{O}_2$  saturation (calculated in Ocean Data View 4), focusing on the upper 60 m of the water column. The absolute geostrophic velocity was calculated by referencing the gridded thermal wind shear to the gridded cross-transect ADCP velocity for each grid pair across the section. To illustrate stratification and mixing processes and the location of WW in relation to our biogeochemical measurements, the hydrographic sections are overlain by contours of potential density ( $\sigma_\theta$ ;  $\text{kg m}^{-3}$ , thin lines) and the delimiting WW isotherm ( $\theta = -1.6^\circ\text{C}$ , thick line). For stations with bottom depths shallower than 60 m, the seafloor is indicated by a dark gray color on the hydrographic section plots and the vertical region between the deepest sample and the seafloor is illustrated in light grey. The statistical significance of differences between WW and non-WW samples for each transect were assessed through a series of T-tests following log transformation of the data.

### 2.2.5 Open water duration

Annual cycles of sea ice concentration for 2010 and 2011 were obtained at each station from daily AMSR-E (Advanced Microwave Scanning Radiometer-Earth Observing System) satellite images at 12.5 km resolution, accessed from the National Snow and Ice Data Center (NSIDC). The sea ice concentrations at each station were then used to calculate open water duration, defined as the number of days that the station location had  $< 50\%$  ice concentration between the date of initial ice retreat and the sampling date. In cases where ice retreated and re-advanced over a particular location before the final retreat (due to wind shifts, for example), we did not include those periods with  $> 50\%$  concentration. Calculated in this way, open water duration is a proxy for the amount of time that phytoplankton at a given station were exposed to the full incident sunlight of the open water environment, as opposed to the lower light conditions present underneath sea ice. For a detailed justification of the 50% ice concentration threshold used to distinguish open water from ice cover in this region, see *Lowry et al.* (2014). Plots of open water duration are presented along with the hydrographic sections to provide environmental context for each transect.

## 2.3 Results

### 2.3.1 Presence and flow of WW

For the seven transects considered in this study, WW was found at 78% (82 of 105) of the stations, demonstrating the prevalence of this water mass laterally throughout our study region. However, WW was observed at only 35% (1678 of 4833) of the one-meter CTD bins in the upper 60 m, a consequence of the non-uniform vertical distribution of WW. WW was frequently observed at depth but was found much less commonly near the surface during our summer sampling period. The salinity range of the WW was relatively wide (31.23–33.38) and overlapped with the salinity range of nearby warmer water.

The flow pathways of WW across the Chukchi shelf observed during the ICESCAPE program were identified and mapped by *Pickart et al.* (2016). The main pathways are included in Fig. 2.1. Much of the WW on the northeast shelf drains through Barrow Canyon (e.g. *Pickart et al.*, 2005; *Weingartner et al.*, 2005). However, as described by *Pickart et al.* (2016), the precise flow paths leading to the canyon are more complex than previously

thought. As seen in Fig. 2.1, a branch of WW enters our study area from the west, presumably emanating from the western-most branch (*Pickart et al.*, 2010), and joins the Central Channel WW pathway. As this combined flow encounters Hanna Shoal it bifurcates, with a portion circulating cyclonically around the shoal and the rest being diverted southward. The southward limb is then believed to turn eastward to join the coastal branch of WW before flowing into Barrow Canyon en route to the Arctic Basin.

### 2.3.2 Vertical sections

Next, we relate the location and nature of the flow of WW through each transect to the various physical and biogeochemical properties, using vertical sections of salinity, nutrients, DIC, phytoplankton biomass, and O<sub>2</sub> saturation, as well as plots of satellite-derived open water duration. We begin our description with the southernmost transect and then follow the pathway of WW around the northern side of Hanna Shoal (Fig. 2.1).

#### Central Channel

The southernmost transect extended west to east across Central Channel to the vicinity of the Alaskan coast (from left to right; Figs. 2.1, 2.2A, and 2.3). Potential temperature along the Central Channel transect (Fig. 2.3A) revealed that WW was present at three distinct locations (the thick black contour in the vertical sections marks the  $-1.6^{\circ}\text{C}$  isotherm, which is the upper limit of WW). The absolute geostrophic velocity (Fig. 2.2A) indicated that the largest volume of WW (located to the west) was flowing to the north within the Central Channel pathway (Fig. 2.1) at speeds as large as  $15 - 20 \text{ cm s}^{-1}$ . A smaller volume of WW was progressing southward at a relatively slow speed ( $\leq 5 \text{ cm s}^{-1}$ ), likely due to a small recirculation from the main pathway (Figs. 2.1 and 2.2A; see also *Pickart et al.*, 2016). The smallest pathway of WW (located to the east) was also flowing northward, advected by the Alaskan Coastal Current at speeds ranging from 15 to  $20 \text{ cm s}^{-1}$ .

The temperature of WW generally decreased with depth. The salinity range of WW in the Central Channel transect was 32.40–33.25 (Fig. 2.3B). The highest salinity WW was located in the Central Channel pathway, while fresher WW was advected by the Alaskan Coastal Current. Note that a small amount of high salinity water ( $\sim 33.30$ ) was also found in warmer ( $\sim 0^{\circ}\text{C}$ ) bottom waters near the coast of Alaska (St. 55; Fig. 2.3B), indicating that WW was not always the highest salinity water mass on the Chukchi shelf. The mean potential density of the WW ( $\sigma_{\theta} = 26.46 \pm 0.13 \text{ kg m}^{-3}$ ) was significantly higher ( $p < 0.001$ )

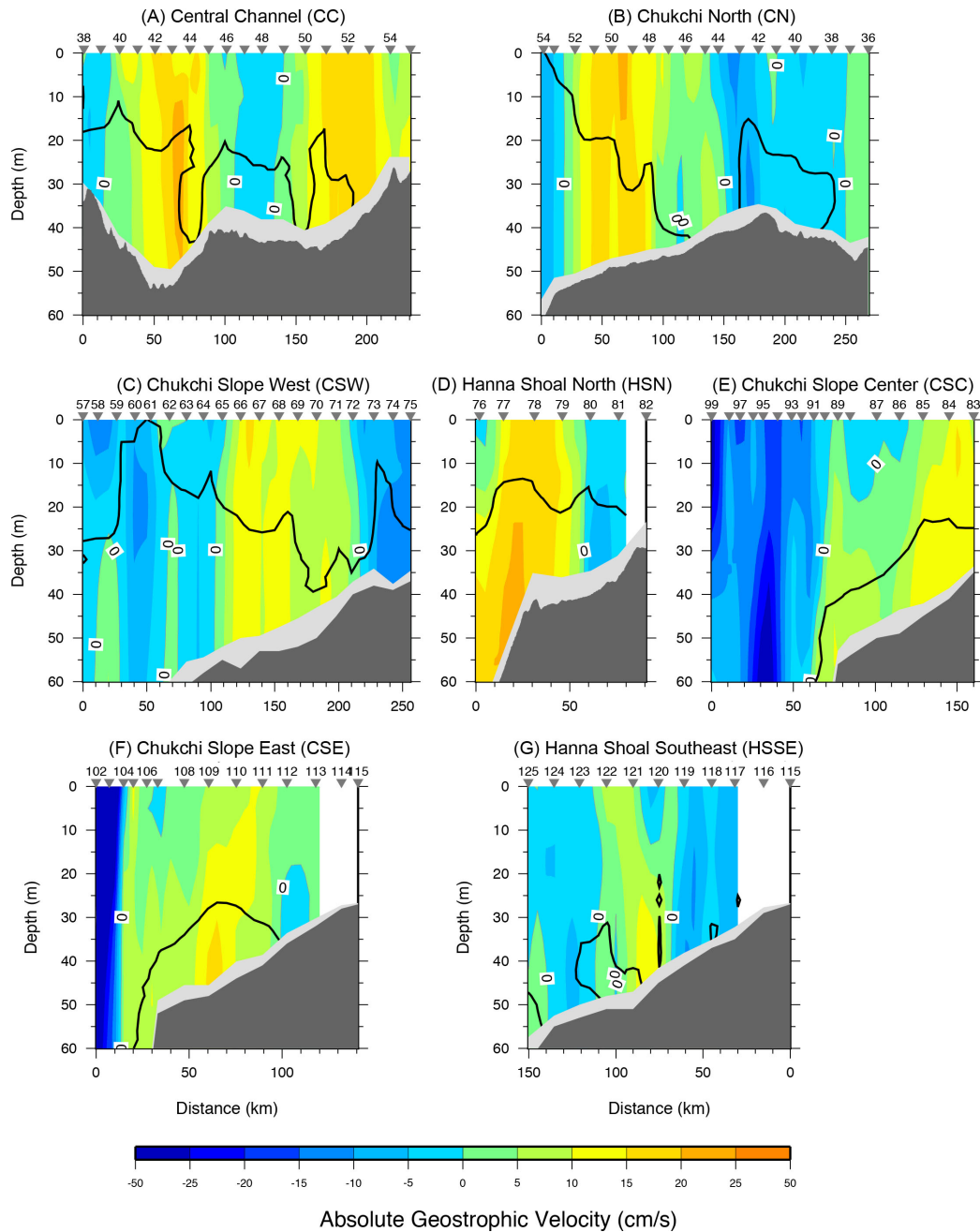


Figure 2.2: Vertical sections of absolute geostrophic velocity illustrating the speed and direction of currents through transects (A) Central Channel, (B) Chukchi North, (C) Chukchi Slope West, (D) Hanna Shoal North, (E) Chukchi Slope Center, (F) Chukchi Slope East, and (G) Hanna Shoal Southeast. Positive values indicate flow into the page, while negative values indicate flow out of the page. Locations where absolute geostrophic velocity equals zero are labeled and sections are overlain by the WW isotherm ( $\theta = -1.6^\circ\text{C}$ ; black line).

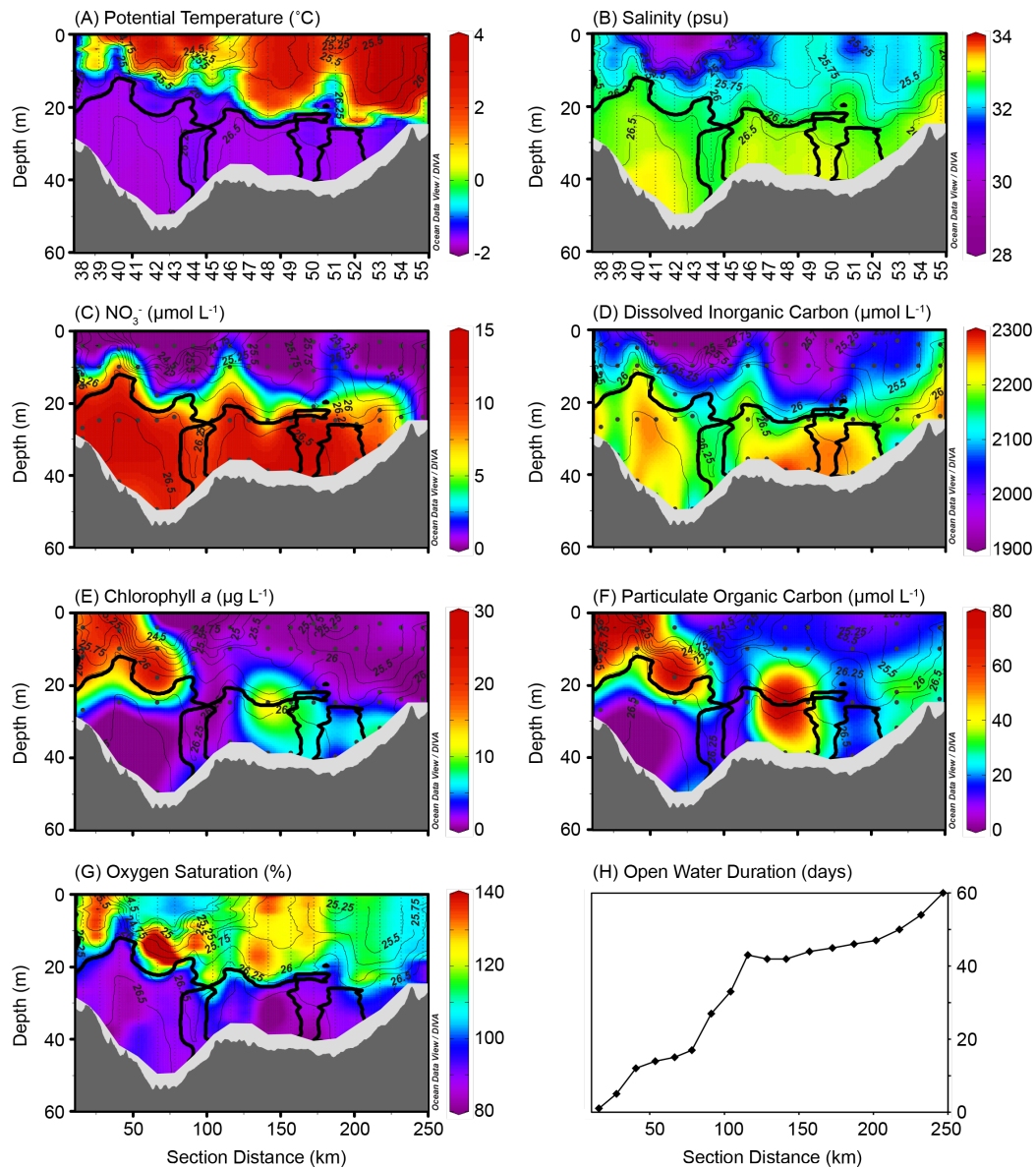


Figure 2.3: The Central Channel transect was sampled on 29 June–1 July 2010 and is displayed here from northwest (left) to southeast (right). (A–G) Hydrographic sections of (A)  $\theta$ , (B) salinity, (C)  $\text{NO}_3^-$ , (D) DIC, (E) Chl *a*, (F) POC, and (G)  $\text{O}_2$  saturation, overlain by  $\sigma_\theta$  ( $\text{kg m}^{-3}$ ; thin black lines with labels) and the WW isotherm ( $\theta = -1.6^{\circ}\text{C}$ ; thick black line). Station numbers are below (A) and (B) and black dots represent sampling depths. (H) Satellite-based open water duration, indicating the number of days each station was in open water from the time of ice retreat until the date of sampling. Note that this transect is referred to as the Central Slope transect in *Gong and Pickart (2015)*.

than that of the non-WW ( $\sigma_\theta = 25.70 \pm 0.63 \text{ kg m}^{-3}$ ), a pattern that was generally true of all seven transects (Table 2.1).

WW was rich in dissolved nutrients, with all three pathways containing higher concentrations of  $\text{NO}_3^-$  (Fig. 2.3C), silicate (not shown), and phosphate (not shown) than the adjacent warmer water. Nutrients were highest at the westernmost stations within the Central Channel WW pathway (Figs. 2.1 and 2.3C), with a maximum  $\text{NO}_3^-$  concentration of  $14.7 \mu\text{mol L}^{-1}$ , and lowest at the easternmost stations within the Alaskan Coastal Current, with a maximum  $\text{NO}_3^-$  concentration of  $11.9 \mu\text{mol L}^{-1}$ . The mean WW  $\text{NO}_3^-$  concentration for all of the stations along the transect ( $12.0 \pm 1.71 \mu\text{mol L}^{-1}$ ) was nearly 6.5-fold higher ( $p < 0.001$ ) than that of the non-WW ( $1.85 \pm 3.15 \mu\text{mol L}^{-1}$ ; Table 2.1). Notably, the Central Channel transect had the highest non-WW mean  $\text{NO}_3^-$  concentration of all seven transects (Table 2.1;  $p < 0.01$ ), due to the substantial presence of remnant WW ( $-1.6^\circ\text{C} < \theta < -1^\circ\text{C}$ ) that was elevated in  $\text{NO}_3^-$  (Fig. 2.3A and 2.3C). Concentrations of DIC (Fig. 2.3D) were also elevated along the WW pathways. On average, WW DIC concentrations in this transect were  $155 \mu\text{mol L}^{-1}$  higher than that of non-WW, with a mean value of  $2203 \pm 52 \mu\text{mol L}^{-1}$  for WW and  $2048 \pm 101 \mu\text{mol L}^{-1}$  for non-WW (Table 2.1;  $p < 0.001$ ). The vertical sections of both  $\text{NO}_3^-$  and DIC show evidence of substantial biological uptake in the upper 20 m of the water column.

There were three distinct areas of elevated phytoplankton biomass in the Central Channel transect (Fig. 2.3E and 2.3F), each in close proximity to a respective WW pathway. The large phytoplankton bloom associated with the northward flowing Central Channel WW pathway (St. 38–43) had the highest biomass, with Chl *a* (Fig. 2.3E) and POC (Fig. 2.3F) concentrations of  $16\text{--}30 \mu\text{g L}^{-1}$  and  $70\text{--}100 \mu\text{mol L}^{-1}$ , respectively, that extended from the surface down to the interface between WW and non-WW at 13–20 m depth. Biomass was also elevated at the interface of the southward flowing WW pathway at 25 m depth ( $15.3 \mu\text{g Chl } a \text{ L}^{-1}$  at St. 48) and immediately inshore of the WW in the Alaskan Coastal Current at 32 m depth ( $8.80 \mu\text{g Chl } a \text{ L}^{-1}$  at St. 53). The lowest concentrations of phytoplankton (e.g.  $< 1 \mu\text{g Chl } a \text{ L}^{-1}$ ; Fig. 2.3E) were found in surface waters that were depleted in nutrients (e.g. upper 15–20 m; St. 44–55) and in the light-limited WW (at 25–50 m depth) shaded by the large phytoplankton bloom in St. 38–43. WW in the Central Channel transect had lower phytoplankton biomass than non-WW (Table 2.1), based on POC concentrations of  $18.7 \pm 12.4 \mu\text{mol L}^{-1}$  and  $36.3 \pm 33.1 \mu\text{mol L}^{-1}$ , respectively ( $p = 0.02$ ). Mean concentrations of Chl *a* for WW and non-WW were  $3.53 \pm 3.75 \mu\text{g L}^{-1}$  and  $5.40 \pm 8.53 \mu\text{g L}^{-1}$ , respectively,

	$\theta$ ( $^{\circ}\text{C}$ )	Salinity	$\sigma_{\theta}$ ( $\text{kg m}^{-3}$ )	$\text{NO}_3^-$ ( $\mu\text{mol L}^{-1}$ )	DIC ( $\mu\text{mol L}^{-1}$ )	Chl $a$ ( $\mu\text{g L}^{-1}$ )	POC ( $\mu\text{mol L}^{-1}$ )	$\text{O}_2$ Sat (%)	
<b>Central Channel</b>	WW	$-1.68 \pm 0.04$	$32.88 \pm 0.16$	$26.46 \pm 0.13$	$12.0 \pm 1.71$	$2203 \pm 52$	$3.53 \pm 3.75$	$18.7 \pm 12.4$	$90.7 \pm 6.8$
	Non-WW	$1.00 \pm 2.18$	$32.12 \pm 0.73$	$25.70 \pm 0.63$	$1.85 \pm 3.15$	$2048 \pm 101$	$5.40 \pm 8.53$	$36.3 \pm 33.1$	$114 \pm 14.4$
<b>Chukchi North</b>	WW	$-1.72 \pm 0.05$	$32.88 \pm 0.29$	$26.46 \pm 0.24$	$12.1 \pm 6.27$	$2225 \pm 65$	$7.98 \pm 9.56$	$23.4 \pm 17.0$	$95.3 \pm 10.9$
	Non-WW	$0.61 \pm 1.54$	$32.23 \pm 0.57$	$25.83 \pm 0.49$	$1.73 \pm 3.76$	$2049 \pm 96$	$2.35 \pm 3.50$	$19.3 \pm 14.2$	$112 \pm 11.7$
<b>Chukchi Slope West</b>	WW	$-1.71 \pm 0.05$	$32.59 \pm 0.42$	$26.23 \pm 0.34$	$12.7 \pm 6.21$	$2216 \pm 77$	$9.18 \pm 8.17$	$19.7 \pm 15.6$	$97.9 \pm 17.0$
	Non-WW	$-0.14 \pm 1.48$	$31.47 \pm 0.88$	$25.25 \pm 0.69$	$1.02 \pm 2.57$	$2003 \pm 76$	$5.33 \pm 7.75$	$31.8 \pm 25.6$	$117 \pm 11.6$
<b>Hanna Shoal North</b>	WW	$-1.72 \pm 0.04$	$32.82 \pm 0.26$	$26.41 \pm 0.21$	$12.4 \pm 5.56$	$2236 \pm 48$	$10.4 \pm 6.02$	$31.7 \pm 12.6$	$93.8 \pm 11.5$
	Non-WW	$-0.43 \pm 1.21$	$31.25 \pm 0.99$	$25.09 \pm 0.80$	$0.09 \pm 0.19$	$1983 \pm 77$	$1.66 \pm 1.36$	$16.3 \pm 6.2$	$119 \pm 8.9$
<b>Chukchi Slope Center</b>	WW	$-1.70 \pm 0.03$	$32.39 \pm 0.21$	$26.07 \pm 0.17$	$13.7 \pm 3.61$	$2252 \pm 16$	$14.2 \pm 19.8$	$44.9 \pm 55.1$	$88.2 \pm 12.6$
	Non-WW	$-1.11 \pm 0.70$	$29.77 \pm 1.47$	$23.93 \pm 1.19$	$0.51 \pm 1.50$	$1996 \pm 81$	$0.61 \pm 1.58$	$5.7 \pm 7.3$	$107 \pm 7.0$
<b>Chukchi Slope East</b>	WW	$-1.70 \pm 0.04$	$32.41 \pm 0.21$	$26.08 \pm 0.17$	$12.5 \pm 3.52$	$2236 \pm 36$	$10.8 \pm 9.51$	$39.4 \pm 29.8$	$89.7 \pm 13.5$
	Non-WW	$-0.82 \pm 0.79$	$30.38 \pm 1.58$	$24.41 \pm 1.3$	$0.90 \pm 2.39$	$1983 \pm 159$	$3.35 \pm 6.55$	$10.3 \pm 8.3$	$108 \pm 8.6$
<b>Hanna Shoal Southeast</b>	WW	$-1.64 \pm 0.03$	$32.39 \pm 0.19$	$25.98 \pm 0.15$	$9.78 \pm 4.45$	$2230 \pm 45$	$4.60 \pm 4.04$	$17.6 \pm 22.9$	$85.6 \pm 8.2$
	Non-WW	$0.23 \pm 1.63$	$31.16 \pm 0.79$	$24.99 \pm 0.68$	$1.22 \pm 2.74$	$2056 \pm 90$	$3.35 \pm 6.55$	$14.1 \pm 10.8$	$105 \pm 7.9$
<b>All Transects</b>	WW	$-1.71 \pm 0.05$	$32.68 \pm 0.37$	$26.30 \pm 0.30$	$12.3 \pm 5.13$	$2222 \pm 63$	$8.64 \pm 9.75$	$25.0 \pm 22.5$	$94.1 \pm 13.8$
	Non-WW	$-0.21 \pm 1.55$	$31.00 \pm 1.49$	$24.87 \pm 1.19$	$1.13 \pm 2.71$	$2019 \pm 107$	$2.79 \pm 5.58$	$19.2 \pm 21.4$	$110 \pm 11.0$

Table 2.1: Mean and standard deviation of  $\theta$ , salinity,  $\sigma_{\theta}$ ,  $\text{NO}_3^-$ , DIC, Chl  $a$ , POC, and  $\text{O}_2$  saturation for all WW ( $\theta \leq -1.6^{\circ}\text{C}$ ) and non-WW ( $\theta > -1.6^{\circ}\text{C}$ ) samples in the upper 60 m of each transect. Bold WW values indicate statistically significant differences from the respective non-WW values ( $p < 0.05$ ).

although these values did not represent a statistically significant difference. We note that the large phytoplankton bloom above the WW in the Central Channel pathway (St. 38–43) greatly influenced the non-WW means of this transect.

The O<sub>2</sub> saturation (Fig. 2.3G) was highest (140–175%) within the large phytoplankton bloom (St. 38–45). Despite the low biomass in the surface waters east of this bloom (St. 44–55), the upper water column was supersaturated (> 100%) with O<sub>2</sub>, indicative of recent photosynthesis throughout the transect. The observations of low POC and Chl *a* in the upper water column paired with high O<sub>2</sub> saturation indicate that photosynthesis was likely followed by the sinking of phytoplankton cells to deeper in the water column, resulting in the higher biomass within WW at these stations. Across the Central Channel transect, the mean O<sub>2</sub> saturation was higher in non-WW ( $114 \pm 14.4\%$ ) than in WW ( $90.7 \pm 6.8\%$ ) ( $p < 0.001$ ), revealing a pattern of supersaturation in the non-WW and undersaturation in WW. This pattern was consistent for all of the transects in this study (Table 2.1).

The satellite-derived open water duration (defined earlier in section 2.2.5) reveals that there was large variation in the timing of ice retreat, with open water duration increasing markedly from west to east across the Central Channel transect (Fig. 2.3H). Waters where the large upper water column phytoplankton bloom was located (St. 38–43) were recently ice-covered (e.g. only one day of open water at St. 38 where Chl *a* concentrations were 16–25  $\mu\text{g L}^{-1}$ ); by contrast, waters with deeper and lower biomass (St. 44–55) had been open for much longer (e.g. 42 days at St. 48 and 50 days at St. 53).

### Chukchi North

Located north of the Central Channel transect, the Chukchi North transect extended northwest to southeast across the Chukchi shelf (from left to right; Figs. 2.1, 2.2B, and 2.4) and was characterized by WW in two distinct locations (Fig. 2.4A). The larger of the two WW pathways was flowing poleward at speeds ranging from 10–20  $\text{cm s}^{-1}$ . This is the northward extension of the Central Channel pathway with a contribution from the western-most pathway that has been diverted eastward from Herald Canyon, due to the topography of the shelf (Pickart *et al.*, 2010, 2016; Fig. 2.1). The smaller WW pathway was progressing southward from the northern Chukchi shelf at a slower speed ( $\leq 5 \text{ cm s}^{-1}$ ) (Figs. 2.1, 2.2B, and 2.4A).

The salinity range of WW in this transect (31.63–33.25) was greater than that of the Central Channel transect, due primarily to the lower salinity WW near the surface in the

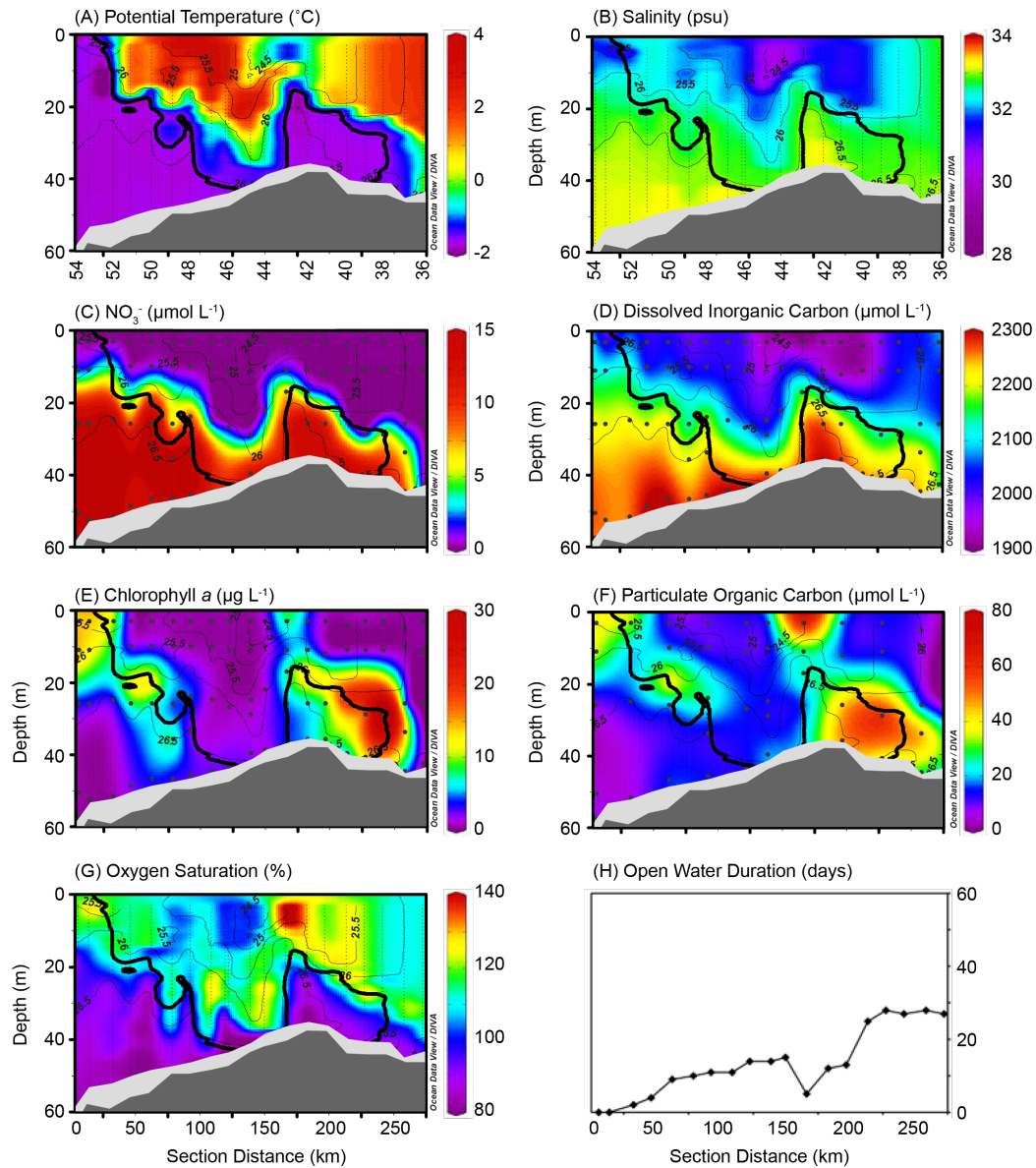


Figure 2.4: The Chukchi North transect was sampled on 3–5 July 2011 and is displayed here from northwest (left) to southeast (right). (A–G) Hydrographic sections of (A)  $\theta$ , (B) salinity, (C)  $\text{NO}_3^-$ , (D) DIC, (E) Chl *a*, (F) POC, and (G)  $\text{O}_2$  saturation, overlain by  $\sigma_\theta$  ( $\text{kg m}^{-3}$ ; thin black lines with labels) and the WW isotherm ( $\theta = -1.6^{\circ}\text{C}$ ; thick black line). Station numbers are below (A) and (B) and black dots represent sampling depths. (H) Satellite-based open water duration, indicating the number of days each station was in open water from the time of ice retreat until the date of sampling. Note that because this transect was sampled in a different year than the Central Channel transect (Fig. 2.3), there are overlapping station numbers between the two transects that refer to different locations.

northwestern stations (54–53) where WW was present throughout the entire water column (Fig. 2.4B). The Chukchi North WW was colder than that of the previous transect ( $p < 0.001$ ), with a mean  $\theta$  of  $-1.72 \pm 0.05^\circ\text{C}$  (Table 2.1).

Concentrations of  $\text{NO}_3^-$  (Fig. 2.4C), silicate (not shown), phosphate (not shown), and DIC (Fig. 2.4D) were related to the distribution of WW, with the depth of the nutricline and the largest DIC gradient mirroring the vertical extent of WW in each of the two pathways.  $\text{NO}_3^-$  concentrations in this transect were seven-fold higher in WW than in non-WW ( $p < 0.001$ ), with mean values of  $12.1 \pm 6.27 \mu\text{mol L}^{-1}$  and  $1.73 \pm 3.76 \mu\text{mol L}^{-1}$ , respectively (Table 2.1). The northwestern stations where WW extended to the surface (St. 54–53) displayed the greatest variation in WW nutrients and DIC, with concentrations ranging from  $\sim 0 \mu\text{mol NO}_3^- \text{ L}^{-1}$  and  $2010 \mu\text{mol DIC L}^{-1}$  at the surface to  $19.7 \mu\text{mol NO}_3^- \text{ L}^{-1}$  and  $2270 \mu\text{mol DIC L}^{-1}$  at depth.

Concentrations of Chl *a* (Fig. 2.4E) and POC (Fig. 2.4F) showed two distinct phytoplankton blooms associated with the two WW pathways, with bloom depth related to the vertical extent of WW. For example, at stations where WW was present near the surface (St. 54–53; 43–42), the Chl *a* and POC maxima were near the surface. As the WW isotherm deepened towards the seafloor (e.g. St. 49–48; 40–38), the depth of maximum biomass also deepened. Note that the apparent discrepancy between Chl *a* and POC data at St. 49 (at  $\sim 35$  m depth) in Fig. 2.4 is an artifact of the absence of POC data at that station. Unlike the Central Channel transect where the highest biomass was located primarily above the WW, blooms along the Chukchi North transect had high biomass ( $10\text{--}50 \mu\text{g Chl } a \text{ L}^{-1}$ ) both at the interface with and within the WW, resulting in a mean Chl *a* concentration that was 3.4 times higher ( $p < 0.001$ ) in WW than in non-WW ( $7.98 \pm 9.56 \mu\text{g L}^{-1}$  and  $2.35 \pm 3.50 \mu\text{g L}^{-1}$ , respectively; Table 2.1). Phytoplankton abundances were low ( $< 1 \mu\text{g Chl } a \text{ L}^{-1}$  and  $< 15 \mu\text{mol POC L}^{-1}$ ) throughout the water column where WW was not present (St. 47–44), in  $\text{NO}_3^-$ -depleted non-WW above the subsurface blooms, and in the light-limited WW beneath the near-surface bloom in the northwest (St. 54–52).

Similar to the previous transect, the upper water column was supersaturated in  $\text{O}_2$ , with higher  $\text{O}_2$  saturation (maximum: 144%) between the surface and the WW isotherm (Fig. 2.4G).  $\text{O}_2$  was also supersaturated within WW near the sea surface (upper 15–20 m) at St. 54–53, in contrast to the previous transect where all WW was undersaturated in  $\text{O}_2$ . Even at stations where phytoplankton biomass was low and there was no WW,  $\text{O}_2$  was supersaturated (102–125%; St. 46–48) and nutrients were depleted except near the seafloor,

signaling previous photosynthesis throughout the upper water column of all stations along the Chukchi North transect. Despite the high biomass contained within WW,  $O_2$  saturation was lower in WW than in non-WW ( $p < 0.001$ ), with mean values of  $95.3 \pm 10.9\%$  and  $112 \pm 11.7\%$ , respectively (Table 2.1).

Ice retreat across the Chukchi North transect (Fig. 2.4H) was characterized by two regions where open water duration increased from west to east: stations 54–44 (0–15 days) and stations 43–36 (5–31 days). Interestingly, both of these increases were correlated with the vertical extent of water column biogeochemical properties (Fig. 2.4A–G). In particular, the depth of maximum phytoplankton biomass, the WW isotherm, and the nitracline were shallowest at stations that were either still ice-covered or recently ice-free, and deepest at stations with longer open water duration. We note that the northwestern bloom (St. 54–48) comprised a portion of the massive under-ice phytoplankton bloom that extended 100 km farther into the fully consolidated ice pack, as described by *Arrigo et al.* (2012, 2014). The fact that the southeastern bloom (St. 43–36) displayed a similar relationship between biogeochemical properties and open water duration suggests that this bloom likely also initiated underneath the ice (see Section 2.4.3 below).

### Chukchi Slope West

The longest and most northern transect extended northwest to southeast from the upper continental slope ( $\sim 150$  m depth) across the Chukchi shelfbreak to the shallow water ( $\sim 40$  m) northwest of Hanna Shoal (from left to right; Figs. 2.1, 2.2C and 2.5). WW was flowing weakly to the west ( $< 10 \text{ cm s}^{-1}$ ; Fig. 2.2C) at the northern end of the transect due to wind-driven upwelling that reversed the (normally eastward-flowing) shelfbreak jet (*Spall et al.*, 2014). At the time of occupation of the section, the eastward flow of the jet was starting to become re-established at deeper levels in the water column. On the shelf, the circulation of WW was the same as observed on the Chukchi North section; i.e., northeastward flowing WW adjacent to equatorward-flowing WW closer to Hanna Shoal (compare Figs. 2.2B and 2.2C shoreward of the shelfbreak). Although restricted to the bottom 10 m at St. 70–72, WW was present at all stations along this  $\sim 300$  km long transect (Fig. 2.5A).

The Chukchi Slope West transect exhibited the widest range in WW salinity,  $\text{NO}_3^-$ , and DIC (Fig. 2.5B–D). Similar to previous transects, WW  $\text{NO}_3^-$  concentrations were high (mean:  $12.7 \pm 6.21 \text{ } \mu\text{mol L}^{-1}$ ; Table 2.1) and the nitracline and the DIC gradient approximately mirrored the WW isotherm (Fig. 2.5C and 2.5D). The highest maximum  $\text{NO}_3^-$

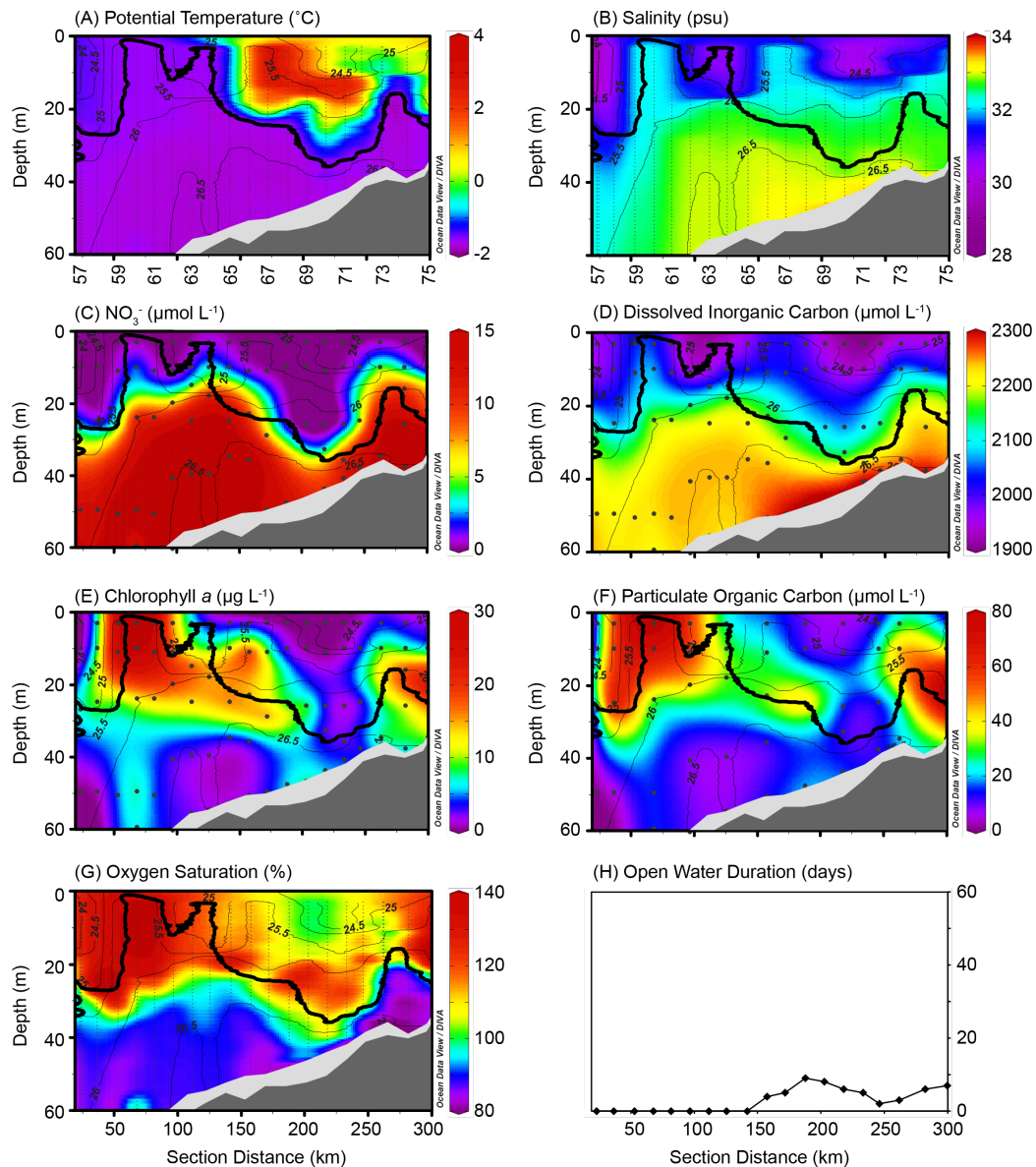


Figure 2.5: The Chukchi Slope West transect was sampled on 7–9 July 2011 and is displayed here from northwest (left) to southeast (right). (A–G) Hydrographic sections of (A)  $\theta$ , (B) salinity, (C)  $\text{NO}_3^-$ , (D) DIC, (E) Chl *a*, (F) POC, and (G)  $\text{O}_2$  saturation, overlain by  $\sigma_{\theta}$  ( $\text{kg m}^{-3}$ ; thin black lines with labels) and the WW isotherm ( $\theta = -1.6^{\circ}\text{C}$ ; thick black line). Station numbers are below (A) and (B) and black dots represent sampling depths. (H) Satellite-based open water duration, indicating the number of days each station was in open water from the time of ice retreat until the date of sampling.

concentrations on the shelf (upper 60 m) were measured in this transect, with a maximum value of  $20.2 \mu\text{mol L}^{-1}$  in WW at St. 66. Surface waters were depleted in  $\text{NO}_3^-$  ( $\sim 0 \mu\text{mol L}^{-1}$ ), even where WW extended to the surface (St. 60–61).

A massive phytoplankton bloom was evident along the Chukchi Slope West transect, with Chl *a* and POC values of  $15\text{--}30 \mu\text{g L}^{-1}$  and  $50\text{--}100 \mu\text{mol L}^{-1}$ , respectively, throughout most of the upper 30–40 m of the water column (Fig. 2.5E and 2.5F). Biomass was lowest ( $< 0.5 \mu\text{g Chl } a \text{ L}^{-1}$ ) at stations where WW was at its minimum vertical extent (St. 68–72). Despite low light conditions caused by shading from the bloom above, concentrations of Chl *a* were relatively high in WW on the shelf beneath the massive phytoplankton bloom (St. 59–68; e.g. 40–60 m), with minimum Chl *a* concentrations of  $1\text{--}2 \mu\text{g L}^{-1}$  and some as high as  $5\text{--}10 \mu\text{g L}^{-1}$ . As with the previous transect, phytoplankton biomass was concentrated near the interface between WW and non-WW (Fig. 2.5E and 2.5F).

$\text{O}_2$  saturation was very high throughout the upper water column (Fig. 2.5G) in both WW and non-WW, with values as high as 130–150% between the surface and 25–30 m in the northwestern portion of the transect. At stations where the WW isotherm was deepest,  $\text{O}_2$  saturation was highest 10–20 m above the WW (St. 70–72). Similar to previous transects,  $\text{O}_2$  was undersaturated in bottom WW. However, due to the high levels of  $\text{O}_2$  produced in WW by the massive phytoplankton bloom at St. 57–69, this transect yielded the highest mean WW  $\text{O}_2$  saturation of all seven transects ( $p < 0.05$ ), with a mean of  $97.9 \pm 17.0\%$  (Table 2.1). Similarly, the  $\text{O}_2$  saturation in non-WW was also very high, with a mean of  $117 \pm 11.6\%$ .

The northwestern half of the Chukchi Slope West transect was still ice-covered at the time of sampling (Fig. 2.5H), with zero days of open water duration at St. 57–65 where the massive under-ice phytoplankton bloom was observed (Arrigo *et al.*, 2012, 2014). Similar to the previous transect, there was a clear relationship between open water duration, the depth of the bloom, and the vertical extent of WW: both WW and the bloom reached the surface underneath the ice (St. 60–61) and extended deeper at stations with longer open water duration (e.g., St. 68–70, with 6–9 days open water duration, a WW isotherm depth of 25–39 m, and a biomass maximum of 35–45 m).

At three stations along the Chukchi Slope West transect, we also measured vertical profiles of the maximum efficiency of photosystem II (Fv:Fm) of phytoplankton (Fig. 2.6).

Fv:Fm values were highest either at or slightly below the interface between WW and non-WW, where  $\text{NO}_3^-$  concentrations were high and light availability was sufficient for photosynthesis. In contrast, Fv:Fm values were lowest in the upper water column where light levels were high but nutrients were depleted ( $\sim 0 \mu\text{mol NO}_3^- \text{ L}^{-1}$ ), and in deeper waters where  $\text{NO}_3^-$  availability was high but light was limiting. For example, at St. 62 where WW was present in the upper water column, Fv/Fm was highest (0.53) several meters below the WW isotherm, reflecting the fact that phytoplankton growth had already depleted nutrients from shallower WW prior to our sampling.

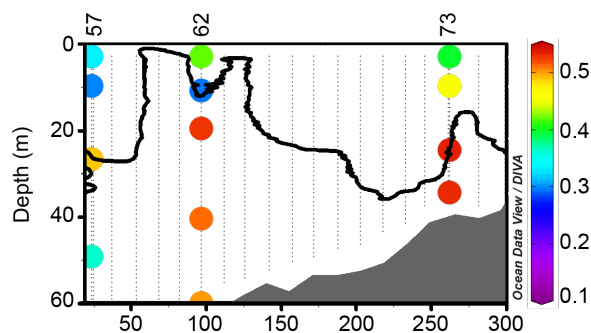


Figure 2.6: Hydrographic section of Fv:Fm for three stations in the Chukchi Slope West transect. The section is overlain by the WW isotherm ( $\theta = -1.6^\circ\text{C}$ ; thick black line), consistent with biogeochemical properties displayed in Fig. 2.5A–G. Station numbers are listed above the plot.

### Hanna Shoal North

Located east of the Chukchi Slope West transect, the Hanna Shoal North section extended northwest to southeast from just beyond the shelf edge toward Hanna Shoal (from left to right; Figs. 2.1, 2.2D, and 2.7A). WW was observed at all stations. During our sampling period, the shelfbreak jet was fully re-established and advecting WW to east fairly rapidly ( $> 20 \text{ cm s}^{-1}$ ). Because of the relatively short distance between Hanna Shoal and the shelf edge, the eastward flowing pathway of WW on the outer shelf was not a distinct feature (as it was in the previous two transects), but instead was located immediately adjacent to the shelfbreak jet (Fig. 2.2D). Inshore of this, the WW returned southward next to Hanna Shoal as it had in the Chukchi Slope West section.

Phytoplankton biomass was high throughout the WW in this transect (Fig. 2.7E), with a mean Chl *a* concentration of  $10.4 \pm 6.02 \mu\text{g L}^{-1}$  (Table 2.1). By contrast, biomass was

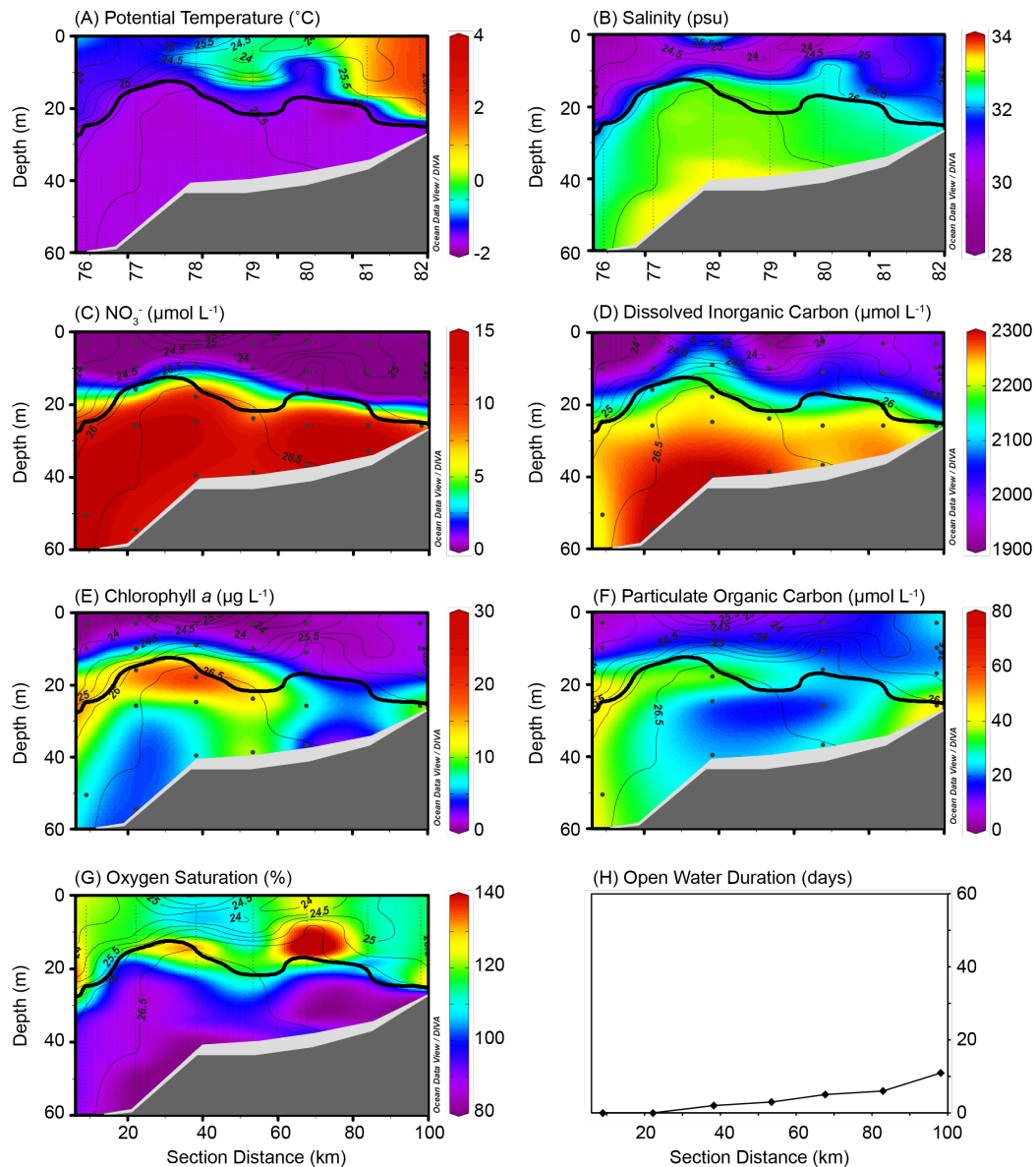


Figure 2.7: The Hanna Shoal North transect was sampled on 9–10 July 2011 and is displayed here from northwest (left) to southeast (right). (A–G) Hydrographic sections of (A)  $\theta$ , (B) salinity, (C)  $\text{NO}_3^-$ , (D) DIC, (E) Chl *a*, (F) POC, and (G)  $\text{O}_2$  saturation, overlain by  $\sigma_{\theta}$  ( $\text{kg m}^{-3}$ ; thin black lines with labels) and the WW isotherm ( $\theta = -1.6^{\circ}\text{C}$ ; thick black line). Station numbers are below (A) and (B) and black dots represent sampling depths. (H) Satellite-based open water duration, indicating the number of days each station was in open water from the time of ice retreat until the date of sampling.

relatively low in the upper 20 m of the water column, with a mean non-WW Chl *a* concentration of  $1.66 \pm 1.36 \mu\text{g L}^{-1}$  (more than 6-fold lower than that of WW;  $p < 0.001$ ). We note that the apparent discrepancy between POC and Chl *a* concentrations results from a lack of POC data at St. 77 and St. 79 (Fig. 2.7E and 2.7F). Similar to previous transects, phytoplankton biomass was concentrated at the interface between WW and non-WW, with the highest Chl *a* concentrations just below the WW isotherm (Fig. 2.7E).

O<sub>2</sub> was supersaturated throughout the upper water column, with high O<sub>2</sub> saturation extending from the surface to just below the WW isotherm (Fig. 2.7G). As with the previous transect, O<sub>2</sub> saturation generally increased with depth towards the WW, with the highest values found just above the WW isotherm. Within WW, O<sub>2</sub> saturation decreased with depth towards the seafloor. This transect exhibited the highest non-WW mean O<sub>2</sub> saturation ( $119 \pm 8.9\%$ ; Table 2.1) of the study ( $p < 0.05$ ), signaling previous photosynthesis by phytoplankton despite the low biomass in non-WW relative to WW.

Most stations along this transect were sampled relatively soon after ice retreat (Fig. 2.7H). Only the southernmost station closest to Hanna Shoal had been open for more than a week prior to sampling (11 days; St. 82). This station also had the least amount of WW. Conversely, the northernmost stations (St. 76–77) were still ice covered at the time of sampling and had the greatest amount of WW. Between these two end points, the remaining stations (St. 78–81) had been open for 2–6 days prior to sampling and had a moderate amount of WW remaining on the shelf.

### Chukchi Slope Center

Extending northeast to southwest from the base of the continental slope ( $\sim 2000$  m) to the shallow waters ( $\sim 35$  m) of Hanna Shoal, the Chukchi Slope Center transect was located east of the Hanna Shoal North transect (Fig. 2.1). WW was observed in the eastward-flowing shelfbreak jet, but not seaward of this. On the shelf, WW was once again being advected eastward in a distinct pathway, but the return flow was absent at this location since the transect was situated to the east of the bifurcation point of WW associated with Hanna Shoal (Fig. 2.1). As described by *Pickart et al.* (2016), the WW advected in the shelf pathway at the Chukchi Slope Center section was noticeably fresher than farther to the west (i.e. upstream), resulting in a lower mean WW salinity in this transect ( $32.39 \pm 0.21$ ) than in the previous transects (Table 2.1). Additionally, non-WW in this transect was the freshest and least dense of all seven transects (Table 2.1), with a mean salinity of  $29.77 \pm 1.47$  and a

mean  $\sigma_\theta$  of  $23.93 \pm 1.19 \text{ kg m}^{-3}$  due in large part to the fresh and buoyant water sampled in the upper 20 m off the shelf in the northeastern stations.

The maximum concentrations of  $\text{NO}_3^-$  and DIC were associated with WW (Fig. 2.8C and 2.8D), although slightly elevated concentrations of  $\text{NO}_3^-$  ( $\sim 1 \mu\text{mol L}^{-1}$ ) and DIC ( $\sim 2150 \mu\text{mol L}^{-1}$ ) were also found in non-WW at 40–60 m depth along the shelfbreak (St. 99–93) due to the upward tilt of the isopycnals progressing onshore. This transect contained very high concentrations of WW  $\text{NO}_3^-$  and DIC relative to the other transects, with means of  $13.7 \pm 3.61 \mu\text{mol L}^{-1}$  and  $2252 \pm 16 \mu\text{mol L}^{-1}$ , respectively (Table 2.1). The difference between mean  $\text{NO}_3^-$  in WW and non-WW ( $0.51 \pm 1.50 \mu\text{mol L}^{-1}$ ) was more than 25-fold ( $p < 0.001$ ), illustrating the extreme nutrient content of WW in relation to warmer waters on the Chukchi shelf.

Extremely high WW mean values of Chl *a* ( $14.2 \pm 19.8 \mu\text{g L}^{-1}$ ) and POC ( $44.9 \pm 55.1 \mu\text{mol L}^{-1}$ ) were observed on the Chukchi Slope Center transect (Table 2.1). These mean values were greatly influenced by an extremely large phytoplankton bloom at the interface between WW and non-WW (St. 85–83), with maximum concentrations of Chl *a* ( $77.0 \mu\text{g L}^{-1}$  at St. 83) and POC ( $155 \mu\text{mol L}^{-1}$  at St. 84) that were the highest of the study (Fig 2.8E and 2.8F). Conversely, biomass was very low in non-WW (except for 10–20 m above the WW isotherm), yielding non-WW mean values that were the lowest of the study ( $0.61 \pm 1.58 \mu\text{g Chl } a \text{ L}^{-1}$  and  $5.7 \pm 7.3 \mu\text{mol POC L}^{-1}$ ;  $p < 0.01$ ). The difference between Chl *a* concentrations in WW and non-WW was 23-fold ( $p < 0.001$ ), resembling the difference in  $\text{NO}_3^-$  concentrations described above.

Open water duration was extremely short in this transect, with the majority of stations still under ice cover at the time of sampling (zero days of open water duration at St. 99–86). The southwestern stations near Hanna Shoal (St. 85–83), where the massive phytoplankton bloom was located, were sampled in open water within 3–6 days of sea ice retreat. There were only 5–6 days of open water prior to sampling at St. 84–83, where the maximum phytoplankton biomass was the highest of this study ( $73\text{--}77 \mu\text{g Chl } a \text{ L}^{-1}$ ).

### Chukchi Slope East

Spanning the northeastern portion of the Chukchi Sea, the Chukchi Slope East transect extended northeast to southwest from the upper slope ( $\sim 350 \text{ m}$ ) to the shallow waters ( $\sim 25 \text{ m}$ ) of Hanna Shoal (from left to right; Figs. 2.1, 2.2F, and 2.9). A single region of WW was located in the center of this transect within the bottom 15–20 m of the water

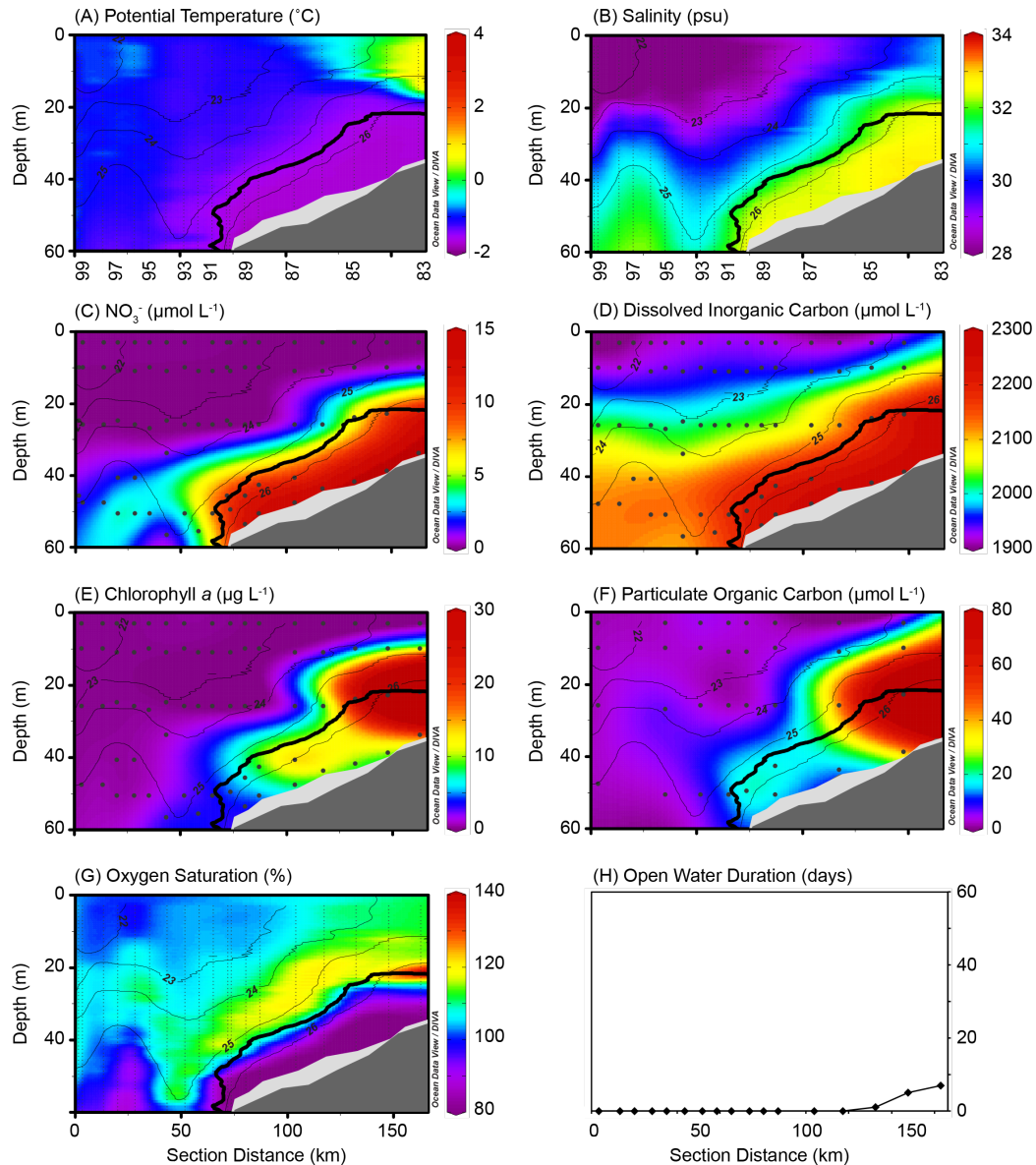


Figure 2.8: The Chukchi Slope Center transect was sampled on 10–12 July 2011 and is displayed here from northeast (left) to southwest (right). (A–G) Hydrographic sections of (A)  $\theta$ , (B) salinity, (C)  $\text{NO}_3^-$ , (D) DIC, (E) Chl *a*, (F) POC, and (G)  $\text{O}_2$  saturation, overlain by  $\sigma_{\theta}$  ( $\text{kg m}^{-3}$ ; thin black lines with labels) and the WW isotherm ( $\theta = -1.6^{\circ}\text{C}$ ; thick black line). Station numbers are below (A) and (B) and black dots represent sampling depths. (H) Satellite-based open water duration, indicating the number of days each station was in open water from the time of ice retreat until the date of sampling.

column. The seaward portion of the WW was being advected by the shelfbreak jet, while the shoreward portion was contained in the shelf pathway advecting the cold water cyclonically around Hanna Shoal (Figs. 2.1 and 2.2F). The mean  $\theta$  ( $-1.70 \pm 0.04^\circ\text{C}$ ) and salinity ( $32.41 \pm 0.21$ ) of WW in the Chukchi Slope East transect was almost identical to that of the Chukchi Slope Center transect (Table 2.1), indicating that there was little modification of the WW as it progressed between the two transects. The range of non-WW salinity (19.74–32.49) was the largest here of all seven transects, with the freshest values at the surface near the shelfbreak (St. 106–108; Fig. 2.9B), indicating recent sea ice melt.

Consistent with previous transects,  $\text{NO}_3^-$  and DIC concentrations were extremely high within WW (Table 2.1), although relatively high concentrations were also found in the northeastern stations on the shelfbreak (St. 102–105) where WW was not present (Figs. 2.9C and 2.9D). Nutrients and DIC were depleted in non-WW in the upper 20–30 m of the water column ( $\sim 0 \mu\text{mol NO}_3^- \text{ L}^{-1}$  and  $1950 \mu\text{mol DIC L}^{-1}$ ). The maximum  $\text{NO}_3^-$  concentration in this transect was  $18.5 \mu\text{mol L}^{-1}$ , the same as the maximum WW concentration along the Chukchi Slope Center transect.

There was a subsurface phytoplankton bloom associated with the nutrient-rich WW, illustrated by high concentrations of Chl *a* and POC (Fig. 2.9E and 2.9F). Biomass was most concentrated at the WW isotherm, with a maximum of  $30.6 \mu\text{g Chl } a \text{ L}^{-1}$  at St. 110 where WW was at its shallowest extent (27 m depth). Biomass was relatively low at St. 106–107, where WW was confined to the light-limited waters below 40 m, and at St. 102–105 on the shelfbreak, where WW was not present. Mean Chl *a* and POC concentrations in WW were very high ( $10.8 \pm 9.51 \mu\text{g L}^{-1}$  and  $39.4 \pm 29.8 \mu\text{mol L}^{-1}$ , respectively; Table 2.1).

Stations at or near the shelfbreak were still ice-covered during our sampling period, with zero days of open water at St. 102–107. The remaining stations (St. 108–115) had been ice-free for 4–17 days, with open water duration increasing from northeast to southwest. The station with the highest biomass ( $> 30 \mu\text{g Chl } a \text{ L}^{-1}$ ) and the largest extent of WW had been open for 12 days prior to sampling (St. 110), while stations closest to Hanna Shoal with no WW remaining on the shelf had been open for longer (15–17 days).

### Hanna Shoal Southeast

The final section sampled along the anti-cyclonic WW pathway around Hanna Shoal was the Hanna Shoal Southeast transect, which extended southwest to northeast from the vicinity of Barrow Canyon towards Hanna Shoal (from left to right; Figs. 2.1, 2.2G, and 2.10).

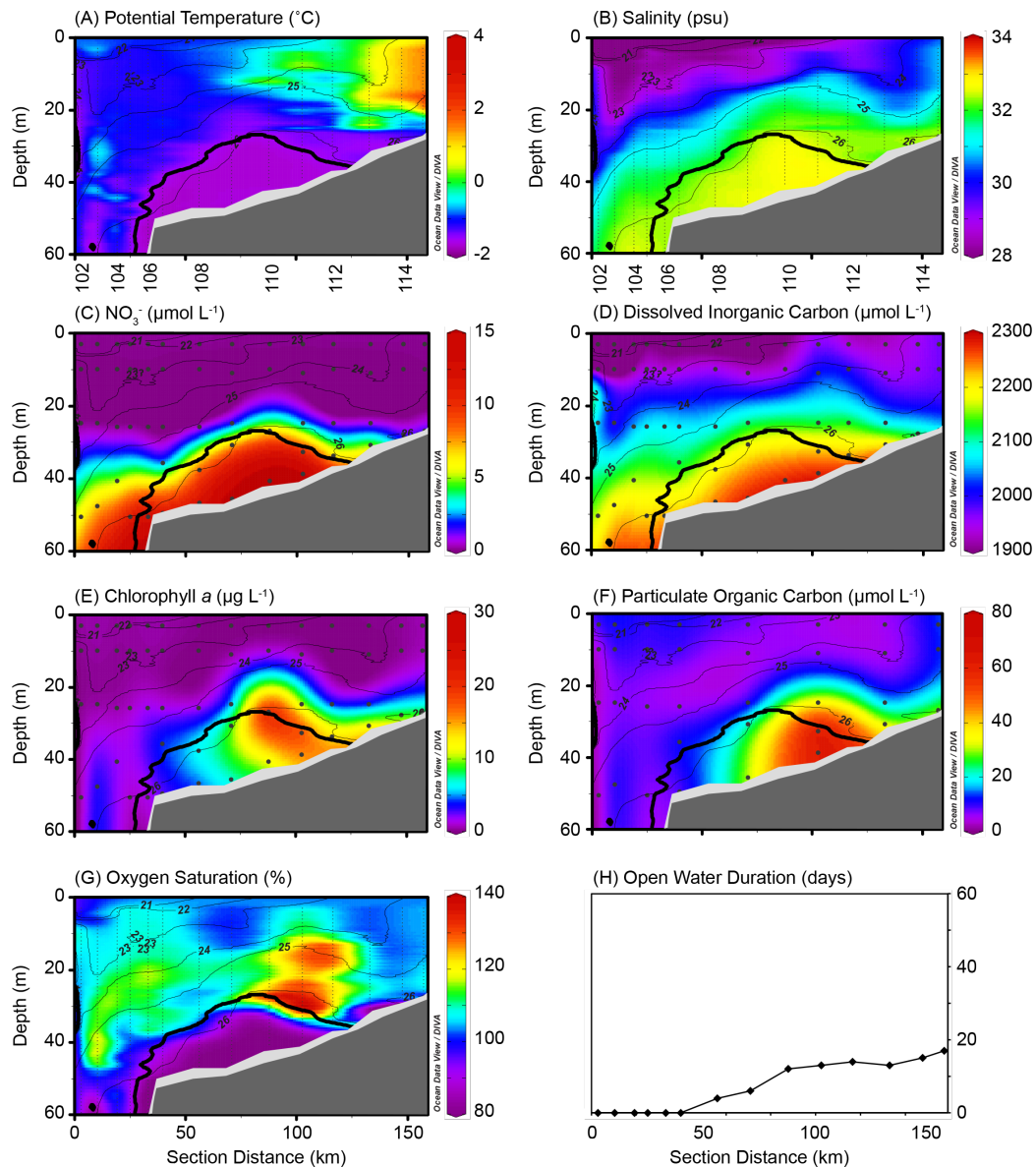


Figure 2.9: The Chukchi Slope East transect was sampled on 14–16 July 2011 and is displayed here from northeast (left) to southwest (right). (A–G) Hydrographic sections of (A)  $\theta$ , (B) salinity, (C)  $\text{NO}_3^-$ , (D) DIC, (E) Chl *a*, (F) POC, and (G)  $\text{O}_2$  saturation, overlain by  $\sigma_{\theta}$  ( $\text{kg m}^{-3}$ ; thin black lines with labels) and the WW isotherm ( $\theta = -1.6^{\circ}\text{C}$ ; thick black line). Station numbers are below (A) and (B) and black dots represent sampling depths. (H) Satellite-based open water duration, indicating the number of days each station was in open water from the time of ice retreat until the date of sampling.

Although the outer shelf advection pathway was quite evident in this transect (Fig. 2.2G), only a small amount of WW was present within the pathway at the time of our sampling. This implies that the Hanna Shoal Southeast transect was near the leading edge of the WW at this point in the summer season, such that there was no WW downstream of this transect during our sampling period (as described in more detail in *Pickart et al. (2016)*). While the mean salinity of WW was similar to that of the previous two transects (Table 2.1), the mean potential temperature ( $-1.64 \pm 0.03^\circ\text{C}$ ) was the highest of all seven transects ( $p < 0.001$ ) and the density was the lowest ( $\sigma_\theta : 25.98 \pm 0.15 \text{ kg m}^{-3}$ ) ( $p < 0.001$ ). This transect contained only a small amount of WW rich in  $\text{NO}_3^-$  (Fig. 2.10C), with a relatively low mean of  $9.78 \pm 4.45 \text{ } \mu\text{mol L}^{-1}$  (Table 2.1). Although still high, the maximum  $\text{NO}_3^-$  value ( $13.8 \text{ } \mu\text{mol L}^{-1}$ ) was also the lowest maximum of all seven transects. In contrast, although DIC concentrations followed a similar pattern to  $\text{NO}_3^-$ , the mean WW DIC concentrations were not the lowest on the shelf (Table 2.1).

Phytoplankton abundance (Fig. 2.10E and 2.10F) was elevated at stations where WW was present and within remnant WW near the seafloor. There were two locations with very high phytoplankton biomass (St. 120 at 16 m and St. 124 at 40 m; both  $\sim 30 \text{ } \mu\text{g Chl } a \text{ L}^{-1}$ ). The bloom at St. 120 was concentrated at  $\sim 18$  m depth, where a small amount of WW provided a source of  $\text{NO}_3^-$  in an otherwise nutrient-depleted section of the upper water column. The bloom at St. 124 was located at the northwestern boundary of the WW, although the highest biomass was contained in remnant WW at the time of sampling.

Consistent with the previous six transects,  $\text{O}_2$  saturation increased near the WW isotherm (Fig. 2.10G). However, the mean values of  $\text{O}_2$  saturation in both WW ( $85.6 \pm 8.2$ ) and non-WW ( $105 \pm 7.9$ ) were very low (Table 2.1), with the latter value representing the lowest non-WW mean of this study ( $p < 0.01$ ).

Every station in this transect had been ice-free for at least two weeks (Fig. 2.10H), with open water duration increasing from 17 days at St. 115 (near Hanna Shoal) to 33 days at St. 125 (closest to the Alaskan coast). The relatively long open water duration of this transect, paired with the relatively small amount of WW, depleted nutrients, and biomass mostly concentrated near the seafloor, indicated that we sampled this location after substantial primary production had already taken place. The only locations where phytoplankton continued to bloom were those that were influenced by a supply of nutrient-rich WW.

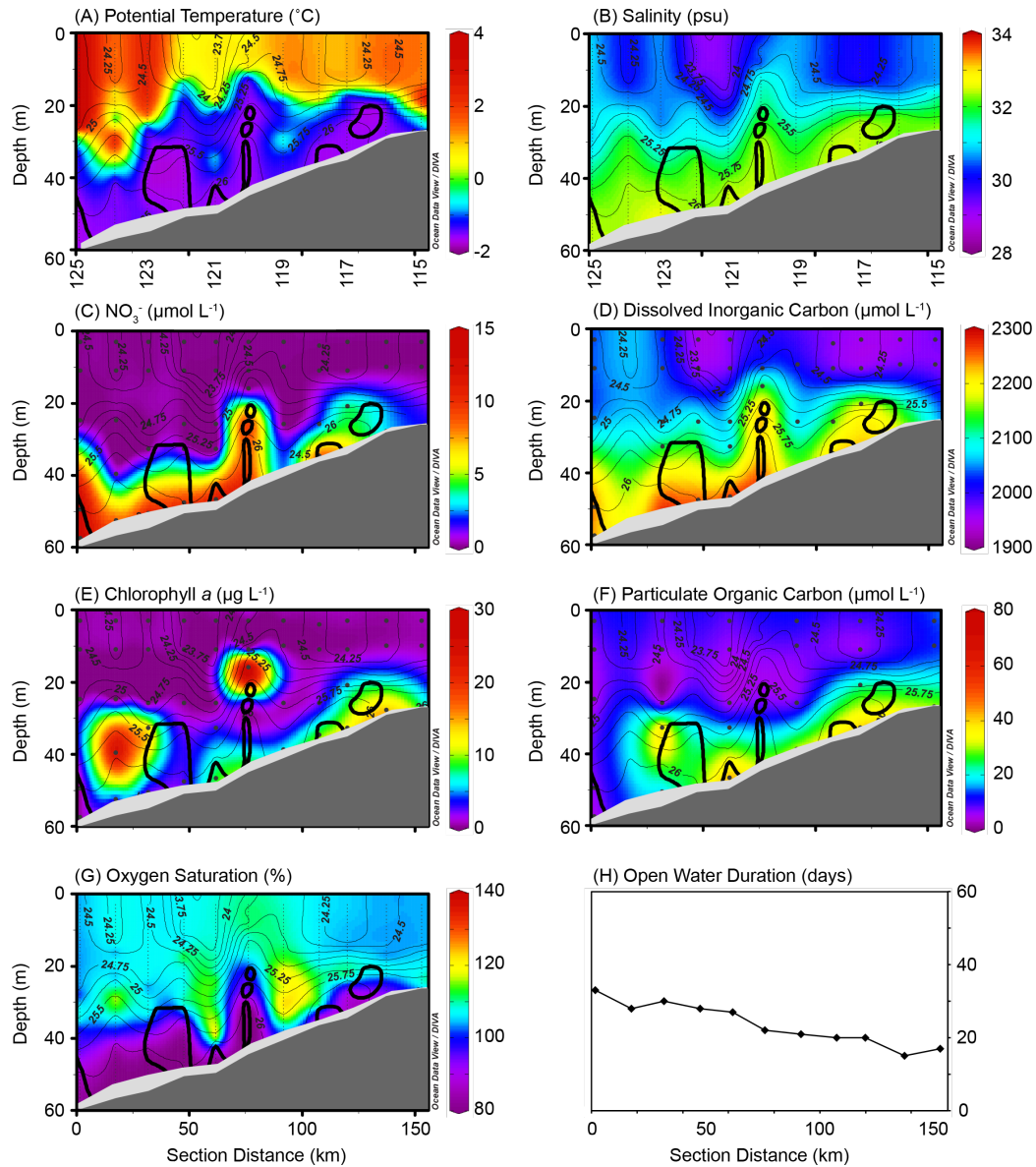


Figure 2.10: The Hanna Shoal Southeast transect was sampled on 16 July 2011 and is displayed here from southeast (left) to northwest (right). (A–G) Hydrographic sections of (A)  $\theta$ , (B) salinity, (C)  $\text{NO}_3^-$ , (D) DIC, (E) Chl *a*, (F) POC, and (G)  $\text{O}_2$  saturation, overlain by  $\sigma_\theta$  ( $\text{kg m}^{-3}$ ; thin black lines with labels) and the WW isotherm ( $\theta = -1.6^{\circ}\text{C}$ ; thick black line). Station numbers are below (A) and (B) and black dots represent sampling depths. (H) Satellite-based open water duration, indicating the number of days each station was in open water from the time of ice retreat until the date of sampling.

## 2.4 Discussion

### 2.4.1 Significance of nutrient-rich WW for phytoplankton blooms

The overarching theme that emerged in this study was that the presence of extremely cold WW ( $\theta \leq -1.6^\circ\text{C}$ ) was consistently associated with phytoplankton blooms. The relationship between phytoplankton and WW was driven not by temperature but by the extremely high nutrient content of this near-freezing water mass, particularly in the case of  $\text{NO}_3^-$ , which is the primary limiting nutrient in the Chukchi Sea (Cota *et al.*, 1996; Codispoti *et al.*, 2005; Tremblay *et al.*, 2006). Plots of  $\theta$  versus  $\text{NO}_3^-$  for all water samples in the seven transects described above (Fig. 2.11A–G) illustrate that the highest concentrations of  $\text{NO}_3^-$  were found at extremely cold temperatures. Although slightly warmer remnant WW ( $-1.6^\circ\text{C} < \theta < 0^\circ\text{C}$ ) occasionally contained relatively high nutrient concentrations, the vast majority of  $\text{NO}_3^-$  found on the Chukchi shelf was associated with WW ( $\theta \leq -1.6^\circ\text{C}$ ), with most concentrations between 5–20  $\mu\text{mol L}^{-1}$ . Summer water masses ( $\theta > 0^\circ\text{C}$ ) contained virtually no  $\text{NO}_3^-$ , with concentrations frequently near 0  $\mu\text{mol L}^{-1}$  and always  $< 3.5 \mu\text{mol L}^{-1}$ . Across all seven transects, the mean  $\text{NO}_3^-$  concentration was more than 10-fold higher in WW than in warmer water ( $p < 0.001$ ), with a mean of  $12.3 \pm 5.13 \mu\text{mol L}^{-1}$  ( $n = 147$ ) for WW and  $1.13 \pm 2.71$  ( $n = 306$ ) for non-WW (Table 2.1). This relationship was consistent between years, as demonstrated by the two transects that were sampled in both 2011 and 2010: Chukchi North (Fig. 2.11B and 2.11H, respectively) and Hanna Shoal North (Fig. 2.11D and 2.11I, respectively). Concentrations of other dissolved nutrients were also very high in WW, although the relationship between water temperature and nutrient content was most consistent in the case of  $\text{NO}_3^-$ . The mean silicate concentration in WW ( $37.3 \pm 12.6 \mu\text{mol L}^{-1}$ ) was nearly five times higher than that of non-WW ( $7.53 \pm 7.89 \mu\text{mol L}^{-1}$ ) ( $p < 0.001$ ). Similarly, the mean phosphate concentration in WW ( $1.76 \pm 0.39 \mu\text{mol L}^{-1}$ ) was 2.4-fold greater than that of non-WW ( $0.73 \pm 0.31 \mu\text{mol L}^{-1}$ ) ( $p < 0.001$ ). Thus, as WW flows across the Chukchi shelf, it provides essential nutrients for phytoplankton that sustain primary production.

Driven by the high nutrient content of WW on the shelf, more phytoplankton biomass accumulated in this water mass than in warmer, nutrient-poor water (Table 2.1). Across all seven transects, the mean Chl *a* concentration was three-fold higher in WW ( $8.64 \pm 9.75 \mu\text{g L}^{-1}$ ;  $n = 133$ ) than in non-WW ( $2.79 \pm 5.58 \mu\text{g L}^{-1}$ ;  $n = 285$ ) ( $p < 0.001$ ). Concentrations of POC were  $\sim 25\%$  higher ( $p < 0.001$ ) in WW than in non-WW, with a

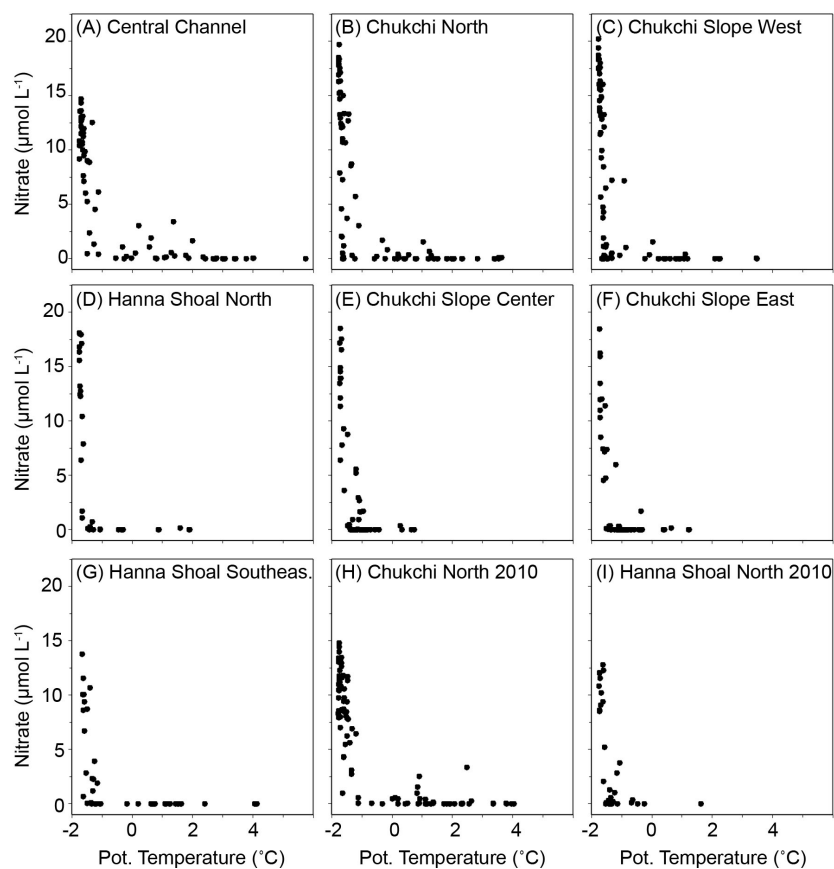


Figure 2.11: Plots of  $\theta$  versus  $\text{NO}_3^-$  for all bottle samples in the upper 60 m from each transect: (A) Central Channel (2010), (B) Chukchi North, (C) Chukchi Slope West, (D) Hanna Shoal North, (E) Chukchi Slope Center, (F) Chukchi Slope East, (G) Hanna Shoal Southeast, (H) Chukchi North (2010), and (I) Hanna Shoal North (2010).

mean of  $25.0 \pm 22.5 \mu\text{mol L}^{-1}$  ( $n = 76$ ) and  $19.2 \pm 21.4 \mu\text{mol L}^{-1}$  ( $n = 164$ ), respectively. Similarly, although data are not shown for individual transects, the mean concentration of particulate organic nitrogen (PON) was  $\sim 40\%$  higher in WW ( $4.00 \pm 4.12 \mu\text{mol L}^{-1}$ ;  $n = 75$ ) than in non-WW ( $2.67 \pm 2.71 \mu\text{mol L}^{-1}$ ;  $n = 162$ ) ( $p < 0.001$ ). Phytoplankton physiology was also enhanced in nutrient-rich WW, with the mean maximum efficiency of photosystem II (Fv:Fm)  $\sim 24\%$  greater for phytoplankton sampled in WW ( $0.494 \pm 0.066$ ;  $n = 6$ ) than for those in non-WW ( $0.389 \pm 0.080$ ;  $n = 22$ ) ( $p = 0.012$ ).

A second theme that emerged was that the vertical position of phytoplankton blooms in the water column was dictated by the vertical extent of WW, with maximum phytoplankton biomass concentrated at the interface between WW and non-WW (either at the same depth

as or just above/below the WW isotherm, illustrated in Figs. 2.3–2.5 and 2.7–2.10). This pattern demonstrates the need of phytoplankton cells to balance nutrient availability with sufficient light for photosynthesis. Although  $\text{NO}_3^-$  concentrations were more than 10-fold higher in WW than adjacent non-WW, light availability was nearly 20-fold lower, with a mean PAR of  $5.99 \pm 44.9 \mu\text{Ein m}^{-2} \text{ s}^{-1}$  in WW ( $n = 1678$  one-meter light profile bins) compared to  $114 \pm 276 \mu\text{Ein m}^{-2} \text{ s}^{-1}$  for non-WW ( $n = 3155$ ) ( $p < 0.001$ ). Consequently, the interface between deeper, nutrient-rich WW and shallower, nutrient-poor water provided a balance between the competing needs of phytoplankton in the Chukchi Sea for  $\text{NO}_3^-$  and sunlight, leading to the presence of surface blooms at stations where WW was present in the upper water column and subsurface blooms at stations where the interface between WW and non-WW was deeper. These results are consistent with previous work demonstrating maximum phytoplankton biomass at the nitracline in the Arctic (*Tremblay et al.*, 2008; *Martin et al.*, 2010; *Ardyna et al.*, 2013), which, not surprisingly, was mostly at the same depth as the interface between WW and non-WW in our study. For a more detailed description of subsurface Chl *a* maxima (SCM) in the context of euphotic depth, the nitracline, and mixed layer depth in the Chukchi and Beaufort Seas, see *Brown et al.* (2015b).

A third theme consistent across the seven transects in this study was that the upper water column was characterized by extremely high  $\text{O}_2$  content, with  $\text{O}_2$  saturation increasing towards the interface between WW and non-WW and decreasing within the WW interior (resulting in the characteristic supersaturation in non-WW and undersaturation in WW; Table 2.1). This feature illustrates that, prior to our sampling, photosynthesis took place primarily in the upper water column where light levels were optimal. By the time of our cruise, the supply of WW was largely confined to the lower part of the water column. Consequently, the deepened WW isotherm resulted in increased photosynthesis at greater depths and a sinking of phytoplankton cells from shallower depths where nutrients were depleted. This pattern resulted in frequent observations of extremely high phytoplankton biomass (e.g.  $30 \mu\text{g Chl } a \text{ L}^{-1}$ ) within WW, with very high  $\text{O}_2$  saturation (e.g. 140%) near the interface between WW and non-WW where cells were actively growing, and low  $\text{O}_2$  saturation (e.g. 80%) in deeper waters, where biomass likely accumulated primarily due to sinking processes. In these relatively deep waters, photosynthesis was limited by reduced light availability from self-shading by the bloom above and thus,  $\text{O}_2$  production by phytoplankton was not sufficient to balance  $\text{O}_2$  losses through respiration.

Finally, to assess whether the relationship between WW and phytoplankton blooms was

widespread in this region, we compared Chl *a* concentrations to measurements of potential temperature at all stations and depths sampled during the ICESCAPE program in 2010 and 2011 (Fig. 2.12). This approach added an additional 198 stations to the seven transects presented here and extended the geographic range to include samples from the southern Chukchi Sea, Barrow Canyon, and the western Beaufort Sea (for locations of all ICESCAPE stations, see *Arrigo* (2015)). Phytoplankton biomass was significantly higher at stations containing WW (at any depth in the water column) than at stations where WW was not present (Fig. 2.12), with depth-integrated Chl *a* concentrations that were 2.5-fold greater at WW stations ( $324 \pm 294 \text{ mg m}^{-2}$ ;  $n = 100$ ) than at non-WW stations ( $133 \pm 205 \text{ mg m}^{-2}$ ;  $n = 202$ ) ( $p < 0.001$ ). Similarly, mean Chl *a* concentrations throughout the water column were 2.8-fold greater at stations containing WW (Fig. 2.12;  $p < 0.001$ ). Thus, the presence of nutrient-rich WW was associated with higher phytoplankton biomass throughout the region across multiple years.

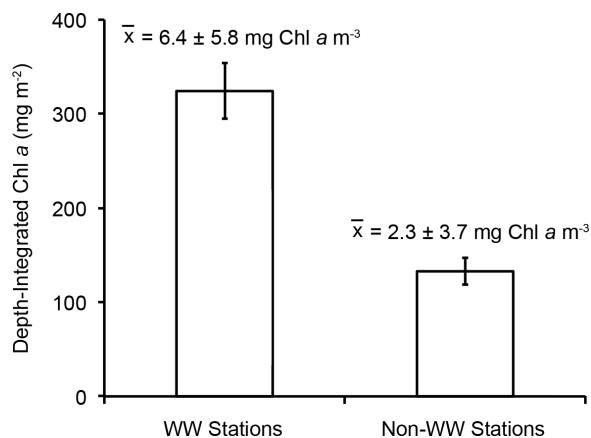


Figure 2.12: Mean depth-integrated Chl *a* values with standard error bars for all winter water (WW) and non-winter water (non-WW) stations ( $n = 100$  and  $n = 202$ , respectively). Water column mean chlorophyll *a* concentrations ( $\bar{x}$ ) and standard deviations ( $\pm$  SD) are also presented for WW and non-WW stations. Note that these values represent all ICESCAPE data collected in 2010 and 2011 and are not limited to shelf waters or the seven transects that we focus on in this study.

#### 2.4.2 Contribution of WW to biological hotspots

In this study, we sampled WW that was transported across the Chukchi shelf via a number of different pathways, including those that traveled through the Central Channel, from

Herald Canyon, and along the Alaskan Coastal Current. These three main WW pathways branched out within the Chukchi Sea into smaller filaments, producing the complex pathway of WW flow illustrated in Fig. 2.1 and described in detail in *Pickart et al.* (2016). Many of these WW pathways ultimately converge in the northeastern Chukchi Sea, within the vicinity of the head of Barrow Canyon (Fig. 2.1). In fact, Barrow Canyon appears to be the primary outflow into the Arctic basin for WW that flows across the Chukchi shelf (*Pickart et al.*, 2005; *Weingartner et al.*, 2005; *Gong and Pickart*, 2015). Notably, the region of WW confluence in the northeastern Chukchi Sea is characterized by extremely high rates of benthic production that support an abundance of benthic-feeding seabird and marine mammal populations *Dunton et al.* (2005); *Loeng et al.* (2005); *Grebmeier et al.* (2006), leading to the classification of this region as a macroinfaunal biomass 'hotspot' in the Pacific Arctic (*Grebmeier et al.*, 2006, 2015).

We suggest that the exceptional productivity of the northeastern Chukchi Sea is driven in large part by the flow and confluence of multiple WW pathways in this region. Our study illustrates that nutrient-rich WW fuels primary production across the Chukchi shelf, resulting in phytoplankton blooms at all locations where WW intersected one of our seven transects. These findings indicate that photosynthesis occurs continuously along WW flow pathways on the shelf, leading to the accumulation of extremely high phytoplankton biomass within WW. Considering that water column grazing rates are relatively low in the Chukchi Sea (*Campbell et al.*, 2009; *Sherr et al.*, 2009), the high concentrations of phytoplankton contained in WW eventually sink to the seafloor. Consequently, the convergence of multiple highly productive WW pathways in the northeastern Chukchi Sea delivers a concentrated food source of sinking phytoplankton to the benthic community over an extended period of time. Thus, the flow of phytoplankton-abundant WW to the northeastern Chukchi Sea may play an essential and previously unrecognized role in sustaining the richness of this biological hotspot.

### 2.4.3 Evidence for under-ice blooms

The massive phytoplankton bloom that we sampled underneath the ice in the northwestern portion of the Chukchi Slope West and Chukchi North transects (Figs. 2.4 and 2.5) was the first fully characterized under-ice bloom to be documented in the Chukchi Sea, as described previously (*Arrigo et al.*, 2012, 2014). In the seven transects presented here, there was additional evidence of under-ice phytoplankton blooms at many stations that were either

still ice covered or very recently ice-free at the time of sampling. For example, the Chukchi North transect contained an additional phytoplankton bloom with very high biomass (St. 43–37) located to the southeast of the previously documented massive under-ice bloom (St. 54–49; Fig. 2.4). The magnitude and vertical position of this phytoplankton bloom in relation to estimates of satellite-derived open water duration indicate similar mechanisms of bloom formation and progression as the nearby under-ice bloom. Thus, although sea ice had already retreated from the location of the southeastern bloom by the time we arrived, it is highly likely that this bloom also began beneath the ice, resulting in the measurements of elevated phytoplankton biomass at the surface in recently-ice free waters during our sampling period.

Comparing the magnitude of phytoplankton biomass in relation to open water duration at many additional stations also reveals evidence of under-ice blooms throughout the Chukchi Sea. For example, as described in Section 2.3.2, the large upper water column phytoplankton bloom in the Central Channel transect (Fig. 2.3) had very high biomass ( $16\text{--}25 \mu\text{g Chl } a \text{ L}^{-1}$  and  $70\text{--}85 \mu\text{mol POC L}^{-1}$ ) at St. 38, which we sampled on the day after sea ice retreat. Similarly, phytoplankton biomass was very high ( $15\text{--}23 \mu\text{g Chl } a \text{ L}^{-1}$ ) at the interface between WW and non-WW in St. 76–79 in the Hanna Shoal North transect (Fig. 2.7), where open water duration was 0–3 days. In the Chukchi Slope Center transect (Fig. 2.8), Chl *a* concentrations exceeded  $70 \mu\text{g L}^{-1}$  at St. 83 and 84, which had only been ice-free for 5–6 days. Across all seven transects comprising 105 stations, there were 21 stations with biomass  $> 20 \mu\text{g L}^{-1}$ , with at least one station per transect. Open water duration at these stations was relatively short, with a mean of  $9.14 \pm 9.37$  days. Such high biomass in recently ice-free waters implies that phytoplankton at many of these stations must have begun to grow underneath the ice, considering that an initial Chl *a* concentration of  $0.02 \mu\text{g L}^{-1}$  at a relatively fast specific growth rate corresponding to a doubling per day ( $0.69 \text{ d}^{-1}$ ) would require two weeks to reach  $> 20 \mu\text{g Chl } a \text{ L}^{-1}$ .

Finally,  $\text{O}_2$  saturation and nutrient concentrations indicate that phytoplankton bloomed in all shelf waters across the seven transects prior to our sampling, regardless of open water duration.  $\text{O}_2$  was supersaturated throughout the upper water column, suggesting that widespread photosynthesis took place, even at stations that were still ice-covered or very recently ice free (e.g. in the Hanna Shoal North and Chukchi Slope Center transects). Similarly,  $\text{NO}_3^-$  and DIC concentrations were depleted throughout the upper water column, providing biogeochemical evidence of uptake by phytoplankton since the start of the growing

season. Since open water duration was relatively short at many locations we sampled, these consistent signals of previous phytoplankton growth provide additional evidence that there were under-ice blooms throughout the study area prior to our sampling. The notion that under-ice blooms are prevalent in this region is consistent with the satellite-based estimate that  $> 70\%$  of shelf waters in the Chukchi Sea support phytoplankton blooms underneath sea ice prior to ice retreat (*Lowry et al.*, 2014).

#### 2.4.4 Conceptual model of phytoplankton blooms in the Chukchi Sea

The relationships between nutrient-rich WW, phytoplankton abundance, and open water duration identified in this study, combined with previous work, allows for the construction of a revised conceptual model of phytoplankton blooms in the Chukchi Sea.

In the winter, sea ice formation and brine rejection lead to convective overturning of the shallow water column on both the Chukchi and Bering Sea shelves (*Muench et al.*, 1988; *Weingartner et al.*, 1998; *Woodgate et al.*, 2005b). This forms near-freezing WW and replenishes the surface ocean with high concentrations of nutrients that are mixed into the water column from the sediments. As the winter progresses, WW is advected into the Chukchi Sea through Bering Strait, and polynyas and smaller leads open up locally on the Chukchi shelf (*Cavalieri and Martin*, 1994; *Iwamoto et al.*, 2014), which results in continued formation of WW. Hence, by the end of the winter, presumably the water column is fully mixed with nutrient-rich WW extending from the surface to the seafloor throughout much of the Chukchi shelf.

As sunlight returns to the ice-covered Chukchi Sea in the spring, solar heating begins to modify sea ice and the underlying water column. Melt ponds form on the surface of the ice (*Polashenski et al.*, 2012, 2015), allowing sunlight to penetrate through the ice and into the water column. As warming continues, melt ponds expand on the relatively flat first-year sea ice that has become characteristic of the Chukchi Sea (*Maslanik et al.*, 2011), increasing the availability of sunlight in the upper ocean. Previous work reveals that up to 55% of incident light is transmitted through first-year melt ponded ice (*Frey et al.*, 2011). WW under the ice warms slightly from its extremely cold formation temperature near  $-1.9^{\circ}\text{C}$ , and also by mixing with more moderate waters entering through Bering Strait (*Gong and Pickart*, 2015). In our study, which took place in June/July, the mean observed WW temperature was  $-1.71 \pm 0.05^{\circ}\text{C}$ .

Once light availability under melt ponded ice is sufficient for primary production, phytoplankton blooms begin in surface waters beneath the ice on the Chukchi shelf (*Arrigo et al.*, 2012, 2014; *Palmer et al.*, 2014), fueled initially by the widespread presence of WW and subsequently by the continued input of WW from the Bering Sea. As phytoplankton blooms develop,  $O_2$  is produced through photosynthesis and nutrients and DIC are utilized for photosynthesis and cell growth. After  $NO_3^-$  is removed from surface waters, phytoplankton cells cease growing and begin to sink, while new cells grow deeper in the water column where nutrients are more abundant. This process continues as the blooms evolve, resulting in the vertical 'migration' of blooms from the surface to the depth of the nitracline (*Brown et al.*, 2015b). Although much of the phytoplankton biomass observed in this study was located in open water and below the surface layer, the numerous observations of high  $O_2$  saturation and depleted  $NO_3^-$  and DIC concentrations throughout the upper water column (including at ice-covered stations) indicate that blooms initiate earlier in surface waters throughout the Chukchi shelf, likely under sea ice and within nutrient-rich water.

As spring transitions to summer and sea ice begins to retreat from the Chukchi Sea, WW is increasingly modified through a combination of solar heating, mixing with summer water masses, and nutrient uptake by phytoplankton. At the same time, WW is flushed off the Chukchi shelf into the Canada Basin and replaced by summer water, so by mid-summer most of the WW is confined primarily to the advective pathways illustrated in Fig. 2.1. The residence time of nutrient-rich WW on the shelf depends largely on the flow speeds and length of the circulation pathways; as such, phytoplankton bloom duration is determined in large part by circulation in the Chukchi Sea. For example, based on hydrographic data collected in Barrow Canyon (*Itoh et al.*, 2015), cold Pacific-origin water travels quickly along the coastal pathway in the Chukchi Sea via the Alaskan Coastal Current, which is consistent with previous studies (e.g. *Weingartner et al.*, 1998). In contrast, the cold water drains for a longer period (hence more slowly) through the summer from the Central Channel pathway around the northern side of Hanna Shoal described here (Fig. 2.1). *Pickart et al.* (2016) compute an average advective speed of approximately  $12 \text{ cm s}^{-1}$  along this pathway, implying a travel time of over three months for the water to progress from Bering Strait to the Hanna Shoal Southeast transect. Hence, this may explain the extended duration of open water phytoplankton blooms in the Chukchi Sea, which were the longest of any Arctic region from 1998–2009, with a mean of  $119 \pm 16.1$  days (*Arrigo and van Dijken*, 2011).

Like its residence time, the vertical extent of WW varies spatially in the summer, extending to the surface at some locations and confined to deeper in the water column at others (with the interface between WW and non-WW approximating the depth of the nitracline). The presence and vertical position of phytoplankton were closely associated with the interface between WW and non-WW, where the nitracline provides a balance between nutrients and light. Conversely, the absence of WW on the shelf is accompanied by  $\text{NO}_3^-$  depletion, resulting in low phytoplankton biomass. Presumably, after WW completely flushes off of the Chukchi shelf in the late summer to early fall when waters are more stratified, phytoplankton concentrations are greatly reduced, with blooms occurring only when episodic mixing and/or storm events bring nutrients to the upper water column (e.g. *Pickart et al.*, 2011; *Ardyna et al.*, 2014).

A key aspect of this conceptual model is the flow of high-nutrient WW across the shelf that both initiates and sustains phytoplankton blooms in the Chukchi Sea. Given that WW forms locally on the shelf in polynyas and leads during the winter, this implies that blooms in surface waters under melt ponded sea ice are likely widespread across the Chukchi shelf in the spring and early summer. Our observations indicate, however, that phytoplankton blooms along the nutrient-rich WW pathways are extended for longer duration than in adjacent waters, with total bloom duration and the magnitude of primary production related to the residence time and vertical extent of WW flow. Considering that the timing of bloom initiation in the Arctic may be shifting to earlier in the season with a warming climate (*Kahru et al.*, 2010; *Arrigo et al.*, 2012), the role of WW in extending blooms may be particularly important to upper trophic level organisms that rely on the consumption of phytoplankton. Similarly, we have shown that WW flowing through the northeastern Chukchi Sea in the summer en route to Barrow Canyon is characterized by extremely high concentrations of phytoplankton cells that likely sink and provide an important and continuous food source for the rich benthic community in this biological 'hotspot' region. This work furthers our understanding of the hydrographic controls on the timing, magnitude, and dynamics of phytoplankton blooms in the Chukchi Sea.

## Acknowledgments

This material is based upon work supported by the National Aeronautics and Space Administration (NASA) under Grant No. NNX10AF42G and the National Science Foundation

Graduate Research Fellowship under Grant No. DGE-0645962 to K.E. Lowry. The authors would like to acknowledge the scientists, captain, and crew of the USCGC Healy for their efforts during the HLY1001 and HLY1101 missions that supported the collection of field data. Additionally, we would like to thank Carolina Nobre for her efforts that improved the visualization of multiple figures presented in this manuscript.

## Chapter 3

# Under-ice bloom development controlled by convective mixing

KATE E. LOWRY, MATTHEW M. MILLS, VIRGINIA SELZ, KATE M. LEWIS, HANNAH JOY-WARREN, GERT L. VAN DIJKEN, AND KEVIN R. ARRIGO

*Earth System Science, Stanford University, Stanford, California, USA*

ROBERT S. PICKART, ASTRID PACINI, AND CAROLINA NOBRE

*Woods Hole Oceanographic Institution, Woods Hole, Massachusetts, USA*

*Spring phytoplankton growth in polar marine ecosystems is limited by the availability of sunlight beneath ice-covered waters, particularly early in the season prior to the onset of snow melt and melt pond formation. Leads of open water increase light transmission to the ice-covered ocean and are therefore potentially important sites for enhanced primary production. Here we explore the role of leads in controlling the initiation of phytoplankton blooms within the sea ice zone of the Arctic Ocean. Data are presented from spring measurements in the Chukchi Sea during the Studies of Under-ice Blooms In the Chukchi Ecosystem (SUBICE) program (May–June 2014). Observations revealed that while fully consolidated sea ice occasionally supported modest under-ice blooms, sea ice with higher concentrations of leads had significantly lower phytoplankton biomass, despite high nutrient concentrations in surface waters beneath the sea ice. Through an analysis of hydrographic and biological properties, we attribute this counterintuitive*

*finding to springtime convective mixing in refreezing leads of open water, which resulted in enhanced vertical mixing and overturning of the shallow water column on the Chukchi shelf in waters with a relatively high lead fraction. Our results demonstrate that waters beneath loosely consolidated sea ice (e.g. 85–95% ice concentration) had weak stratification and were frequently mixed below the critical depth (the depth at which depth-integrated production balances depth-integrated respiration). These findings are supported by model calculations of under-ice light, primary production, and critical depth at varied lead fractions. This model demonstrates that under-ice blooms can form in stratified waters beneath snow-covered sea ice but not in more deeply mixed waters where the fraction of refreezing leads is higher. This study seeks to better understand the physical drivers of under-ice phytoplankton bloom dynamics in this rapidly changing seasonally ice-covered ecosystem.*

This chapter is in preparation for submission to *Journal of Geophysical Research: Oceans*.

### 3.1 Introduction

Each year, the physical environment of the Arctic Ocean undergoes a series of seasonal changes in solar irradiance and sea ice cover that drives the productivity of the marine ecosystem (Loeng *et al.*, 2005). While winter in the Arctic Ocean is characterized by darkness and expansive sea ice, in the summer the region receives up to 24 hours of sunlight per day and contains large stretches of open water (Parkinson and Cavalieri, 2008), particularly in the continental shelf regions such as the Chukchi and Beaufort Seas that border the western Arctic basin (Arrigo *et al.*, 2008). Spring and fall in these regions are transitional periods when sunlight and sea ice extent wax and wane; as the intensity of solar radiation decreases in the fall, sea ice cover begins to advance, while in the spring an increase in solar radiation is accompanied by sea ice melt in lower-latitude waters. Physical and biogeochemical properties of seawater are highly dynamic in the spring and fall owing to these seasonally changing conditions, yet understudied due to the difficulty of sampling ice-covered waters via ship or satellite. While most polar oceanographic research focuses on the more accessible summer months, a limited number of studies has sought to characterize physical and biological processes during other times of year (e.g. Woodgate *et al.*, 2005b;

*Ardyna et al.*, 2014).

An important consequence of these seasonal changes is that water mass properties in the Arctic Ocean are dramatically transformed over the annual cycle. During the advance of sea ice cover in the fall, salt is excluded from the freezing ice through brine rejection, producing a layer of relatively fresh sea ice. The excluded cold, saline, and dense brine sinks to its density equilibrium and is replaced by more buoyant seawater through convection, thereby mixing the water column. Brine rejection and subsequent convective mixing continues through the winter as more sea ice is produced in areas of open water such as sea ice leads and polynyas (*Smith IV and Morison*, 1993; *Weingartner et al.*, 1998; *Pickart et al.*, 2016). These physical winter processes form the dense near-freezing (potential temperature ( $\theta$ )  $\leq -1.6^\circ\text{C}$ ) water mass referred to as winter water (WW). The nutrient content of WW formed on the shallow shelves is relatively high compared to other water masses, owing to the exchange with remineralized nutrients from the benthos. In particular, on the Chukchi shelf, convective mixing can completely overturn the water column, resulting in a uniform and extremely nutrient-rich water mass (*Lowry et al.*, 2015; *Pacini et al.*, 2016; *Pickart et al.*, 2016). In the summer, WW is increasingly modified through solar heating and/or lateral mixing, as well as through biological activity, and is eventually transported to depth in the Arctic basin (*Gong and Pickart*, 2015; *Itoh et al.*, 2015, 2012; *Woodgate et al.*, 2005a). At the same time, WW in the Chukchi Sea is gradually replaced by warmer, fresher, nutrient-poor summer water masses from the Pacific Ocean (*Woodgate et al.*, 2005b; *Gong and Pickart*, 2015).

Field work as part of the NASA-funded Impacts of Climate on EcoSystems and Chemistry of the Arctic Pacific Environment (ICESCAPE) program in the Chukchi Sea in June–July 2010 and 2011 (*Arrigo*, 2015, 2016) confirmed that WW is a significant nutrient source for phytoplankton at the base of the marine food web. An analysis of hydrographic sections and biogeochemical properties in the Chukchi Sea revealed that WW was consistently associated with summer phytoplankton blooms of great magnitude and duration (*Lowry et al.*, 2015). Concentrations of nitrate, the primary limiting nutrient for phytoplankton growth in the Arctic Ocean (*Cota et al.*, 1996; *Codispoti et al.*, 2005; *Tremblay and Gagnon*, 2009), were more than 10-fold higher (e.g.  $>10\ \mu\text{mol L}^{-1}$ ) in WW than in adjacent water masses (*Lowry et al.*, 2015), demonstrating the importance of WW as the primary source of nutrients for growth by phytoplankton. Additionally, the complex flow paths of WW across the Chukchi shelf in the summer extend the residence time of the nutrient-rich water mass on the shelf (*Pickart et al.*, 2016). These results suggest that wintertime convection

and subsequent WW advection during the summer are critical for sustaining the immense phytoplankton blooms found in the Chukchi Sea and supporting the hotspots of biological activity in the region (*Lowry et al.*, 2015), such as those documented in *Grebmeier et al.* (2015).

The western Arctic Ocean has been dramatically transformed by climate change in recent decades, particularly in the Chukchi Sea and surrounding regions. The seasonal cycle of sea ice retreat and advance has intensified, with more ice melting each year and returning as thin first-year sea ice rather than the once-prevalent thicker multi-year ice (*Maslanik et al.*, 2011). Sea ice in this region retreated up to two months earlier and advanced more than a month later in 2010–11 as compared to 1979–80 (*Stammerjohn et al.*, 2012), corresponding to up to a three month increase in the open water growing season in some areas. Open water phytoplankton primary production increased by 42% in the Chukchi Sea from 1998 to 2012 according to satellite estimates (*Arrigo and van Dijken*, 2015), indicating that productivity is associated with, and is likely a consequence of, the reduced sea ice cover. In 2011, an unprecedented and massive phytoplankton bloom was found beneath the fully consolidated ice pack in the Chukchi Sea (*Arrigo et al.*, 2012, 2014), indicating that the under-ice environment is becoming more suitable for phytoplankton growth. The presence of melt ponds on the sea ice (Fig. 3.1A), which transmit up to 55% of the incident irradiance to the underlying water column (*Frey et al.*, 2011), supported extremely high growth rates and depth-integrated biomass within the bloom (Fig. 3.1B). Evidence that under-ice blooms have become prevalent in recent decades in the Chukchi Sea is also supported by satellite work (*Lowry et al.*, 2014) and modeling studies (*Palmer et al.*, 2014; *Zhang et al.*, 2015), indicating that phytoplankton blooms may be shifting to an earlier time of year, with potential consequences for resident and migratory upper trophic level species (*Arrigo et al.*, 2014).

Motivated by the discovery of under-ice blooms and the resulting ecosystem implications, the NSF-funded Study of Under-ice Blooms In the Chukchi Ecosystem (SUBICE) team conducted an extensive characterization of the Chukchi Sea in May–June 2014, resulting in the first early season study of hydrography, nutrients, and phytoplankton beneath the ice. The field sampling took place primarily during pre-bloom conditions, prior to melt pond formation. Leads of open water (illustrated in Fig. 3.1C) were prevalent throughout the study region, acting as windows (*Pegau and Paulson*, 2001) for solar radiation to penetrate the otherwise dark water column beneath sea ice with snow (illustrated in Fig. 3.1D),

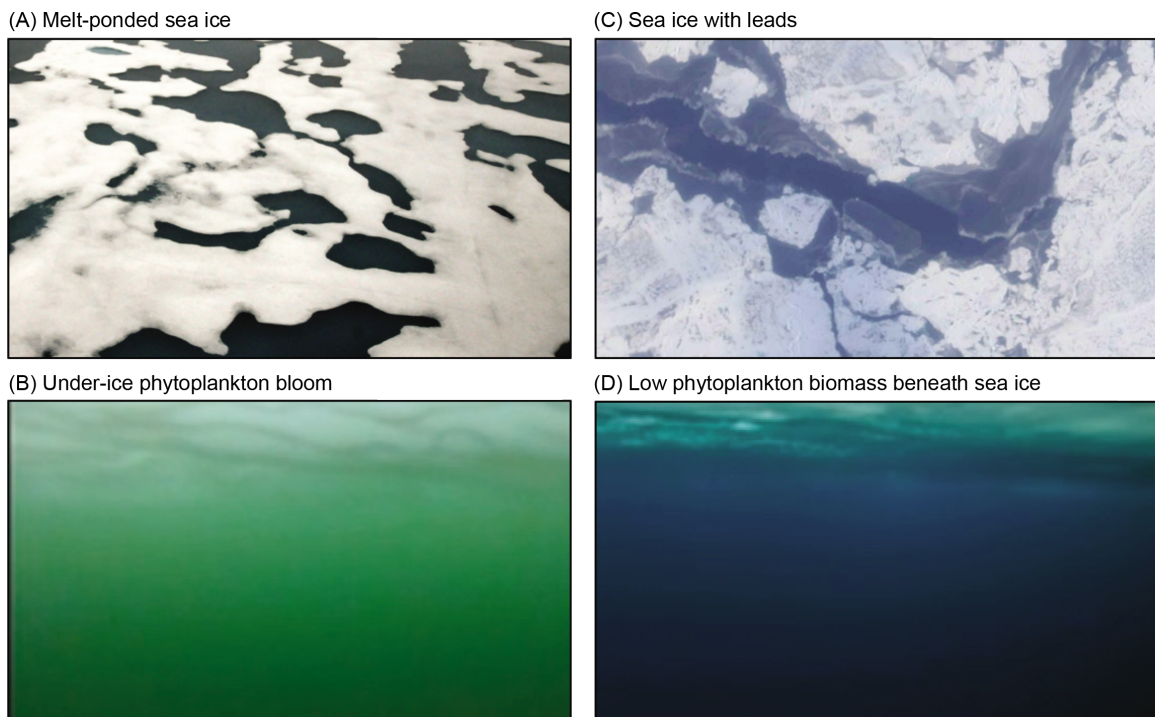


Figure 3.1: Photographs of (A) melt-ponded sea ice, (B) waters characterized by a massive under-ice phytoplankton bloom, (C) sea ice with leads, and (D) waters characterized by low phytoplankton biomass beneath sea ice (for illustrative purposes). Image credits: (A, B, and D) NASA ICESCAPE Team and (C) NASA ARISE Mission.

which strongly attenuates sunlight (*Perovich, 2002*). The purpose of the present work is to characterize the mechanisms that control the development of under-ice phytoplankton blooms in the Chukchi Sea, with particular emphasis on the role of sea ice leads. By combining an analysis of field observations from SUBICE with satellite sea ice imagery and a theoretical model of irradiance and primary production at varied ice concentrations, we explore the influence of open water leads on under-ice phytoplankton growth and test the hypothesis that phytoplankton blooms can form beneath snow-covered sea ice when leads are present. This early season characterization of under-ice phytoplankton dynamics is critical for understanding the current state of the ecosystem and the response to continued climate change.

## 3.2 Materials and Methods

### 3.2.1 Data collection

#### Field sampling

The SUBICE field campaign was conducted in the Chukchi Sea aboard *USCGC Healy* in May–June 2014. During the field expedition, the SUBICE team sampled the water column at 230 hydrographic stations, primarily on the continental shelf of the northeastern Chukchi Sea where the present analysis is focused (Fig. 3.2). At each station, conductivity-temperature-depth (CTD) casts were made using dual temperature (SBE3), conductivity (SBE4c), and pressure (Digiquartz 0–10,000 psi) sensors attached to the ship’s 30-liter, 12-position rosette system. Additional sensors on the rosette included dissolved oxygen (SBE43), photosynthetically active radiation (PAR) (Biospherical QSP-2300), fluorescence (WET Labs ECO-AFL/FL), and beam transmission (WET Labs C-Star). Discrete seawater samples were collected at a set of standard depths (2, 5, 10, 25, 50, 75, and 100 m) in addition to the depth of the subsurface fluorescence maximum (if present) and near the bottom (typically 2–3 m above the seafloor). Currents were measured using the ship’s hull-mounted Ocean Surveyor 150 KHz unit (OS150) Acoustic Doppler Current Profiler (ADCP) system.

#### Shipboard and laboratory analysis

Seawater samples collected during the cruise were analyzed for a suite of biogeochemical and biological parameters. Nutrient analysis was performed onboard the ship using a Seal Analytical continuous flow Auto-Analyzer 3 and a modification of the method of *Armstrong et al.* (1967) to measure the concentration of nitrate ( $\text{NO}_3^-$ ), ammonium ( $\text{NH}_4^+$ ), nitrite ( $\text{NO}_2^-$ ), phosphate ( $\text{PO}_4^{3-}$ ), and silicate ( $\text{Si}(\text{OH})_4$ ). Seawater samples for dissolved oxygen ( $\text{O}_2$ ) were analyzed using standard Winkler titrations to calibrate sensor measurements from the CTD casts.

For analysis of chlorophyll *a* (Chl *a*) concentration, seawater was filtered onto 25 mm Whatman GF/F filters of 0.7  $\mu\text{m}$  nominal pore size. The filters were then extracted in the dark in 5 mL of 90% acetone for 24 hrs at +3°C prior to measurement (*Holm-Hansen et al.*, 1965) on a Turner Designs 10-AU fluorometer calibrated with pure Chl *a* (Sigma). For analysis of particulate organic carbon and nitrogen (POC and PON), seawater was filtered onto pre-combusted (4 hrs at 450°C) GF/Fs. Filter blanks were made with ~50 mL of

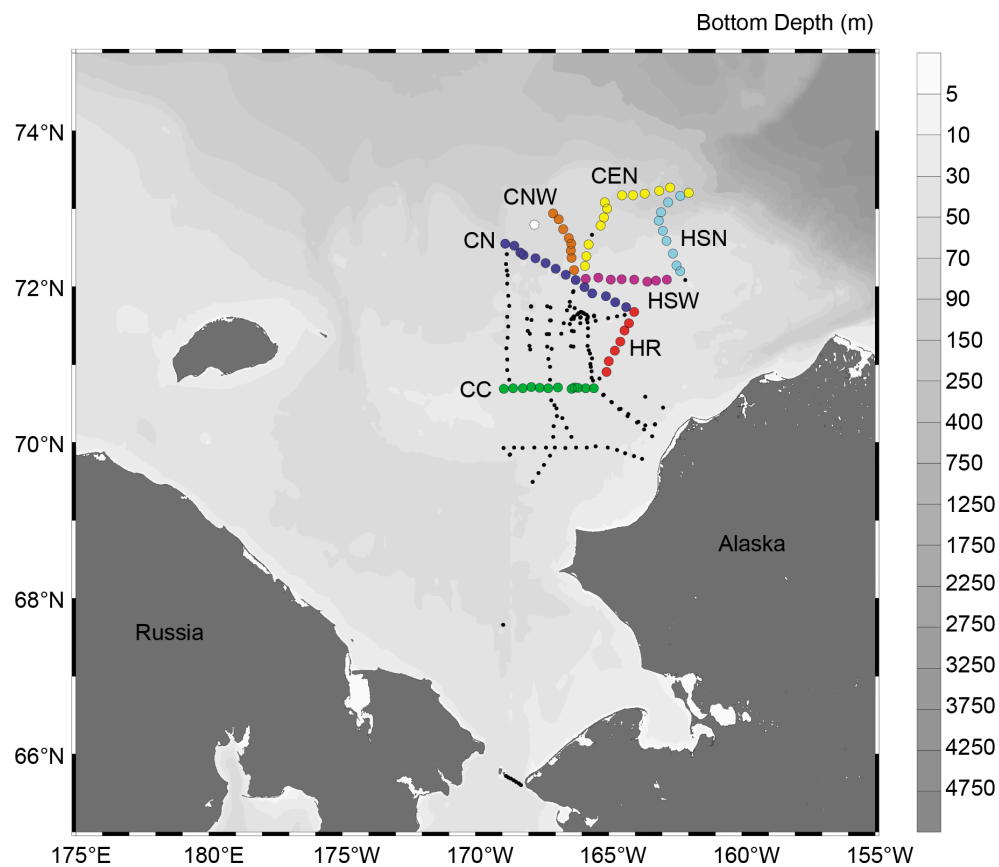


Figure 3.2: Bathymetric map of the Chukchi Sea displaying the locations of 230 stations occupied during the SUBICE field program. The 72 stations included in the present analysis are illustrated with large colored dots and comprise seven transects. Transects are labeled and listed here in order of sampling: Central Channel (CC; green), Hanna Ridge (HR; red), Chukchi North (CN; blue), Chukchi Northwest (CNW; orange), Hanna Shoal West (HSW; magenta), Hanna Shoal North (HSN; cyan), and Central Shelf (CEN; yellow). The transects do not include the station in white.

0.2  $\mu\text{m}$  filtered seawater. Filters were immediately dried in an oven at 60°C and stored dry. Samples and blanks were later fumed with concentrated HCl, dried again at 60°C, and packed into tin capsules (Costech Analytical Technologies, Inc.) for elemental analysis on an Elementar Vario EL Cube (Elementar Analysensysteme GmbH) interfaced to a PDZ Europa 20-20 isotope ratio mass spectrometer (Sercon Ltd). Standards included glutamic acid and peach leaves.

Phytoplankton physiology was assessed using a fast repetition rate fluorometer (FRRf) with excitation at 470 nm to measure the maximum efficiency of photosystem II (Fv:Fm) of

seawater samples (Kolber *et al.*, 1998). The samples were dark-acclimated for  $\sim 30$  minutes at *in situ* temperature and measured in triplicate within one hour of collection. Blanks were prepared for each sample via gentle filtration through a  $0.2\ \mu\text{m}$  polycarbonate syringe filter before measurement using identical protocols. Fv:Fm values were corrected for blank effects (Cullen and Davis, 2003).

Phytoplankton photosynthetic parameters were determined at the surface and subsurface (typically 10 or 25 m depth) from photosynthesis ( $P$ ) versus irradiance ( $E$ ) curves. In the P-E method (Lewis and Smith (1983), as modified by Arrigo *et al.* (2010)), seawater samples labeled with  $^{14}\text{C}$ -bicarbonate were incubated under a range of light levels (0 to  $522\ \mu\text{Ein m}^{-2}\ \text{s}^{-1}$ ) and later assayed for  $^{14}\text{C}$  incorporation using a Perkin Elmer WinSpectral 1414 liquid scintillation counter. The resultant P-E curves provide estimates of maximum Chl  $a$ -normalized (\*) photosynthetic rates ( $P_{\text{max}}^*$ ) ( $\text{mg C mg}^{-1}\ \text{Chl } a\ \text{h}^{-1}$ ), light limited efficiency of photosynthesis ( $\alpha^*$ ) ( $\text{mg C mg}^{-1}\ \text{Chl } a\ \text{h}^{-1}\ (\mu\text{Ein m}^{-2}\ \text{s}^{-1})^{-1}$ ), photoinhibition ( $\beta^*$ ) ( $\text{mg C mg}^{-1}\ \text{Chl } a\ \text{h}^{-1}\ (\mu\text{Ein m}^{-2}\ \text{s}^{-1})^{-1}$ ), and the light-saturation intensity parameter ( $E_K$ ) ( $\mu\text{Ein m}^{-2}\ \text{s}^{-1}$ ), after correcting for  $P_0^*$  (the amount of carbon uptake/release at  $0\ \mu\text{Ein m}^{-2}\ \text{s}^{-1}$ ). Using a nonlinear least-squares curve-fitting program (lsqcurvefit) in MATLAB, P-E curves were fit to the model of Webb *et al.* (1974).

$$P^* = P_m^* \left( 1 - \exp \left[ \frac{-\alpha^* E}{P_m^*} \right] \right) - P_0^* \quad (3.1)$$

P-E curves were also fit to the model of Platt *et al.* (1980) which includes a photoinhibition term ( $\beta$ ), but the model was disregarded due to insignificant  $\beta$  values at the stations used for this study. Significance for P-E curves was determined using criteria of  $p < 0.05$  and  $R^2 > 0.6$ , as in Palmer *et al.* (2013).

### Sea ice cover

Daily satellite images from the Special Sensor Microwave Imager (SSM/I) at 25 km resolution were obtained from the National Snow and Ice Data Center (Cavalieri *et al.*, 1996) and used to characterize the sea ice concentration at each hydrographic station for the date it was sampled. During the cruise, sea ice concentration was also estimated through visual ‘ice watch’ observations taken every two hours from the bridge of the *USCGC Healy*. Satellite sea ice concentrations were extracted at the locations of all of the visual recordings during SUBICE for comparison, yielding a strong correlation between the satellite and *in situ*

observations ( $R = 0.83$ ;  $p < 0.01$ ). Satellite-derived sea ice concentrations were used for this study to represent a larger spatial area surrounding the location of each hydrographic station. The presence of sea ice leads was determined from the amount of open water at each station (i.e. the inverse of sea ice fraction) and is referred to as the lead fraction. Measurements of snow depth and sea ice thickness were also made at each ice station.

### 3.2.2 Data analysis

#### Station selection

This study focuses solely on phytoplankton growth that started beneath the ice, therefore it is important to consider the role of advection of open water phytoplankton into our ice-covered study region. To do so, we evaluated the potential influence of advection on each station based on the expected transport of phytoplankton from adjacent-ice free waters. Satellite ocean color imagery from MODIS Aqua revealed the presence of an open water phytoplankton bloom south of our study region that was located northwest of Bering Strait and roughly centered at  $67.5^{\circ}\text{N}$ ,  $170^{\circ}\text{W}$ . The northernmost edge of the bloom extended to  $69^{\circ}\text{N}$  on 13 May 2014, five days before we began sampling stations at  $\sim 70.7^{\circ}\text{N}$ . We calculated the date that the water containing the bloom would be advected to each station assuming a relatively fast northward flowing current of  $17.5 \text{ cm s}^{-1}$ , a rate equivalent to the fastest northward flowing current observed during SUBICE. This speed is 1.7-fold faster than the realistic mean current speed estimated for waters transiting the shelf in the spring ( $10.5 \text{ cm s}^{-1}$ ) (Pickart *et al.*, 2016) and was chosen to be highly conservative. Stations sampled after this date were flagged as potentially influenced by advection of open water phytoplankton and were removed from our analysis. We also flagged 10 additional stations near the coast as potentially influenced by advection of open water phytoplankton along the northeastward flowing Alaska Coastal Current, leaving a total of 72 stations that were included in the present analysis. These stations were sampled 18 May–2 June 2014 and comprise seven transects across a latitudinal range of  $\sim 70.7$ – $73.3^{\circ}\text{N}$  (Fig. 3.2). The bottom depth of the stations ranged from 36 to 195 m.

#### Water column structure

Density profiles were constructed from measurements of temperature and salinity at each station. The mixed layer depth (MLD) was determined using a robust method to visually

inspect each profile and manually estimate the extent of the upper mixed layer and the location where the profile permanently crossed outside of an envelope of two standard deviations beyond the density range of the upper mixed layer, following *Pickart and Torres (2002)*; *Våge et al. (2015)*. This method was also used to define the depth range of the bottom boundary layer. The mixed layer (ML) slope was then calculated as the vertical change in density in the upper mixed layer divided by the MLD. The strength of the interface between the upper mixed layer and bottom boundary layer at each station was assessed through the stratification index, defined as the change in density over the vertical range of the interface. When the stratification index was  $< 0.01 \text{ kg m}^{-3}$ , the water column was considered to be fully mixed from top to bottom (*Pacini et al., 2016*).

### Primary production and community respiration

Rates of daily gross primary production (GPP) were estimated for under-ice phytoplankton using measured P-E parameters and irradiance at 1 m depth intervals in the water column. Daily cycles of irradiance were calculated for each station using the hourly mean incident surface PAR from the ship's mast during the sampling period (18 May–2 June 2014). Light transmission through the ice to the ocean surface was calculated using the satellite-derived ice concentration at each station and modeled estimates of light attenuation through ice and leads. For example, for a station with 90% ice concentration, 90% of the incident irradiance over the day was transmitted through simulated snow, ice, and sea ice algae, while 10% of the incident irradiance was transmitted through a simulated lead of open water. The thickness of snow (0.09 m), sea ice (1.12 m), and the algal layer beneath the ice (0.02 m) were set to represent the average field conditions observed during SUBICE (see Section 3.3.1). A detailed description of the light transmission model, including the diffuse attenuation coefficients and specular reflection calculations for sea ice and water, is presented in Section 3.2.3.

After calculating irradiance just below the ocean surface for a given ice concentration, profiles of corrected PAR (%) from the CTD rosette were used to compute light transmission through the water column. Normalized photosynthetic rates ( $P^*$ ) at varying irradiance ( $E$ ) were calculated from the mean P-E parameters using Equation 3.1 (Section 3.2.1).  $P^*$  ( $\text{mg C mg}^{-1} \text{ Chl } a \text{ m}^{-3} \text{ h}^{-1}$ ) and depth profiles of Chl  $a$  were then used to estimate GPP ( $\text{mg C m}^{-3} \text{ d}^{-1}$ ) at each depth and the total depth-integrated GPP ( $\text{mg C m}^{-2} \text{ d}^{-1}$ ) was calculated over a 24-hr daily cycle for each station.

Community respiration was estimated based on the difference in apparent oxygen utilization (AOU) between two sets of stations located along the northward flowing Central Channel pathway. AOU is defined as the deficit in dissolved  $O_2$  relative to saturation and was calculated in Ocean Data View (*Schlitzer, 2014*). We compared mean values in the upper 35 m at three stations on the southern Central Channel transect (St. 13–15, refer to Fig. 3.9 for location) and three stations on the northern Chukchi North transect (St. 62–64, refer to Fig. 3.10 for location) to determine the change in AOU ( $18.5 \mu\text{mol } O_2 \text{ kg}^{-1}$ ) along the flow pathway using a range of advective speeds ( $6.0\text{--}10.5 \text{ cm s}^{-1}$ ) based on field observations from SUBICE and estimates of the realistic mean current speed (*Pickart et al., 2016*). Over this range, we estimated that it would take between 19 and 33 days for water to flow between the two sets of three stations ( $\sim 170 \text{ km}$ ). Assuming uniform respiration, no early season primary production during the pathway transit time, and a 9-day delay in sampling between the transects, we estimated a range of respiration rates of  $0.44\text{--}0.67 \text{ mmol } O_2 \text{ m}^{-3} \text{ d}^{-1}$ . These values compare well with observed rates in the region; for example, a rate of  $0.9 \pm 0.4 \text{ mmol } O_2 \text{ m}^{-3} \text{ d}^{-1}$  was measured in the Chukchi Sea in Spring 2004 (*Cottrell et al., 2006*). Using a respiration coefficient of 0.8 C: $O_2$  (*Nguyen et al., 2012*) yielded a range of respiration rates of  $4.4\text{--}6.6 \text{ mg C m}^{-3} \text{ d}^{-1}$ . Community respiration was assumed to be uniform laterally and vertically for waters flowing across the Chukchi Sea in the spring. This highest estimate of community respiration was used in calculations of critical depth for stations during the cruise (Section 3.2.2), while the lowest estimate was used to simulate early season pre-bloom conditions in a theoretical modeling exercise (Section 3.2.3). We also present mean estimates of net community production (NCP), calculated for each station by subtracting community respiration from GPP.

### Euphotic depth and critical depth

The euphotic depth ( $Z_{\text{eu}}$ ) at each station was calculated as the depth at which PAR was  $\sim 1\%$  of the value just below the surface ocean (*Hill et al., 2005; Moran et al., 2005; Brown et al., 2015b*). To correct for spurious values from the PAR sensor mounted on the CTD rosette system at the ocean surface, PAR in the upper two meters was linearly extrapolated from log-transformed PAR measurements from 2–6 m of the water column. PAR measurements were corrected for variation in incident solar radiation during the CTD deployment, as in *Palmer et al. (2013)*, as well as the physical distance between the CTD and PAR sensors ( $\sim 1.5 \text{ m}$ ). The critical depth ( $Z_{\text{cr}}$ ) at each station was defined as the depth where the

depth-integrated primary production balanced the depth-integrated community respiration, following *Sverdrup* (1953). At stations where the theoretical  $Z_{cr}$  exceeded the bottom depth, the  $Z_{cr}$  was set to the bottom depth for the purpose of calculating a mean  $Z_{cr}$  for all stations.

### Hydrographic sections

For the seven transects of this study (Fig. 3.2), vertical sections for hydrographic properties were constructed using a Laplacian-spline interpolator in Matlab, as in *Pickart et al.* (2016). In this analysis, we include sections of  $\theta$ , salinity,  $\text{NO}_3^-$ , Chl *a*,  $\text{O}_2$  saturation, and Fv:Fm overlain with potential density contours. To visualize the vertical extent of mixing and light availability in relation to phytoplankton biomass, sections of Chl *a* concentration are overlain with lines indicating the MLD and the  $Z_{cr}$ . Hydrographic sections are displayed along with context maps and plots of sea ice concentration and the stratification index along each section.

### Statistical analyses

To assess how sea ice concentration, water column structure, and environmental conditions control biological and biogeochemical properties, we performed single and multiple linear regression analysis. Depth-integrated means of biological variables were calculated for the ML and the full water column (WC) for statistical analysis. Correlations between variables were determined through Pearson's correlations using Student's t distributions for transformation of the correlations. We also performed t-tests to compare means of water column structure properties at extremely high ice concentration ( $\geq 98\%$ ) versus sea ice with leads.

A multiple linear regression model was developed to understand the relative importance of physical and environmental variables in predicting phytoplankton biomass in the ML. The relative importance of each variable was quantified as the percent of  $R^2$  explained using the *relaimpo* package in R (*Grömping*, 2006). To meet model assumptions, Chl *a* was log-transformed and the potential for multicollinearity of predictor variables was assessed through the condition number (*Belsley et al.*, 1980), which was less than 3. In all cases, statistical significance is represented through  $p$ -values, using a criterion of  $p < 0.05$ .

### 3.2.3 Model of irradiance, production, and critical depth beneath sea ice with leads

To investigate the range of sea ice concentrations that support the early season growth of phytoplankton beneath snow-covered sea ice, we constructed a model of under-ice PAR, GPP, and  $Z_{\text{cr}}$  in sea ice with leads. The model simulates the following components of the under-ice environment: the transmittance of incident PAR to the ocean surface through sea ice and leads of open water, the daily cycle of PAR in the water column for waters advecting beneath sea ice with leads, and GPP by under-ice phytoplankton based on under-ice PAR. The output of the model is used to compute GPP and  $Z_{\text{cr}}$  under the ice at varied lead fractions. A detailed description of each component is presented below.

#### Transmission of incident PAR through sea ice and the water column

As in Section 3.2.2, we use the mean hourly surface PAR measurements from SUBICE (18 May–2 June 2014) to simulate a daily cycle of incident PAR in the Chukchi Sea. To calculate light transmission from the atmosphere into the sea ice or open water, specular reflection was set at 5% for the atmosphere-snow interface and was calculated as a function of solar zenith angle for open water (*Kirk*, 2011), assuming a flat ocean surface (there are few waves in leads within the sea ice zone). We calculated the solar zenith angle for the mean sampling latitude ( $\sim 72.1^\circ\text{N}$ ) and date (25 May), yielding a specular reflection range of  $\sim 3.5\%$  at noon to  $\sim 72\%$  at midnight, corresponding to a daily mean transmission of  $\sim 75\%$  of incident PAR to the surface ocean. These estimates of incident light transmission through ice and leads were also used in calculations of GPP and  $Z_{\text{cr}}$  at each station, as described in Section 3.2.2.

We calculated light transmission through snow/sea ice assuming attenuation through a layer of snow on top of the ice and a layer of algae in the bottom 0.02 m of the ice. The following attenuation coefficients for PAR were used for dry snow, interior white ice, and sea ice algae:  $K_{\text{d snow}} = 21.4 \text{ m}^{-1}$ ,  $K_{\text{d ice}} = 1.59 \text{ m}^{-1}$ , and  $K_{\text{d algae}} = 10.0 \text{ m}^{-1}$ . Irradiance ( $E_0$ ) ( $\mu\text{Ein m}^{-2} \text{ s}^{-1}$ ) at the top of a particular layer (either snow, ice, or algae) was transmitted through that layer according to Beer’s Law as

$$E_z = E_0 e^{-K_d z} \quad (3.2)$$

where  $z$  is the layer thickness and  $K_d$  is the attenuation coefficient for that layer. Light is propagated first through the snow layer, then the sea ice, and finally the algal layer at the

bottom of the ice. A snow depth of 0.07 m was used for the model to represent early season pre-bloom conditions, prior to additional snow accumulation on the ice during spring, as we observed during SUBICE. The thickness of sea ice (1.12 m) and the algal layer beneath the ice (0.02 m) were chosen to represent the field conditions observed during SUBICE, as in Section 3.2.2.

Light transmission through the water column was calculated at 1 m depth intervals using and attenuation coefficient ( $K_{d \text{ water}}$ ) ( $\text{m}^{-1}$ ) that was calculated as a function of Chl  $a$  concentration as

$$K_{d \text{ water}} = 0.04 + 0.05 \times \text{Chl } a^{0.681}. \quad (3.3)$$

### Simulating advection of waters beneath sea ice and open water leads

To account for the advection of water through an ice cover of a given lead fraction, the model assumes a 24-hour daily cycle at a fixed location with alternating periods of ice and open water. Leads were simulated as hourly increments of open water within the sea ice, with each hour corresponding to a lead width of  $\sim 0.4$  km for the advection of waters at a speed of  $0.105 \text{ m s}^{-1}$ . For example, 100% ice concentration was simulated as a daily cycle with 24 hrs of sea ice and zero hrs of open water, while  $\sim 92\%$  ice concentration was simulated as a daily cycle with 22 hrs of sea ice and two hrs of open water. Variation in total light transmitted into the water column due to the time of day of the leads and the lead interval size (e.g. two consecutive hours of open water simulating one large lead versus two separate hours of open water simulating two smaller leads) was controlled by randomly distributing the hours when leads were present over the daily cycle and running 50,000 simulations for each lead fraction. This strategy was designed to approximate realistic conditions in which phytoplankton are advected beneath leads of varying size and at varying times of day relative to solar noon. For each simulated daily cycle of sea ice and leads, PAR was transmitted through snow, ice, and algae during intervals of sea ice and through open water during lead intervals, as described in Section 3.2.3.

### Calculations of GPP and $Z_{\text{cr}}$ at varied lead fractions

For each daily cycle of sea ice and leads, the simulated PAR in the water column was used to estimate GPP at each depth using the mean P-E parameters for under-ice phytoplankton and Equation 3.1, as in Section 3.2.2. Daily GPP ( $\text{mg C m}^{-3} \text{ d}^{-1}$ ) was calculated assuming

a uniformly low phytoplankton abundance ( $0.1 \text{ mg Chl } a \text{ m}^{-3}$ ) to represent pre-bloom conditions. This value was equivalent to the minimum concentration measured in the upper 20 m of the water column during the SUBICE early season field sampling. Daily GPP profiles at each station were computed from the means and standard deviations of all model combinations for each lead fraction. For the  $Z_{\text{eu}}$  calculation we used the lower respiration estimate ( $4.4 \text{ mg C m}^{-3} \text{ d}^{-1}$ ; Section 3.2.2) to represent pre-bloom conditions. Results of the model are used to provide context for the field data and investigate the controls on early season development of under-ice phytoplankton blooms.

### 3.3 Results

#### 3.3.1 Physical environment

##### Sea ice cover

The Chukchi Sea was characterized by extensive sea ice cover with leads of open water during our early season sampling period in May–June 2014. While sea ice concentrations were high at all 72 stations, with a mean of  $95.5 \pm 3.6\%$  (Fig. 3.3A), there was regional variation in the abundance of sea ice leads (Fig. 3.3A). The eastern stations had the highest sea ice concentrations (95–100%) and therefore the fewest leads, while the central and southern stations had relatively lower sea ice concentrations (84–95%) with more open water leads. There were 24 stations with 98–100% ice cover, which we refer to as fully consolidated sea ice. Observations from the bridge and field measurements during ice stations indicated that the dominant type of ice was first-year sea ice that had formed during the previous winter. Based on the seven ice stations that were sampled over the date range of this analysis, first-year sea ice thickness ranged from 0.43 to 1.50 m, with an average thickness of  $1.12 \pm 0.37$  m. Snow depth on first-year sea ice ranged from 0.05 to 0.15 m, with an average depth of  $0.09 \pm 0.04$  m. The bottom 0.02 m of the sea ice frequently harbored a layer of sea ice algae, as described by *Selz et al.* [in prep]. There were no melt ponds on the sea ice during our sampling period. Frequent refreezing of open water leads (as illustrated in Fig. 3.1C) was visually observed during the cruise and was consistent with the cold air temperatures (e.g.  $-5$  to  $-7^\circ\text{C}$ ) during the spring sampling period.

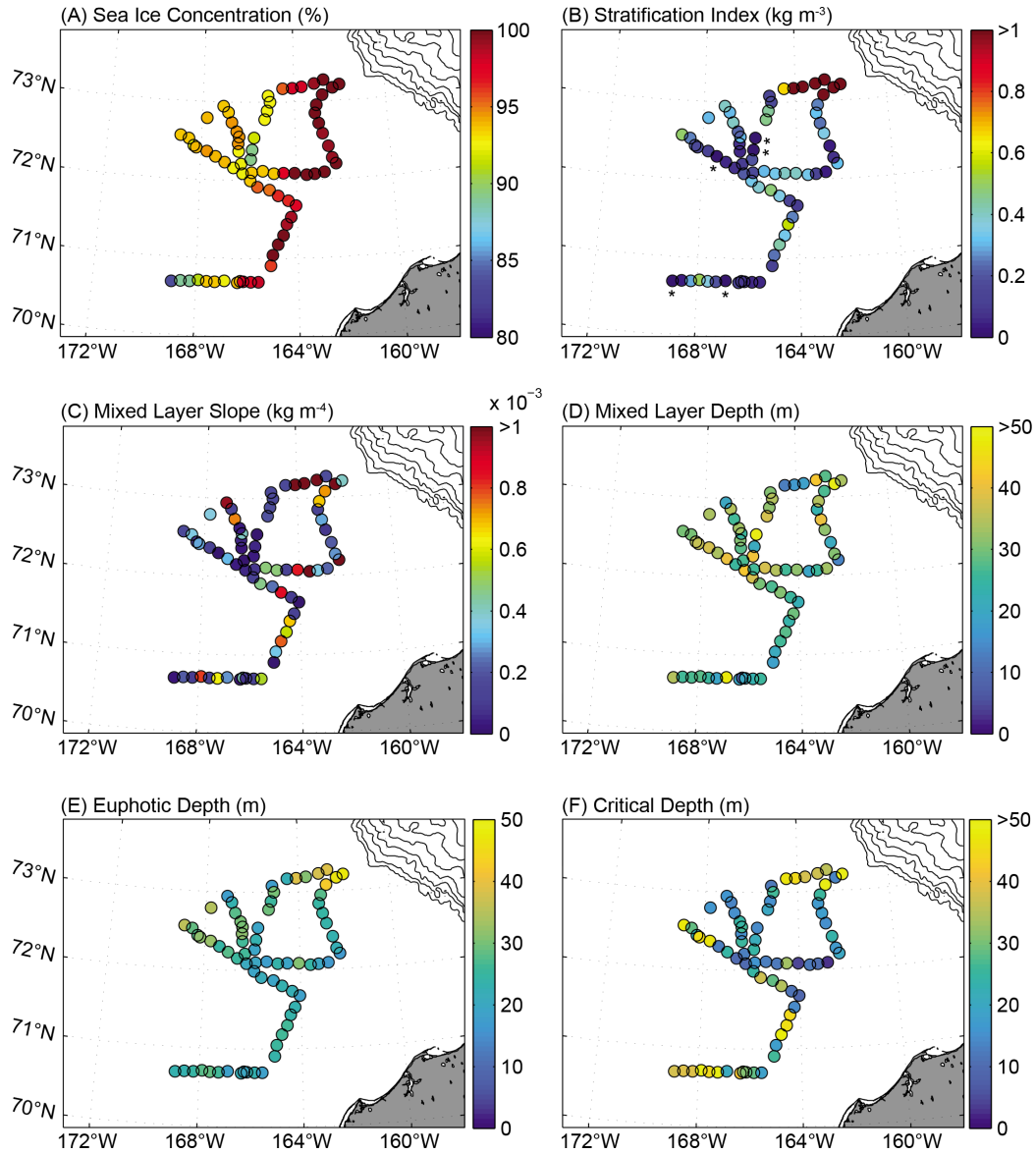


Figure 3.3: Maps of physical properties at each station in the Chukchi Sea, including (A) Sea Ice Concentration (%), (B) Stratification Index ( $\text{kg m}^{-3}$ ), (C) Mixed Layer Slope ( $\text{kg m}^{-4}$ ), (D) Mixed Layer Depth (MLD) (m), (E) Euphotic Depth (ED), and (F) Critical Depth ( $Z_{cr}$ ) (m). Bathymetric contours are displayed on 500 m intervals from 500 m to 3500 m. Fully overturned stations are defined by stratification index  $\leq 0.01 \text{ kg m}^{-3}$  and marked with asterisks on (B).

### Hydrography and water column structure

The shallow water column of the Chukchi Sea consisted almost exclusively of near-freezing WW. The mean  $\theta$  across all 72 stations and over all depths was  $-1.71 \pm 0.05^\circ\text{C}$ , with a range of  $-1.78$  to  $0.09^\circ\text{C}$ . The mean salinity for these waters was  $32.1 \pm 0.54$ , with a range of 30.4–34.6. Potential density ranged from 24.4 to  $27.8 \text{ kg m}^{-3}$  with a mean of  $25.8 \pm 0.5 \text{ kg m}^{-3}$ . Hydrographic sections of water mass properties are presented in Section 3.3.3.

Based on the structure of the water column during the spring sampling period, the Chukchi Sea was characterized as a weakly stratified two-layer system, with an upper mixed layer and a bottom boundary layer separated by an interface. The stratification index (defined in Section 3.2.2 as the difference in density over the vertical range of the interface) was very low for waters on the shelf (Fig. 3.3B), revealing that much of the Chukchi Sea was poised for overturning of the water column at the time of sampling. The water column was completely overturned by vertical mixing at five stations where the stratification index was  $< 0.01 \text{ kg m}^{-3}$  (marked by asterisks in Fig. 3.3B). These stations were in sharp contrast to the highly stratified northeastern outer shelf stations, where stratification indices ranged from 0.68 to  $3.2 \text{ kg m}^{-3}$ . With the exception of these eight northeastern stations, the mean stratification index was only  $0.23 \pm 0.15 \text{ kg m}^{-3}$ . In general, the eastern and northern stations were more strongly stratified, while the central and southern stations were more weakly stratified, with the stratification index following a similar spatial pattern to that of lead fraction (Fig. 3.3B).

The ML slope, which is a measure of the stratification within the upper mixed layer (Fig. 3.3C), similarly demonstrated weak stratification in many locations. The mean ML slope was  $0.45 \pm 0.71 \times 10^{-3} \text{ kg m}^{-4}$ . Upper mixed layers were most strongly stratified in the northeastern outer shelf waters and most weakly stratified in the central and southern stations, following a similar spatial pattern to stratification index (Fig. 3.3C) and the inverse of sea ice concentration (Fig. 3.3B). MLD ranged from 8 to 60 m, with a mean of  $30 \pm 9.1 \text{ m}$  (Fig. 3.3D). At the five fully overturned stations, the MLD extended to the seafloor. Relatively shallow MLDs (e.g.  $< 25 \text{ m}$ ) were generally found in the southeastern stations, while deeper MLDs (e.g.  $> 25 \text{ m}$ ) were found at many of the central, northern, and western stations. A further description of the hydrographic conditions of the Chukchi Sea during the SUBICE field program is presented in *Pacini et al.* (2016).

### Euphotic depth and critical depth

$Z_{\text{eu}}$  in the Chukchi Sea ranged from 17 to 47 m (Fig. 3.3E). The  $Z_{\text{eu}}$  range was smaller than that of MLD, and the mean  $Z_{\text{eu}}$  ( $26 \pm 6.6$  m) was  $\sim 4$  m shallower than the mean MLD. Stations with the deepest  $Z_{\text{eu}}$  were at the northeastern outer shelf, while the shallowest were at the southern, central, and southeastern stations.  $Z_{\text{cr}}$  ranged from 3 to 64 m (Fig. 3.3E). There were eight stations where the  $Z_{\text{cr}}$  exceeded the bottom depth. The mean  $Z_{\text{cr}}$  ( $26 \pm 14$  m) was roughly equal to the mean  $Z_{\text{eu}}$  and  $\sim 4$  m shallower than the mean MLD.  $Z_{\text{cr}}$  was deepest in the southern and outer shelf stations and shallowest in the central shelf stations. For the remainder of this analysis, we consider the  $Z_{\text{cr}}$  rather than the  $Z_{\text{eu}}$ , as the  $Z_{\text{cr}}$  is a more relevant measure for phytoplankton growth than the  $Z_{\text{eu}}$  in ice-covered waters.

### 3.3.2 Nutrients, phytoplankton, and productivity

Nutrient concentrations were very high throughout the Chukchi Sea, consistent with the widespread presence of near-freezing winter water, which is generally rich in nutrients. Based on the 387 discrete water column nutrient measurements, the mean  $\text{NO}_3^-$  concentration was  $11.2 \pm 3.58$   $\mu\text{mol L}^{-1}$ , with values ranging from 0.42 to  $17.0$   $\mu\text{mol L}^{-1}$ . Concentrations of  $\text{PO}_4^{3-}$  and  $\text{Si}(\text{OH})_4$  were also very high, with means of  $1.77 \pm 0.32$   $\mu\text{mol L}^{-1}$  and  $44.2 \pm 12.7$   $\mu\text{mol L}^{-1}$ , respectively. Within the upper mixed layer, the mean  $\text{NO}_3^-$  concentration was  $10.9 \pm 3.70$   $\mu\text{mol L}^{-1}$ . These extremely high nutrient concentrations indicate that phytoplankton growth was not limited by nutrients.

Despite the high nutrient concentrations, phytoplankton biomass was relatively low at most stations. The mean water column Chl *a* concentration across all samples was  $0.40 \pm 0.38$   $\mu\text{g L}^{-1}$ . The mean ML Chl *a* concentration was  $0.46 \pm 0.36$   $\mu\text{g L}^{-1}$ , ranging from 0.13 to  $1.88$   $\mu\text{g Chl } a \text{ L}^{-1}$ . Concentrations of POC and PON were also low, with mean values of  $3.9 \pm 1.5$   $\mu\text{g L}^{-1}$  and  $0.53 \pm 0.24$   $\mu\text{g L}^{-1}$  ( $N = 210$ ), respectively. Consistent with the low phytoplankton biomass, the water column was generally undersaturated in  $\text{O}_2$ , with a mean  $\text{O}_2$  saturation of  $87.2 \pm 5.66\%$  (ranging from 76.1 to 104%). On average, phytoplankton were not very physiologically active, with a mean Fv:Fm across of  $0.31 \pm 0.12$  ( $N = 99$ ) and a range of 0.02–0.54.

The photosynthetic parameters used to estimate GPP for under-ice phytoplankton were:  $P_m^* = 4.41 \pm 2.19$   $\text{mg C mg}^{-1} \text{ Chl } a \text{ hr}^{-1}$  and  $\alpha^* = 0.106 \pm 0.068$   $\text{mg C mg}^{-1} \text{ Chl } a \text{ hr}^{-1}$  ( $\mu\text{Ein m}^{-2} \text{ s}^{-1}$ ) $^{-1}$  ( $N = 7$ ). The corresponding  $E_K$  was  $59.4 \pm 52.9$   $\mu\text{Ein m}^{-2} \text{ s}^{-1}$ . For

reference, estimates of depth-integrated GPP at each station ranged from 0.03 to 0.86 g C m<sup>-2</sup> d<sup>-1</sup>, with a mean of 0.20±0.14 g C m<sup>-2</sup> d<sup>-1</sup>. After subtracting community respiration at each depth, the resulting estimated depth-integrated NCP ranged from -1.14 to 0.65 g C m<sup>-2</sup> d<sup>-1</sup>, with a mean of -0.15±0.21 g C m<sup>-2</sup> d<sup>-1</sup>. These under-ice production estimates illustrate that community respiration exceeded gross primary production throughout much of the region during our early season sampling period.

### 3.3.3 Hydrographic sections

To illustrate controls on under-ice phytoplankton blooms in the spring, we present hydrographic sections of physical and biological properties. We divided the transects into three categories based on phytoplankton biomass: three transects with active under-ice phytoplankton blooms, two with low phytoplankton biomass, and two with developing under-ice blooms. For each transect, hydrographic and biogeochemical data are presented along with sea ice concentration, stratification index, MLD, and  $Z_{cr}$  at each station.

#### Phytoplankton blooms beneath fully consolidated sea ice

Of the three under-ice bloom transects we sampled, the most intense phytoplankton bloom was located on the Hanna Ridge transect. This section extended northeast to southwest and was sampled 22–23 May 2014 (Fig. 3.4A). Fully consolidated sea ice covered most stations, with 100% ice concentration at all but the northernmost and southernmost endpoints (St. 41 and 34) that had a 96–97% ice concentration (Fig. 3.4B). The stratification index (Fig. 3.4B) was very low (0.10–0.12 kg m<sup>-3</sup>) at the endpoints and higher (0.25–0.57 kg m<sup>-3</sup>) at the interior stations with 100% ice cover. ML slope (refer to Fig. 3.3C) followed the same pattern, with values as high as  $0.8 \times 10^{-3}$  kg m<sup>-4</sup> beneath the fully consolidated ice, indicating relatively high stratification within the upper mixed layer. As with most of the region, the water column was composed entirely of near-freezing WW ( $\theta \leq -1.6^\circ\text{C}$ ) (Fig. 3.4C). Consistent with measurements of stratification index and ML slope, the salinity and density through the water column were more uniform at the endpoints, while the interior stations were characterized by more vertical variation in salinity and density (Fig. 3.4D). Nutrient concentrations were extremely high throughout the water column, with a range of ~13–17  $\mu\text{mol NO}_3^- \text{ L}^{-1}$  (Fig. 3.4E). The highest concentrations of Chl *a* were found within the upper 10 m of the interior stations (particularly St. 40–38), with values of ~1–3  $\mu\text{g L}^{-1}$  demonstrating the presence of a ~60 km wide under-ice phytoplankton bloom in the more

stratified waters beneath the fully consolidated sea ice (Fig. 3.4F). At these stations, the bloom extended to the MLD ( $\sim 25$  m; purple dotted line), while the  $Z_{cr}$  (grey dotted line) was nearly twice as deep, extending beyond the seafloor ( $> 45$  m; Fig. 3.4F). Oxygen was undersaturated throughout the water column but highest ( $\sim 90\%$ ) in the phytoplankton bloom center (Fig. 3.4G). Fv:Fm was also highest in the phytoplankton bloom, with values  $> 0.45$  extending to the MLD ( $\sim 25$  m; Fig. 3.4H). Phytoplankton biomass was lowest at the endpoint stations that were weakly stratified and had more open water leads (i.e. 3–4% concentration).

A second under-ice phytoplankton bloom was observed nearly a week later (28–30 May 2014) along the Hanna Shoal North transect, which extended south from the northern outer shelf to Hanna Shoal (Fig. 3.5A). This transect was also located in fully consolidated sea ice (99–100%; Fig. 3.5B). The stratification index was extremely high at the two outer shelf stations ( $\sim 1$ – $3$  kg m $^{-3}$ ; St. 82–81) and low to moderate ( $\sim 0.05$ – $0.35$  kg m $^{-3}$ ) across the rest of the transect (Fig. 3.5B). Sections of  $\theta$  and salinity (Figs. 3.5C–D) and density contours illustrate that stations in the center of the transect (St. 79–75) were fairly uniform hydrographically. Nutrient concentrations were high (9–13  $\mu\text{mol NO}_3^- \text{ L}^{-1}$ ) at most stations (Fig. 3.5E), although some of the lowest concentrations of  $\text{NO}_3^-$  ( $\sim 1.0$   $\mu\text{mol L}^{-1}$ ) we observed were located at the outer shelf stations due to exchange with a different water mass. Chl *a* concentrations were  $> 0.5$   $\mu\text{g L}^{-1}$  in the upper 10 m except for at St. 77. A phytoplankton bloom ( $\sim 1.5$   $\mu\text{g Chl } a \text{ L}^{-1}$ ;  $\sim 30$  km wide) was present at St. 81 (Fig. 3.5F), where the MLD (27 m) was 2.4-fold shallower than the  $Z_{cr}$  (64 m). There was also enhanced phytoplankton biomass at St. 74, where MLD shoaled to 14 m, above the  $Z_{cr}$  (20 m). Oxygen was undersaturated except for in the relatively warmer, lower nutrient, outer shelf waters (up to 103%) (Fig. 3.5G). Relatively high oxygen saturations ( $> 90\%$ ) and Fv:Fm ( $> 0.4$ ; Fig. 3.5H) were measured at the stations harboring phytoplankton blooms.

The Central Shelf transect, which was sampled immediately after the Hanna Shoal North transect (30 May–2 June 2014), extended southwest from the outer shelf waters to the central Chukchi shelf (Fig. 3.6A). The northern half of the transect contained fully consolidated sea ice with very few leads (98–100% ice concentration) and was very highly stratified (index:  $\sim 1$ – $3$  kg m $^{-3}$ ), while the southern stations were characterized by  $\sim 10\%$  open water leads (89–92% ice concentration) and much weaker stratification (Fig. 3.6B), with a fully overturned water column at St. 96 and 97 (recall Fig. 3.3B). Sections of  $\theta$  and salinity (Figs. 3.6C–D) along with density contours reveal that hydrography in the southern half of the transect

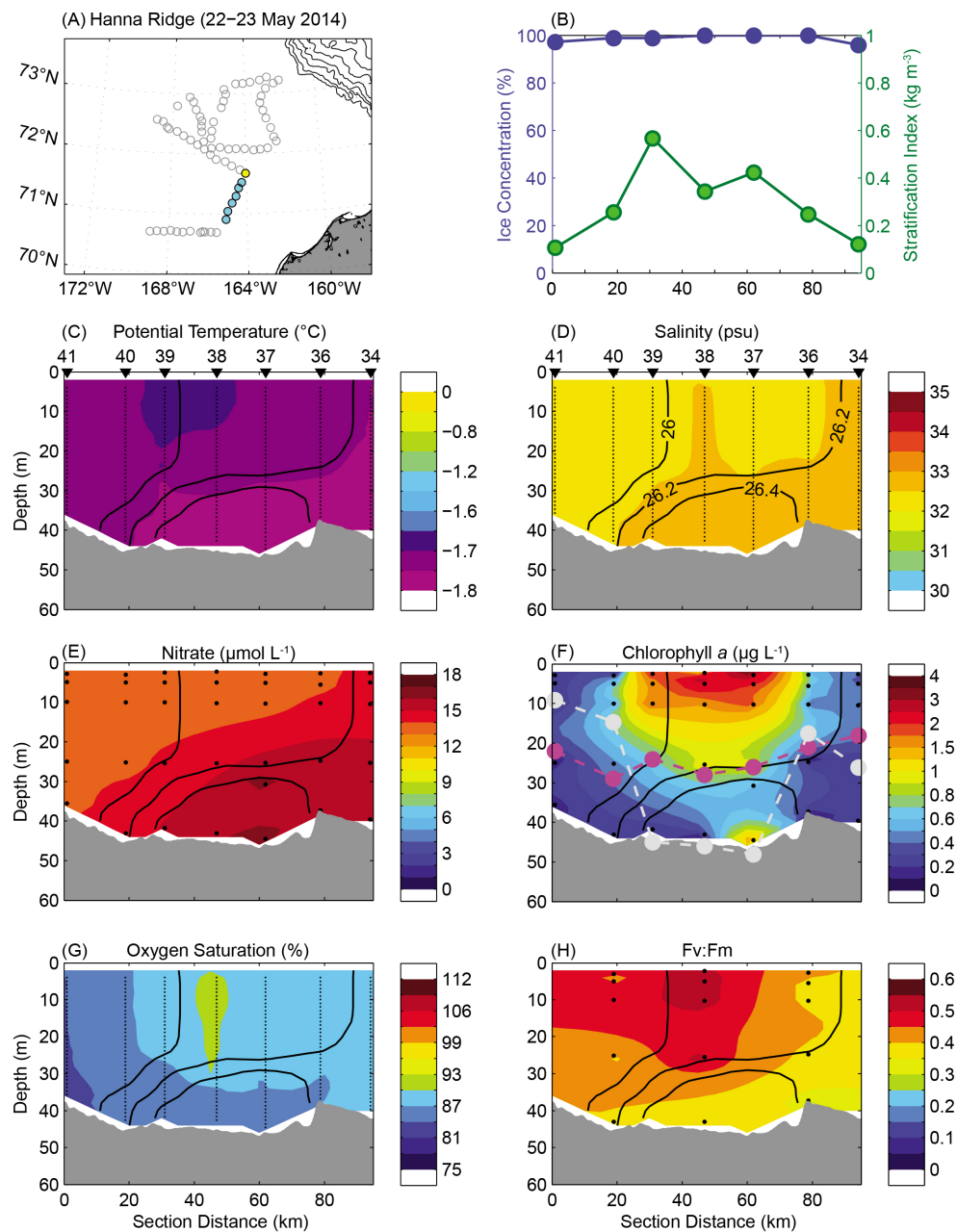


Figure 3.4: Hydrographic sections for the Hanna Ridge transect, sampled 22–23 May 2014. (A) Map illustrating the transect location, with the first station of the section marked in yellow. (B) Sea ice concentration (%) and stratification index ( $\text{kg m}^{-3}$ ) at each station along the section. (C)  $\theta$  ( $^{\circ}\text{C}$ ) with station labels. (D) Salinity (psu) with labeled potential density contours ( $\text{kg m}^{-3}$ ) and station labels. (E)  $\text{NO}_3^-$  concentration ( $\mu\text{mol L}^{-1}$ ). (F) Chl *a* concentration ( $\text{mg L}^{-1}$ ) overlain with MLD (magenta dotted line) and  $Z_{\text{cr}}$  (grey dotted line). (G)  $\text{O}_2$  saturation (%). (H) Fv:Fm.

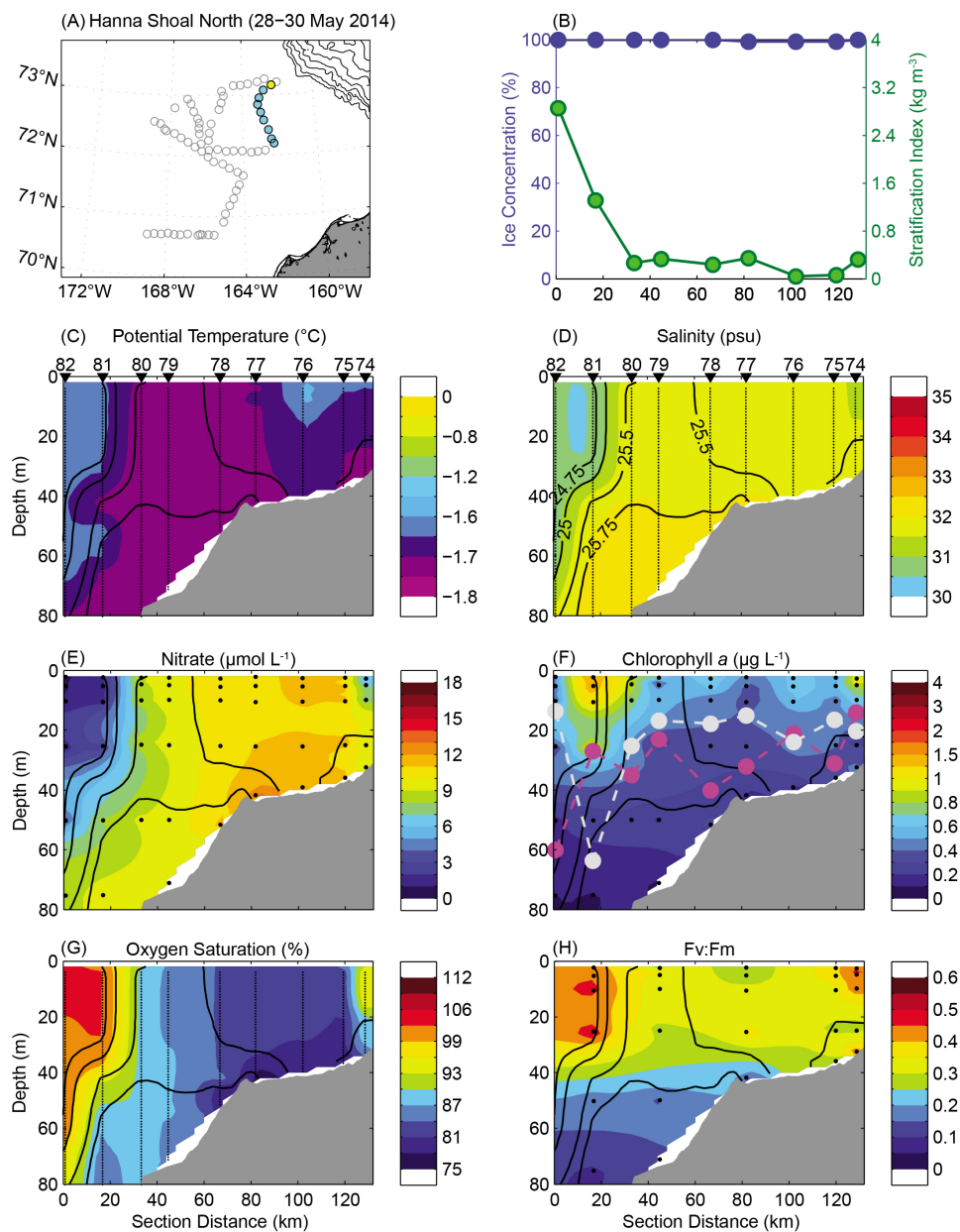


Figure 3.5: Hydrographic sections for the Hanna Shoal North transect, sampled 28–30 May 2014. (A) Map illustrating the transect location, with the first station of the section marked in yellow. (B) Sea ice concentration (%) and stratification index ( $\text{kg m}^{-3}$ ) at each station along the section. (C)  $\theta$  ( $^{\circ}\text{C}$ ) with station labels. (D) Salinity (psu) with labeled potential density contours ( $\text{kg m}^{-3}$ ) and station labels. (E)  $\text{NO}_3^-$  concentration ( $\mu\text{mol L}^{-1}$ ). (F) Chl *a* concentration ( $\text{mg L}^{-1}$ ) overlain with MLD (magenta dotted line) and  $Z_{\text{cr}}$  (grey dotted line). (G)  $\text{O}_2$  saturation (%). (H) Fv:Fm. Note the increased scale for stratification index.

(St. 91–98) was vertically homogeneous, providing evidence of enhanced convective mixing beneath the sea ice with higher lead fraction relative to the fully consolidated sea ice. Similar to the Hanna Shoal North transect, nutrient concentrations were high on the central shelf ( $9\text{--}14 \mu\text{mol NO}_3^- \text{ L}^{-1}$ ) and low ( $> 0.4 \mu\text{mol NO}_3^- \text{ L}^{-1}$ ) on the outer shelf (Fig. 3.6E). An under-ice phytoplankton bloom ( $\sim 1 \mu\text{g Chl } a \text{ L}^{-1}$ ) extended  $\sim 80$  km beneath the fully consolidated sea ice (St. 83–89) and was located in waters with shallow MLDs relative to the  $Z_{\text{cr}}$ , while waters beneath the more loosely consolidated sea ice contained lower phytoplankton biomass ( $\sim 0.3 \mu\text{g Chl } a \text{ L}^{-1}$ ) and had deeper MLDs relative to the shallower  $Z_{\text{cr}}$  (Fig. 3.6F). Oxygen (Fig. 3.6G) was near saturation (96–103%) in the bloom waters, highest (104%) at the outer shelf waters, and undersaturated at the remaining stations, similar to the Hanna Shoal North transect. Fv:Fm (Fig. 3.6H) was highest ( $\sim 0.5$ ) in waters characterized by the bloom and lowest ( $\sim 0.3$ ) at St. 96 and St. 97 where the water column was fully overturned.

### Low biomass in loosely consolidated sea ice with leads

Phytoplankton biomass was low (e.g.  $0.2\text{--}0.4 \mu\text{g Chl } a \text{ L}^{-1}$ ) along the Chukchi Northwest and Hanna Shoal West transects. The Chukchi Northwest transect extended northwest to southeast and was sampled 24–25 May 2014 (Fig. 3.7A). As opposed to the under-ice bloom transects, there were leads of open water at all stations (92–94% ice concentration). The stratification index was relatively low ( $< 0.4 \text{ kg m}^{-3}$ ) across the transect, especially at the southernmost stations ( $0.05\text{--}0.1 \text{ kg m}^{-3}$ ) (Fig. 3.7B). The combination of vertically homogeneous hydrographic properties (Figs. 3.7C–D) with the low stratification indices in the loosely consolidated ice pack provide evidence of convective mixing. Despite the high nutrient concentrations ( $9\text{--}14 \mu\text{mol NO}_3^- \text{ L}^{-1}$ ) in the near-freezing WW, phytoplankton biomass was low ( $< 0.4 \mu\text{g Chl } a \text{ L}^{-1}$ ) and MLD exceeded the  $Z_{\text{cr}}$  at all stations except for St. 51, where MLD and  $Z_{\text{cr}}$  were approximately equal (Figs. 3.7E–F). Oxygen was undersaturated (76–92%) throughout the transect, and Fv:Fm was relatively low ( $< 0.4$ ) at most stations (Figs. 3.7G–H).

Similar features were observed along the Hanna Shoal West transect, which extended west to east from the central shelf of the Chukchi Sea and was sampled on 27–28 May 2014 (Fig. 3.8A). Leads of open water were present on the western half of the transect (96% ice concentration), while fully consolidated sea ice (100%) characterized the eastern stations. Similar to the previous transect, the stratification index was relatively low ( $< 0.4 \text{ kg m}^{-3}$ )

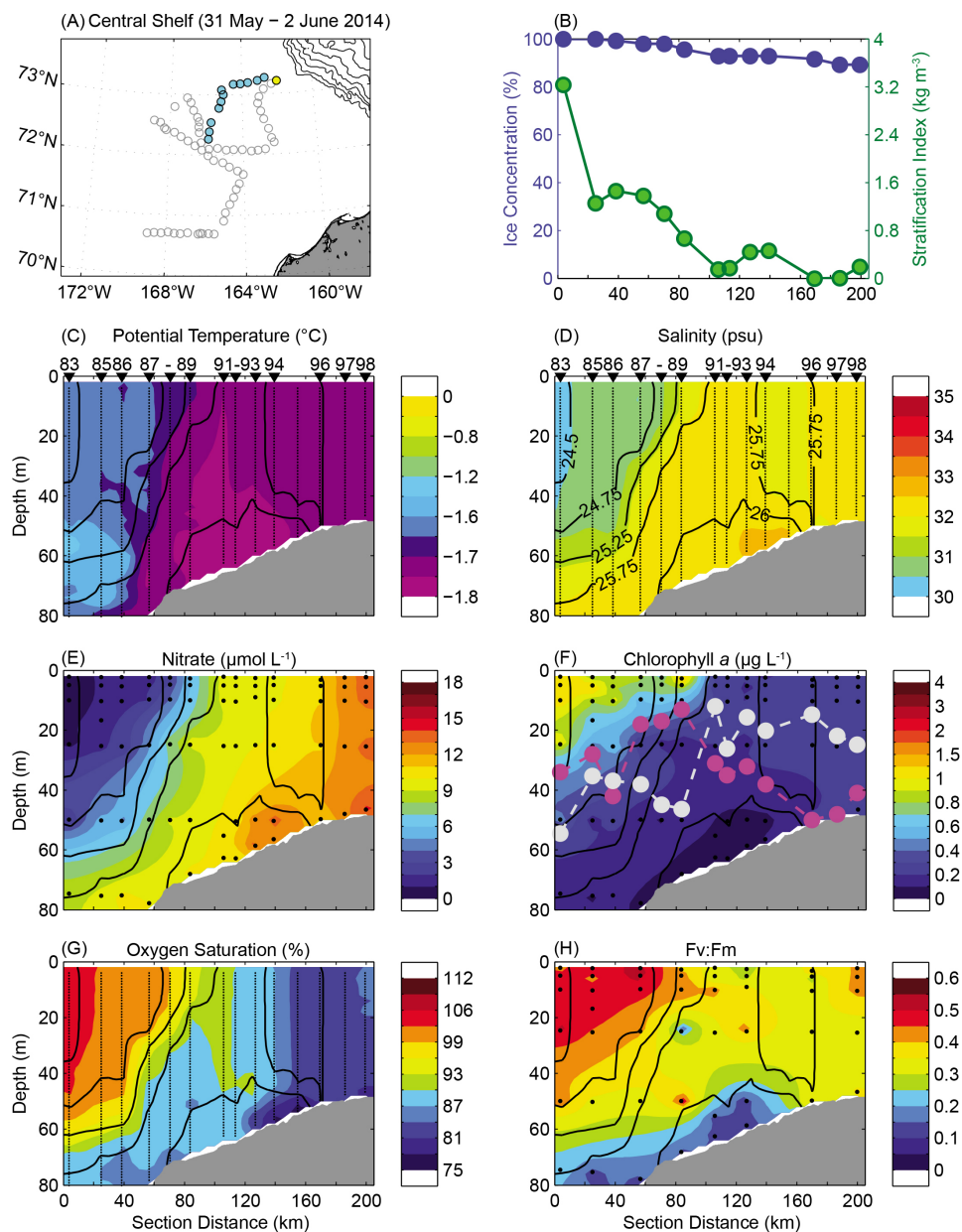


Figure 3.6: Hydrographic sections for the Central Shelf transect, sampled 30 May–2 June 2014. (A) Map illustrating the transect location, with the first station of the section marked in yellow. (B) Sea ice concentration (%) and stratification index ( $\text{kg m}^{-3}$ ) at each station along the section. (C)  $\theta$  ( $^{\circ}\text{C}$ ) with station labels. (D) Salinity (psu) with labeled potential density contours ( $\text{kg m}^{-3}$ ) and station labels. (E)  $\text{NO}_3^-$  concentration ( $\mu\text{mol L}^{-1}$ ). (F) Chl *a* concentration ( $\text{mg L}^{-1}$ ) overlain with MLD (magenta dotted line) and  $Z_{\text{cr}}$  (grey dotted line). (G)  $\text{O}_2$  saturation (%). (H) Fv:Fm. Note the increased scale for stratification index.

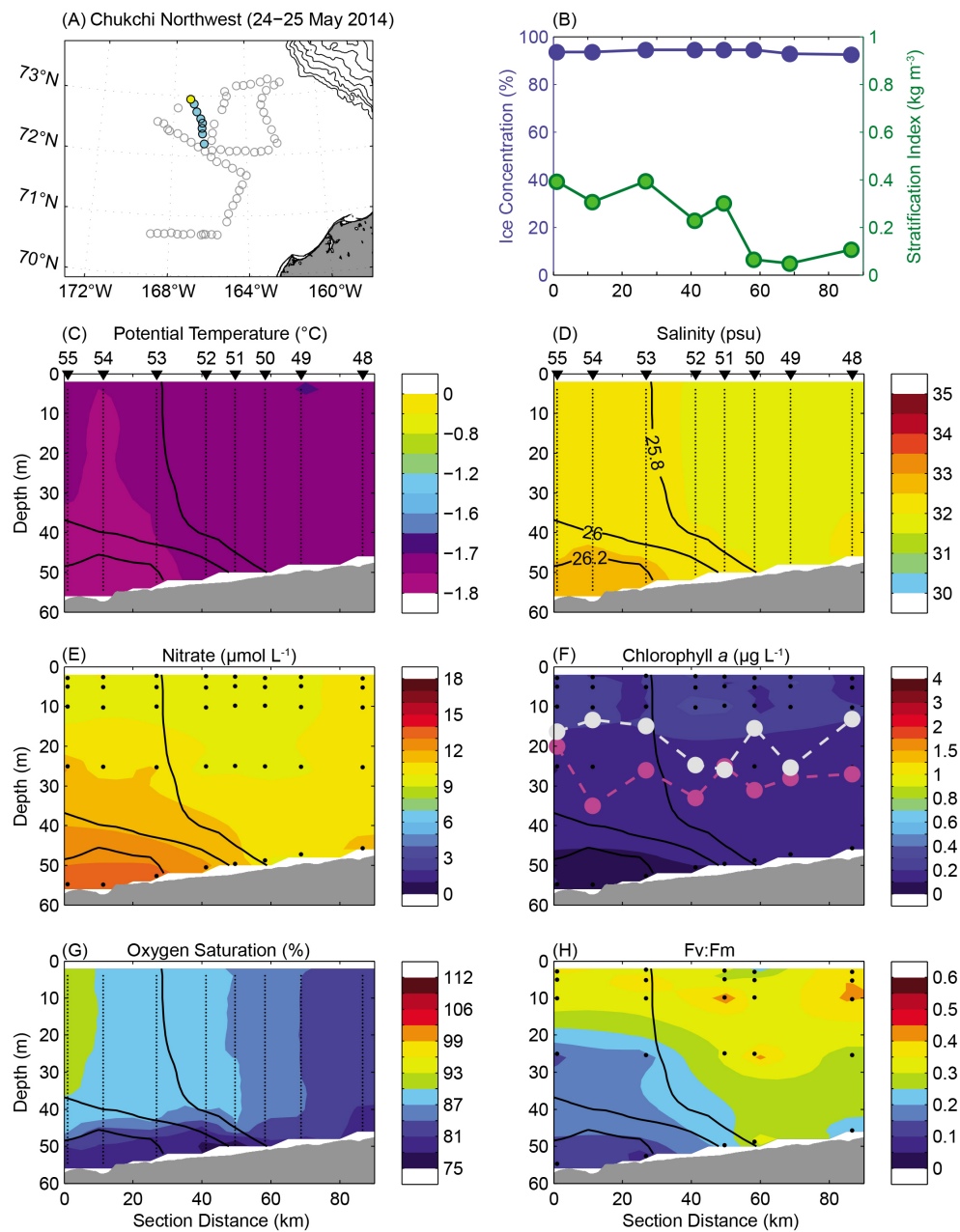


Figure 3.7: Hydrographic sections for the Chukchi Northwest transect, sampled 24–25 May 2014. (A) Map illustrating the transect location, with the first station of the section marked in yellow. (B) Sea ice concentration (%) and stratification index ( $\text{kg m}^{-3}$ ) at each station along the section. (C)  $\theta$  ( $^{\circ}\text{C}$ ) with station labels. (D) Salinity (psu) with labeled potential density contours ( $\text{kg m}^{-3}$ ) and station labels. (E)  $\text{NO}_3^-$  concentration ( $\mu\text{mol L}^{-1}$ ). (F) Chl *a* concentration ( $\text{mg L}^{-1}$ ) overlain with MLD (magenta dotted line) and  $Z_{\text{cr}}$  (grey dotted line). (G)  $\text{O}_2$  saturation (%). (H) Fv:Fm.

and hydrographic properties were fairly uniform with depth, especially in the upper 30 m (Figs. 3.8B–D). Despite an abundance of nutrients ( $9\text{--}14 \mu\text{mol NO}_3^- \text{ L}^{-1}$ ), phytoplankton biomass was low, with most Chl *a* concentrations  $< 0.4 \mu\text{g L}^{-1}$  (Fig. 3.8E–F). There was slightly higher Chl *a* at St. 70–71 and in the upper 5 m at St. 68, all which had higher ice concentrations than the western stations with lower biomass (St. 65–67). The MLD was deeper than the  $Z_{\text{cr}}$  at all but St. 68. Oxygen was undersaturated (78–94%) and Fv:Fm was relatively low (0.25–0.4) throughout the transect (Figs. 3.8G–H). Together, these sections of physical and biogeochemical properties from Hanna Shoal West and Chukchi Northwest transects illustrate examples of pre-bloom waters in loosely consolidated sea ice.

### Developing phytoplankton blooms in stratified and shallow waters

The final two transects (Central Channel and Chukchi North) demonstrated evidence of developing phytoplankton blooms. The Central Channel transect extended from west to east across the Central Channel flow pathway and was the first transect sampled on 18–19 May 2014 (Fig. 3.9A). The lowest ice concentrations of all stations were found along the western half of this transect (84–94%), and the stratification index was very low ( $< 0.2 \text{ kg m}^{-3}$ ) at all but three stations (St. 12–14) (Fig. 3.9B). The water column was fully overturned at St. 10 and 16 (recall Fig. 3.3B), and hydrographic properties were fairly uniform with depth at most stations (Fig. 3.9C–D). Nutrient concentrations were extremely high (Fig. 3.9E), with the highest  $\text{NO}_3^-$  concentrations ( $\sim 17 \mu\text{mol L}^{-1}$ ) located in the fully overturned water column at St. 16, indicating that convective overturning at this station may have recently contributed to the input of additional nutrients from the seafloor. In contrast to other transects, phytoplankton biomass was greatest at St. 10 (Fig. 3.9F), which was fully overturned and had the greatest lead fraction ( $\sim 16\%$ ). High phytoplankton biomass at this well-mixed station was likely supported by the shallow bottom depth (38 m), which constrained the MLD to within the  $Z_{\text{cr}}$ . At other stations on the transect, phytoplankton biomass was higher under more consolidated sea ice (St. 18–22), signaling the early development of an under-ice bloom, and lower in the deeper waters beneath sea ice with leads (St. 11–16), consistent with previous transects (Fig. 3.9F). Oxygen was undersaturated (85–90%) throughout the water column (Fig. 3.9G). Fv:Fm was highest ( $> 0.4$ ) at the anomalously shallow station and beneath the fully consolidated sea ice (Fig. 3.9H) within the developing phytoplankton bloom waters.

The Chukchi North transect extended northwest to southeast across the Chukchi shelf

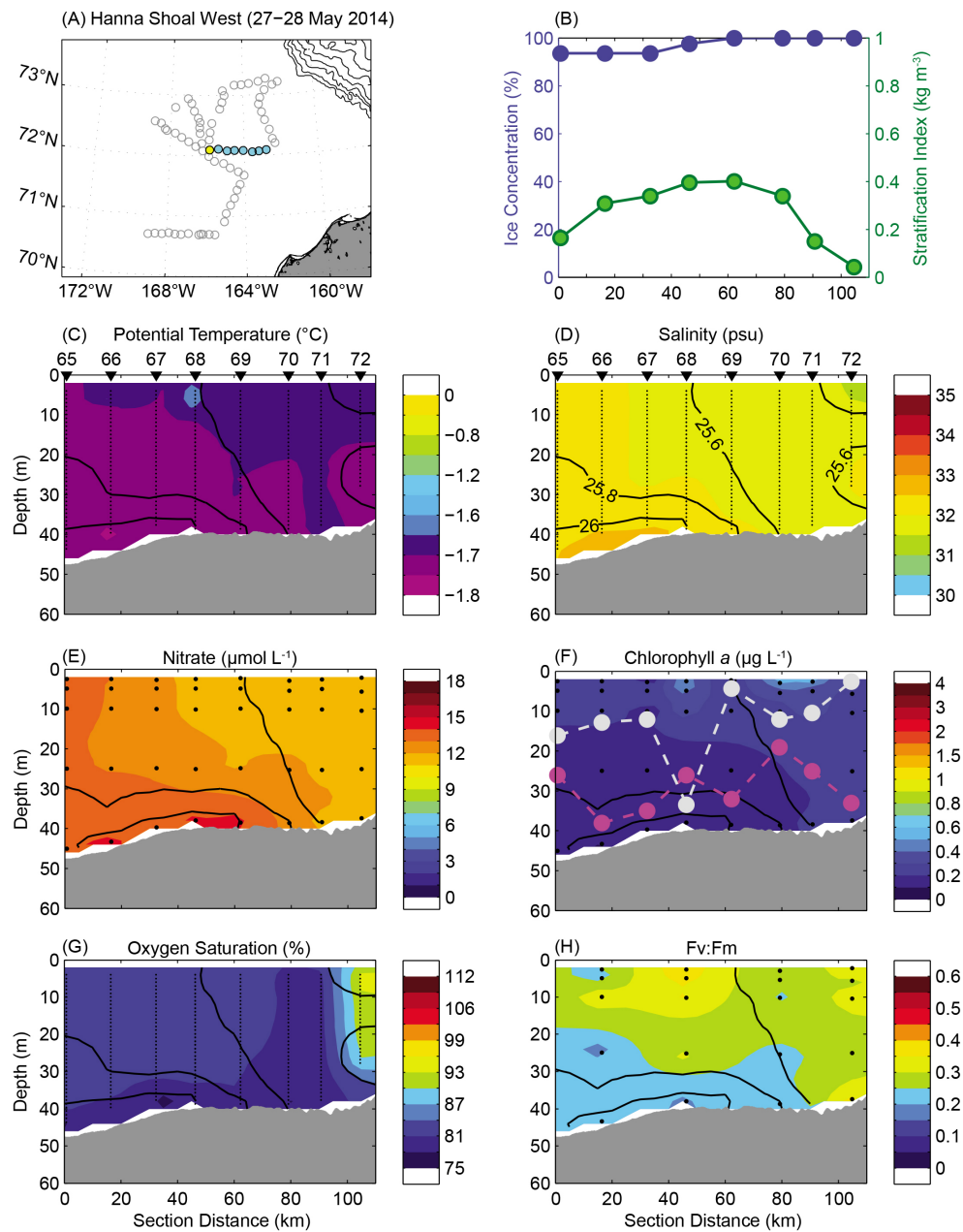


Figure 3.8: Hydrographic sections for the Hanna Shoal West transect, sampled 27–28 May 2014. (A) Map illustrating the transect location, with the first station of the section marked in yellow. (B) Sea ice concentration (%) and stratification index ( $\text{kg m}^{-3}$ ) at each station along the section. (C)  $\theta$  ( $^{\circ}\text{C}$ ) with station labels. (D) Salinity (psu) with labeled potential density contours ( $\text{kg m}^{-3}$ ) and station labels. (E)  $\text{NO}_3^-$  concentration ( $\mu\text{mol L}^{-1}$ ). (F) Chl *a* concentration ( $\text{mg L}^{-1}$ ) overlain with MLD (magenta dotted line) and  $Z_{\text{cr}}$  (grey dotted line). (G)  $\text{O}_2$  saturation (%). (H) Fv:Fm.

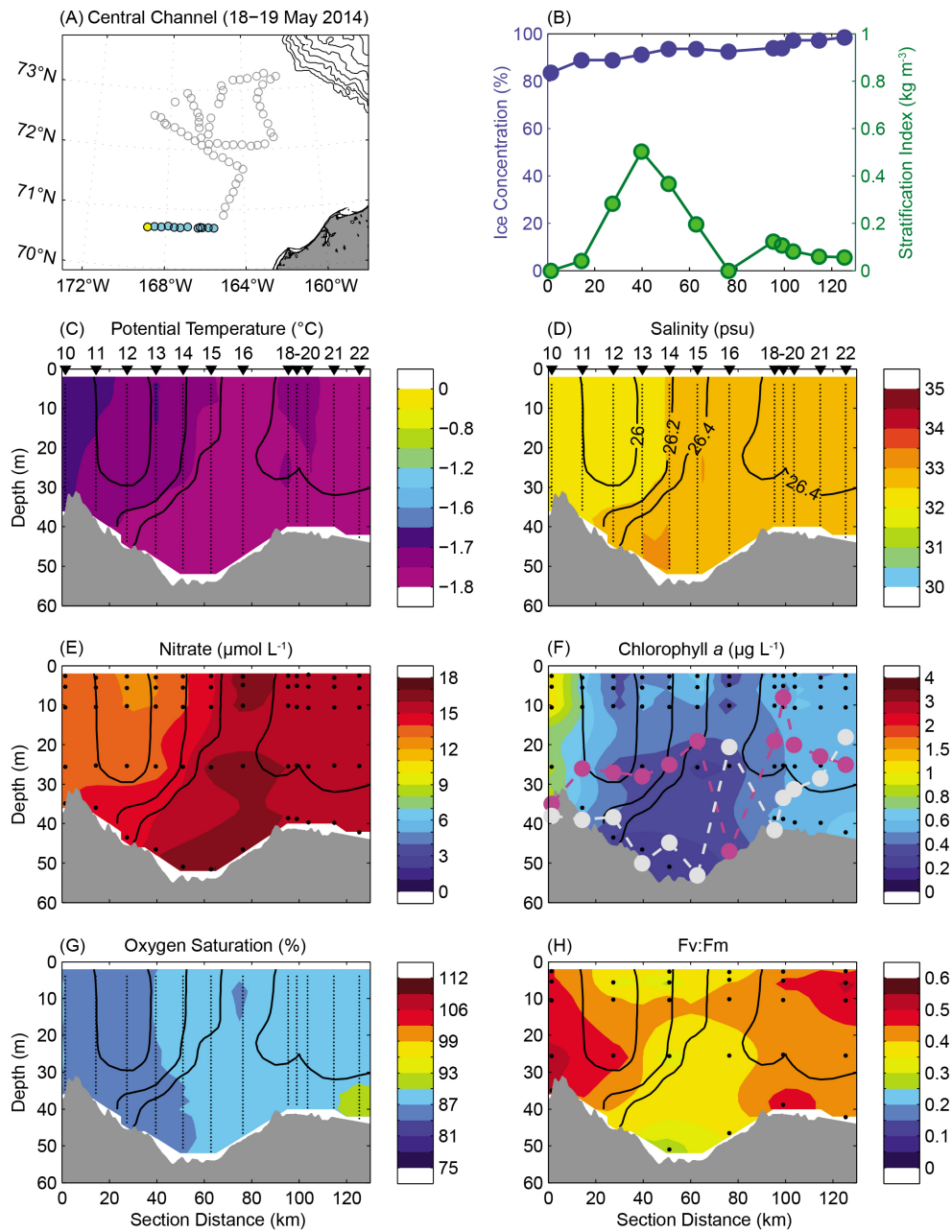


Figure 3.9: Hydrographic sections for the Central Channel transect, sampled 18–19 May 2014. (A) Map illustrating the transect location, with the first station of the section marked in yellow. (B) Sea ice concentration (%) and stratification index ( $\text{kg m}^{-3}$ ) at each station along the section. (C)  $\theta$  ( $^{\circ}\text{C}$ ) with station labels. (D) Salinity (psu) with labeled potential density contours ( $\text{kg m}^{-3}$ ) and station labels. (E)  $\text{NO}_3^-$  concentration ( $\mu\text{mol L}^{-1}$ ). (F) Chl *a* concentration ( $\text{mg L}^{-1}$ ) overlain with MLD (magenta dotted line) and  $Z_{\text{cr}}$  (grey dotted line). (G)  $\text{O}_2$  saturation (%). (H) Fv:Fm.

and was sampled 23–24 and 26–27 May 2014 (Fig. 3.10A). There were leads at all stations on the transect, with ice concentration ranging from 92–94%. The stratification index was variable across the transect, ranging from 0.0 to 0.5 kg m<sup>-3</sup> (Fig. 3.10B). Sections of  $\theta$  and salinity demonstrate that the upper 30 m of the water column was fairly uniform (Figs. 3.10C–D). Like the previous transect, nutrient concentrations were high throughout, while phytoplankton biomass was relatively low, oxygen was undersaturated, and Fv:Fm was low (Figs. 3.10E–H). The MLD ranged from 25 to 40 m and was deeper than the  $Z_{\text{cr}}$  at several stations. Elevated concentrations of Chl *a* ( $\sim 0.6 \mu\text{g L}^{-1}$ ) demonstrated that phytoplankton blooms were beginning to develop at two locations where the MLD was shallow relative to the  $Z_{\text{cr}}$  (St. 60–61 and St. 45–43; Fig. 3.10F), which also generally coincided with higher stratification indices. Together, these transects demonstrate that phytoplankton blooms begin to develop where the MLD is shallower than the  $Z_{\text{cr}}$ , which is more frequent in stratified waters beneath more consolidated sea ice and beneath open water leads in areas where mixing is constrained by shallow bottom depths.

### 3.3.4 Hydrographic and bio-physical relationships

#### Sea ice concentration, water column structure, and nutrients

Across all 72 stations, lead fraction was negatively correlated with stratification index and ML slope and positively correlated with MLD and ML  $\text{NO}_3^-$  (Table 3.1). These relationships indicate that waters beneath sea ice with leads were more weakly stratified with deeper and more homogeneous MLDs, as well as elevated nutrient levels. Stratification index was positively correlated with the ML slope (Table 3.1), confirming that the ML was also less stratified when the stratification index was weaker (i.e. more mixing). Lead fraction was also positively correlated with WC  $\text{NO}_3^-$  ( $R = 0.28$ ;  $p < 0.05$ ), indicating that the water column beneath ice with more leads contained more nutrients. Both stratification index and ML slope were inversely correlated with ML  $\text{NO}_3^-$  ( $R = -0.76$  and  $R = -0.49$ , respectively;  $p < 0.01$ ; Table 3.1) and WC  $\text{NO}_3^-$  concentrations ( $R = -0.52$  and  $R = -0.37$ , respectively;  $p < 0.01$ ), demonstrating that well-mixed water columns had higher nutrient content than more stratified waters. MLD was not significantly correlated with stratification index, ML slope, or ML  $\text{NO}_3^-$  (Table 3.1).

To illustrate how water column structure differed beneath fully consolidated sea ice and sea ice with leads, we compared properties at the 24 stations characterized by  $\geq 98\%$  ice

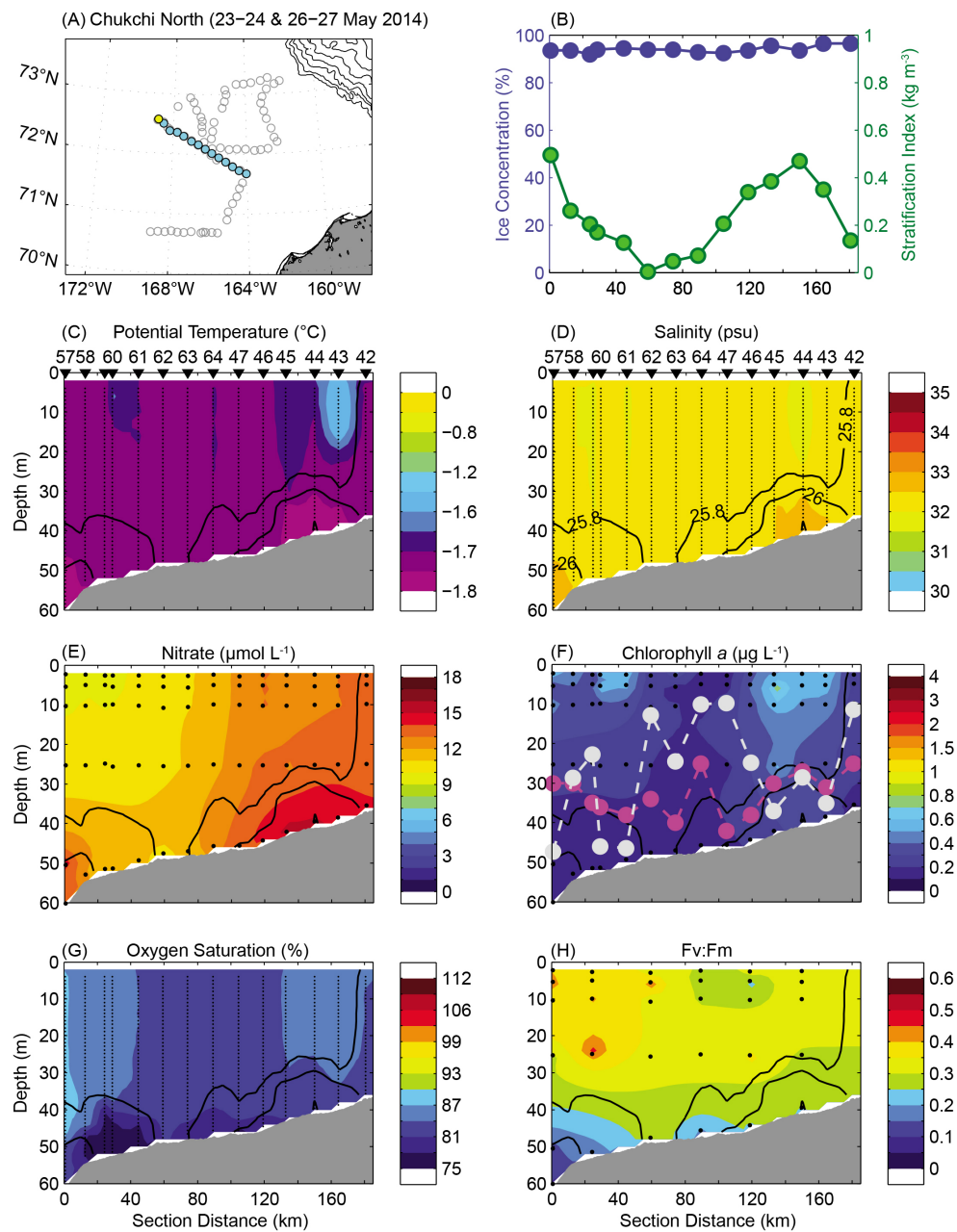


Figure 3.10: Hydrographic sections for the Chukchi North transect, sampled 23–24 May and 26–27 May 2014. (A) Map illustrating the transect location, with the first station of the section marked in yellow. (B) Sea ice concentration (%) and stratification index ( $\text{kg m}^{-3}$ ) at each station along the section. (C)  $\theta$  ( $^{\circ}\text{C}$ ) with station labels. (D) Salinity (psu) with labeled potential density contours ( $\text{kg m}^{-3}$ ) and station labels. (E)  $\text{NO}_3^-$  concentration ( $\mu\text{mol L}^{-1}$ ). (F) Chl  $a$  concentration ( $\text{mg L}^{-1}$ ) overlain with MLD (magenta dotted line) and  $Z_{\text{cr}}$  (grey dotted line). (G)  $\text{O}_2$  saturation (%). (H) Fv:Fm.

	Lead Frac. (%)	Strat. Index (kg m <sup>-3</sup> )	ML Slope (kg m <sup>-4</sup> )	MLD (m)	ML NO <sub>3</sub> <sup>-</sup> (μmol L <sup>-1</sup> )
Lead Frac. (%)	1.0	-	-	-	-
Strat. Index (kg m <sup>-3</sup> )	<b>-0.38**</b>	1.0	-	-	-
ML Slope (kg m <sup>-4</sup> )	<b>-0.35**</b>	<b>0.50**</b>	1.0	-	-
MLD (m)	<b>0.24*</b>	0.17	-0.12	1.0	-
ML NO <sub>3</sub> <sup>-</sup> (μmol L <sup>-1</sup> )	<b>0.33*</b>	<b>-0.76**</b>	<b>-0.49**</b>	-0.14	1.0

Table 3.1: Pearson’s correlation matrix demonstrating relationships between physical and environmental properties, including Lead fraction (defined as the inverse of sea ice concentration), Stratification Index, Mixed Layer (ML) Slope, Mixed Layer Depth (MLD), and mean ML NO<sub>3</sub><sup>-</sup>. Bold values indicate significance at  $p < 0.05$  (\*) and  $p < 0.01$  (\*\*) ( $N = 72$ ).

concentration with those at the 48 stations with lower ice concentration (84–98%). The mean stratification index was more than 3-fold greater ( $p < 0.01$ ) beneath the fully consolidated sea ice than beneath more loosely consolidated sea ice, with means of  $0.71 \pm 0.85$  kg m<sup>-3</sup> and  $0.22 \pm 0.16$  kg m<sup>-3</sup>, respectively. Similarly, the ML slope was more than 4-fold greater ( $p < 0.001$ ) beneath fully consolidated ice, with a mean of  $0.9 \pm 1.0 \times 10^{-3}$  kg m<sup>-4</sup>, as compared to  $0.2 \pm 0.2 \times 10^{-3}$  kg m<sup>-4</sup> beneath the loosely consolidated ice. These results support the notion that there is minimal vertical mixing beneath sea ice without leads, as is further discussed in Section 3.4.1.

### Environmental conditions and biological properties

ML Chl *a* was negatively correlated with lead fraction and MLD and positively correlated with stratification index (Table 3.2), confirming that higher phytoplankton biomass was located beneath more fully consolidated sea ice and in more stratified waters. Phytoplankton biomass was not correlated with ML NO<sub>3</sub><sup>-</sup>, consistent with the lack of nutrient limitation at the time of sampling, or with ML slope. Fv:Fm was positively correlated with stratification index (Table 3.2), demonstrating that phytoplankton were healthier in more stratified waters. Fv:Fm was not significantly correlated with lead fraction, ML slope, MLD, or ML NO<sub>3</sub><sup>-</sup>. O<sub>2</sub> saturation was negatively correlated with lead fraction and positively correlated

	Lead Frac. (%)	Strat. Index (kg m <sup>-3</sup> )	ML Slope (kg m <sup>-4</sup> )	MLD (m)	ML NO <sub>3</sub> <sup>-</sup> (μmol L <sup>-1</sup> )
ML Chl <i>a</i> (μg L <sup>-1</sup> )	<b>-0.36**</b>	<b>0.30*</b>	0.21	<b>-0.28*</b>	-0.13
ML Fv:Fm	-0.10	<b>0.38**</b>	0.14	-0.23	-0.28
ML O <sub>2</sub> Sat. (%)	<b>-0.29*</b>	<b>0.78**</b>	<b>0.50**</b>	-0.08	<b>-0.72**</b>
Z <sub>cr</sub> (m)	0.03	<b>0.33**</b>	0.17	<b>-0.24*</b>	-0.18

Table 3.2: Pearson’s correlation matrix demonstrating relationships between physical and environmental properties (see Table 3.1) and mean biological properties in the upper mixed layer (ML), including phytoplankton biomass (Chl *a*) ( $N = 72$ ), physiology (Fv:Fm) ( $N = 38$ ), and oxygen saturation (O<sub>2</sub> Sat.) ( $N = 72$ ), as well as critical depth (Z<sub>cr</sub>) ( $N = 72$ ). Bold values indicate significance at  $p < 0.05$  (\*) and  $p < 0.01$  (\*\*).

with stratification index and ML slope (Table 3.2), indicating that O<sub>2</sub> saturation was higher at more stratified stations with fewer open water leads. Z<sub>cr</sub> was positively correlated with stratification index and inversely correlated with MLD (Table 3.2), indicating that more stratified waters with shallower MLD had deeper Z<sub>cr</sub>. There was no relationship between Z<sub>cr</sub> and lead fraction, ML slope, or ML NO<sub>3</sub><sup>-</sup> (Table 3.2).

We also evaluated relationships between the ratio of Z<sub>cr</sub>:MLD and mean biological properties in the upper mixed layer to determine if conditions are more favorable for phytoplankton when this ratio is maximized. Consistent with observations, Z<sub>cr</sub>:MLD was positively correlated with Fv:Fm (0.53;  $p < 0.01$ ;  $N = 38$ ) and O<sub>2</sub> saturation ( $R = 0.42$ ;  $p < 0.01$ ;  $N = 72$ ). Z<sub>cr</sub>:MLD was not correlated with lead fraction, stratification index, or ML NO<sub>3</sub><sup>-</sup>. The correlation between Chl *a* and Z<sub>cr</sub>:MLD was omitted because Chl *a* was used to calculate Z<sub>cr</sub>.

### Under-ice phytoplankton response to environmental conditions

To assess how under-ice phytoplankton are influenced by the complex interactions between these physical and biogeochemical properties, we constructed a multiple linear regression model (Table 3.3), using log-transformed ML Chl *a* as the biological response variable. Lead fraction, stratification index, MLD, and ML NO<sub>3</sub><sup>-</sup> were assigned as environmental predictors. The model was statistically significant ( $R^2 = 0.31$ ;  $p < 0.001$ ), illustrating

Parameter	Estimate $\beta$	$p$ -value	Relative Importance (%)
Intercept	$-0.70 \pm 0.41$	0.09	
Lead Fraction (%)	$-0.04 \pm 0.02$	0.10	27.2%
Stratification Index ( $\text{kg m}^{-1}$ )	<b><math>0.53 \pm 0.19</math></b>	<b><math>&lt; 0.01</math></b>	<b>27.7%</b>
Mixed Layer Depth (m)	<b><math>-0.02 \pm 0.01</math></b>	<b><math>&lt; 0.01</math></b>	<b>39.0%</b>
Mixed Layer $\text{NO}_3^-$ ( $\mu\text{mol L}^{-1}$ )	$0.04 \pm 0.03$	0.17	6.1%

Table 3.3: Multiple linear regression parameter estimates ( $\pm$  standard error) and relative importance of environmental predictors in explaining the variance in log-transformed mean Chl  $a$  in the upper mixed layer ( $N = 72$  stations). Bold values indicate significance ( $p < 0.05$ ). Although the intercept was only significant at the 91% confidence interval, the model was significant at  $p < 0.001$  ( $R^2 = 0.31$ ).

that together these predictor variables explained 31% of the variance in ML Chl  $a$  across the 72 stations. The most important factor controlling phytoplankton biomass was MLD, which contributed 39.0% of the explained variance (Table 3.3). Stratification index and lead fraction were the next most important factors, contributing 27.7% and 27.2% of the explained variance, respectively, although lead fraction was statistically significant only at the 90% confidence interval (Table 3.3). The least important factor was ML  $\text{NO}_3^-$ , which contributed only 6.1% of the explained variance in the model. ML slope was not significantly correlated with phytoplankton biomass and was therefore not included in the multiple linear regression model.

### 3.3.5 Theoretical model of irradiance, primary production, and critical depth beneath sea ice with leads

Field observations from SUBICE demonstrate the presence of modest under-ice phytoplankton blooms beneath fully consolidated sea ice with snow, yet low phytoplankton biomass in waters with 5–15% lead fraction. To understand whether light availability is sufficient for under-ice blooms to develop beneath 100% ice cover and at low lead fractions, we constructed a model of irradiance, GPP, and  $Z_{\text{cr}}$  in ice-covered waters for pre-bloom concentrations of phytoplankton at varied lead fraction (refer to Section 3.2.3 for model details). The modeled light levels at the surface ocean beneath 100% ice cover ranged from 4 to 60  $\mu\text{Ein m}^{-2} \text{ s}^{-1}$

over the daily cycle, corresponding to a transmission of  $\sim 1.5\%$ . In open water leads, surface PAR ranged from 40 to  $\sim 1900 \mu\text{Ein m}^{-2} \text{ s}^{-1}$  over the day. Bottom depth was not constrained to avoid interference with calculations of deeper  $Z_{\text{cr}}$  at low ice concentrations.

Beneath 100% ice cover with snow, GPP exceeded community respiration in the upper 4 m of the water column, yielding a  $Z_{\text{cr}}$  of 6.6 m (Fig. 3.11A). This suggests that there is enough light in surface waters for a phytoplankton bloom to begin in a stratified water column beneath fully consolidated sea ice with up to 0.07 m snow cover. However, if the water column is actively mixed beyond the relatively shallow  $Z_{\text{cr}}$ , community respiration will exceed GPP in the upper ML and prevent phytoplankton bloom development. As the presence of open water leads in the sea ice increases, irradiance in the water column also increases, resulting in greater estimates of GPP relative to respiration and deeper  $Z_{\text{cr}}$ . For example, at ice concentrations of 96, 92, and 83%, the  $Z_{\text{cr}}$  was 10 m, 14 m (Fig. 3.11B), and 23 m (Fig. 3.11C), respectively.

The  $Z_{\text{cr}}$  for pre-bloom waters increased from several meters to 150 m (Fig. 3.11D) as sea ice concentration in the model varied from 100% (no leads) to 0% (completely ice-free waters). The ice concentration at which the  $Z_{\text{cr}}$  exceeded the mean bottom depth (50 m) for waters on the shallow continental shelf of the Chukchi Sea was 67%. Thus, at greater ice concentrations, overturning of the water column results in vertical mixing deeper than  $Z_{\text{cr}}$ , preventing the development of under-ice blooms. These findings are consistent with field results, illustrating that phytoplankton can bloom in stratified waters even at very high ice concentration and that convective mixing in leads can prevent bloom development.

## 3.4 Discussion

### 3.4.1 Enhanced convective mixing beneath sea ice with leads

Hydrographic conditions during SUBICE revealed that the water column beneath leads in sea ice was weakly stratified and poised for overturning on relatively short time scales, while waters beneath fully consolidated sea ice were more stratified. As described by *Pacini et al.* (2016), the most likely mechanism for enhanced mixing within leads is convection due to the refreezing of surface waters (as opposed to wind mixing), which was frequently observed during the spring sampling period. The observations presented here and in *Pacini et al.* (2016) build on previous studies of the importance of convective mixing in WW formation and water column overturning during the initial freeze-up in autumn and in sea ice leads

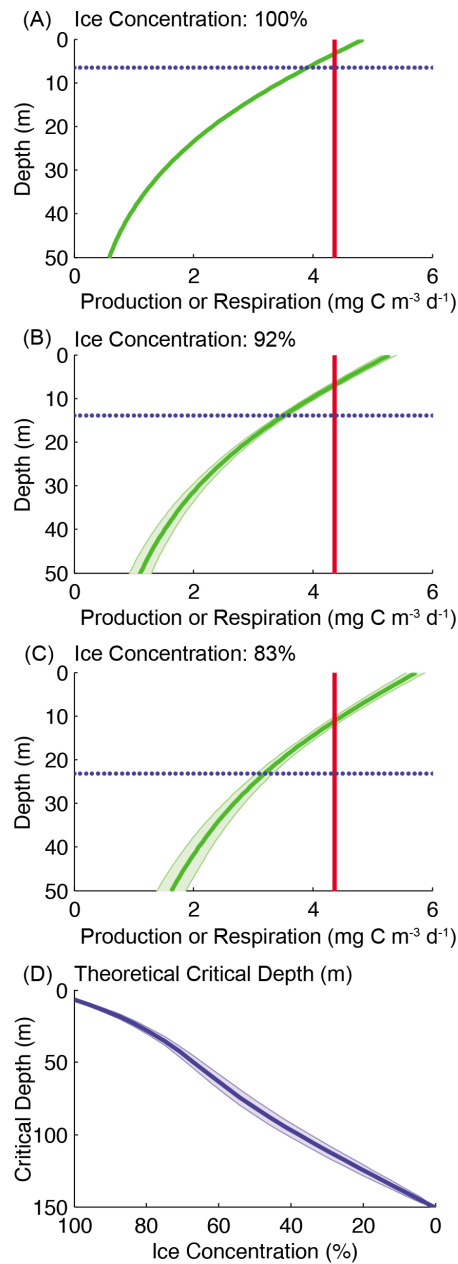


Figure 3.11: Results from a theoretical model of under-ice irradiance, gross primary production, and critical depth ( $Z_{cr}$ ) at varied lead fraction. (A, B, C) Theoretical profiles of production (solid green line with shading for mean  $\pm$  standard deviation of 50,000 model simulations), respiration (solid red line), and  $Z_{cr}$  (dotted blue line) at (A) 100% ice concentration, (B) 92% ice concentration, and (C) 83% ice concentration. (D) Theoretical  $Z_{cr}$  (solid blue line with shading for mean  $\pm$  standard deviation) at varied ice concentration (0-100%).

and polynyas during winter (*Weingartner et al.*, 1998; *Woodgate et al.*, 2005b; *Smith IV and Morison*, 1993; *Pickart et al.*, 2016). Our results illustrate that convection is also an important driver of physical and biological processes in the spring when sunlit waters are pre-conditioned for phytoplankton blooms.

### 3.4.2 Importance of leads in the absence of convection

While the contribution of sea ice algae to under-ice primary production has been recognized for decades (*Horner and Schrader* (1982); *Gosselin et al.* (1997); *Gradinger* (2009), the potential importance of phytoplankton in ice-covered waters is only recently beginning to be understood. For example, in most current estimates of net primary production in seasonally ice-covered regions (e.g. *Pabi et al.*, 2008; *Arrigo and van Dijken*, 2011; *Bélanger et al.*, 2013), phytoplankton primary production beneath the ice is assumed to be negligible due to light limitation. Prior to the massive under-ice phytoplankton bloom observed during ICESCAPE (*Arrigo et al.*, 2012, 2014), the long-standing paradigm of phytoplankton in this region was that blooms begin in the marginal ice zone after ice retreat, with ice-edge blooms considered to be near-ubiquitous and substantial contributors to total primary production in the Arctic (*Hameedi*, 1978; *Perrette et al.*, 2011). The unexpectedly high accumulation of phytoplankton biomass observed beneath the ice in 2011 demonstrated the role of melt ponds in illuminating the water column for phytoplankton growth (*Frey et al.*, 2011; *Arrigo et al.*, 2012), motivating additional studies of light transmission and phytoplankton bloom development beneath melt ponded sea ice (*Palmer et al.*, 2014; *Zhang et al.*, 2015).

To our knowledge, the present study is the first to consider whether open water leads in sea ice play a similar role to melt ponds in transmitting sunlight for phytoplankton blooms in ice-covered waters. Results from our theoretical model indicate that, in fact, even at very high ice concentration, leads substantially increase light penetration to the upper water column and could play an important role in facilitating the development of under-ice blooms. This concept is supported by a handful of previous observations of enhanced phytoplankton biomass in sea ice with leads (*English*, 1961; *Bursa*, 1963; *Gosselin et al.*, 1997) and to a limited extent in our observations (Section 3.3.3). Over most of the Chukchi Sea, however, we observed low phytoplankton biomass in weakly-stratified and nutrient-rich waters beneath sea ice with leads. These results demonstrate the essential role of convective mixing in re-freezing leads in preventing or delaying the development of phytoplankton blooms within the sea ice zone. Despite the increased light transmission through leads, as phytoplankton

are convectively mixed to deeper depths, the total light dose that phytoplankton receive is reduced. As first described by *Sverdrup* (1953), vertical mixing prevents blooms where  $MLD > Z_{cr}$ , and in these waters blooms cannot form until convective overturning ceases, consistent with the notion that the shutdown of turbulent convection triggers the onset of spring phytoplankton blooms (*Taylor and Ferrari*, 2011). We expect that in the absence of convective mixing, either later in the season or in warmer atmospheric conditions, transmission of sunlight through leads supports the development of under-ice phytoplankton blooms, with leads playing a similar role to that of melt ponds.

### 3.4.3 Modest under-ice blooms even beneath fully consolidated sea ice

A particularly noteworthy outcome of the SUBICE expedition is the discovery of modest phytoplankton blooms ( $\sim 1\text{--}3 \mu\text{g Chl } a \text{ L}^{-1}$ ) in stratified waters beneath fully consolidated sea ice with snow. These surprising field observations were validated by the theoretical model calculations, which demonstrate that first-year sea ice transmits sufficient light for phytoplankton blooms to develop in the surface waters of a very stable water column, even with low or moderate snow cover (e.g. 0.07 m). Although only  $\sim 30\%$  of the study region was characterized by fully consolidated sea ice during SUBICE, observations from these locations indicate that blooms can begin beneath 100% sea ice cover prior to melt pond formation if the water column is well-stratified. We note that as phytoplankton biomass increases, primary production and  $Z_{cr}$  also increase, such that once an under-ice bloom begins in highly stratified surface waters, it can continue to develop even with some subsequent mixing of the upper ML.

Considering that the time between melt pond formation and sea ice retreat is typically only a few weeks (consistent with *Perovich et al.* (2003); *Palmer et al.* (2014)), the finding that blooms can begin prior to the onset of melt ponds demonstrates that the temporal span of under-ice phytoplankton blooms may be greater than previously realized. In fact, light transmission beneath snow-covered sea ice may play an important role in increasing background phytoplankton concentrations prior to melt pond formation, thus contributing importantly to the development of extremely productive under-ice blooms several weeks later. Although field data are not available prior to melt pond formation at the location of the massive under-ice phytoplankton bloom observed during ICESCAPE (*Arrigo et al.*, 2012), we suggest that the presence of a modest under-ice bloom such as we observed during SUBICE would facilitate rapid subsequent accumulation of biomass beneath sea ice once

melt ponds form. Thus, it is possible that the extraordinarily high depth-integrated biomass beneath fully consolidated sea ice observed during ICESCAPE (*Arrigo et al.*, 2014) evolved from a more modest bloom beneath snow-covered sea ice prior to pond formation.

#### 3.4.4 Implications for marine ecosystems in the changing Arctic Ocean

Sea ice conditions in the Arctic Ocean are being dramatically altered by climate change, with reductions in the thickness and age of sea ice accompanied by earlier ice retreat in recent decades (e.g. *Maslanik et al.*, 2011; *Kwok and Rothrock*, 2009; *Stammerjohn et al.*, 2012). The fate of polar marine ecosystems in this region critically depends on response of phytoplankton at the base of the food web to these abrupt changes in the physical environment. Recent field, satellite, and modeling work suggests that the timing of peak primary production in continental shelf regions of the Arctic Ocean may be shifting to earlier in the season due to earlier ice retreat (*Kahru et al.*, 2010) and the presence of under-ice phytoplankton blooms (*Arrigo et al.*, 2012; *Lowry et al.*, 2014; *Palmer et al.*, 2014) beneath the thin first-year sea ice that is becoming increasingly prevalent in this region (*Maslanik et al.*, 2011).

Results of this study demonstrate that first-year sea ice can support early season phytoplankton blooms prior to melt pond formation, indicating that the potential of the sea ice zone to support primary production by phytoplankton may be even greater than recently recognized (*Arrigo et al.*, 2014). Additionally, while the significance of leads in sea ice as habitat for upper trophic levels such as polar bears and ringed seals has been documented (e.g. *Stirling*, 1997), prior to this study the role of leads in supporting phytoplankton growth in the sea ice zone was not well characterized. Our findings illustrate the importance of leads and convective mixing in controlling the spatial and temporal distributions of spring phytoplankton in the sea ice zone and further demonstrate the complexity of phytoplankton bloom dynamics in this region. To better understand the response of phytoplankton and upper trophic levels to continued changes in sea ice and hydrographic conditions, additional field and modeling studies of under-ice primary production and food web dynamics in this region are necessary.

## Acknowledgments

We would like to acknowledge the captain, crew, and science party of the *USCGC Healy* for their contributions during HLY1401. Field data collection and analysis for the SUBICE

program was supported by the National Science Foundation (NSF) Grant No. PLR-1304563 to KRA. Funding for KEL was provided through the NSF Graduate Research Fellowship Program (Grant No. DGE-0645962), the Stanford University Department of Earth System Science, and the Stanford University Gerald J. Lieberman Fellowship.

## Chapter 4

# Effects of visible light and ultraviolet radiation on under-ice phytoplankton

KATE E. LOWRY, KATE M. LEWIS, MATTHEW M. MILLS, AND KEVIN R. ARRIGO

*Earth System Science, Stanford University, Stanford, California, USA*

ATSUSHI MATSUOKA

*Department of Biology, Laval University, Quebec City, Quebec, Canada*

*Recent observations of phytoplankton blooms beneath first-year Arctic sea ice indicate that the under-ice light environment is more suitable for phytoplankton growth than previously thought. To understand the factors that contribute to high growth rates and phytoplankton biomass accumulation beneath the ice, this study investigates the effects of visible light (photosynthetically active radiation; PAR) and ultra-violet radiation (UVR) on under-ice phytoplankton. During the Study of Under-ice Blooms In the Chukchi Ecosystem (SUBICE) field program in May-June 2014 in the Chukchi Sea, we conducted shipboard deck incubation experiments to measure the responses of under-ice phytoplankton across a gradient of PAR and UVR conditions. We test the hypothesis that the under-ice environment is ideally suited for phytoplankton growth due to light attenuation that reduces the damaging effects of high PAR and UVR on photosynthetic cells. Across 12 experiments, maximum phytoplankton growth and photosynthetic rates were significantly higher in the reduced PAR and UVR treatments that simulated*

*the under-ice environment than in the control that simulated the open water environment, indicating lower inhibition beneath the sea ice as compared to open water. While differences observed in the longer-term growth indicators such as phytoplankton biomass and nutrient uptake were not significant over the four-day incubation period, the shorter-term acclimation parameters, including variable fluorescence and chlorophyll *a*, indicate that phytoplankton can achieve greater primary production beneath the ice than in open water due to the more optimal light environment. This study provides important context for recent field observations and for improving our understanding of this rapidly changing ecosystem.*

This chapter is in preparation for submission as part of a special issue on the results of the Study of Under-ice Blooms In the Chukchi Ecosystem (SUBICE) field program.

## 4.1 Introduction

Prior to anthropogenic climate change, the Chukchi Sea in the Arctic Ocean was largely characterized by thick snow-covered multi-year ice that attenuated nearly all of the incident solar radiation (Maslanik *et al.*, 2011; Perovich *et al.*, 2011), leaving the underlying ocean dark and free of phytoplankton blooms. However, in recent decades, as more sunlight penetrates the relatively thin first-year sea ice (Kwok and Rothrock, 2009; Perovich and Polashenski, 2012) that now covers  $\sim 98\%$  of this region (Polashenski *et al.*, 2015), observations indicate that the under-ice environment is becoming increasingly suitable for phytoplankton growth (Frey *et al.*, 2011). In 2011, a massive phytoplankton bloom was discovered beneath melt-ponded first year sea ice in the Chukchi Sea as part of the Impacts of Climate on EcoSystems and Chemistry of the Arctic Pacific Environment (ICESCAPE) field expedition (Arrigo *et al.*, 2012). Phytoplankton growth rates were unprecedented in the under-ice bloom, averaging  $0.9 \text{ d}^{-1}$  and as high as  $1.6 \text{ d}^{-1}$ , substantially higher than the maximum growth rates predicted for near-freezing waters (Eppley, 1972). Similarly, depth-integrated phytoplankton biomass ( $\sim 1300 \text{ mg chlorophyll } a \text{ m}^{-2}$ ) in the bloom was equivalent to the highest measurements anywhere in the world (Arrigo *et al.*, 2014).

Comparing satellite-based estimates of net primary production in these seasonally ice-covered waters to *in situ* measurements from the under-ice bloom indicates that estimates of total primary production in this region may be  $\sim 10$ -fold too low (Arrigo *et al.*, 2014).

Additionally, satellite and modeling work indicate that, as a result of increased light due to decreased snow and ice cover, under-ice blooms were widespread in the Chukchi Sea from 1998–2013 (*Lowry et al.*, 2014; *Zhang et al.*, 2015) and that under-ice blooms are important contributors to total net primary production (*Palmer et al.*, 2014). Together, these results indicate that the presence of phytoplankton blooms is likely to be both novel and increasing, representing a potential shift in the timing of peak primary production in this region to earlier in the season (*Arrigo et al.*, 2012). Yet, we are only beginning to understand the physical and biological processes that contribute to under-ice phytoplankton bloom development and the effects of continued changes in sea ice and hydrography on primary production in this seasonally ice-covered ecosystem.

To understand the factors controlling the spatial and temporal distribution and productivity of phytoplankton blooms beneath the ice and in open water, a series of recent studies have focused on the availability of nutrients and sunlight. Additional work from the NASA-funded ICESCAPE program in June–July 2010 and 2011 and the subsequent NSF-funded SUBICE (Study of Under-ice Blooms In the Chukchi Ecosystem) expedition in May–June 2014 illustrated that the nutrient content of the winter water that flows across the Chukchi shelf in the spring and summer is extremely high (*Lowry et al.*, 2015; *Pickart et al.*, 2016), with pre-bloom  $\text{NO}_3^-$  concentrations as high as 13–17  $\mu\text{mol L}^{-1}$  in surface waters across the region (*Arrigo et al.*, 2016). The ice-covered water column of the Chukchi Sea is therefore pre-conditioned for spring phytoplankton blooms of great magnitude, given sufficient light availability. This concept was reinforced through additional observations of modest under-ice phytoplankton blooms prior to melt pond formation on the sea ice during SUBICE (*Lowry et al.*, 2016). However, in locations that were deeply mixed due to convection in refreezing leads of open water (*Pacini et al.*, 2016), phytoplankton concentrations were low despite sufficient nutrient availability as a consequence of reduced light in the upper mixed layer (*Lowry et al.*, 2016). These findings demonstrate the importance of light, rather than nutrient availability, in controlling phytoplankton growth in the sea ice zone of the Chukchi Sea.

One possible explanation for what allowed the under-ice phytoplankton bloom observed during ICESCAPE to reach such high growth rates and biomass accumulation despite extremely cold temperatures is that the under-ice environment provides the ideal light conditions for phytoplankton growth (*Arrigo et al.*, 2014; *Palmer et al.*, 2014). Measured transmission of incident PAR (photosynthetically active radiation; 400–700 nm) through the

melt-ponded sea ice that covered the bloom was up to 55%, more than three times that of the adjacent bare ice ( $\sim 15\%$ ) (Frey *et al.*, 2011). Furthermore, sea ice and snow cover strongly attenuate ultraviolet radiation (UVR, 280–400 nm) (Perovich and Govoni, 1991; Perovich, 1993, 2002), which damages genetic material of phytoplankton and inhibits photosynthesis, resulting in reduced rates of primary production (Booth *et al.*, 1997; Vernet, 2000). The negative impacts of high UVR on marine phytoplankton are particularly important in high-latitude waters and have been studied extensively in the Antarctic (Helbling *et al.*, 1992; Holm-Hansen *et al.*, 1993; Holm-Hansen, 1997) and to a lesser extent in the Arctic (Bischof *et al.*, 2002; Helbling and Villafane, 2002; Hessen *et al.*, 2012). We propose that the UVR-attenuating characteristics of sea ice, paired with the moderately high transmission of PAR through melt-ponds, plays an important role in supporting extremely high growth rates beneath the sea ice as observed in 2011. Our hypothesis is that sea ice shields phytoplankton from damaging levels of UVR and PAR, allowing photosynthetic cells to maximize allocation of resources to growth rather than processes related to photoprotection and repair of UVR photodamage.

To test this hypothesis, we investigated the effects of PAR and UVR on phytoplankton growth beneath the ice by conducting a dozen shipboard incubation experiments during SUBICE. In each experiment, we exposed under-ice phytoplankton communities to a gradient of reduced PAR and UVR treatments over a 4-day period to simulate variations of the under-ice light environment relative to that of an open water control. Results focus on how phytoplankton biomass, physiology, growth rates, and light absorption are affected by different levels of PAR and UVR transmission. This aim of this study is to characterize the unique properties of the under-ice light environment that support the development and productivity of phytoplankton blooms in the sea ice zone of the Arctic Ocean. More broadly, this research seeks to improve our knowledge of the implications of continued changes in sea ice for phytoplankton at the base of the food web in this biologically-rich and highly dynamic ecosystem.

## 4.2 Methods

### 4.2.1 Field sampling

Oceanographic fieldwork was conducted in the Chukchi Sea as part of the NSF-funded SUBICE program aboard *USCGC Healy* in May–June 2014. During the field expedition,

we sampled the water column at 230 hydrographic stations on the continental shelf of the Chukchi Sea (Fig. 4.1), using the ship’s 30-liter 12-position rosette system. Seawater samples were collected at standard depths, with surface (1–3 m) waters collected at 12 stations for the incubation experiments. A further description of field sampling during SUBICE is presented in Lowry et al. (in prep). Mixed layer depth (MLD) was calculated at each station from the density profiles using a robust visual inspection method, as in *Våge et al. (2015)*; *Lowry et al. (2016)*; *Pacini et al. (2016)*.

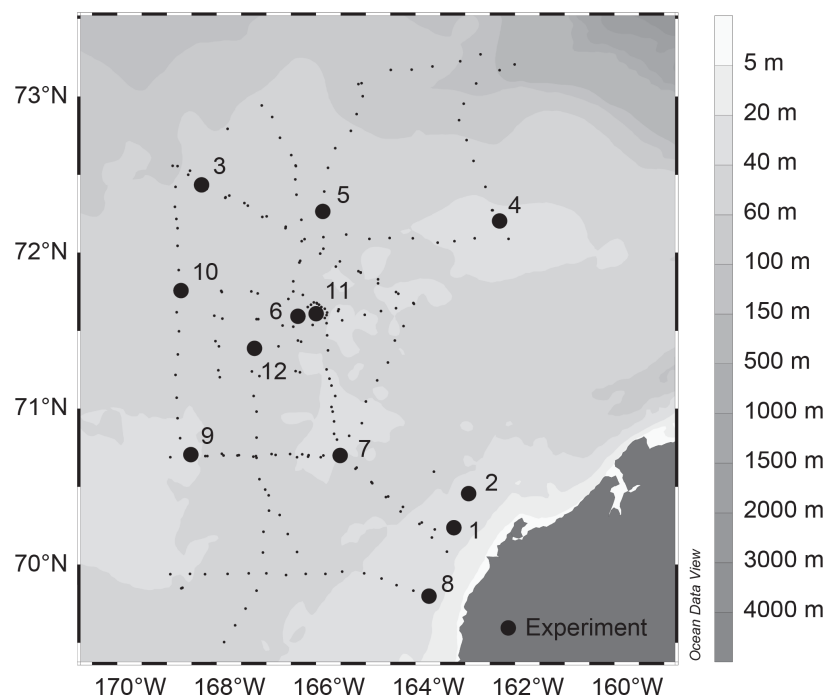


Figure 4.1: Map of incubation experiment station locations overlain on a map of hydrographic stations occupied during the SUBICE expedition in the Chukchi Sea in May–June 2014, with numbers indicating the order in which experiments were conducted.

#### 4.2.2 Experimental design and sampling

At 12 hydrographic stations (Fig. 4.1), ~100 L of seawater was collected from the surface sampling depth for bioassay experiments to study the effects of reduced PAR and UVR on phytoplankton growth and physiology. During the CTD rosette sampling, seawater was screened for grazers with 100  $\mu\text{m}$  Nitex mesh and placed in UV-transparent 4 L Whirlpak bags for incubation at *in situ* water temperature in flow-through incubators on the deck of the

ship. Methods are consistent with previous studies on the effects of UVR on phytoplankton via incubation experiments (Vernet, 2000). Nutrients were not added at any point.

Open water conditions were simulated through the experimental control, in which phytoplankton were exposed to levels of PAR and UVR expected in ice-free surface waters (referred to hereafter as high PAR and high UVR, or HH; see Table 4.1). The under-ice environment was simulated via four treatments that created a gradient of high and low PAR and high, low, and no UVR conditions (HL, HN, LL, LN; see Table 4.1). Mesh neutral density screening was used to reduce the transmission of incident PAR to the desired level for each treatment and the control (Table 4.1). Similarly, UVR-blocking incubator lids were used to shield UVR fluxes within the low and no UVR treatment incubators, with lids composed of Acrylite OP-3 that filters out incoming UV-B (280–315 nm) and UV-A (315–400 nm) radiation. Small holes (5/8" diameter) were used to remove 30% of the material in the low UVR treatment lid, allowing moderate UVR transmission relative to no UVR treatment and the open water control. The resulting transmission of PAR and UVR to seawater in the control and treatment incubations (Table 4.1) was confirmed using a TRIOS Ramses spectral radiometer and a LICOR PAR sensor.

Abbreviation	PAR Level	UVR Level	PAR Transmission	UVR Transmission	Simulated Conditions
HH - Control	High	High	45%	30%	Open Water
HL	High	Low	40%	10%	Ponded Ice
HN	High	None	40%	0%	Ponded Ice
LL	Low	Low	15%	10%	Bare Ice
LN	Low	None	15%	0%	Bare Ice

Table 4.1: Incubation experiment design and light conditions. The control (HH) simulated open water with high PAR and high UVR, while the four treatments (HL, HN, LL, and LN) simulated under-ice conditions across a gradient of reduced PAR and UVR transmission.

Experiments were performed in triplicate and incubated over a four-day period, with sampling intervals based on measurement type using the analytical methods described in Section 4.2.3. Samples for the initial time points (T0) were taken immediately for the full suite of analytical measurements following the CTD cast as part of the hydrographic station analysis. Experiments were sampled daily (T24, T48, T72, T96; hrs after experiment start) for variable fluorescence, at the mid- and final time points (T48 and T96) for concentrations

of nutrients and chlorophyll *a* (Chl *a*), and at the final time point (T96) only for analysis of phytoplankton photosynthetic rates, particulate absorption spectra, carbon uptake rates, non-photochemical quenching (only Exp. 8–12), and pigment analysis. Due to sample analysis limitations, only one replicate for each treatment and control was analyzed for nutrient concentration, phytoplankton photosynthetic rate, and particulate absorption spectrum.

### 4.2.3 Analytical methods

#### Nutrients

Seawater was analyzed on board ship for concentrations of nitrate ( $\text{NO}_3^-$ ), ammonium ( $\text{NH}_4^+$ ), nitrite ( $\text{NO}_2^-$ ), phosphate ( $\text{PO}_4^{3-}$ ), and silicate ( $\text{Si}(\text{OH})_4$ ) using a Seal Analytical continuous flow Auto-Analyzer 3 and a modification of the method of *Armstrong et al.* (1967).

#### Phytoplankton biomass

Seawater samples for analysis of chlorophyll *a* (Chl *a*) concentration were filtered onto 25 mm Whatman glass fiber filters (GF/F) of 0.7  $\mu\text{m}$  nominal pore size. Filters were extracted in 5 mL of 90% acetone in the dark for 24 hrs at  $+3^\circ\text{C}$  prior to measurement (*Holm-Hansen et al.*, 1965) on a Turner Designs 10-AU fluorometer calibrated with pure Chl *a* (Sigma). Seawater samples for analysis of particulate organic carbon and nitrogen (POC and PON) were filtered onto pre-combusted (4 hrs at  $450^\circ\text{C}$ ) GF/Fs. Filters were immediately dried in an oven at  $60^\circ\text{C}$  and stored dry, along with filter blanks which were made with  $\sim 50$  mL of 0.2  $\mu\text{m}$  filtered seawater. Samples and blanks were fumed with concentrated HCl, dried again at  $60^\circ\text{C}$ , and packed into tin capsules (Costech Analytical Technologies, Inc.) for elemental analysis on an Elementar Vario EL Cube (Elementar Analysensysteme GmbH) interfaced to a PDZ Europa 20-20 isotope ratio mass spectrometer (Sercon Ltd) using glutamic acid and peach leaves as standards. Elemental analysis was performed at the University of California Davis Stable Isotope Facility. POC concentrations at the initial ( $T = 0$  hrs) and final ( $T = 96$  hrs) time points were used to calculate phytoplankton specific growth rates ( $\mu$ ,  $\text{d}^{-1}$ ) using the equation:

$$\text{POC}_{T96} = \text{POC}_{T0} e^{\mu T} \quad (4.1)$$

### Phytoplankton photosynthetic rates

Phytoplankton photosynthetic parameters were determined from photosynthesis ( $P$ ) versus irradiance ( $E$ ) curves. In the P-E method (*Lewis and Smith, 1983*), seawater samples labeled with  $^{14}\text{C}$ -bicarbonate were incubated under a range of light levels (0 to  $522 \mu\text{Ein m}^{-2} \text{s}^{-1}$ ) and assayed for  $^{14}\text{C}$  incorporation using a Perkin Elmer WinSpectral 1414 liquid scintillation counter. The P-E curves provide estimates of maximum Chl  $a$ -normalized (\*) photosynthetic rates ( $P_{\text{max}}^*$ ) ( $\text{mg C mg Chl } a^{-1} \text{ h}^{-1}$ ), light limited efficiency of photosynthesis ( $\alpha^*$ ) ( $\text{mg C mg}^{-1} \text{ Chl } a \text{ h}^{-1} (\mu\text{Ein m}^{-2} \text{s}^{-1})^{-1}$ ), and the light-saturation intensity parameter ( $E_K$ ) ( $\mu\text{Ein m}^{-2} \text{s}^{-1}$ ), after correcting for  $P_0^*$  (the amount of carbon uptake/release at  $0 \mu\text{Ein m}^{-2} \text{s}^{-1}$ ). We used a nonlinear curve-fitting program (lsqcurvefit) in Matlab to fit P-E curves to the model of *Webb et al. (1974)*

$$P^* = P_m^* \left( 1 - \exp \left[ \frac{-\alpha^* E}{P_m^*} \right] \right) - P_0^*. \quad (4.2)$$

The model of *Platt et al. (1980)* was tested but disregarded due to insignificant  $\beta$  values, as in *Lowry et al. (2016)*. As in *Palmer et al. (2013)*, P-E curve significance was determined using criteria of  $p < 0.05$  and  $R^2 > 0.6$ , and the maximum growth rate ( $\mu_{\text{max}}$ ,  $\text{d}^{-1}$ ) was calculated by dividing  $P_{\text{max}}^*$  by the ratio of POC:Chl  $a$ .

### Variable fluorescence

A fast repetition rate fluorometer (FRRf) with excitation at 470 nm was used to measure variable fluorescence (*Kolber et al., 1998*). Samples were dark-acclimated for  $\sim 30$  min at *in situ* temperature and measured within one hr of sampling. Blanks effects were corrected (*Cullen and Davis, 2003*) by preparing a blank for each sample via gentle filtration through a  $0.2 \mu\text{m}$  polycarbonate syringe filter before measurement using identical protocols. Using the FRRf, we measured the maximum photochemical efficiency (Fv:Fm), maximum effective cross-sectional area ( $\sigma$ ) ( $\text{\AA}^2 \text{ photon}^{-1}$ ), and electron turnover time ( $\tau$ ) of photosystem II.

### Phytoplankton absorption spectra

After filtering seawater under low vacuum onto 25 mm GF/Fs, we measured light absorbance (or optical density) of particles ( $\text{OD}_p$ , unitless) between 200 and 800 nm using a Varian Cary 100 spectrophotometer equipped with an integrating sphere. After the measurement, the

GF/F was placed in a clean glass petri dish and methanol was added to extract phytoplankton pigments retained on the filters (*Kishino et al.*, 1985). Absorbance of detrital particles, det ( $OD_{\text{det}}(\lambda)$ , unitless) was determined on the de-pigmented filter using the same spectrophotometer. Throughout the measurements, the Transmittance-Reflectance (so-called T-R) method proposed by *Tassan and Ferrari* (1995) was applied to minimize the backscattering effect of particles retained on the GF/Fs. The corresponding and appropriate pathlength amplification effect caused by the highly scattering GF/F, known as the  $\beta$ -factor (*Mitchell et al.*, 2002), was taken into account for the specific geometry of this instrument (*Tassan and Ferrari*, 2002). We converted these OD values into absorption coefficients for total particles ( $a_p(\lambda)$ ,  $\text{m}^{-1}$ ) and det ( $a_{\text{det}}(\lambda)$ ,  $\text{m}^{-1}$ ) using the averages of the measured values between 795 and 800 nm ( $OD_{\text{null},j}$ , dimensionless) for the null correction

$$a_j(\lambda) = 2.303 \frac{A(OD_j(\lambda) - OD_{\text{null},j})}{\beta V} \quad (4.3)$$

where  $j$  denotes either total particles (p) or detritus (det) retained on the filter. The coefficient 2.303 is a factor for converting base  $e$  to base 10 logarithms,  $A$  is the clearance area of the filter ( $\text{m}^2$ ), and  $V$  is the sample volume ( $\text{m}^3$ ). Finally, we obtained absorption coefficients of phytoplankton ( $a_\phi(\lambda)$ ,  $\text{m}^{-1}$ ) by subtracting  $a_{\text{det}}(\lambda)$  from  $a_p(\lambda)$

$$a_\phi(\lambda) = a_p(\lambda) - a_{\text{det}}(\lambda). \quad (4.4)$$

The Chl  $a$ -specific phytoplankton absorption coefficient,  $a_{\text{ph}}^*(\lambda)$ , ( $\text{m}^2 \text{mg}^{-1}$ ) was calculated by dividing  $a_\phi(\lambda)$  by the Chl  $a$  concentration of each sample. Additionally, we calculated the mean Chl  $a$ -specific absorption coefficient ( $\bar{a}^*$ ) ( $\text{m}^2 \text{mg}^{-1}$  Chl  $a$ ) using the equation:

$$\bar{a}^* = \frac{\sum_{\lambda=400}^{\lambda=700} a_{\text{ph}}^* E(\lambda)}{\sum_{\lambda=400}^{\lambda=700} E(\lambda)} \quad (4.5)$$

where  $E(\lambda)$  ( $\mu\text{Ein m}^{-2} \text{s}^{-1}$ ) is the spectral irradiance of the photosynthetron light source. Finally, we computed the maximum quantum yield of photosynthesis ( $\Phi_m$ ) ( $\text{mol C mol}^{-1}$  photons) as:

$$\Phi_m = \frac{P^*}{43.2 E \bar{a}^*}, \quad (4.6)$$

where  $E$  is the light level from the photosynthetron light source at which  $\Phi_m$  was highest, following the method of *Johnson and Barber* (2003).

We estimated an index of mycosporine-like amino acids (MAAs; UVR absorbing protective compounds) by comparing the peak in UVR absorption relative to the peak in red visible absorption by Chl a. Thus, the MAA index was defined as the difference between  $a_{\text{ph}}^*$  ( $\lambda$ ) at 330 nm and 360 nm relative to that of 675 nm.

### Pigment analysis

Samples were collected for analysis of phytoplankton pigment composition via High Performance Liquid Chromatography (HPLC) using the method of *Zapata et al.* (2000). For sample collection, seawater was filtered onto 25 mm GF/Fs, with filters immediately flash-frozen in liquid nitrogen prior to storage at  $-80^{\circ}\text{C}$  until analysis at the University of Laval in Quebec, Canada. In addition to the standard photosynthetic and xanthophyll pigments, samples were also collected for analysis via HPLC of MAA concentration.

#### 4.2.4 Sea ice cover

Sea ice cover (%) at locations where seawater was collected for incubation experiments was determined from Special Sensor Microwave Imager (SSM/I) satellite ice imagery at 25 km resolution for the date the station was sampled. Satellite imagery were obtained from the National Snow and Ice Data Center (*Cavalieri et al.*, 1996). Satellite sea ice concentrations were validated through visual ‘ice watch’ observations, yielding a strong correlation between satellite and *in situ* observations, as reported by Lowry et al. (in prep). Visual estimates of sea ice cover from photographs taken during occupation of the 12 stations from the *USCGC Healy* Aloft Conn camera also compared well with sea ice concentrations derived from the satellite data ( $R = 0.88$ ;  $p < 0.001$ ).

#### 4.2.5 Statistical analysis

Differences between treatments and the control were compared through one-way ANOVA analysis of physiological and biogeochemical properties in individual experiments, as in *Alderkamp et al.* (2015), and of mean values and relative changes across all experiments. We also analyzed the significance of trends over a gradient of decreasing total radiation, using the following estimates of total radiation based on PAR + UVR transmission: HH (75%), HL (50%), HN (40%), LL (25%), LN (15%). Statistical analysis was performed in Matlab and significance was determined using a criterion of  $p < 0.05$ .

## 4.3 Results

### 4.3.1 Experiment starting conditions

Experiments were conducted with waters collected from 12 stations distributed throughout the SUBICE sampling region (Fig. 4.1). The latitude and longitude of experiment stations ranged from 69.8 to 72.4° N and 162.3 to 168.7° W, respectively. All experiments were conducted with waters collected on the shallow continental shelf of the Chukchi Sea, with the bottom depth of experiment stations ranging from 26 m in coastal waters at the southernmost location (Exp. 8) to 54 m at the most northeastern station (Exp. 3). Experiments were collected at stations sampled from 20 May to 16 June 2014 (Table 4.2) over a range of times from 0300 to 1600 relative to local solar noon, which ranged from 1145 to 1215 during the spring sampling period. Most of the region was ice covered at the time of sampling, with four experiments stations characterized by 100% sea ice cover (Exp. 1, 2, 4, 11), and all but one experiment station covered by at least 75% sea ice cover (Exp. 8; 25% ice cover). The mixed layer depth (MLD) of the experiment stations ranged from 8 to 41 m, with water for six experiments collected from stations with relatively shallow MLD (<20 m) and six collected from stations with deeper MLD (>20 m). With the exception of the warmer shallow coastal ice-free station (Exp. 8;  $-0.16^{\circ}$  C), surface waters at all stations were characterized by near-freezing WW ( $-1.76$  to  $-1.64^{\circ}$  C). Salinity in surface waters ranged from 31.5 to 33.0. Consistent with the presence of WW, nutrient concentrations were relatively high ( $3.1\text{--}14 \mu\text{mol NO}_3^- \text{ L}^{-1}$ ) in surface waters at all experiment stations except for Exp. 8, which had undetectable levels of surface  $\text{NO}_3^-$ . Phytoplankton biomass was relatively high in most experiments, with Chl *a* >  $1 \mu\text{g L}^{-1}$  in all but two experiments (Exp. 3 and Exp. 5). Initial phytoplankton biomass was highest (Chl *a* >  $5 \mu\text{g L}^{-1}$ ) in Exp. 1, 8, 9, and 11.

### 4.3.2 Phytoplankton biomass response

The phytoplankton biomass response was assessed through changes in concentrations of Chl *a*, POC, PON, and nutrients in the simulated ice-free control (HH) and four reduced PAR and UVR treatments (HL, HN, LL, LN; Table 4.1). Results are presented as mean relative changes from the initial (T0) value averaged across all 12 experiments (Fig. 4.2A–D) and absolute concentrations shown separately for each individual experiment (Figs. 4.3, 4.4, 4.5).

#	Station	Date	Time	Ice Cover (%)	MLD (m)	$\theta$ ( $^{\circ}\text{C}$ )	Salinity (psu)	$\text{NO}_3^-$ ( $\mu\text{mol L}^{-1}$ )	Chl <i>a</i> ( $\mu\text{g L}^{-1}$ )
1	30	20 May	16:00	100	15	-1.67	32.99	3.1	9.3
2	31	21 May	10:30	100	23	-1.76	32.65	12.0	1.5
3	59	26 May	15:00	92	35	-1.71	31.99	9.9	0.3
4	74	28 May	08:30	100	14	-1.64	31.46	5.9	1.0
5	98	2 June	03:00	89	41	-1.73	32.05	13.4	0.3
6	104	3 June	16:00	78	31	-1.72	32.39	12.9	1.6
7	120	7 June	08:30	95	30	-1.73	32.59	11.9	1.8
8	128	8 June	06:00	25	16	-0.16	31.45	0.0	5.4
9	160	11 June	15:00	92	8	-1.74	32.55	12.3	6.1
10	168	12 June	12:00	94	22	-1.67	32.36	14.0	2.5
11	196	15 June	14:00	100	19	-1.66	32.61	13.8	5.6
12	203	16 June	12:30	99	13	-1.68	32.55	13.2	1.3

Table 4.2: List of experiment initial conditions for each station where surface waters were collected for incubation experiments, including the station number, sample date and local time (i.e. incubation start), ice concentration, and mixed layer depth (MLD), along with measurements of potential temperature ( $\theta$ ), salinity, and concentrations of nitrate ( $\text{NO}_3^-$ ) and chlorophyll *a* (Chl *a*).

### Chlorophyll *a* concentration

Over the four-day incubation period, Chl *a* generally increased from initial concentrations during the experiments. Relative changes across all experiments (Fig. 4.2A) and results from the individual experiments at the intermediate time point (T48) demonstrate that there was typically very little change in Chl *a* after two days. By the final time point, however, Chl *a* increased markedly in most experiments (Fig. 4.2A and Fig. 4.3). Averaged across all 12 experiments (Fig. 4.2A), Chl *a* concentration increased by 55% in the control (HH), 90-95% in the reduced UVR treatments (HL and HN), and 110-150% in the reduced PAR and reduced UVR treatments (LL and LN) by the final time point (T96). Although there were no significant differences between the control and the four treatments averaged across all experiments or in all but one of the individual experiments (Exp. 3; Fig. 4.3), the trend in increased Chl *a* concentration across the gradient of reduced UVR and PAR was statistically significant ( $p < 0.01$ ).

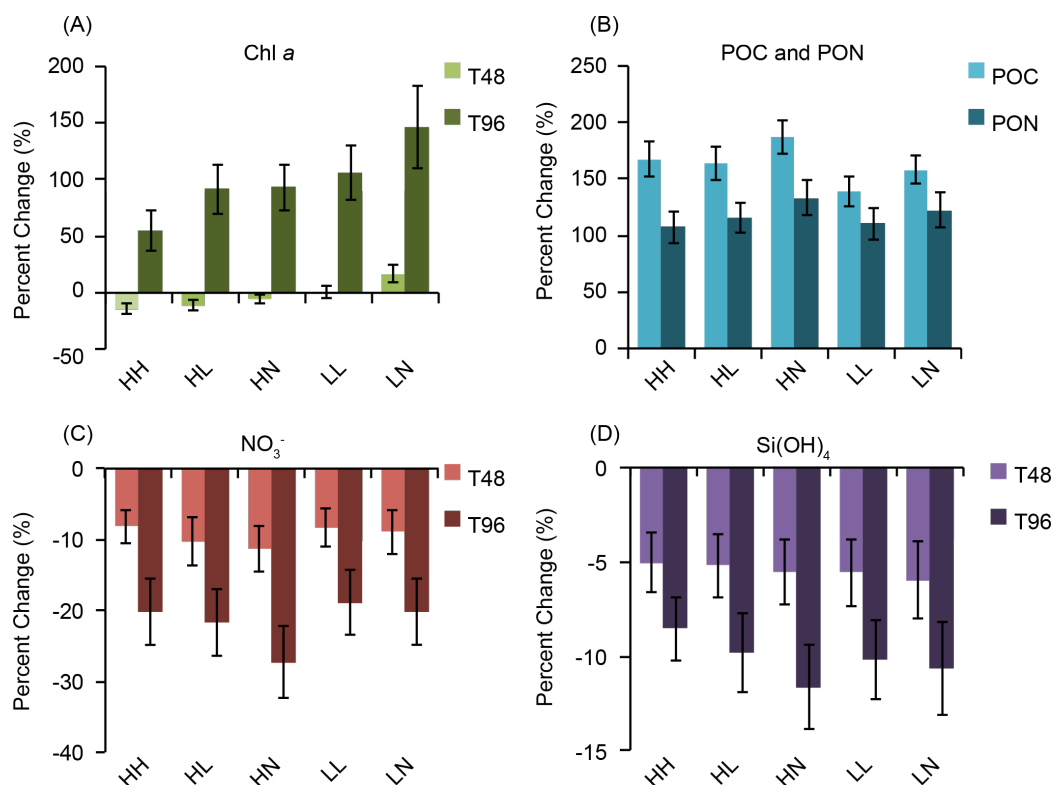


Figure 4.2: Mean percent change (%) relative to the initial time point (T0) across all 12 experiments for (A) Chl *a* concentration (at T48 and T96), (B) POC and PON concentration (at T96 only) (C) nitrate ( $\text{NO}_3^-$ ) concentration (T48 and T96), and (D) silicate ( $\text{Si}(\text{OH})_4$ ) concentration (T48 and T96) for the control (HH) and four reduced PAR and UVR treatments (HL, HN, LL, LN; Table 4.1). Error bars denote standard deviation.

### Particulate organic carbon and nitrogen concentration

Concentrations of POC and PON increased from initial concentrations over the four-day experiments, with a mean increase of 168% in the control (HH) and 130-187% in the reduced PAR and UVR treatments (Fig. 4.2B). PON followed a similar pattern, with a mean increase of 108% in the control (HH), 116-133% at reduced UVR (HL and HN), 102-123% at reduced PAR and reduced UVR (LL and LN). The increase in POC and PON relative to initial concentrations was consistent in all 12 experiments (Fig. 4.4). There were no significant differences in POC or PON between the treatments and the control in individual experiments.

Similarly, there were no significant differences between treatments and the control in the average phytoplankton growth rates calculated from changes in POC over the four-day

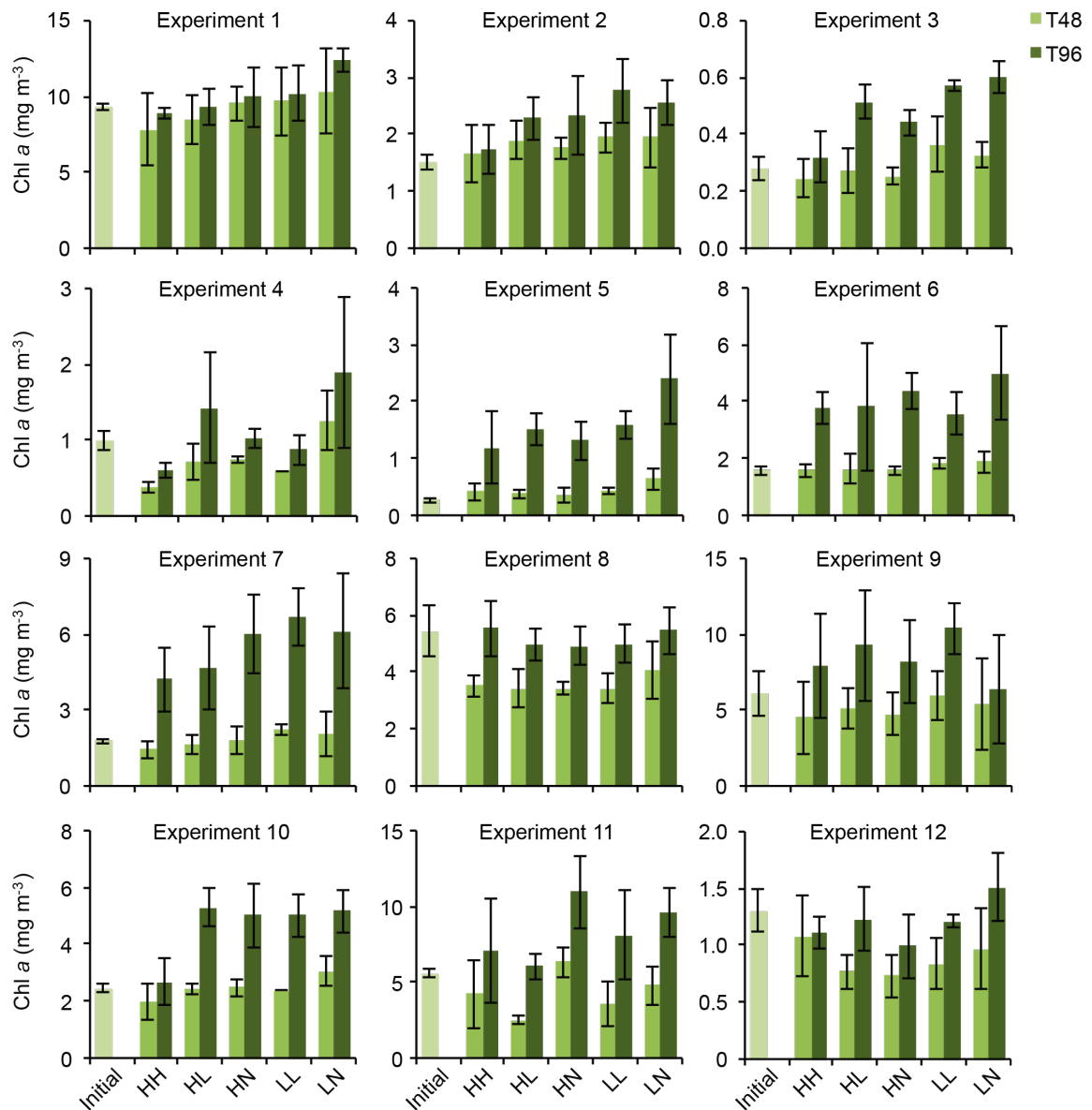


Figure 4.3: Chlorophyll *a* (Chl *a*) concentrations in individual experiments at the initial (T0), intermediate (T48), and final time points (T96) for the control (HH) and four reduced PAR and UVR treatments (HL, HN, LL, LN; Table 4.1). Error bars denote standard deviation of experiment triplicates (except for T0, for which error bars denote the measurement standard deviation).

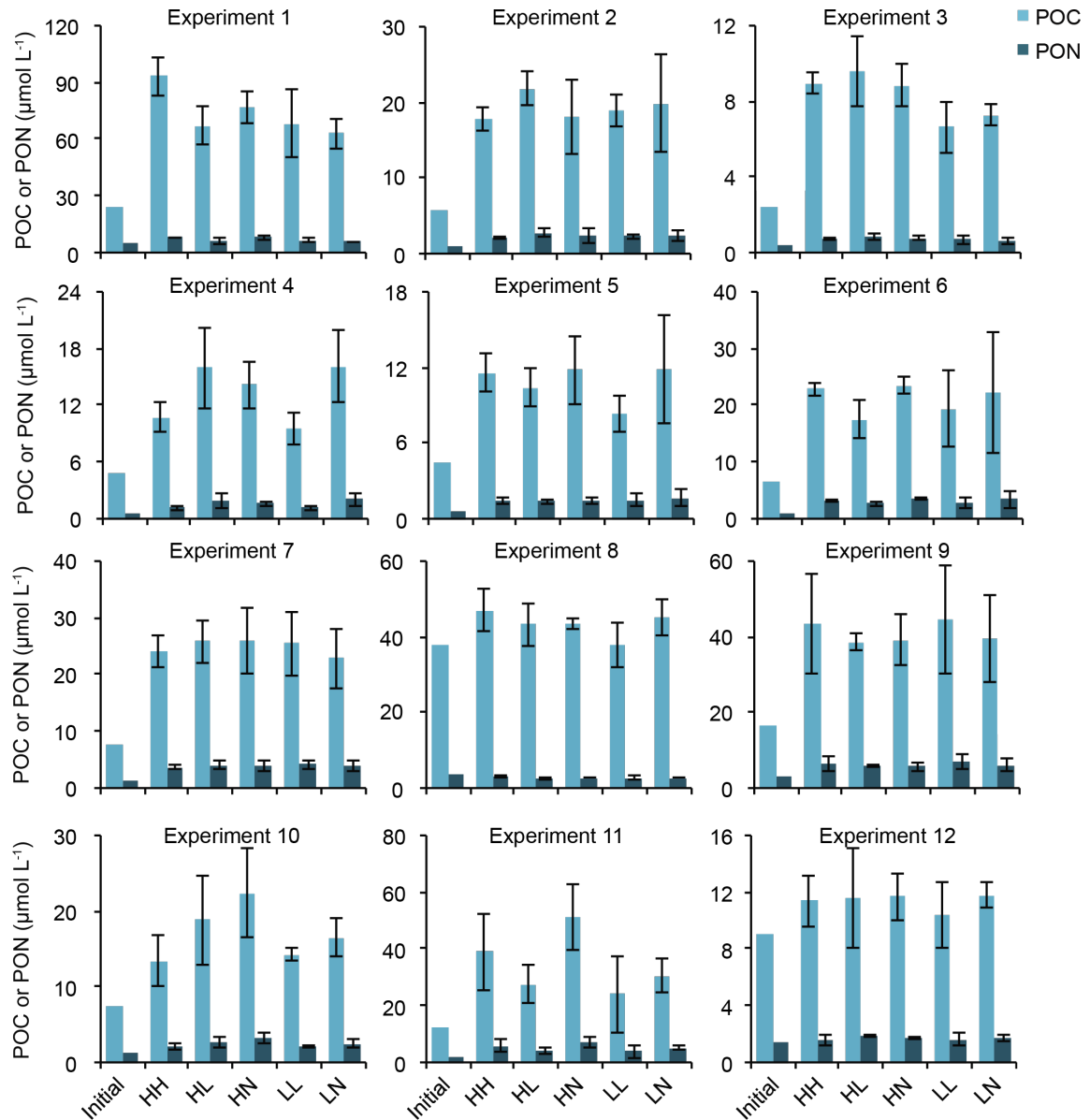


Figure 4.4: Particulate organic carbon (POC) and particulate organic nitrogen (PON) concentrations in individual experiments at the initial (T0) and final time point (T96) for the control (HH) and four reduced PAR and UVR treatments (HL, HN, LL, LN; Table 4.1). Error bars denote standard deviation of experiment triplicates (except for T0, for which replicates are unavailable).

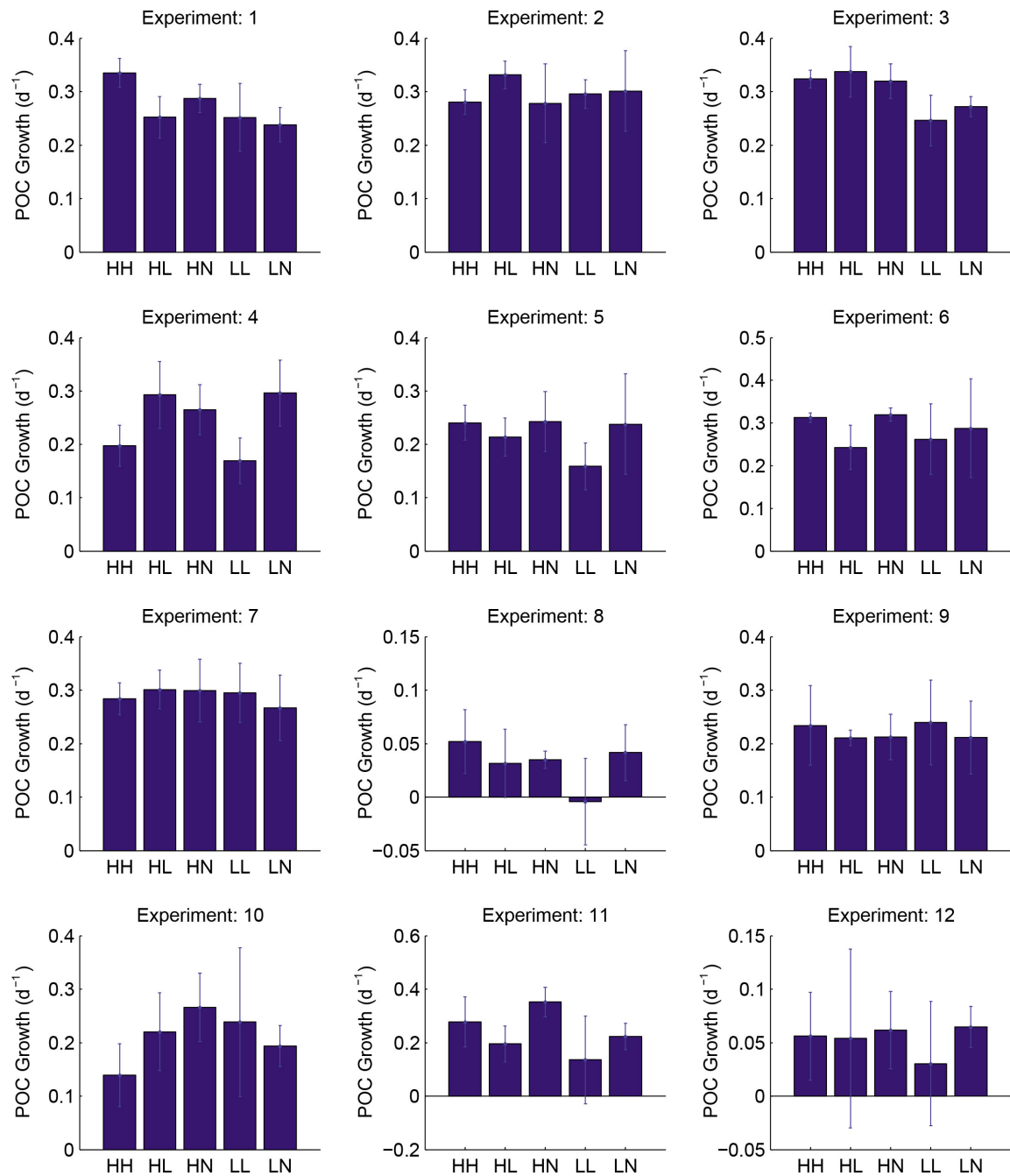


Figure 4.5: Average growth rates over four days in individual experiments based on changes in particulate organic carbon (POC) concentration at the final time point (T96) relative to initial (T0) for the control (HH) and four reduced PAR and UVR treatments (HL, HN, LL, LN; Table 4.1). Error bars denote standard deviation of experiment triplicates.

incubations. The average POC-specific growth rate across all experiments was  $0.22 \pm 0.11$   $\text{d}^{-1}$ . The maximum POC growth rate across all 12 experiments was  $0.37$   $\text{d}^{-1}$  in the control,  $0.39$  and  $0.41$   $\text{d}^{-1}$  in the reduced UVR treatments (HL and HN, respectively), and  $0.39$  and  $0.42$   $\text{d}^{-1}$  in the reduced PAR and reduced UVR treatments (LL and LN, respectively). POC-specific growth rates for the individual experiments exhibited significant differences ( $p < 0.05$ ) between treatments (Fig. 4.5) only in Exp. 3 (lower at reduced PAR) and Exp. 4 (higher in all treatments except for LL).

### Phytoplankton cellular ratios

Averaged over all 12 experiments, the mean POC:Chl a ratio (Table 4.3) was highest in the control ( $\sim 130$ ; HH), moderate in the reduced UVR treatments ( $\sim 100$ ; HL and HN), and lowest in the reduced UVR and PAR treatments ( $\sim 80$ ; LL and LN). The 1.6-fold difference between the control and the LL and LN treatments was statistically significant ( $p < 0.001$ ). Similarly, the decreasing trend in POC:Chl a over a gradient of reduced total radiation was significant ( $p < 0.05$ ). There were four individual experiments with significant differences between the reduced UVR and PAR treatments relative to the control (Exp. 1, 3, 10, and 11). Comparing the average POC:Chl a across all 12 experiments at T0 ( $67 \pm 47$ ) to that of T96 indicated that POC:Chl a roughly doubled in the control (HH), moderately increased in the reduced UVR treatments (HL and HN), and slightly increased in the reduced UVR and reduced PAR treatments (LL and LN).

The mean initial POC:PON ratio was  $6.7 \pm 1.6$  for all 12 experiments, with a range of 5.1 (Exp. 1) to 10.6 (Exp. 8). The POC:PON ratio generally increased over the four-day incubation period across all treatments and the control (Table 4.3), with no significant differences when averaged across all experiments or in all but one (Exp. 9) of the individual experiments. The increasing trend in POC:PON over a gradient of reduced total radiation was only significant at the 90% confidence interval.

### Nutrient utilization

Consistent with phytoplankton growth in all experiments, there was some nutrient utilization by phytoplankton in all experiments, although only to a small extent in some (Fig. 4.6). Averaged over all 12 experiments (Fig. 4.2C),  $\text{NO}_3^-$  concentrations decreased by 20% in the control, 22 to 27% in the reduced UVR treatments (HL and HN, respectively), and 19 to 20% in the reduced PAR and UVR treatments (LL and LN, respectively). A similar pattern

	HH (Control)	HL	HN	LL	LN
POC:Chl <i>a</i>	130 ± 86	86 ± 53	110 ± 59	<b>78 ± 37**</b>	<b>82 ± 48**</b>
POC:PON	8.9 ± 2.9	8.5 ± 3.1	8.6 ± 2.8	7.9 ± 2.7	8.4 ± 3.1
NO <sub>3</sub> <sup>-</sup> uptake	1.7 ± 1.5	1.9 ± 2.9	2.6 ± 3.3	1.5 ± 1.5	1.7 ± 1.3
Si(OH) <sub>4</sub> uptake	2.6 ± 2.6	2.8 ± 2.9	3.6 ± 3.3	2.9 ± 2.9	2.8 ± 3.0
PO <sub>4</sub> <sup>3-</sup> uptake	0.16 ± 0.11	0.17 ± 0.12	0.20 ± 0.13	0.16 ± 0.11	0.16 ± 0.11
Fv:Fm	0.38 ± 0.01	<b>0.47 ± 0.01**</b>	<b>0.46 ± 0.1**</b>	<b>0.52 ± 0.01**</b>	<b>0.52 ± 0.01**</b>
$\sigma$	370 ± 12	400 ± 12	410 ± 11	<b>460 ± 12**</b>	<b>450 ± 12**</b>

Table 4.3: Mean ± standard deviation for phytoplankton cellular ratios, nutrient uptake ( $\mu\text{mol L}^{-1}$ ), and variable fluorescence parameters averaged across all experiment controls and treatments. Bold values indicate significant differences from the control at  $p < 0.01$  (\*\*) and  $p < 0.05$  (\*) based on one-way ANOVA analysis.

was observed for Si(OH)<sub>4</sub> (Fig. 4.2D) and PO<sub>4</sub><sup>3-</sup> (not shown) concentrations, although there were no significant differences between treatments. The average nutrient utilization in the control across all 12 experiments (Table 4.3) was  $1.7 \pm 1.5 \mu\text{mol L}^{-1}$  for NO<sub>3</sub><sup>-</sup> and  $2.6 \pm 2.6 \mu\text{mol L}^{-1}$  for Si(OH)<sub>4</sub>, with a general pattern of increased nutrient utilization across a gradient of reduced UVR in both the high and low PAR scenarios, although the trend was not significant. On average, utilization of both NO<sub>3</sub><sup>-</sup> and Si(OH)<sub>4</sub> was  $\sim 1 \mu\text{mol L}^{-1}$  greater in the HN treatments than in the HH control (Table 4.3), although the differences were not statistically significant between the control and treatment or over a gradient of reduced total radiation. We note that utilization of Si(OH)<sub>4</sub> was consistently greater than that of NO<sub>3</sub><sup>-</sup> when averaged over all 12 experiments, indicating a dominance by diatoms.

### 4.3.3 Phytoplankton physiological response

#### Variable fluorescence

Across all 12 experiments, Fv:Fm decreased by 10% in the control relative to initial conditions. In contrast, Fv:Fm increased by 9-11% in the reduced UVR treatments (HL and HN, respectively) and by 21% in the reduced PAR and UVR treatments (LL and LN; Fig. 4.7A). The Fv:Fm response to differences in PAR and UVR was relatively fast, as indicated by the results at the T24 (not shown) and T48 (Fig. 4.7A) time points. The increased Fv:Fm in the reduced light treatments relative to the control was significant ( $p < 0.01$ ) when averaged across all experiments and when considered over a gradient of total radiation ( $p < 0.01$ ).

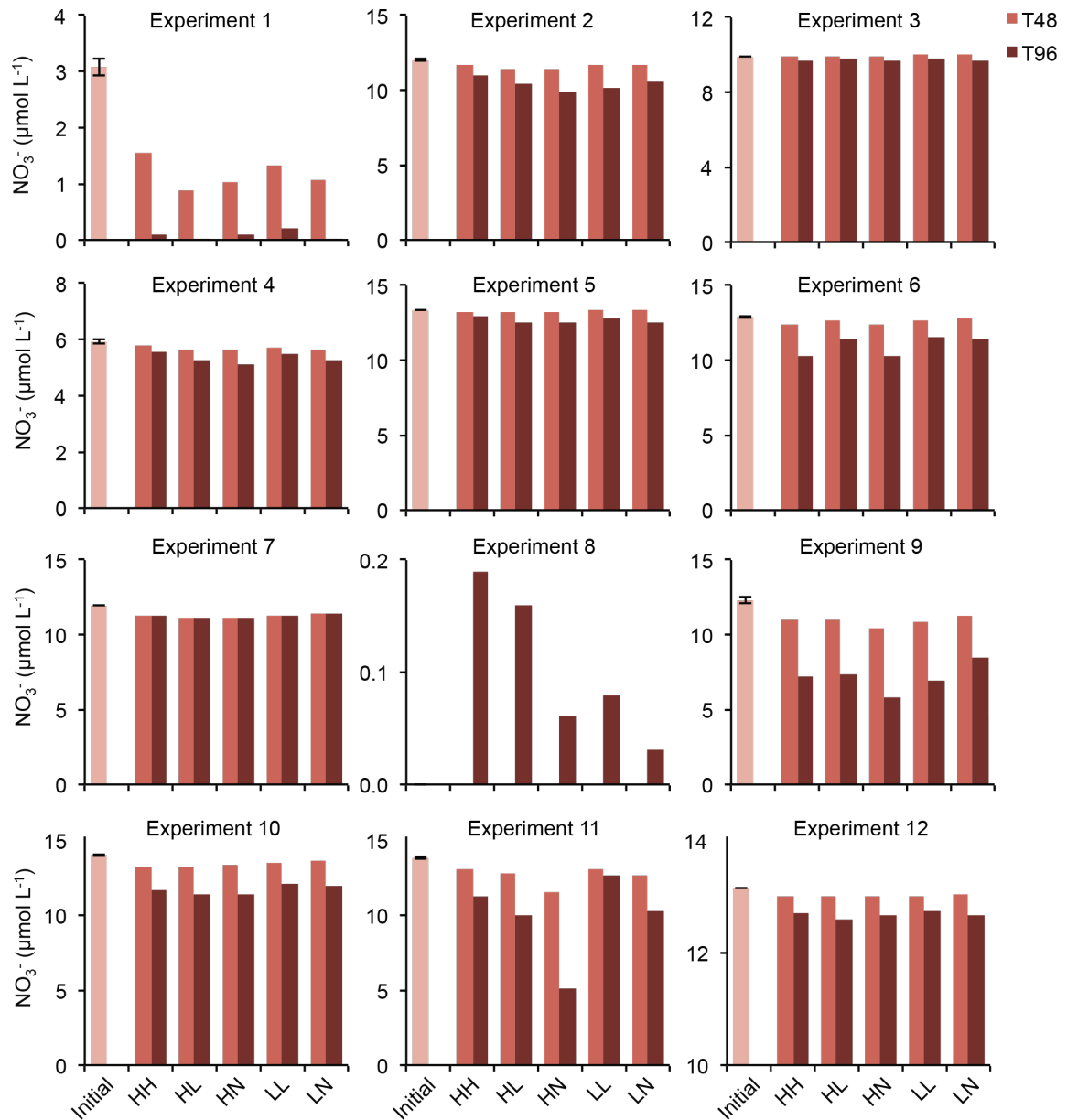


Figure 4.6: Nitrate ( $\text{NO}_3^-$ ) concentrations in individual experiments at the initial (T0), intermediate (T48), and final time points (T96) for the control (HH) and four reduced PAR and UVR treatments (HL, HN, LL, LN; Table 4.1). Error bars denote standard deviation of initial  $\text{NO}_3^-$  concentration across multiple rosette bottles used to collect water for experiments.

The increase in Fv:Fm in the reduced PAR and UVR relative to the control (HH) was also significant ( $p < 0.01$ ) in all 12 of the individual experiments (Fig. 4.8).

Similarly, there was a significant increase ( $p < 0.01$ ) in the mean maximum effective cross-sectional area ( $\sigma$ ) in the reduced PAR and UVR treatments (LL and LN) relative to the control (Table 4.3). Averaged over all experiments,  $\sigma$  significantly increased along a gradient of reduced UVR and PAR ( $p < 0.01$ ) and when calculated as a relative percent change from the initial condition (Fig. 4.7B). There were no significant changes in  $\tau$  (electron turnover time) when averaged across all experiments.

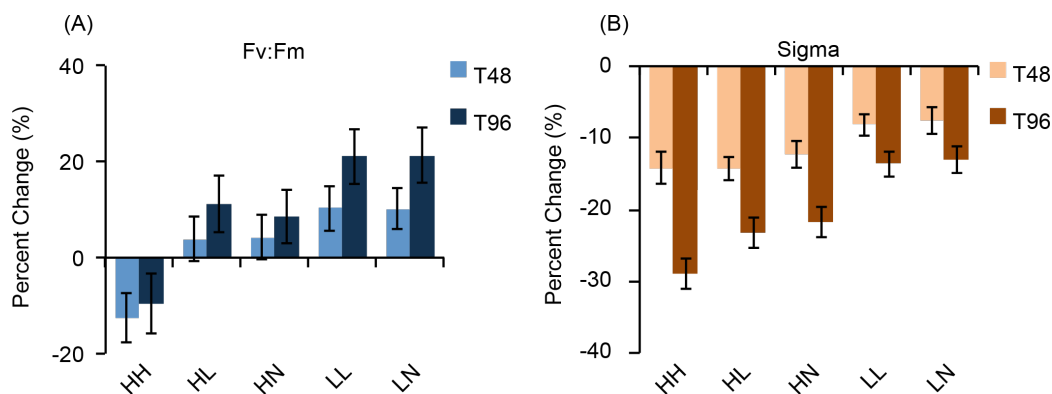


Figure 4.7: Mean percent change (%) at the intermediate (T48) and final (T96) time points relative to the initial (T0) across all 12 experiments for (A) the maximum photochemical efficiency (Fv:Fm) and (B) the maximum effective cross-sectional area ( $\sigma$ ) of photosystem II for the control (HH) and four reduced PAR and UVR treatments (HL, HN, LL, LN; Table 4.1). Error bars denote standard deviation.

### Photosynthetic parameters and light absorption

The maximum photosynthetic rate ( $P_{\max}^*$ ) averaged over all experiments increased significantly over a gradient of reduced total radiation ( $p < 0.01$ ) (Fig. 4.9A). The mean value of  $P_{\max}^*$  was  $7.9 \pm 5.5$  mg C hr<sup>-1</sup> in the control,  $8.8 \pm 5.5$  mg C hr<sup>-1</sup> and  $9.3 \pm 5.5$  mg C hr<sup>-1</sup> in the reduced UVR treatments (HL and HN, respectively), and  $11 \pm 5.0$  mg C hr<sup>-1</sup> and  $11 \pm 7.0$  mg C hr<sup>-1</sup> in the reduced UVR and PAR treatments (LL and LN, respectively) (mean  $\pm$  SD), demonstrating inhibition of photosynthesis at higher PAR and higher UVR.

The maximum growth rate ( $\mu_{\max}$ ) based on significant P-E curves averaged across all experiments at T96 was twice as high in the reduced PAR and no UVR treatment ( $1.1 \pm 0.6$  d<sup>-1</sup>) (LN; Fig. 4.9B) than in the control ( $0.5 \pm 0.2$  d<sup>-1</sup>). The same relationship was

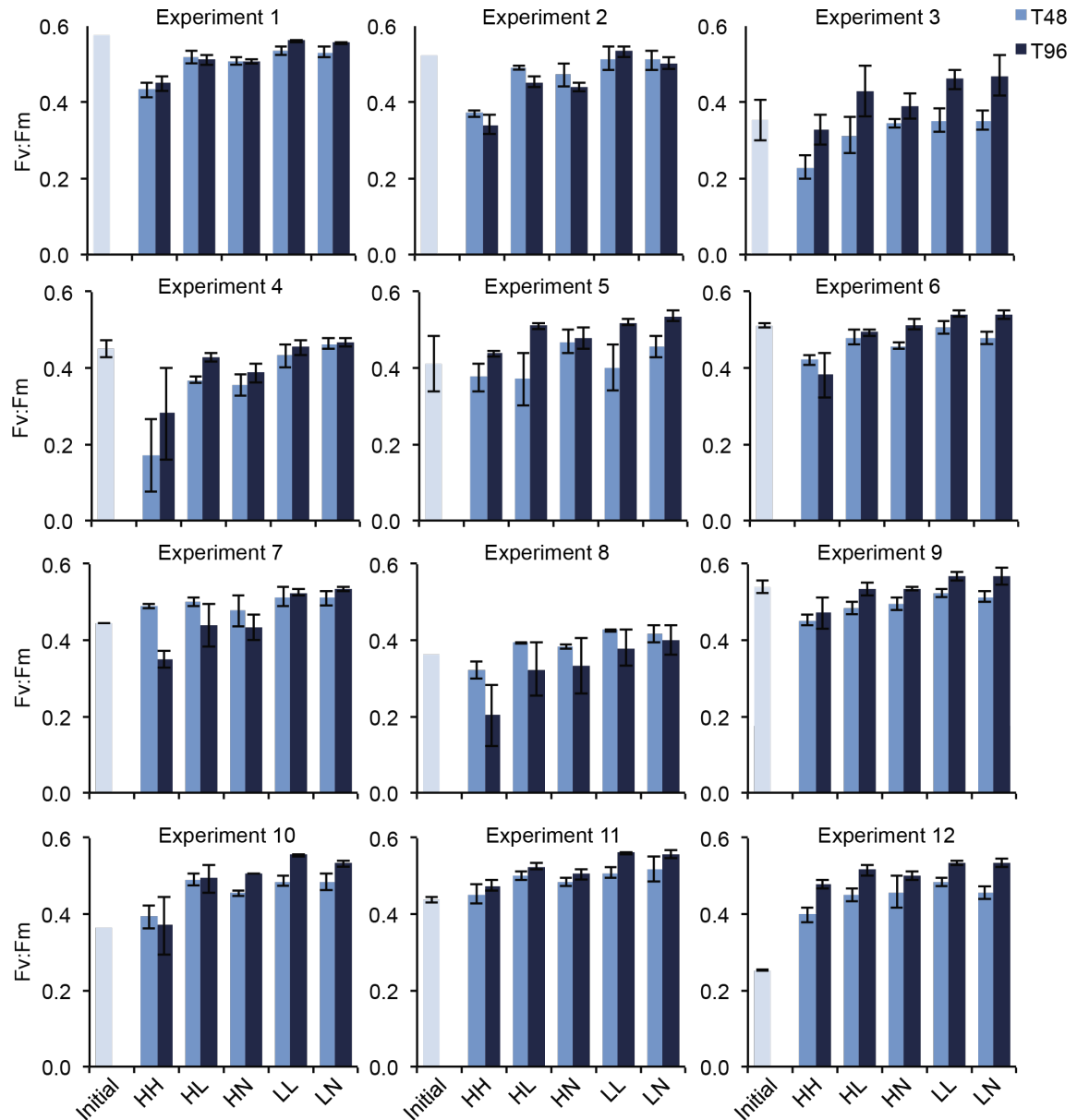


Figure 4.8: Fv:Fm (maximum efficiency of photosystem II) in individual experiments at the intermediate (T48) and final time points (T96) relative to the initial (T0) for the control (HH) and four reduced PAR and UVR treatments (HL, HN, LL, LN; Table 4.1). Error bars denote standard deviation of experiment triplicates (except for T0, for which error bars denote the measurement standard deviation when available).

observed for the maximum  $\mu_{\max}$  in the 12 individual experiments, which was as high as  $1.9 \text{ d}^{-1}$  in the reduced PAR and no UVR treatment (LN) as compared to  $0.88 \text{ d}^{-1}$  in the control.

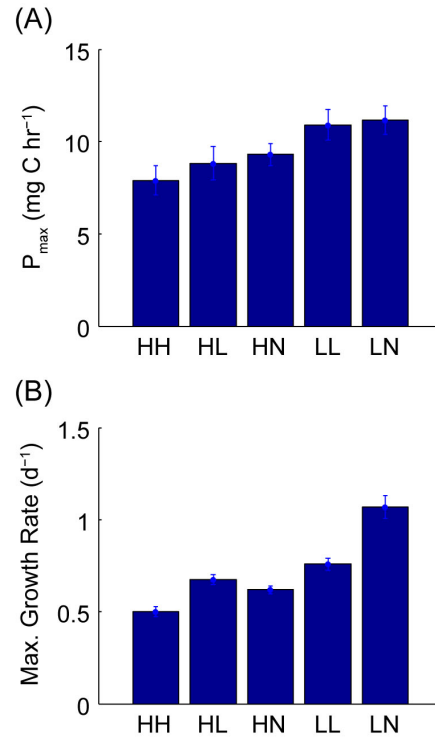


Figure 4.9: Average rates over all 12 experiments for (A) maximum photosynthetic rate and (B) maximum growth rate at the final time point (T96) for the control (HH) and treatments (HL, HN, LL, LN; Table 1). Error bars denote standard error.

Averaged over all experiments, there were no significant differences between the control and the reduced UVR and PAR treatments or significant trends for  $\alpha^*$ ,  $E_K$ ,  $\bar{a}^*$  or  $\Phi_m$ . Similarly, there were no significant differences or trends across treatments for the MAA index of UVR absorption.

## 4.4 Discussion

### 4.4.1 Effects of UVR and PAR on polar marine phytoplankton

Results from a number of previous experimental, field, and laboratory studies have demonstrated that the overall consequence of high UVR on phytoplankton is decreased rates of

primary production (e.g. *Holm-Hansen et al.*, 1993; *Smith and Cullen*, 1995; *Vernet*, 2000; *Arrigo et al.*, 2003), with UVR-inhibition of both light-limited and light-saturated carbon uptake (*Cullen et al.*, 1992; *Holm-Hansen*, 1997; *Neale et al.*, 1998). The observed photosynthetic response of phytoplankton to UVR exposure is highly variable, with differences attributed to the degree of adaptation to *in situ* conditions and to phytoplankton community composition (*Vernet*, 2000). Similarly, high PAR causes inhibition of photosynthesis through photodamage to phytoplankton cells, with variation in the response being critically dependent on the light history of the phytoplankton and level of acclimation prior to exposure (e.g. *Villafañe et al.*, 2003; *Alderkamp et al.*, 2011). Previous work suggests that photosynthesis may be more inhibited in polar phytoplankton than in temperate or tropical communities (e.g. *Lesser*, 1996), potentially due to the discrepancy between temperature-dependent enzyme-driven recovery rates and temperature-independent photodamage processes (*Vernet*, 2000). The short-term response of phytoplankton to high PAR and high UVR frequently differs from the long-term response because different processes are involved in the damage and acclimation mechanisms (as reviewed by *Vernet*, 2000), and because phytoplankton are able to adjust to new light environments through photoacclimation, which takes place on time scales ranging from minutes to days (*Falkowski and LaRoche*, 1991). Here we consider the effects of reduced UVR and PAR in terms of both short-term acclimation and long-term growth to understand the response of phytoplankton to under-ice light conditions as compared those of open water.

#### 4.4.2 Short-term phytoplankton acclimation

In the present study, the most compelling evidence that the under-ice light environment is ideally suited for phytoplankton is based on observations of the short-term physiological responses. Notably, the instantaneous maximum phytoplankton growth rates ( $\mu_{\max}$ ) were more than twice as high in the low PAR and no UVR treatment than in the high PAR and high UVR control, with  $\mu_{\max}$  from the experimental treatments on par with those observed in the unprecedented under-ice phytoplankton bloom during ICESCAPE (mean:  $0.9 \text{ d}^{-1}$ ; maximum:  $1.6 \text{ d}^{-1}$ ; *Arrigo et al.*, 2014). Similarly, the increase in maximum photosynthetic rates ( $P_{\max}^*$ ) that we observed across a gradient of reduced total radiation is consistent with inhibition of photosynthesis and growth rates at high PAR and high UVR (e.g. *Lesser*, 1996). Thus, phytoplankton growing under simulated under-ice conditions grew twice as fast as those in simulated ice-free conditions.

Another indicator that the under-ice environment may be more suitable for phytoplankton growth due to reduced radiative stress was demonstrated by variable fluorescence measurements. While Fv:Fm consistently increased in the treatments that simulated under-ice light conditions relative to initial conditions, Fv:Fm in the high PAR and high UVR control consistently decreased. The significant differences in Fv:Fm between the control and all treatments illustrates that the physiological response was due to both reduced PAR and reduced UVR, with a detectable response even at the intermediate time points. The fact that  $P_{\max}^*$  increased along with  $\sigma$  at lower total radiation while the specific absorption coefficient ( $\bar{a}^*$ ) did not indicate that reduced radiation was likely associated with increased photochemistry rather than changes in the optical cross-section or increased photoinhibition, which can also result in increased  $\sigma$ .

Finally, although Chl *a* is often used as a proxy for phytoplankton biomass, the differences we observed in Chl *a* between the control and treatments are likely due to changes in cell pigmentation due to photoacclimation rather than changes in growth rate. Evidence for this was illustrated by the increase in POC:Chl *a* ratios over the course of the experiments, ranging from a slight increase in the low PAR and low UVR treatments to a doubling in the high PAR and high UVR control. These results are consistent with loss of pigmentation per cell at higher total radiation, which is considered to be a typical response to increased UVR and PAR exposure that can occur within a few hours of exposure (e.g. *Gerber and Häder, 1995; Maske and Latasa, 2011*). These results indicate that prior to the start of the experiments, phytoplankton were generally acclimated to lower PAR and UVR conditions than those of the experiments, even in the reduced PAR treatments that simulated bare ice. This finding is consistent with that fact that most experiments were conducted with phytoplankton collected from waters with high concentrations of sea ice with moderate snow cover, which attenuates substantially more sunlight than bare or ponded sea ice.

#### 4.4.3 Long-term phytoplankton growth

In contrast to the short-term acclimation response described above, there was no statistically significant response for the longer-term phytoplankton growth measurements (i.e. concentrations of POC and PON and nutrients). The lack of a significant response may be due to the relatively short duration of the four-day incubation experiments relative to the longer timescale needed for detection of significant changes in phytoplankton biomass accumulation and nutrient consumption at the low temperatures of the experiments. Regardless, the

patterns of relative changes in POC and PON and nutrient concentrations over a gradient of reduced UVR conditions (HH-HL-HN and LL-LN) are consistent with what we would expect (i.e. higher biomass and nutrient consumption at reduced UVR flux; Fig. 4.2), even though they were not statistically significant. Further, although there were no significant differences in POC-based growth rates, we note that this measurement represents the average growth over four days, in contrast to the maximum growth rates ( $\mu_{\max}$ ) derived from photosynthetic parameters described above, which are instantaneous measurements after four days of exposure to the experimental PAR and UVR conditions. Thus, given the significant differences we observed in photosynthetic rates, maximum growth rates, and variable fluorescence, we expect that a phytoplankton growth response of POC and PON accumulation and nutrient uptake would be observed in experiments of longer duration.

At the same time, however, the capability of phytoplankton to adjust to increased PAR and UVR through photoacclimation (e.g. *Falkowski and LaRoche*, 1991; *Villafañe et al.*, 2003; *van de Poll et al.*, 2006) indicates that over longer timescales of exposure, the phytoplankton community may gradually become less sensitive to the damaging effects of high PAR and high UVR. For example, phytoplankton can increase cellular xanthophyll cycle pigments (*van de Poll et al.*, 2006; *van de Poll and Buma*, 2009) and incorporate photoprotective pigments such as MAAs to absorb harmful excess UVR (e.g. *Bischof et al.*, 2002; *Helbling and Villafane*, 2002). However, the metabolic costs associated with these photoacclimation processes (e.g. *Vernet*, 2000) may still result in lower phytoplankton growth rates in open water than beneath the sea ice, as observed in the field during ICESCAPE (*Palmer et al.*, 2013). Additionally, long-term acclimation to higher PAR and UVR may be accompanied by changes in phytoplankton community composition due to species-specific repair and protection mechanisms (e.g. *Vernet*, 2000; *Hessen et al.*, 2012). More work is needed to better understand the long-term acclimation of under-ice phytoplankton to increased PAR and UVR, as well as the resulting implications for primary production and phytoplankton community composition before and after sea ice retreat.

#### 4.4.4 Implications for phytoplankton in the under-ice environment

Consistent with field observations of extraordinary phytoplankton growth beneath first-year sea ice (*Arrigo et al.*, 2012), our results demonstrate that the under-ice light environment is ideally suited for phytoplankton growth due to the attenuation of excessive PAR and UVR by sea ice. While we cannot fully separate the effects of visible light and UVR, our

findings illustrate that both high PAR and high UVR are damaging for phytoplankton, as demonstrated by lower photosynthetic rates and efficiency in the simulated ice-free control as compared to the four simulated under-ice treatments. In our experiments, the short-term phytoplankton acclimation response was typically greater in the treatments designed to approximate the conditions beneath meter-thick bare sea ice ( $\sim 15\%$  PAR transmission) than in the treatments designed to approximate the conditions beneath melt-ponded sea ice ( $\sim 40\%$  PAR transmission). However, this result is likely due to the early season (May-June) sampling of waters beneath sea ice with snow cover ( $\sim 1\%$  PAR transmission; *Lowry et al.*, 2016), such that phytoplankton cells were acclimated to lower light than in the experimental conditions. We expect that later in the season, when phytoplankton are acclimated to increased PAR transmitted through melt-ponded sea ice, very high phytoplankton growth rates would be achieved in high PAR and low UVR conditions, consistent with field observations beneath melt ponds (*Arrigo et al.*, 2012; *Palmer et al.*, 2013).

Our experimental results provide evidence that the reduced transmission of PAR and UVR through sea ice contributes to making the under-ice environment optimal for phytoplankton growth. This work provides context for recent field observations of unprecedented phytoplankton blooms in the ice-covered Chukchi Sea and furthers our understanding of this relatively understudied ecosystem. To fully understand the factors that contribute to the success of phytoplankton blooms beneath the sea ice and the implications of continued changes in Arctic sea ice cover will require additional field, lab, and experimental work.

## Acknowledgments

We would like to acknowledge the captain and crew of the *USCGC Healy* and members of the SUBICE team for their support in field sampling and assistance with maintaining flow-through of the deck incubators during below-freezing spring conditions. Funding to support K.E.L. was provided by the NSF Graduate Research Fellowship (Grant No. DGE-0645962) and the Stanford University Gerald J. Lieberman Fellowship. Project support was provided by NSF Grant No. PLR-1304563 to K.R.A. We would also like to thank Hannah Joy-Warren, Virginia Selz, and Gert van Dijken of Stanford University for their contributions to discussions and efforts toward this study.

# Bibliography

- Alderkamp, A.-C. C., V. Garçon, H. J. W. de Baar, and K. R. Arrigo (2011), Short-term photoacclimation effects on photoinhibition of phytoplankton in the Drake Passage (Southern Ocean), *Deep Sea Research Part I: Oceanographic Research Papers*, 58(9), 943–955.
- Alderkamp, A.-C. C., G. L. van Dijken, K. E. Lowry, T. L. Connelly, M. Lagerström, R. M. Sherrell, C. Haskins, E. Rogalsky, O. Schofield, S. E. Stammerjohn, P. L. Yager, and K. R. Arrigo (2015), Fe availability drives phytoplankton photosynthesis rates during spring bloom in the Amundsen Sea Polynya, Antarctica, *Elementa Science of the Anthropocene*, 3(000043), 1–26.
- Ardyna, M., M. Babin, M. Gosselin, E. Devred, S. Bélanger, A. Matsuoka, and J. É. Tremblay (2013), Parameterization of vertical chlorophyll *a* in the Arctic Ocean: impact of the subsurface chlorophyll maximum on regional, seasonal, and annual primary production estimates, *Biogeosciences*, 10(6), 4383–4404.
- Ardyna, M., M. Babin, M. Gosselin, E. Devred, L. Rainville, and J.-E. Tremblay (2014), Recent Arctic Ocean sea ice loss triggers novel fall phytoplankton blooms, *Geophysical Research Letters*, 41(17), 6207–6212.
- Armstrong, F., C. R. Stearns, and J. Strickland (1967), The measurement of upwelling and subsequent biological process by means of the Technicon Autoanalyzer® and associated equipment, *Deep-Sea Research*, 14, 381–389.
- Arrigo, K. R. (2015), Impacts of Climate on EcoSystems and Chemistry of the Arctic Pacific Environment (ICESCAPE), *Deep Sea Research Part II: Topical Studies in Oceanography*, 118, 1–6.
- Arrigo, K. R. (2016), Impacts of climate on ecosystems and chemistry of the Arctic Pacific

- environment (ICESCAPE III), *Deep Sea Research Part II: Topical Studies in Oceanography*, 130(C), 1–5.
- Arrigo, K. R., and G. L. van Dijken (2011), Secular trends in Arctic Ocean net primary production, *Journal of Geophysical Research: Oceans (1978–2012)*, 116, C09,011.
- Arrigo, K. R., and G. L. van Dijken (2015), Continued increases in Arctic Ocean primary production, *Progress in Oceanography*, 136(C), 60–70.
- Arrigo, K. R., D. Lubin, G. L. van Dijken, O. Holm-Hansen, and E. Morrow (2003), Impact of a deep ozone hole on Southern Ocean primary production, *Journal of Geophysical Research*, 108(C5), 3154.
- Arrigo, K. R., G. L. van Dijken, and S. Pabi (2008), Impact of a shrinking Arctic ice cover on marine primary production, *Geophysical Research Letters*, 35(19), L19,603.
- Arrigo, K. R., M. Mills, L. Kropuenske, G. L. van Dijken, A.-C. C. Alderkamp, and D. Robinson (2010), Photophysiology in Two Major Southern Ocean Phytoplankton Taxa: Photosynthesis and Growth of *Phaeocystis antarctica* and *Fragilariopsis cylindrus* under Different Irradiance Levels, *Integrative and Comparative Biology*, 50(6), 950–966.
- Arrigo, K. R., D. K. Perovich, R. S. Pickart, and Z. W. Brown (2012), Massive phytoplankton blooms under Arctic sea ice, *Science*, 336, 1408–1408.
- Arrigo, K. R., D. K. Perovich, R. S. Pickart, Z. W. Brown, G. L. van Dijken, K. E. Lowry, M. M. Mills, M. A. Palmer, W. M. Balch, N. R. Bates, C. R. Benitez-Nelson, E. Brownlee, K. E. Frey, S. R. Laney, J. Mathias, A. Matsuoka, B. G. Mitchell, G. W. K. Moore, R. A. Reynolds, H. M. Sosik, and J. H. Swift (2014), Phytoplankton blooms beneath the sea ice in the Chukchi Sea, *Deep Sea Research Part II: Topical Studies in Oceanography*, 105, 1–16.
- Arrigo, K. R., G. L. van Dijken, K. E. Lowry, and M. M. Mills (2016), Improved Estimates of Primary Production in the Chukchi Sea, in *Ocean Sciences Meeting*, New Orleans, LA.
- Bates, N. R., M. H. P. Best, and D. A. Hansell (2005), Spatio-temporal distribution of dissolved inorganic carbon and net community production in the Chukchi and Beaufort Seas, *Deep Sea Research Part II: Topical Studies in Oceanography*, 52(24-26), 3303–3323.

- Bates, N. R., J. T. Mathis, and L. W. Cooper (2009), Ocean acidification and biologically induced seasonality of carbonate mineral saturation states in the western Arctic Ocean, *Journal of Geophysical Research: Oceans (1978–2012)*, *114*, C11,007.
- Bates, N. R., W. J. Cai, and J. T. Mathis (2011), The ocean carbon cycle in the western Arctic Ocean: Distributions and air-sea fluxes of carbon dioxide, *Oceanography*, *24*(3), 186–201.
- Bélanger, S., J. K. Ehn, and M. Babin (2007), Impact of sea ice on the retrieval of water-leaving reflectance, chlorophyll a concentration and inherent optical properties from satellite ocean color data, *Remote Sensing of Environment*, *111*(1), 51–68.
- Bélanger, S., M. Babin, and J. Tremblay (2013), Increasing cloudiness in Arctic damps the increase in phytoplankton primary production due to sea ice receding, *Biogeosciences*.
- Belsley, D. A., E. Kuh, and R. E. Welsch (1980), *Detecting and assessing collinearity*, Identifying Influential Data and Sources of Collinearity, John Wiley & Sons, Inc., Hoboken, NJ, USA.
- Bischof, K., D. Hanelt, and C. Wiencke (2002), UV Radiation and Arctic Marine Macroalgae, in *UV Radiation and Arctic Ecosystems*, pp. 227–243, Springer Berlin Heidelberg, Berlin, Heidelberg.
- Booth, C. R., J. H. Morrow, and T. P. Coohill (1997), Impacts of solar UVR on aquatic microorganisms, *Photochemistry and Photobiology*, *65*(2), 252–269.
- Brown, Z. W., K. L. Casciotti, R. S. Pickart, J. H. Swift, and K. R. Arrigo (2015a), Aspects of the marine nitrogen cycle of the Chukchi Sea shelf and Canada Basin, *Deep Sea Research Part II: Topical Studies in Oceanography*, *118*, 73–87.
- Brown, Z. W., K. Lowry, M. A. Palmer, and G. L. van Dijken (2015b), Characterizing the subsurface chlorophyll a maximum in the Chukchi Sea and Canada Basin, *Deep Sea Research Part II: Topical Studies in Oceanography*, *118*, 88–104.
- Bursa, A. (1963), Phytoplankton in coastal waters of the Arctic Ocean at Point Barrow, Alaska, *Arctic*.
- Campbell, R. G., E. B. Sherr, C. J. Ashjian, S. Plourde, B. F. Sherr, V. Hill, and D. A. Stockwell (2009), Mesozooplankton prey preference and grazing impact in the western

- Arctic Ocean, *Deep Sea Research Part II: Topical Studies in Oceanography*, 56(17), 1274–1289.
- Carmack, E., and P. Wassmann (2006), Food webs and physical–biological coupling on pan-Arctic shelves: Unifying concepts and comprehensive perspectives, *Progress in Oceanography*, 71, 446–477.
- Cavaliere, D. J., and S. Martin (1994), The contribution of Alaskan, Siberian, and Canadian coastal polynyas to the cold halocline layer of the Arctic Ocean, *Journal of Geophysical Research: Oceans (1978–2012)*, 99(C9), 18,343–18,362.
- Cavaliere, D. J., C. L. Parkinson, P. Gloersen, and H. J. Zwally (1996), Sea Ice Concentrations from Nimbus-7 SMMR and DMSP SSM/I-SSMIS Passive Microwave Data, Version 1., *NASA National Snow and Ice Data Center Distributed Active Archive Center*.
- Coachman, L. K., K. Aagaard, and R. B. Tripp (1975), *Bering Strait: The Regional Physical Oceanography*, University of Washington Press, Seattle, Washington.
- Codispoti, L. A., C. Flagg, V. Kelly, and J. H. Swift (2005), Hydrographic conditions during the 2002 SBI process experiments, *Deep Sea Research Part II: Topical Studies in Oceanography*, 52(24-26), 3199–3226.
- Codispoti, L. A., C. N. Flagg, and J. H. Swift (2009), Hydrographic conditions during the 2004 SBI process experiments, *Deep Sea Research Part II: Topical Studies in Oceanography*, 56(17), 1144–1163.
- Codispoti, L. A., V. Kelly, A. Thessen, P. Matrai, S. Suttles, V. Hill, M. Steele, and B. Light (2013), Synthesis of primary production in the Arctic Ocean: III. Nitrate and phosphate based estimates of net community production, *Progress in Oceanography*, 110(C), 126–150.
- Comiso, J. C. (2012), Large decadal decline of the Arctic multiyear ice cover, *Journal of Climate*, 25(4), 1176–1193.
- Comiso, J. C., C. L. Parkinson, R. Gersten, and L. Stock (2008), Accelerated decline in the Arctic sea ice cover, *Geophysical Research Letters*, 35(1), L01,703.
- Cooper, L. W., T. E. Whitledge, J. M. Grebmeier, and T. Weingartner (1997), The nutrient, salinity, and stable oxygen isotope composition of Bering and Chukchi Seas waters in and

- near the Bering Strait, *Journal of Geophysical Research: Oceans (1978–2012)*, *102*(C6), 12,563–12,573.
- Cota, G. F., L. R. Pomeroy, W. G. Harrison, E. P. Jones, F. Peters, W. M. Sheldon, and T. R. Weingartner (1996), Nutrients, primary production and microbial heterotrophy in the southeastern Chukchi Sea: Arctic summer nutrient depletion and heterotrophy, *Marine Ecology Progress Series*, *135*(1-3), 247–258.
- Cottrell, M. T., R. R. Malmstrom, V. Hill, and A. E. Parker (2006), The metabolic balance between autotrophy and heterotrophy in the western Arctic Ocean, *Deep Sea Research I*, *53*(11), 1831–1844.
- Coupel, P., H. Y. Jin, M. Joo, R. Horner, H. A. Bouvet, M. A. Sicre, J. C. Gascard, J. F. Chen, V. Garçon, and D. Ruiz-Pino (2012), Phytoplankton distribution in unusually low sea ice cover over the Pacific Arctic, *Biogeosciences*, *9*(11), 4835–4850.
- Cullen, J. J., and R. F. Davis (2003), The blank can make a big difference in oceanographic measurements, *Limnology and Oceanography Bulletin*, *12*(29), 29–35.
- Cullen, J. J., P. J. Neale, and M. P. Lesser (1992), Biological Weighting Function for the Inhibition of Phytoplankton Photosynthesis by Ultraviolet Radiation, *Science*, *258*(5082), 646–650.
- Doney, S. C., D. M. Glover, S. J. McCue, and M. Fuentes (2003), Mesoscale variability of Sea-viewing Wide Field-of-view Sensor (SeaWiFS) satellite ocean color: Global patterns and spatial scales, *Journal of Geophysical Research: Oceans (1978–2012)*, *108*(C2), 3024.
- Dunton, K. H., J. L. Goodall, S. V. Schonberg, J. M. Grebmeier, and D. R. Maidment (2005), Multi-decadal synthesis of benthic–pelagic coupling in the western arctic: Role of cross-shelf advective processes, *Deep Sea Research Part II: Topical Studies in Oceanography*, *52*(24–26), 3462–3477.
- English, T. S. (1961), Some biological oceanographic observations in the central North Polar Sea drift station Alpha, 1957-1958, *13*, 1–80.
- Eppley, R. W. (1972), Temperature and phytoplankton growth in the sea, *Fish Bull*, *70*(4).
- Falkowski, P. G., and J. LaRoche (1991), Acclimation to spectral irradiance in algae, *Journal of Phycology*, *27*(1), 8–14.

- Frey, K. E., D. K. Perovich, and B. Light (2011), The spatial distribution of solar radiation under a melting Arctic sea ice cover, *Geophysical Research Letters*, 38(22), L22,501.
- Gao, Z., L. Chen, H. Sun, B. Chen, and W.-J. Cai (2012), Distributions and air-sea fluxes of carbon dioxide in the Western Arctic Ocean, *Deep Sea Research Part II: Topical Studies in Oceanography*, 81-84, 46–52.
- Gerber, S., and D.-P. Häder (1995), Effects of enhanced solar irradiation on chlorophyll fluorescence and photosynthetic oxygen production of five species of phytoplankton, *FEMS microbiology ecology*, 16(1), 33–41.
- Gong, D., and R. S. Pickart (2015), Summertime circulation in the eastern Chukchi Sea, *Deep Sea Research Part II: Topical Studies in Oceanography*, 118, 18–31.
- Gosselin, M., M. Levasseur, P. Wheeler, R. Horner, and B. Booth (1997), New measurements of phytoplankton and ice algal production in the Arctic Ocean, *Deep Sea Research Part II: Topical Studies in Oceanography*, 44(8), 1623–1644.
- Gradinger, R. (2009), Sea-ice algae: Major contributors to primary production and algal biomass in the Chukchi and Beaufort Seas during May/June 2002, *Deep Sea Research Part II: Topical Studies in Oceanography*, 56(17), 1201–1212.
- Grebmeier, J. M. (2012), Shifting patterns of life in the Pacific Arctic and Sub-Arctic Seas, *Annual Review of Marine Science*, 4(1), 63–78.
- Grebmeier, J. M., L. W. Cooper, H. M. Feder, and B. I. Sirenko (2006), Ecosystem dynamics of the Pacific-influenced Northern Bering and Chukchi Seas in the Amerasian Arctic, *Progress in Oceanography*, 71(2-4), 331–361.
- Grebmeier, J. M., B. A. Bluhm, L. W. Cooper, S. L. Danielson, K. R. Arrigo, A. L. Blanchard, J. T. Clarke, R. H. Day, K. E. Frey, R. R. Gradinger, M. Kędra, B. Konar, K. J. Kuletz, S. H. Lee, J. R. Lovvorn, B. L. Norcross, and S. R. Okkonen (2015), Ecosystem characteristics and processes facilitating persistent macrobenthic biomass hotspots and associated benthivory in the Pacific Arctic, *Progress in Oceanography*, 136(C), 92–114.
- Grömping, U. (2006), Relative importance for linear regression in R: the package relaimpo, *Journal of Statistical Software*, 17(1).

- Hameedi, M. J. (1978), Aspects of water column primary productivity in the Chukchi Sea during summer, *Marine Biology*, 48(1), 37–46.
- Hansell, D., T. Whitledge, and J. J. Goering (1993), Patterns of nitrate utilization and new production over the Bering-Chukchi shelf, *Continental Shelf Research*, 13(5-6), 601–627.
- Helbling, E. W., and V. E. Villafane (2002), UV Radiation Effects on Phytoplankton Primary Production: A Comparison Between Arctic and Antarctic Marine Ecosystems, in *UV Radiation and Arctic Ecosystems*, pp. 203–226, Springer Berlin Heidelberg, Berlin, Heidelberg.
- Helbling, E. W., V. Villafane, M. Ferrario, and O. Holm-Hansen (1992), Impact of natural ultraviolet radiation on rates of photosynthesis and on specific marine phytoplankton species., *Marine Ecology Progress Series*, 80(1), 89–100.
- Henriksen, K., T. H. Blackburn, B. A. Lomstein, and C. P. McRoy (1993), Rates of nitrification, distribution of nitrifying bacteria and inorganic N fluxes in northern Bering-Chukchi shelf sediments, *Continental Shelf Research*, 13(5-6), 629–651.
- Hessen, D. O., H. Frigstad, P. J. Færøvig, M. W. Wojewodzcic, and E. Leu (2012), UV radiation and its effects on P-uptake in arctic diatoms, *Journal of experimental marine biology and ecology*, 411, 45–51.
- Hill, V., and G. F. Cota (2005), Spatial patterns of primary production on the shelf, slope and basin of the Western Arctic in 2002, *Deep Sea Research Part II: Topical Studies in Oceanography*, 52(24-26), 3344–3354.
- Hill, V., G. F. Cota, and D. Stockwell (2005), Spring and summer phytoplankton communities in the Chukchi and Eastern Beaufort Seas, *Deep Sea Research Part II: Topical Studies in Oceanography*, 52(24-26), 3369–3385.
- Holm-Hansen, O. (1997), Short-and Long-Term Effects of UVA and UVB on Marine Phytoplankton Productivity, *Photochemistry and Photobiology*, 65(2), 266–268.
- Holm-Hansen, O., C. J. Lorenzen, R. W. Holmes, and J. D. H. Strickland (1965), Fluorometric determination of chlorophyll, *ICES Journal of Marine Science*, 30(1), 3–15.
- Holm-Hansen, O., E. W. Helbling, and D. Lubin (1993), Ultraviolet radiation in Antarctica: inhibition of primary production, *Photochemistry and Photobiology*, 58(4), 567–570.

- Horner, R., and G. C. Schrader (1982), Relative contributions of ice algae, phytoplankton and benthic microalgae to primary production in nearshore regions of the Beaufort Sea, *Arctic*, 35(4), 485–503.
- Hunt, G. J. L., A. L. Blanchard, P. Boveng, P. Dalpadado, K. F. Drinkwater, L. Eisner, R. R. Hopcroft, K. M. Kovacs, B. L. Norcross, P. Renaud, M. Reigstad, M. Renner, H. R. Skjoldal, A. Whitehouse, and R. A. Woodgate (2013), The Barents and Chukchi Seas: Comparison of two Arctic shelf ecosystems, *Journal of Marine Systems*, 109-110, 43–68.
- Itoh, M., K. Shimada, T. Kamoshida, F. McLaughlin, E. Carmack, and S. Nishino (2012), Interannual variability of Pacific Winter Water inflow through Barrow Canyon from 2000 to 2006, *Journal of Oceanography*, 68(4), 575–592.
- Itoh, M., R. S. Pickart, T. Kikuchi, Y. Fukamachi, K. I. Ohshima, D. Simizu, K. R. Arrigo, S. Vagle, J. He, C. J. Ashjian, J. T. Mathis, S. Nishino, and C. Nobre (2015), Water properties, heat and volume fluxes of Pacific water in Barrow Canyon during summer 2010, *Deep Sea Research I*, 102(C), 43–54.
- Iwamoto, K., K. I. Ohshima, and T. Tamura (2014), Improved mapping of sea ice production in the Arctic Ocean using AMSR-E thin ice thickness algorithm, *Journal of Geophysical Research*, 119, 3574–3594.
- Jakobsson, M. (2002), Hypsometry and volume of the Arctic Ocean and its constituent seas, *Geochemistry, Geophysics, Geosystems*, 3(5), 1–18.
- Jakobsson, M., A. Grantz, Y. Kristoffersen, R. Macnab, R. W. Macdonald, E. Sakshaug, R. Stein, and W. Jokat (2004), The Arctic Ocean: Boundary Conditions and Background Information, in *The Organic Carbon Cycle in the Arctic Ocean*, pp. 1–32, Springer Berlin Heidelberg, Berlin, Heidelberg.
- Johnson, Z., and R. T. Barber (2003), The low-light reduction in the quantum yield of photosynthesis: potential errors and biases when calculating the maximum quantum yield, *Photosynthesis Research*, 75(1), 85–95.
- Joo, H. M., S. H. Lee, S. W. Jung, H.-U. Dahms, and J. H. Lee (2012), Latitudinal variation of phytoplankton communities in the western Arctic Ocean, *Deep Sea Research Part II: Topical Studies in Oceanography*, 81-84, 3–17.

- Kahru, M., V. Brotas, M. Manzano-Sarabia, and B. G. Mitchell (2010), Are phytoplankton blooms occurring earlier in the Arctic?, *Global Change Biology*, 17(4), 1733–1739.
- Kirchman, D., V. Hill, M. T. Cottrell, and R. Gradinger (2009), Standing stocks, production, and respiration of phytoplankton and heterotrophic bacteria in the western Arctic Ocean, *56*(17), 1237–1248.
- Kirk, J. T. O. (2011), *Light and Photosynthesis in Aquatic Ecosystems*, third edition ed., Cambridge University Press, New York.
- Kishino, M., M. Takahashi, N. Okami, and S. Ichimura (1985), Estimation of the spectral absorption coefficients of phytoplankton in the sea, *Bulletin of Marine Science*, 37, 634–642.
- Kolber, Z. S., O. Prášil, and P. G. Falkowski (1998), Measurements of variable chlorophyll fluorescence using fast repetition rate techniques: defining methodology and experimental protocols, *Biochimica et Biophysica Acta (BBA) - Bioenergetics*, 1367(1-3), 88–106.
- Kwok, R., and D. A. Rothrock (2009), Decline in Arctic sea ice thickness from submarine and ICESat records: 1958–2008, *Geophysical Research Letters*, 36(15), L15,501.
- Lee, S. H., T. E. Whitledge, and S.-H. Kang (2007), Recent carbon and nitrogen uptake rates of phytoplankton in Bering Strait and the Chukchi Sea, *Continental Shelf Research*, 27(17), 2231–2249.
- Lee, S. H., H.-J. Kim, and T. E. Whitledge (2009), High incorporation of carbon into proteins by the phytoplankton of the Bering Strait and Chukchi Sea, *Continental Shelf Research*, 29(14), 1689–1696.
- Lee, S. H., H. M. Joo, M. S. Yun, and T. E. Whitledge (2012), Recent phytoplankton productivity of the northern Bering Sea during early summer in 2007, *Polar Biology*, 35(1), 83–98.
- Lesser, M. P. (1996), Elevated temperatures and ultraviolet radiation cause oxidative stress and inhibit photosynthesis in symbiotic dinoflagellates, *Limnology and Oceanography*, 41(2), 271–283.

- Lewis, M., and J. C. Smith (1983), A small volume, short-incubation-time method for measurement of photosynthesis as a function of incident irradiance, *Marine Ecology Progress Series*, 13, 99–102.
- Li, W. K. W., F. A. McLaughlin, C. Lovejoy, and E. C. Carmack (2009), Smallest algae thrive as the Arctic Ocean freshens, *Science*, 326(5952), 539–539.
- Loeng, H., K. Brander, E. Carmack, S. Denisenko, K. Drinkwater, B. Hansen, K. Kovacs, P. Livingston, F. McLaughlin, and E. Sakshaug (2005), Marine Systems, in *Arctic Climate Impact Assessment*, pp. 453–538, Cambridge University Press, Cambridge, UK.
- Lowry, K., G. L. van Dijken, and K. R. Arrigo (2014), Evidence of under-ice phytoplankton blooms in the Chukchi Sea from 1998 to 2012, *Deep Sea Research Part II: Topical Studies in Oceanography*, 105, 105–117.
- Lowry, K., R. S. Pickart, M. Mills, and Z. W. Brown (2015), The influence of winter water on phytoplankton blooms in the Chukchi Sea, *Deep Sea Research Part II: Topical Studies in Oceanography*, 118, 53–72.
- Lowry, K., R. S. Pickart, M. M. Mills, A. Pacini, C. Nobre, and K. R. Arrigoa (2016), Does active convection within leads in sea ice delay phytoplankton blooms?, in *Ocean Sciences Meeting*, New Orleans, LA.
- Martin, J., J. É. Tremblay, J. Gagnon, G. Tremblay, A. Lapoussière, C. Jose, M. Poulin, M. Gosselin, Y. Gratton, and C. Michel (2010), Prevalence, structure and properties of subsurface chlorophyll maxima in Canadian Arctic waters, *Marine Ecology Progress Series*, 412, 69–84.
- Martin, S., and R. Drucker (1997), The effect of possible Taylor columns on the summer ice retreat in the Chukchi Sea, *Journal of Geophysical Research: Oceans (1978–2012)*, 102(C5), 10,473.
- Martini, K. I., P. J. Stabeno, C. Ladd, P. Winsor, T. J. Weingartner, C. W. Mordy, and L. B. Eisner (2016), Dependence of subsurface chlorophyll on seasonal water masses in the Chukchi Sea, *Journal of Geophysical Research: Oceans (1978–2012)*, 121(3), 1755–1770.
- Maske, H., and M. Latasa (2011), Solar ultraviolet radiation dependent decrease of particle

- light absorption and pigments in lake phytoplankton, *Canadian Journal of Fisheries and Aquatic Sciences*, 54(3), 697–704.
- Maslanik, J., J. Stroeve, C. Fowler, and W. Emery (2011), Distribution and trends in Arctic sea ice age through spring 2011, *Geophysical Research Letters*, 38(13), L13,502.
- Matsuoka, A., V. Hill, Y. Huot, M. Babin, and A. Bricaud (2011), Seasonal variability in the light absorption properties of western Arctic waters: Parameterization of the individual components of absorption for ocean color applications, *Journal of Geophysical Research: Oceans (1978–2012)*, 116(C2), C02,007.
- Mills, M. M., Z. W. Brown, K. Lowry, G. L. van Dijken, S. Becker, S. Pal, C. R. Benitez-Nelson, M. M. Downer, A. L. Strong, J. H. Swift, R. S. Pickart, and K. R. Arrigo (2015), Impacts of low phytoplankton  $\text{NO}_3^- : \text{PO}_4^{3-}$  utilization ratios over the Chukchi Shelf, Arctic Ocean, *Deep Sea Research Part II: Topical Studies in Oceanography*, 118, 105–121.
- Mitchell, B. G., M. Kahru, and J. Wieland (2002), Determination of spectral absorption coefficients of particles, dissolved material and phytoplankton for discrete water samples, in *Ocean Optics Protocols for Satellite Ocean Color Sensor Validation, Revision*, NASA, Greenbelt, Maryland.
- Moran, S. B., R. P. Kelly, K. Hagstrom, J. N. Smith, J. M. Grebmeier, L. W. Cooper, G. F. Cota, J. J. Walsh, N. R. Bates, D. Hansell, W. Maslowski, R. P. Nelson, and S. Mulsow (2005), Seasonal changes in POC export flux in the Chukchi Sea and implications for water column-benthic coupling in Arctic shelves, *Deep Sea Research Part II: Topical Studies in Oceanography*, 52(24-26), 3427–3451.
- Muench, R. D., J. D. Schumacher, and S. A. Salo (1988), Winter currents and hydrographic conditions on the northern central Bering Sea shelf, *Journal of Geophysical Research: Oceans (1978–2012)*, 93(C1), 516–526.
- Neale, P. J., R. F. Davis, and J. J. Cullen (1998), Interactive effects of ozone depletion and vertical mixing on photosynthesis of Antarctic phytoplankton, *Nature*, 392(6676), 585–589.
- Nguyen, D., R. Maranger, J.-E. Tremblay, and M. Gosselin (2012), Respiration and bacterial carbon dynamics in the Amundsen Gulf, western Canadian Arctic, *Journal of Geophysical Research: Oceans (1978–2012)*, 117(C9), C00G16.

- Overland, J. E., and A. Roach (1987), Northward flow in the Bering and Chukchi seas, *Journal of Geophysical Research: Oceans (1978–2012)*, *92*(C7), 7097–7105.
- Pabi, S., G. L. van Dijken, and K. R. Arrigo (2008), Primary production in the Arctic Ocean, 1998–2006, *Journal of Geophysical Research: Oceans (1978–2012)*, *113*(C8).
- Pacini, A., R. S. Pickart, G. W. K. Moore, and K. Våge (2016), Hydrographic structure and modification of Pacific winter water on the Chukchi Sea shelf in late spring, in *Ocean Sciences Meeting*, New Orleans, LA.
- Padman, L., and S. Erofeeva (2004), A barotropic inverse tidal model for the Arctic Ocean, *Geophysical Research Letters*, *31*(2).
- Palmer, M. A., G. L. van Dijken, B. G. Mitchell, B. J. Seegers, K. Lowry, M. M. Mills, and K. R. Arrigo (2013), Light and nutrient control of photosynthesis in natural phytoplankton populations from the Chukchi and Beaufort seas, Arctic Ocean, *Limnology and Oceanography*, *58*(6), 2185–2205.
- Palmer, M. A., B. T. Saenz, and K. R. Arrigo (2014), Impacts of sea ice retreat, thinning, and melt-pond proliferation on the summer phytoplankton bloom in the Chukchi Sea, Arctic Ocean, *Deep Sea Research Part II: Topical Studies in Oceanography*, *105*, 85–104.
- Paquette, R. G., and R. H. Bourke (1981), Ocean circulation and fronts as related to ice melt-back in the Chukchi Sea, *Journal of Geophysical Research: Oceans (1978–2012)*, *86*(C5), 4215.
- Parkinson, C. L., and D. J. Cavalieri (2008), Arctic sea ice variability and trends, 1979–2006, *Journal of Geophysical Research: Oceans (1978–2012)*, *113*(C7), C07,003–28.
- Parkinson, C. L., and J. C. Comiso (2013), On the 2012 record low Arctic sea ice cover: Combined impact of preconditioning and an August storm, *Geophysical Research Letters*, *40*(7), 1356–1361.
- Pegau, W. S. (2002), Inherent optical properties of the central Arctic surface waters, *Journal of Geophysical Research: Oceans (1978–2012)*, *107*(C10), SHE16–1–7.
- Pegau, W. S., and C. A. Paulson (2001), The albedo of Arctic leads in summer, *Annals of Glaciology*, *33*(1), 221–224.

- Perovich, D. K. (1993), A theoretical model of ultraviolet light transmission through Antarctic sea ice, *Journal of Geophysical Research*, 98(C12), 22–579–22–587.
- Perovich, D. K. (2002), Ultraviolet Radiation and the Optical Properties of Sea Ice and Snow, in *UV Radiation and Arctic Ecosystems*, pp. 73–89, Springer Berlin Heidelberg, Berlin, Heidelberg.
- Perovich, D. K., and J. W. Govoni (1991), Absorption coefficients of ice from 250 to 400 nm, *Geophysical Research Letters*, 18(7), 1233–1235.
- Perovich, D. K., and C. M. Polashenski (2012), Albedo evolution of seasonal Arctic sea ice, *Geophysical Research Letters*, 39(8).
- Perovich, D. K., and J. A. Richter-Menge (2015), Regional variability in sea ice melt in a changing Arctic, *Phil Trans R Soc A*, 373(2045), 20140,165.
- Perovich, D. K., T. C. Grenfell, J. A. Richter-Menge, B. Light, W. B. Tucker, and H. Eicken (2003), Thin and thinner: Sea ice mass balance measurements during SHEBA, *Journal of Geophysical Research: Oceans (1978–2012)*, 108(C3), 8050.
- Perovich, D. K., K. F. Jones, B. Light, H. Eicken, T. Markus, J. Stroeve, and R. Lindsay (2011), Solar partitioning in a changing Arctic sea-ice cover, *Annals of Glaciology*, 52(57), 192–196.
- Perrette, M., A. Yool, G. D. Quartly, and E. E. Popova (2011), Near-ubiquity of ice-edge blooms in the Arctic, *Biogeosciences*, 8(2), 515–524.
- Pickart, R. S., and D. J. Torres (2002), Hydrography of the Labrador Sea during active convection, *J. Phys. Oceanogr*, 32, 428–457.
- Pickart, R. S., T. J. Weingartner, L. J. Pratt, S. Zimmermann, and D. J. Torres (2005), Flow of winter-transformed Pacific water into the Western Arctic, *Deep Sea Research Part II: Topical Studies in Oceanography*, 52(24-26), 3175–3198.
- Pickart, R. S., L. J. Pratt, D. J. Torres, T. E. Whitledge, A. Y. Proshutinsky, K. Aagaard, T. A. Agnew, G. Moore, and H. J. Dail (2010), Evolution and dynamics of the flow through Herald Canyon in the western Chukchi Sea, *Deep Sea Research Part II: Topical Studies in Oceanography*, 57(1), 5–26.

- Pickart, R. S., M. A. Spall, G. W. K. Moore, T. J. Weingartner, R. A. Woodgate, K. Aagaard, and K. Shimada (2011), Upwelling in the Alaskan Beaufort Sea: Atmospheric forcing and local versus non-local response, *Progress in Oceanography*, 88(1-4), 78–100.
- Pickart, R. S., M. A. Spall, and J. T. Mathis (2013), Dynamics of upwelling in the Alaskan Beaufort Sea and associated shelf–basin fluxes, *Deep Sea Research I*, 76, 35–51.
- Pickart, R. S., G. W. K. Moore, C. Mao, F. Bahr, C. Nobre, and T. J. Weingartner (2016), Circulation of winter water on the Chukchi shelf in early Summer, *Deep Sea Research Part II: Topical Studies in Oceanography*, 130(C), 56–75.
- Platt, T., C. L. Gallegos, and W. G. Harrison (1980), Photoinhibition of photosynthesis in natural assemblages of marine phytoplankton, *Journal of Marine Research*, 38, 687–701.
- Polashenski, C. M., D. Perovich, and Z. Courville (2012), The mechanisms of sea ice melt pond formation and evolution, *Journal of Geophysical Research: Oceans (1978–2012)*, 117(C1), C01,001.
- Polashenski, C. M., D. K. Perovich, D. K. Perovich, K. E. Frey, K. E. Frey, L. W. Cooper, C. I. Logvinova, R. Dacic, B. Light, H. P. Kelly, L. D. Trusel, and M. Webster (2015), Physical and morphological properties of sea ice in the Chukchi and Beaufort Seas during the 2010 and 2011 NASA ICESCAPE missions, *Deep Sea Research Part II: Topical Studies in Oceanography*, 118, 7–17.
- Rösel, A., and L. Kaleschke (2012), Exceptional melt pond occurrence in the years 2007 and 2011 on the Arctic sea ice revealed from MODIS satellite data, *Journal of Geophysical Research: Oceans (1978–2012)*, 117(C5).
- Sakshaug, E., and H. Skjoldal (1989), Life at the ice edge., *Ambio*, 18(1), 60–67.
- Schlitzer, R. (2014), Ocean Data View, <http://odv.awi.de>.
- Serreze, M., M. Holland, and J. Stroeve (2007), Perspectives on the Arctic’s shrinking sea-ice cover, *Science*, 315(5818), 1533–1536.
- Sherr, E. B., B. F. Sherr, and A. J. Hartz (2009), Microzooplankton grazing impact in the Western Arctic Ocean, *Deep Sea Research Part II: Topical Studies in Oceanography*, 56(17), 1264–1273.

- Smith, R. C., and J. J. Cullen (1995), Effects of UV radiation on phytoplankton, *Reviews of Geophysics*, 33(S2), 1211–1223.
- Smith IV, D. C., and J. H. Morison (1993), A numerical study of haline convection beneath leads in sea ice, *Journal of Geophysical Research*, 98(C6), 1–15.
- Sorteberg, A., and J. E. Walsh (2008), Seasonal cyclone variability at 70 N and its impact on moisture transport into the Arctic, *Tellus*, 60(3), 570–586.
- Spall, M. A. (2007), Circulation and water mass transformation in a model of the Chukchi Sea, *Journal of Geophysical Research: Oceans (1978–2012)*, 112(C5).
- Spall, M. A., R. S. Pickart, E. T. Brugler, G. W. K. Moore, L. Thomas, and K. R. Arrigo (2014), Role of shelfbreak upwelling in the formation of a massive under-ice bloom in the Chukchi Sea, *Deep Sea Research Part II: Topical Studies in Oceanography*, 105, 17–29.
- Springer, A., and C. P. McRoy (1993), The paradox of pelagic food webs in the northern Bering Sea—III. Patterns of primary production, *Continental Shelf Research*, 13(5-6), 575–599.
- Stammerjohn, S., R. Massom, D. Rind, and D. Martinson (2012), Regions of rapid sea ice change: An inter-hemispheric seasonal comparison, *Geophysical Research Letters*, 39(6), L06,501.
- Stirling, I. (1997), The importance of polynyas, ice edges, and leads to marine mammals and birds, *Journal of Marine Systems*, 10(1-4), 9–21.
- Stroeve, J. C., M. C. Serreze, M. M. Holland, J. E. Kay, J. Malanik, and A. P. Barrett (2011), The Arctic's rapidly shrinking sea ice cover: a research synthesis, *Climatic Change*, 110(3-4), 1005–1027.
- Strong, A. L., K. Lowry, Z. W. Brown, M. M. Mills, G. L. van Dijken, R. S. Pickart, L. W. Cooper, K. E. Frey, R. Benner, C. G. Fichot, J. T. Mathis, N. R. Bates, and K. R. Arrigo (2016), Mass balance estimates of carbon export in different water masses of the Chukchi Sea shelf, *Deep Sea Research Part II: Topical Studies in Oceanography*, 130(C), 88–99.
- Sukhanova, I. N., M. V. Flint, L. A. Pautova, D. A. Stockwell, J. M. Grebmeier, and V. M. Sergeeva (2009), Phytoplankton of the western Arctic in the spring and summer

- of 2002: Structure and seasonal changes, *Deep Sea Research Part II: Topical Studies in Oceanography*, 56(17), 1223–1236.
- Sverdrup, H. U. (1953), On conditions for the vernal blooming of phytoplankton, *Journal du Conseil International pour l'Exploration de la Mer*, (18), 287–295.
- Tassan, S., and G. M. Ferrari (1995), An alternative approach to absorption measurements of aquatic particles retained on filters, *Limnology and Oceanography*, 40(8), 1358–1368.
- Tassan, S., and G. M. Ferrari (2002), A sensitivity analysis of the ‘Transmittance–Reflectance’ method for measuring light absorption by aquatic particles, *Journal of Plankton Research*, 24(8), 757–774.
- Taylor, J. R., and R. Ferrari (2011), Shutdown of turbulent convection as a new criterion for the onset of spring phytoplankton blooms, *Limnology and Oceanography*, 56(6), 2293–2307.
- Tremblay, J., and J. Gagnon (2009), The effects of irradiance and nutrient supply on the productivity of Arctic waters: a perspective on climate change, in *Influence of Climate Change on the Changing Arctic and Sub-Arctic Conditions*, edited by J. C. J. Nihoul and A. G. Kostianoy, pp. 73–93, Springer Science + Business Media B. V.
- Tremblay, J., C. Michel, K. Hobson, M. Gosselin, and N. Price (2006), Bloom dynamics in early opening waters of the Arctic Ocean, *Limnology and Oceanography*, 51(2), 900–912.
- Tremblay, J.-E., K. Simpson, J. Martin, L. Miller, Y. Gratton, D. G. Barber, and N. M. Price (2008), Vertical stability and the annual dynamics of nutrients and chlorophyll fluorescence in the coastal, southeast Beaufort Sea, *Journal of Geophysical Research: Oceans (1978–2012)*, 113, C07S90.
- Våge, K., G. W. K. Moore, S. Jónsson, and H. Valdimarsson (2015), Water mass transformation in the Iceland Sea, *Deep Sea Research I*, 101(C), 98–109.
- van de Poll, W. H., and A. G. J. Buma (2009), Does ultraviolet radiation affect the xanthophyll cycle in marine phytoplankton?, *Photochemical & Photobiological Sciences*, 8(9), 1295–1301.
- van de Poll, W. H., A.-C. C. Alderkamp, P. J. Janknegt, J. Roggeveld, and A. G. J. Buma (2006), Photoacclimation modulates excessive photosynthetically active and ultraviolet

- radiation effects in a temperate and an Antarctic marine diatom, *Limnology and Oceanography*, 51(3), 1239–1248.
- Vernet, M. (2000), Effects of UV radiation on the physiology and ecology of marine phytoplankton, in *The Effects of UV Radiation in the Marine Environment*, edited by S. de Mora, S. Demers, and M. Vernet, pp. 1–34, Cambridge University Press.
- Villafañe, V. E., K. Sundbäck, F. L. Figueroa, and E. W. Helbling (2003), Photosynthesis in the aquatic environment as affected by UVR, in *UV Effects in Aquatic Organisms and Ecosystems*, edited by E. W. Helbling and H. E. Zagarese, pp. 357–397, Royal Society of Chemistry.
- Walsh, J. J., C. P. McRoy, L. K. Coachman, J. J. Goering, J. J. Nihoul, T. Whitledge, T. H. Blackburn, P. L. Parker, C. D. Wirick, P. G. Shuert, J. M. Grebmeier, A. Springer, R. D. Tripp, D. Hansell, S. Djenidi, E. Deleersnijder, K. Henriksen, B. A. Lund, P. Andersen, F. E. Mullerkarger, and K. Dean (1989), Carbon and nitrogen cycling within the Bering/Chukchi Seas - Source regions for organic matter effecting AOU demands of the Arctic Ocean, *Progress in Oceanography*, 22(4), 277–359.
- Walsh, J. J., D. A. Dieterle, F. R. Chen, J. M. Lenes, W. Maslowski, J. J. Cassano, T. E. Whitledge, D. Stockwell, M. Flint, I. N. Sukhanova, and J. Christensen (2011), Trophic cascades and future harmful algal blooms within ice-free Arctic Seas north of Bering Strait: A simulation analysis, *Progress in Oceanography*, 91(3), 312–343.
- Wang, D., S. M. Henrichs, and L. Guo (2006), Distributions of nutrients, dissolved organic carbon and carbohydrates in the western Arctic Ocean, *Continental Shelf Research*, 26(14), 1654–1667.
- Wang, J., G. F. Cota, and J. C. Comiso (2005), Phytoplankton in the Beaufort and Chukchi Seas: distribution, dynamics, and environmental forcing, *Deep Sea Research Part II: Topical Studies in Oceanography*, 52(24), 3355–3368.
- Wang, M., and J. E. Overland (2009), A sea ice free summer Arctic within 30 years?, *Geophysical Research Letters*, 36(7), L07,502.
- Webb, W. L., M. Newton, and D. Starr (1974), Carbon dioxide exchange of *Alnus rubra*, *Oecologia*, 17(4), 281–291.

- Weingartner, T., K. Aagaard, R. Woodgate, S. Danielson, Y. Sasaki, and D. Cavalieri (2005), Circulation on the north central Chukchi Sea shelf, *Deep Sea Research Part II: Topical Studies in Oceanography*, 52(24–26), 3150–3174.
- Weingartner, T. J., D. J. Cavalieri, K. Aagaard, and Y. Sasaki (1998), Circulation, dense water formation, and outflow on the northeast Chukchi shelf, *Journal of Geophysical Research: Oceans (1978–2012)*, 103(C4), 7647–7661.
- Woodgate, R. A., and K. Aagaard (2005a), Revising the Bering Strait freshwater flux into the Arctic Ocean, *Geophysical Research Letters*, 32(2), L02,602.
- Woodgate, R. A., and K. Aagaard (2005b), Monthly temperature, salinity, and transport variability of the Bering Strait through flow, *Geophysical Research Letters*, 32(4), L04,601.
- Woodgate, R. A., K. Aagaard, J. H. Swift, K. K. Falkner, and W. M. J. Smethie (2005a), Pacific ventilation of the Arctic Ocean’s lower halocline by upwelling and diapycnal mixing over the continental margin, *Geophysical Research Letters*, 32(18), L18,609.
- Woodgate, R. A., K. Aagaard, and T. J. Weingartner (2005b), A year in the physical oceanography of the Chukchi Sea: Moored measurements from autumn 1990–1991, *Deep Sea Research Part II: Topical Studies in Oceanography*, 52(24–26), 3116–3149.
- Woodgate, R. A., T. J. Weingartner, and R. Lindsay (2012), Observed increases in Bering Strait oceanic fluxes from the Pacific to the Arctic from 2001 to 2011 and their impacts on the Arctic Ocean water column, *Geophysical Research Letters*, 39(24), L24,603.
- Zapata, M., F. Rodríguez, and J. L. Garrido (2000), Separation of chlorophylls and carotenoids from marine phytoplankton: a new HPLC method using a reversed phase column and pyridine mobile phases, *Marine Ecology Progress Series*, 195, 29–45.
- Zhang, J., Y. H. Spitz, M. Steele, C. J. Ashjian, R. Campbell, L. Berline, and P. Matrai (2010), Modeling the impact of declining sea ice on the Arctic marine planktonic ecosystem, *Journal of Geophysical Research: Oceans (1978–2012)*, 115(C10015), 1–24.
- Zhang, J., C. J. Ashjian, R. Campbell, and Y. H. Spitz (2015), The influence of sea ice and snow cover and nutrient availability on the formation of massive under-ice phytoplankton blooms in the Chukchi Sea, *Deep Sea Research Part II: Topical Studies in Oceanography*, 118, 122–135.